
Vol. 31, Iss. 1

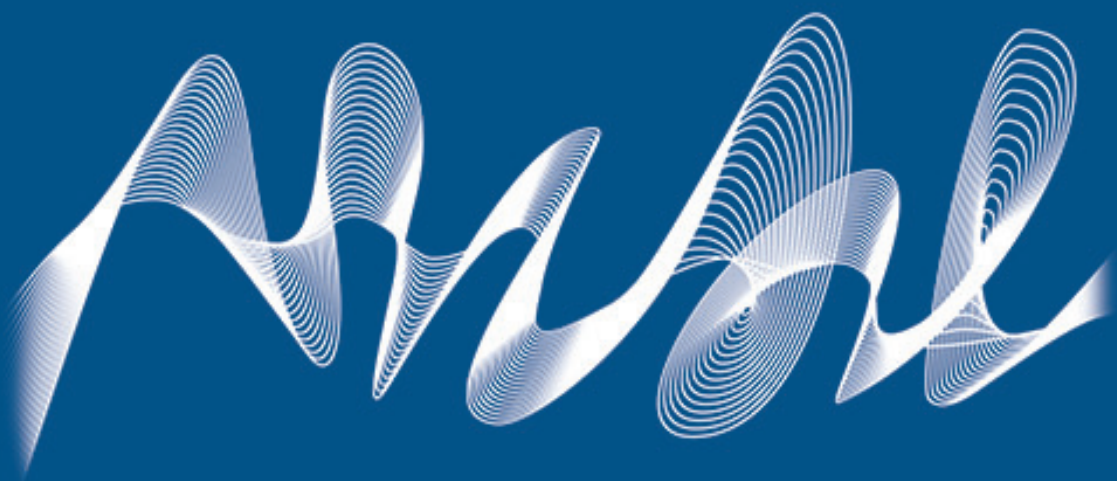
January – February

2024



Physical Oceanography

<http://physical-oceanography.ru/>



ISSN 1573-160X

Vol. 31, no. 1. 2024

January – February

Founded in January 1987

Publication frequency:

6 issues per year

Physical Oceanography

Scientific and theoretical journal

FOUNDER AND PUBLISHER:

Federal State Budget Scientific Institution

Federal Research Centre

“Marine Hydrophysical Institute of RAS”

Peer reviewed scientific journal.

The Journal publishes original research results, review articles (at the editorial board's request) and brief reports on the following sections of hydrophysics:

- thermohydrodynamics of the ocean and atmosphere;
- analysis of observational results and methods of calculation of ocean hydrophysical fields;
- experimental and expeditionary studies;
- satellite hydrophysics;
- mathematical modelling of marine systems;
- automation of scientific research of the seas and oceans.

Objectives

- familiarisation of the world and Russian scientific community with the results of theoretical, experimental and expeditionary studies of the World Ocean;
- exchange of scientific information, experience, research and observation data with specialists from different regions of the country and abroad;
- increase of publication activity of national authors, rating of scientific organisations of Russia and level of national publications in the world scientific community according to their citation data;
- theoretical and practical assistance to scientists in preparing articles for printing that meet modern requirements of publication and scientific ethics;
- strengthening the popularity and authority of the publication, increasing the number of regular subscribers

The Journal is indexed in:

Google Scholar
Web of Science (ESCI)
Scopus
EBSCO Publishing

journal@mhi-ras.ru

<http://physical-oceanography.ru/>

Founder, Publisher and Editorial Office address:

2, Kapitanskaya St., Sevastopol, 299011

Russia

Phone, fax: + 7 (8692) 54-02-23

EDITORIAL BOARD

- Sergey K. Kononov** – Editor-in-Chief, Director of FSBSI FRC MHI, corresponding member of RAS, Dr.Sci. (Geogr.), ORCID ID: 0000-0002-5200-8448, secretary@mhi-ras.ru (Sevastopol, Russia)
- Vladimir N. Belokopytov** – Deputy Editor-in-Chief, Head of Department of FSBSI FRC MHI, Dr.Sci. (Geogr.), ORCID ID: 0000-0003-4699-9588, (Sevastopol, Russia)
- Aleksandr I. Kubryakov** – Deputy Editor-in-Chief, Deputy Director for Science, FSBSI FRC MHI, Dr.Sci. (Phys.-Math.), ORCID ID: 0000-0003-1899-9230, ResearcherID: F-8959-2014, (Sevastopol, Russia)
- Igor K. Ivashchenko** – Executive Editor, Senior Scientist of FSBSI FRC MHI, Ph.D. (Econ.), (Sevastopol, Russia)
- Yuri V. Artamonov** – Head Scientist Researcher of FSBSI FRC MHI, Dr.Sci. (Geogr.), ResearcherID: AAC-6651-2020 (Sevastopol, Russia)
- Sergey V. Berdnikov** – Director of FRC SSC of RAS, Dr.Sci. (Geogr.), ORCID ID: 0000-0002-3095-5532 (Rostov-on-Don, Russia)
- Valery G. Bondur** – Scientific Supervisor of ISR "AEROCOSMOS", academician of RAS, Dr.Sci. (Techn.), ORCID ID: 0000-0002-2049-6176 (Moscow, Russia)
- Demuri I. Demetrasvili** – Head of the sector of mathematical modeling of geophysical processes of sea and atmosphere, the Nodia Institute of Geophysics of the Javakhishvili Tbilisi State University, Dr.Sci. (Phys.-Math.), ORCID ID: 0000-0002-4789-4852 (Tbilisi, Georgia)
- Sergey A. Dobrolyubov** – Dean of Faculty of Geography of MSU, academician of RAS, Dr.Sci. (Geogr.), prof., ResearcherID: A-9688-2012 (Moscow, Russia)
- Grigory I. Dolgikh** – Director of POI FEB of RAS, Dr.Sci. (Phys.-Math.), academician of RAS, prof., ORCID ID: 0000-0002-2806-3834 (Vladivostok, Russia)
- Vladimir A. Dulov** – Head of Laboratory of FSBSI FRC MHI, Dr.Sci. (Phys.-Math.), prof., ORCID ID: 0000-0002-0038-7255, (Sevastopol, Russia)
- Vladimir V. Efimov** – Head of Department of FSBSI FRC MHI, Dr.Sci. (Phys.-Math.), prof., ResearcherID: P-2063-2017, (Sevastopol, Russia)
- Vladimir V. Fomin** – Head of Department of FSBSI FRC MHI, Dr.Sci. (Phys.-Math.), ORCID ID: 0000-0002-9070-4460, (Sevastopol, Russia)
- Isaac Gertman** – Head of the Physical Oceanography Department of Israel Oceanographic & Limnological Research, Head of IOLR data center ISRAMAR, Ph.D. (Geogr.), ORCID ID: 0000-0002-6953-6722 (Haifa, Israel)
- Dmitry G. Gryazin** – Head of Department, Chief Metrologist of SRC of the "Concern CSRI Elektropribor" JSC, Dr.Sci. (Techn.), prof. of Mechatronics of ITMO University, Scopus AuthorID: 25638150600, (Saint Petersburg, Russia)
- Rashit A. Ibraev** – Chief Scientist Researcher of INM of RAS, corresponding member of RAS, Dr.Sci. (Phys.-Math.), ORCID ID: 0000-0002-9099-4541 (Moscow, Russia)
- Vasilily V. Knysh** – Head Scientist Researcher of FSBSI FRC MHI, Dr.Sci. (Phys.-Math.), prof., ResearcherID: B-3603-2018 (Sevastopol, Russia)
- Gennady K. Korotaev** – Scientific Supervisor of FSBSI FRC MHI, corresponding member of RAS, Dr.Sci. (Phys.-Math.), prof., ResearcherID: K-3408-2017 (Sevastopol, Russia)
- Vladimir N. Kudryavtsev** – Executive Director of Satellite Oceanography Laboratory of RSHU, Dr.Sci. (Phys.-Math.), prof., ResearcherID: G-1502-2014 (Saint-Petersburg, Russia)
- Michael E. G. Lee** – Head of Department of FSBSI FRC MHI, Dr.Sci. (Phys.-Math.), prof., ORCID ID: 0000-0002-2292-1877 (Sevastopol, Russia)
- Gennady G. Matishov** – Deputy President of RAS, Deputy academician-Secretary of the Department of Earth Sciences of Supervisor of RAS – Head of the Oceanology, Atmospheric Physics and Geography Section, Scientific Supervisor of SSC of RAS, Supervisor of MMBI KSC of RAS, academician of RAS, Dr.Sci. (Geogr.), prof., ORCID ID: 0000-0003-4430-5220 (Rostov-on-Don, Russia)
- Nikolay A. Rimski-Korsakov** – Deputy Director (Marine Engineering) of FSBSI P.P. Shirshov IO of RAS, Dr.Sci. (Techn.), ResearcherID: K-8378-2017 (Moscow, Russia)
- Angelo Rubino** – Professor of Ca' Foscari University, Ph.D. (Phys. Oceanogr.), ORCID ID: 0000-0003-3857-4811 (Venice, Italy)
- Anatoly S. Samodurov** – Head of Department of FSBSI FRC MHI, Dr.Sci. (Phys.-Math.), ResearcherID: V-8642-2017 (Sevastopol, Russia)
- Georgy I. Shapiro** – Head of Plymouth Ocean Forecasting Centre of the University of Plymouth, Dr.Sci. (Phys.-Math.), prof. in Phys. Oceanogr., (Plymouth, Great Britain)
- Naum B. Shapiro** – Head Scientist Researcher of FSBSI FRC MHI, Dr.Sci. (Phys.-Math.), ResearcherID: A-8585-2017 (Sevastopol, Russia)
- Mikhail V. Shokurov** – Head Scientist Researcher of FSBSI FRC MHI, Dr.Sci. (Phys.-Math.), ORCID ID: 0000-0003-1595-8281 (Sevastopol, Russia)
- Elena F. Vasechkina** – Deputy Director of FSBSI FRC MHI, Chief Research Associate of FSBSI FRC MHI, Dr.Sci. (Geogr.), ORCID ID: 0000-0001-7007-9496 (Sevastopol, Russia)
- Elizaveta V. Zabolotskikh** – Head Scientist Researcher of RSHU, Dr.Sci. (Phys.-Math.), Scopus Author ID: 6506482460 (Saint Petersburg, Russian)
- Vladimir B. Zalesny** – Head Scientific Researcher of INM of RAS, Dr.Sci. (Phys.-Math.), prof., ORCID ID: 0000-0003-3829-3374 (Moscow, Russia)
- Andrey G. Zatsepin** – Chief of Laboratory of FSBSI P.P. Shirshov IO of RAS, Chief Research Associate of FSBSI P.P. Shirshov IO of RAS, Dr.Sci. (Phys.-Math.), ORCID ID: 0000-0002-5527-5234 (Moscow, Russia)
- George Zodiatis** – Senior Researcher of Laboratory of Coastal and Marine Research of the Institute of Applied and Computational Mathematics, for Research and Technology Foundation – Hellas, Ph.D. (Oceanol.), ResearcherID: J-3032-2013 (Heraklion, Crete, Greece)

CONTENTS

Vol. 31, no. 1. 2024

January – February, 2024

ANALYSIS OF OBSERVATIONS AND METHODS OF CALCULATING HYDROPHYSICAL FIELDS IN THE OCEAN

- Korchemkina E. N., Mankovskaya E. V.** Spectral reflectance coefficient, color characteristics and relative transparency of the Black Sea waters in spring, 2019 and 2021: Comparative variability and empirical relationships..... 3
- Sizov A. A., Bayankina T. M., Pososhkov V. L., Yurovskiy A. V.** Interdecadal variability of large-scale atmospheric circulation in the Atlantic-European sector conditioning surface temperature anomalies in the Black, Barents and Norwegian seas 18
- Shatilina T. A., Moroz V. V., Tsitsiashvili G. Sh., Radchenkova T. V.** Formation of large anomalies in the thermal conditions of waters on the western and eastern shelf of the Sakhalin Island 33
- Konik A. A., Atadzhanova O. A.** Variability of decadal horizontal thermohaline gradients on the surface of the Barents Sea during summer season in 1993–2022 46
- Medvedev I. P.** Variance of short-period sea level oscillations in the Black Sea: Seasonal and interannual variations..... 59

EXPERIMENTAL AND FIELD RESEARCH

- Zapevalov A. S., Garmashov A. V.** Ratio between trough and crest of surface waves in the coastal zone of the Black Sea..... 71
- Andrulionis N. Yu., Zavialov I. B., Rozhdestvenskiy S. A.** Major ion composition of waters in the Kerch Strait and the adjacent areas 79

MATHEMATICAL MODELING OF MARINE SYSTEMS

- Pavlushin A. A.** Energy flows between the mean currents and the mesoscale eddies in the eastern and western parts of the Black Sea 99
- Efimov V. V., Yarovaya D. A.** Numerical modeling of the Black Sea response to the intrusion of abnormally cold air in January 23–25, 2010 120
- Chikin A. L., Chikina L. G.** Mathematical model of a flooding process in the Don delta during extreme surges 135



All the materials of the journal are available under Creative Commons Attribution-NonCommercial 4.0 International (CC BY-NC 4.0)

Spectral Reflectance Coefficient, Color Characteristics and Relative Transparency of the Black Sea Waters in Spring, 2019 and 2021: Comparative Variability and Empirical Relationships

E. N. Korchemkina , E. V. Mankovskaya

Marine Hydrophysical Institute of RAS, Sevastopol, Russian Federation

 korchemkina@mhi-ras.ru

Abstract

Purpose. The work is purposed at studying spatial variability of the sea reflectance coefficient using the field data, as well as at obtaining empirical relationships between the colorimetric and bio-optical characteristics and comparing them with the already published data.

Methods and Results. The measurement data on spectral reflectance coefficient of the water column and the Secchi disk depth obtained in the expeditions of the R/V *Professor Vodyanitsky* in the northern and northeastern parts of the Black Sea in April 18 – May 13, 2019 and April 22 – May 8, 2021 were used. Based on the reflectance spectra, the following color characteristics were calculated: dominant wavelength, water color purity, hue angle, and the inherent optical characteristics (absorption of dissolved organic matter and backscattering by suspended particles). Variability of the sea reflectance coefficient and its color characteristics was analyzed for similar periods in spring 2019 and 2021. For the combined data for 2019 and 2021, the relationships between the Secchi disk depth and the reflectance coefficient at maximum, as well as the dominant wavelength were obtained and compared to the known data. For the first time, the empirical relationships connecting the hue angle with the dissolved organic matter absorption and the backscattering by suspended particles were obtained to calculate the inherent optical characteristics of the Black Sea waters.

Conclusions. The distribution of the reflectance coefficient observed in 2019 is more typical of late spring, whereas the similar distribution observed in 2021 rather indicates the continuing winter-spring development of phytoplankton communities that is typical of the deep part of the Black Sea waters in the years with cold winters. Significant correlations between the colorimetric and bio-optical parameters of seawater were established. They can be used as a part of the empirical and semi-analytical algorithms for comprehensive assessing (including application of remote sensing data) the hydrooptical characteristics of the Black Sea waters.

Keywords: spectral reflectance coefficient, Secchi disk depth, dominant wavelength, color purity, hue angle, chromaticity diagram, absorption by dissolved organic matter, particles backscattering, Secchi disk, ocean color

Acknowledgements: The work was carried out within the framework of a state assignment on topics No. FNNN-2024-0016 and No. FNNN-2024-0012, the data were obtained in the 106th and 116th cruises of the R/V *Professor Vodyanitsky* (Center for Collective Use “R/V *Professor Vodyanitsky*” of the Federal State Budgetary Scientific Institution of Federal Research Center “A. O. Kovalevsky Institute of Biology of the Southern Seas of RAS”).

For citation: Korchemkina, E.N. and Mankovskaya, E.V., 2024. Spectral Reflectance Coefficient, Color Characteristics and Relative Transparency of the Black Sea Waters in Spring, 2019 and 2021: Comparative Variability and Empirical Relationships. *Physical Oceanography*, 31(1), pp. 3-17.

© 2024, E. N. Korchemkina, E. V. Mankovskaya

© 2024, Physical Oceanography

Introduction

Marine Hydrophysical Institute of RAS has accumulated and is constantly expanding an array of data from measurements of seawater optical parameters, such as spectral reflectance coefficient of the water column, beam attenuation coefficient,



Secchi disk depth (relative transparency), etc. The analysis of these data provides a good opportunity to study, first of all, the variability of spectral reflectance coefficient, which is the main parameter measured both by contact methods and remotely, as well as color characteristics of water and relationships with other bio-optical parameters.

Various areas of the World Ocean differ in the visible color of waters, which can vary from deep blue to almost brown. The color change is due to the content of impurities of various origins in the water. The spectral reflectance coefficient spectrum and its shape contain information about the color characteristics of water.

The first oceanologic characteristic of water color was the Forel–Ule scale ¹ with different color numbers of test tubes. The result of using this color scale can be somewhat subjective since the color is determined visually. To objectively assess the water color, we use the parameters that represent color in mathematical form based on the three-component theory of human color vision: color coordinates and hue angle, dominant wavelength and color purity ² [1, 2].

This work presents measurement data of spectral reflectance coefficient (Rrs) of the water column and the Secchi disk depth obtained in 2019 and 2021 during the expeditions to the northern and northeastern parts of the Black Sea. The purpose of this work is to analyze the reflectance coefficient spatial variability based on field data, as well as to obtain empirical relationships between color and bio-optical characteristics and compare them with literature data. The work is to some extent a continuation of our paper [3], since in 2021 new contact optical measurement data were obtained in the same area of the sea and during the same period of the year. That let us carry out a comparative analysis of variability of reflectance coefficient and color characteristics of the Black Sea waters, as well as establish new empirical dependencies and clarify those previously obtained.

The use of empirical formulas for the relationship between the studied parameters is a simple way of modeling in the case where the physical nature of the relationship is not important. Empirical relationships between hydro-optical characteristics are regional and seasonal in nature and provide satisfactory results with the correct choice of conditions and variability ranges of the studied parameters. Since color characteristics of seawater are easy to determine, the relationships between them and bio-optical parameters have been used for a long time ³. They are applied as part of empirical and semi-analytical algorithms [4] for a comprehensive assessment of seawater hydro-optical characteristics. Considering certain corrections [5], color characteristics can be calculated from satellite measurements which expands their scope of application.

Materials and methods

This paper examines measurement data of spectral reflectance coefficient (Rrs) of the water column and the Secchi disk depth obtained during R/V *Professor*

¹ Jerlov, N.G., 1976. *Marine Optics*. Amsterdam: Elsevier, 230 p.

² Shifrin, K.S., 1983. [Secchi Disc Depth and the Sea Color]. In: *Introduction to Ocean Optics*. Leningrad: Gidrometeoizdat, pp. 23-30 (in Russian).

³ Mankovsky, V.I., Solov'iev, M.V. and Mankovskaya, E.V., 2009. [*Hydrooptical Properties of the Black Sea. Handbook*]. Sevastopol: MHI NAS of Ukraine, pp. 40-41 (in Russian).

Vodyanitsky expeditions in spring 2019 and 2021 in the Black Sea. The survey was carried out in the Black Sea northern and northeastern parts (42.5°–45.8°N; 31.5°–39.8°E) from 18 April 2019 to 13 May 2019 (106th cruise) and from 22 April 2021 to 8 May 2021 (116th cruise). The spectral reflectance coefficient measurements were carried out from the vessel with a spectrophotometer developed in the Marine Optics and Biophysics Department of Marine Hydrophysical Institute of RAS [6]. The Secchi disk depth (relative transparency) was determined using a standard technique ⁴.

Based on the measured reflectance coefficient spectra, the following color characteristics were calculated: dominant wavelength in the sea radiance spectrum, water color purity and hue angle.

A quantitative assessment of the water color is a dominant wavelength λ_{dom} in the sea radiance spectrum ². It is based on the colorimetric system X, Y, Z (Fig. 1), where the x, y, z chromaticity coordinates are calculated using the following formulas:

$$X = \int_{400}^{700} R_{rs}(\lambda)\bar{x}(\lambda)d\lambda; \quad x = X/(X + Y + Z);$$

$$Y = \int_{400}^{700} R_{rs}(\lambda)\bar{y}(\lambda)d\lambda; \quad y = Y/(X + Y + Z);$$

$$Z = \int_{400}^{700} R_{rs}(\lambda)\bar{z}(\lambda)d\lambda; \quad z = Z/(X + Y + Z);$$

where $\bar{x}(\lambda), \bar{y}(\lambda), \bar{z}(\lambda)$ are functions of spectral sensitivity of the human eye. λ_{dom} value is equal to the wavelength of monochromatic light (called dominant), which must be mixed in a certain proportion with the white light to obtain visible color of the sea (Fig. 1).

Water color purity P is the proportion (percentage) where monochromatic light (dominant wavelength) must be mixed with white light to produce visible color of the sea. The water color purity is related to its transparency: highly transparent waters are characterized by high color purity, while in turbid waters the color purity is low [3]. The value of P is determined by the ratio of two collinear distances $P = E\lambda_d/EA$ (Fig. 1, *bottom*).

For any given point (x, y) on the chromaticity diagram, the value of hue angle α is defined as the value of the angle (in degrees) between the segment connecting the “white point” with the given point (x, y) and X axis [2]. That is, the hue angle α (in degrees) is determined by the following expression:

$$\alpha = (180/\pi)(\arctg((y - y_w)/(x - x_w)))\text{mod } 2\pi,$$

where $x_w = y_w = 1/3$ are coordinates of the white point on the chromaticity diagram (Fig. 1, *bottom*). Blue-green and blue colors correspond to the hue angles

⁴ SOI, 1977. [Determination of the Relative Transparency and Colour of Sea Water]. In: A. N. Ovsyannikov, N. T. Filatov and I. F. Kirillov, eds., 1977. [*Guide to Hydrological Work in the Oceans and Seas*]. Leningrad: Gidrometeoizdat, pp. 299-303 (in Russian).

exceeding 180° . The hue angle decreases with the shift of the dominant wavelength towards the long-wavelength region (Fig. 2).

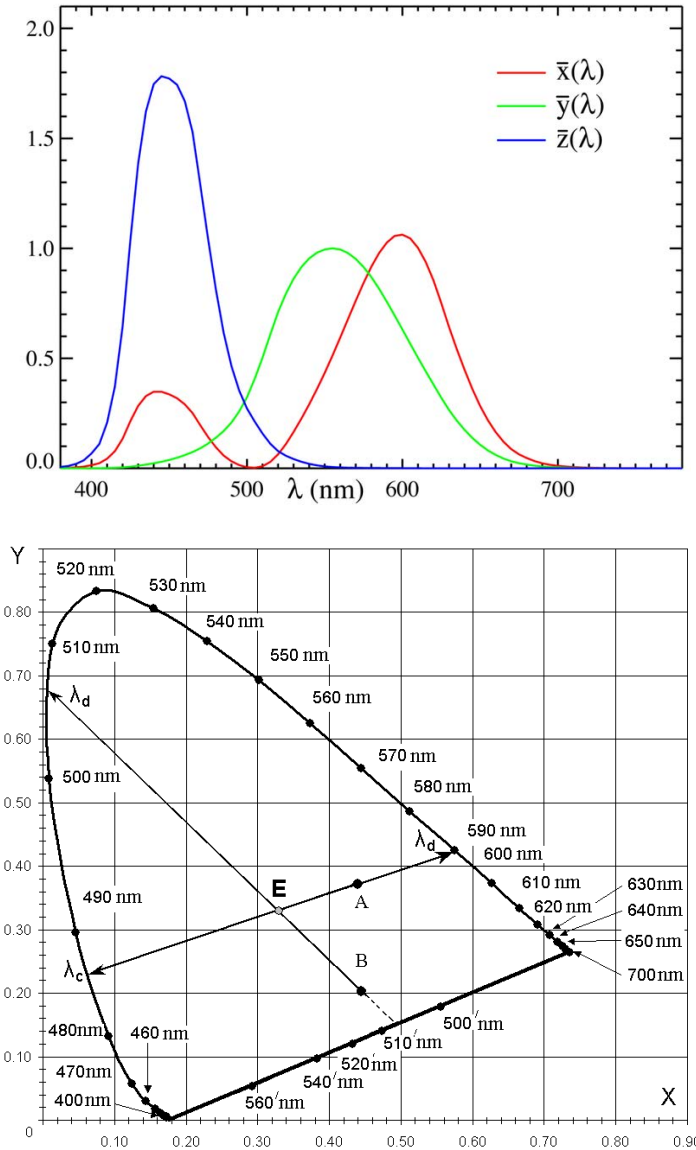


Fig. 1. Spectral sensitivity functions for a standard observer according to CIE 1931⁵ [1] (top); color triangle in x , y coordinates⁶ (bottom): point E is the white color; points A and B are some arbitrary colors; λ_d is the position of dominant wavelength

⁵ Wikimedia Commons. File: CIExy1931.png. [online] Available at: https://upload.wikimedia.org/wikipedia/commons/8/87/CIE1931_XYZCMF.png [Accessed: 23 January 2023].

⁶ Larionova, E.V., 2013. [Physical Foundations of Color]. St. Petersburg, 113 p. (in Russian).

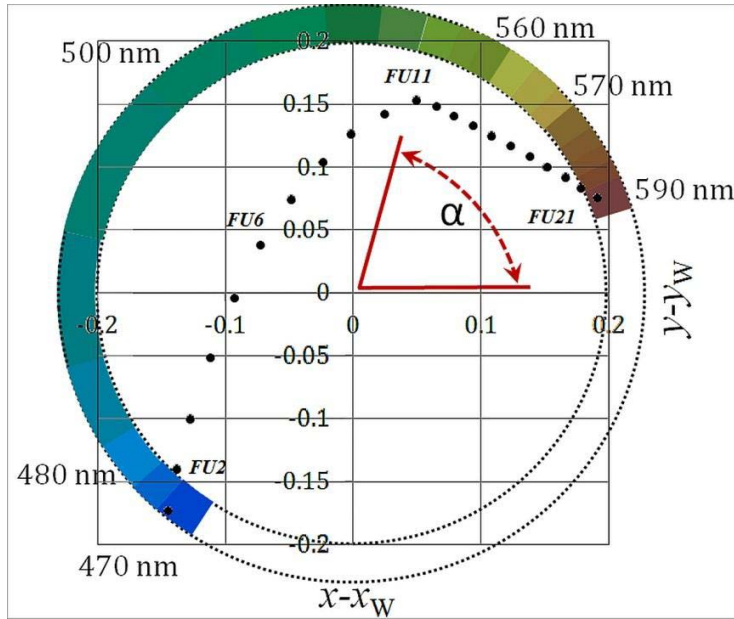


Fig. 2. Chromaticity diagram showing the correspondence of color hue angle α to the white point (x_w, y_w) of the FU scale colors. The dominant wavelength of the specific segment is indicated in nm [2, p. 25667]

We calculate the absorption by dissolved organic matter and suspended particles backscattering using a semi-analytical algorithm [6], where the spectrum of reflectance coefficient has the following form:

$$R_{rs}(\lambda) = k \frac{b_{bw}(\lambda) + b_{bp}(550)(550/\lambda)^\nu}{a_w(\lambda) + C_{ph} a_{ph}^*(\lambda) + a_{org}(440)e^{-S(\lambda-440)}},$$

where $k = 0.15$; $b_{bw}(\lambda)$ is pure water backscattering [7]; $a_w(\lambda)$ is absorption by pure water [8]; $a_{ph}^*(\lambda)$ is a spectrum of specific absorption by phytoplankton pigments (normalized to the chlorophyll a concentration) [9]; $\nu = 1$ is a backscattering spectral slope dependent on particle size⁷; $S = 0.018$ is a spectral slope of absorption by dissolved organic matter [10]; $b_{bp}(550)$ is suspended particle backscattering at 550 nm; C_{ph} is a concentration of phytoplankton pigments and $a_{org}(440)$ is absorption by dissolved organic matter at 440 nm.

Comparative variability of reflectance coefficient and color characteristics

Optical expeditionary measurements were carried out for similar spring periods of 2019 and 2021 which makes it possible to analyze variability of reflectance coefficient and seawater color characteristics.

⁷ Monin, A.S., ed., 1983. *Optics of the Ocean: [In 2 Volumes]*. Moscow: Nauka (in Russian).

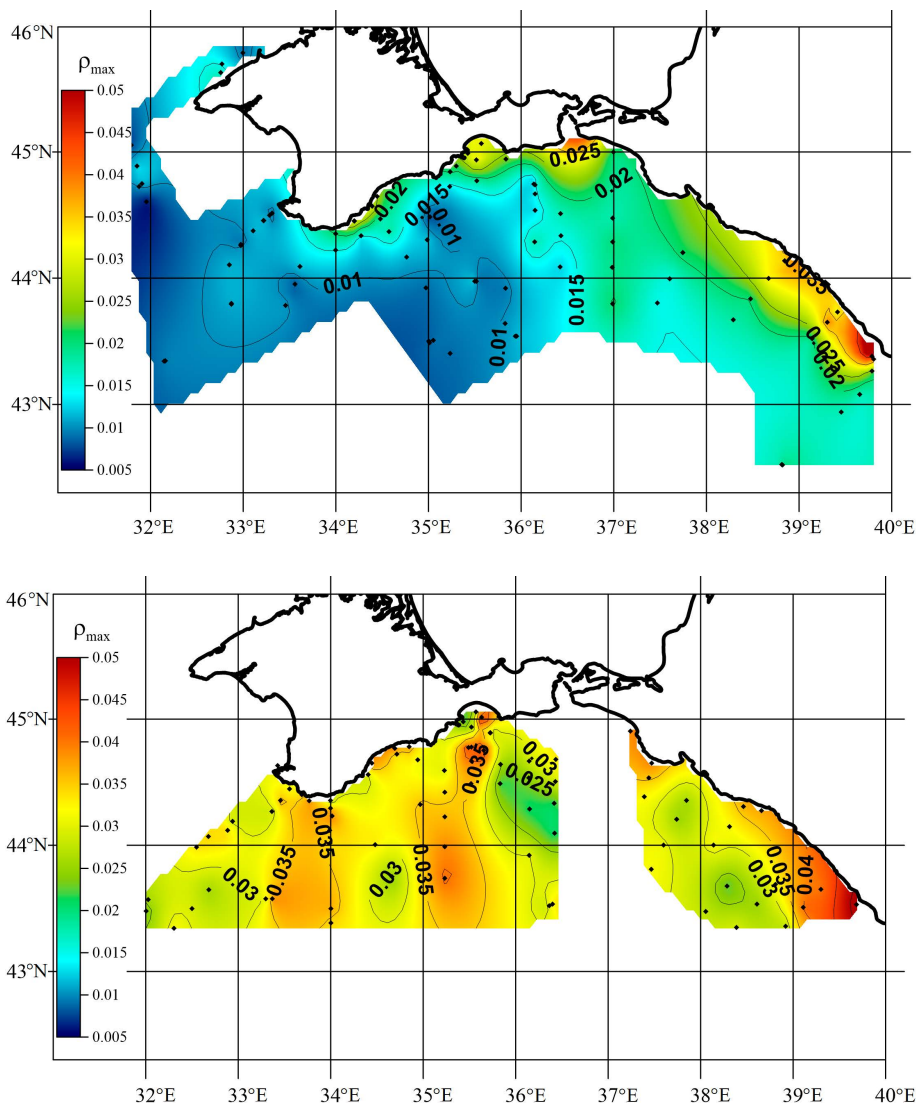


Fig. 3. Distribution of the reflectance coefficient spectral maxima: *a* – in 2019; *b* – in 2021. Black dots show the stations where reflectance measurements were taken

In 2019, the spectra of the water column reflectance coefficient were obtained at 89 stations, in 2021 – at 68. The distribution of the reflectance coefficient spectral maxima according to the expeditionary data is given in Fig. 3. Four regions in the area under study were identified for further analysis:

- 1) northwestern shelf (only in 2019);
- 2) coastal zone of Crimea with depths of up to 200 m;
- 3) coastal zone of the Caucasus with depths of up to 1000 m;
- 4) central deep-sea part.

It should be noted that the division into regions was carried out differently than in paper [3]. Near the Caucasian coast, the shelf zone with depths of up to 200 m

extends 5–6 km off the coast and river plumes propagate beyond it. Therefore, 1000 m isobath that is located, on average, 15 km off the coast was chosen as the coastal zone boundary. In the previous paper, the “eastern part” was different (the area east of 37°E). In the present paper, part of this area was included in the “central deep-sea part.”

The average reflectance coefficient spectra for the selected areas are presented in Fig. 4. The measured and calculated optical characteristics of seawater, averaged over a set of stations in the corresponding region, are given in the Table.

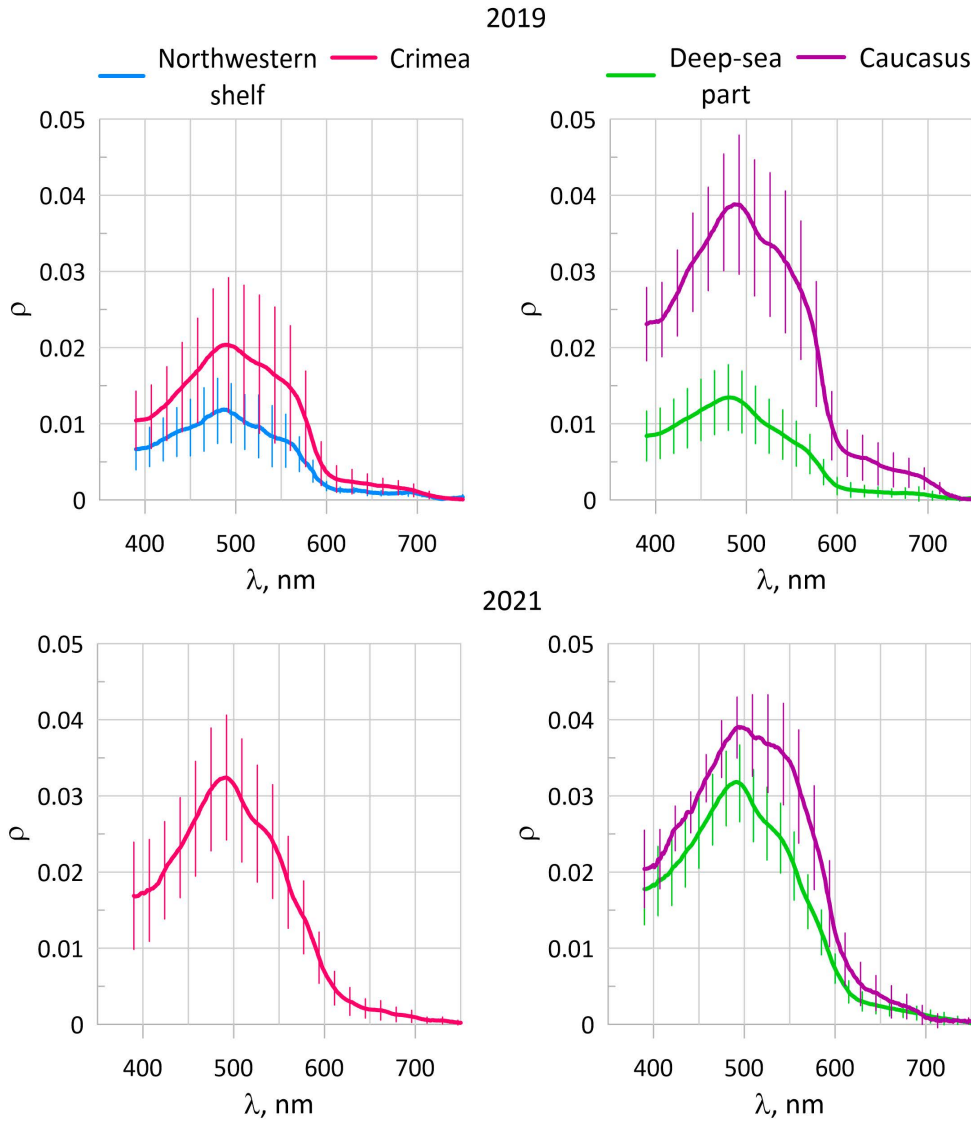


Fig. 4. *Rrs* spectra averaged over the regions and their standard deviation (shown by shading) based on the measurement data obtained in 2019 and 2021

Secchi disk depth (Z_d , m), R_{rs} and its characteristics

Region	Z_d , m	ρ_{max}	λ_{max} , nm	λ_{dom} , nm	P , %	α , °
<i>2019</i>						
Northwestern shelf	12 ± 3	0.012 ± 0.004	485 ± 9	489 ± 2	38 ± 3	192 ± 7
Coastal zone of Crimea	8 ± 3	0.021 ± 0.009	491 ± 6	491 ± 4	35 ± 7	192 ± 16
Central deep-sea part	13 ± 4	0.014 ± 0.004	482 ± 7	485 ± 2	45 ± 6	203 ± 9
Coastal zone of the Caucasus	6 ± 2	0.039 ± 0.009	486 ± 6	489 ± 3	35 ± 7	185 ± 10
<i>2021</i>						
Coastal zone of Crimea	8 ± 2	0.032 ± 0.008	492 ± 5	490 ± 2	36 ± 6	187 ± 7
Central deep-sea part	7 ± 1	0.032 ± 0.005	491 ± 6	490 ± 2	36 ± 4	187 ± 8
Coastal zone of the Caucasus	4 ± 1	0.040 ± 0.005	503 ± 12	495 ± 6	26 ± 7	155 ± 20

Note: ρ_{max} is the R_{rs} spectral maximum; λ_{max} is the corresponding wavelength (nm); λ_{dom} is the dominant wavelength (nm); P is color purity (%); α is hue angle (°). The region-averaged values are given, ± standard deviations over the whole ensemble of measurements.

The R_{rs} in 2019 varies significantly: from 0.005...0.01 (at the spectral maximum) in the area of the northwestern shelf and in the central deep-sea part to 0.03...0.05 in the coastal zones of Crimea and the Caucasus (Fig. 4). The shape of all R_{rs} spectra is characteristic of the Black Sea waters. Small differences are observed where the R_{rs} maximum is located. It is situated in the vicinity of 480 nm in the central deep-sea part and at the northwestern shelf and in the vicinity of 490 nm in the coastal zone of Crimea. The R_{rs} spectrum shape is different for waters in the Sochi region, where a plume was recorded due to the Mzymta River runoff. Here, the R_{rs} spectrum maximum is shifted towards long waves up to 497 nm.

In 2021, the R_{rs} values varied slightly throughout the entire study area. There was practically no difference between the deep-sea and coastal parts both in the spectra shape and in the R_{rs} values. The exception was the R_{rs} values in the Feodosia Bay area. The spread of maximum values was observed from 0.05 in the bay to 0.02 at the shelf outside the bay. Along the Caucasian coast, we also recorded the highest R_{rs} values which were due to river runoff, a known source of suspended matter. In general, the R_{rs} values in 2021 were higher than in 2019.

Observations of the Secchi disk depth Z_d were performed for 69 stations in 2019 and for 48 stations in 2021. In 2019, the observed spread of values ranged from 4 m in the plume near the Caucasus coast to 23 m in the deep-sea part of the Black Sea. In 2021, the spread ranged from 5 to 12 m both in the deep-sea part and in the coastal zone of Crimea, which corresponds to the observed low variability of R_{rs} .

According to all measurements of reflectance coefficient spectra, the variability range of the dominant wavelength values in 2019 was 482-496 nm. According to the chromaticity diagram (see Fig. 2), the color is characterized as blue in the wavelength range of 480-490 nm and blue-green in the range of 490-500 nm. The color shift towards longer wavelengths is estimated to correspond to an increase in the organic matter content in the water.

In 2019, estimated color purity values ranged from 24 to 56%. Low values, i.e., more turbid waters, were observed in the plume near Sochi, near Yalta and Feodosia, as well as in the area of 33°E, 44°N. At these stations, the waters had a more greenish tint than the waters of the rest of the test site according to visual assessments. High color purity values were obtained for the eastern part of the deep-sea region.

In 2021, the variability range of the dominant wavelength values was 486-509 nm. Waters with a greenish tint were observed in the coastal zone off the Caucasus coast, where low color purity values ($P = 13\%$) were also recorded. High values (up to 47%), as in 2019, were noted in the deep-water part.

The meteorological data analysis revealed that weather conditions in 2019 were warmer (air temperature averaged $\sim 2^\circ\text{C}$ higher and was above 0°C in January – March) and there was less precipitation than in 2021. The differences in climate conditions affected formation features of the fields of hydro-optical characteristics. The pattern of R_{rs} distribution differs despite the same calendar periods for carrying out optical measurements. In 2019, the observed R_{rs} distribution was more typical of the spring period, while in 2021 it was more typical of the local climatic winter. This situation is confirmed by the distributions of chlorophyll a and the total suspended matter concentrations obtained from expeditionary measurements. According to biological determinations, chlorophyll a concentrations were on average 2–4 times higher in 2021, which indicates the ongoing winter-spring development of phytoplankton communities. This feature of phytoplankton seasonal dynamics is inherent in the open waters of the Black Sea and is usually observed from January to March [11, 12]. Moreover, the amount of biomass and the duration of phytoplankton development are higher in the years with cold winters than in the years with warm winters [11].

Empirical relationships between color characteristics of reflectance coefficient

Previously, we obtained empirical relationships for the Secchi disk depth, the R_{rs} spectral maximum and the dominant wavelength in our work [3]. The new field data obtained in 2021 make it possible to clarify these relationships, since the measurements were made with the same instrument using the same methodology in similar areas and during the same periods of the year.

For the entire data array for 2019 and 2021, the relation equations for the Secchi disk depth Z_d and the reflectance coefficient values at the maximum ρ_{\max} and the dominant wavelength λ_{dom} have the following form (Fig. 5):

$$\ln\rho_{\max} = -1.08\ln Z_d - 1.59; R = 0.82,$$

$$\ln\lambda_{\text{dom}} = -0.014\ln Z_d + 6.22; R = 0.73.$$

In [13], based on measurements taken in the waters of the tropical Atlantic Ocean, the formula of $\lambda_{\text{dom}} = f(Z_d)$ relationship was obtained for Z_d values within the range of 10–41 m:

$$\ln\lambda_{\text{dom}} = -0.032\ln Z_d + 6.27; R = 0.99.$$

The corresponding relationship is shown by the dashed line in Fig. 5, *right*. This formula in [13] is recommended to be used when estimating λ_{dom} in various waters for Z_d values in the range of 5–41 m. However, according to the considered data from

contact measurements in 2019 and 2021, there is a difference between the empirical relationships proposed in [13] and the ones we obtained. The divergence of the curves is explained by different concentrations of small particles (radii less than 1 μm) in the suspension in the Black Sea and in the tropical Atlantic Ocean waters. According to work [14], the higher the concentration of fine suspended matter, the lower the Secchi disk depth under equal conditions of sea illumination and the light attenuation by water. According to guidebook³ and work [15], the concentration of fine particles in the Black Sea is 5–6 times higher than in the tropical Atlantic Ocean waters, and accordingly the Z_d values are lower.

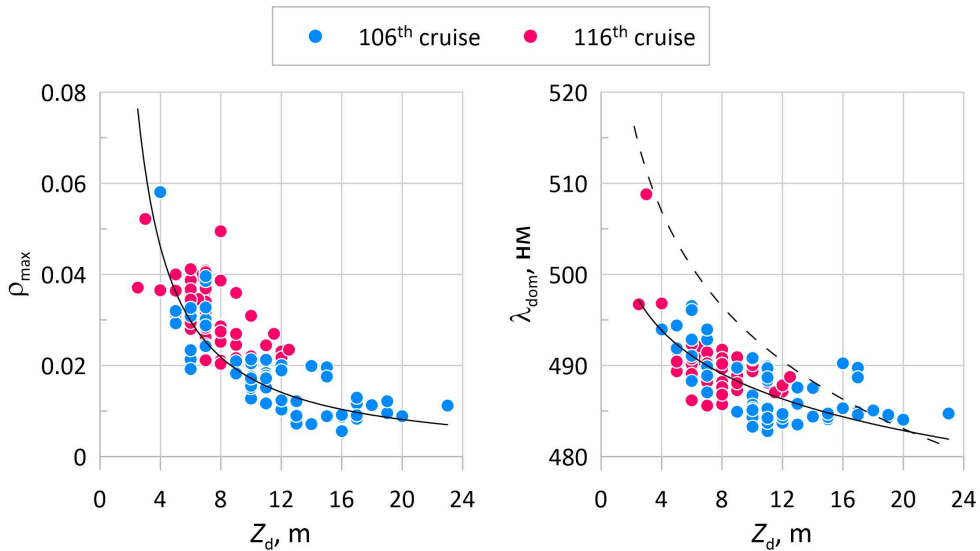


Fig. 5. Relationship between the Secchi disk depth and the reflectance coefficient spectral maximum (*left*) as well as the dominant wavelength (*right*). Solid line is the approximation of the contact measurements in 2019 and 2021, dashed line is the relation equation from [13]

The intersection of the curves $\lambda_{\text{dom}} = f(Z_d)$ at $Z_d = 20$ m (Fig. 5, *right*) can be explained as follows. The concentration of fine suspended matter in the sea decreases from coastal areas, where it reaches its maximum, to central regions due to gradual deposition of fine suspended matter. In areas with $Z_d = 20$ m, the concentration of fine suspended matter was the same as in the waters of the tropical Atlantic Ocean.

Between the values of the Secchi disk depth Z_d and the color purity P (Fig. 6, *left*) a direct correlation takes place:

$$\ln P = 0.42 \ln Z_d - 1.89; R = 0.79.$$

An inverse relationship is observed between color purity P and the dominant wavelength λ_{dom} (Fig. 6, *right*). The corresponding relation equation is:

$$\ln P = 0.04 - 26.02 \ln \left(\frac{\lambda_d}{531} \right); R = 0.91.$$

In [13], the relationship between the water color purity and the relative transparency $P = f(Z_d)$ based on reflectance spectra measurements of the tropical

Atlantic Ocean waters ($Z_d = 10\text{...}41$ m) and in the Black Sea ($Z_d = 3\text{...}16$ m) is expressed by the formula:

$$\ln P = 0.82 \ln Z_d + 1.34; R = 0.98,$$

and the relationship between color purity and the dominant wavelength is expressed by the formula:

$$\ln P = 1.34 - 25.63 \ln(\lambda_d/531).$$

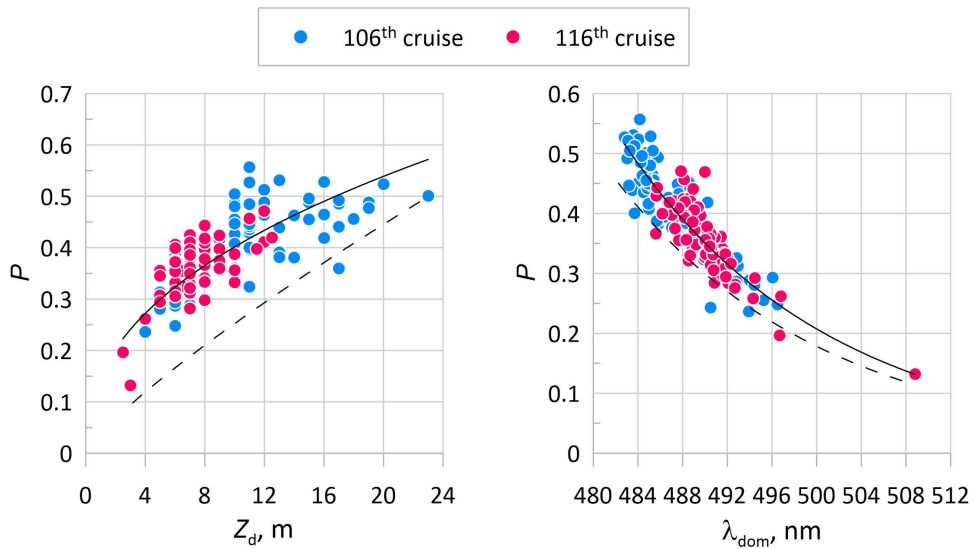


Fig. 6. Relationship between the color purity and the Secchi disk depth (*left*) as well as the dominant wavelength (*right*). Solid line is the approximation of the contact measurements in 2019 and 2021, dashed line is the relation equation from [13]

For the Atlantic Ocean waters, the values of Secchi disk depth Z_d exceeding 10 m and the corresponding part of the relation line $P = f(Z_d)$ from [13] indicated by the dashed line (Fig. 6, *left*) approaches the dependence obtained in our study. Within the range of the Secchi disk depth values 3–23 m observed according to the measurement data in 2019 and 2021, the relation line from [13] lies lower than what we obtained. The difference is due to the fact that the relationship formula in [13] was obtained mainly from Rrs measurements in the Atlantic Ocean and for the Black Sea waters less than ten values from [16, p. 66] were applied. This is also explained by different ratio of large suspended organic particles and small particles of mainly mineral origin in the water. Thus, at the same Secchi disk depth Z_d color purity values may differ and vice versa. For example, in our study the water color purity varied from $P = 13\%$ at $Z_d = 3$ m to $P = 50\%$ at $Z_d = 23$ m. We observed cases when the color purity values were slightly higher (55%), but at the same time the relative transparency was smaller ($Z_d = 10\text{...}13$ m).

The graph in Fig. 6, *left* clearly shows the difference between the location of sets of points for two expeditions. In 2021 (red dots), the concentration of suspended organic particles is higher than in 2019 (blue dots) due to the ongoing winter-spring phytoplankton development, which is reflected in the color purity values – they are

lower. If the data on the composition and abundance of phytoplankton community is available, this type of relationship $P = f(Z_d)$ can presumably be used to assess bio-optical state of the Black Sea waters.

In the Black Sea, the seawater color is determined mainly by dissolved and suspended organic matter; an increase in the light absorption by organic matter in the short-wavelength region of the spectrum leads to the Rrs maximum shift and, as a result, the dominant wavelength shift towards long waves. The hue angle is some function of the dominant wavelength and is therefore related to absorption by organic matter.

In [17], a relationship between the absorption by dissolved organic matter α_{org} and the hue angle α is obtained. It is a polynomial of degree 3:

$$\log(\alpha_{org}(440)) = -7.406 \cdot 10^{-7} \alpha^3 + 2.999 \cdot 10^{-4} \alpha^2 - 0.04493 \alpha + 1.984; R = 0.96.$$

The equation was obtained for various waters of the World Ocean for a wide range of hue angle variability from 50° to 225° . It can also be used for type 2 waters (in accordance with the classification of A. Morel and L. Prieur [18]) with high content of dissolved organic matter and suspended matter. The hue angle value is determined from the remotely measured sea reflectance coefficient Rrs .

The field data in our study have much smaller spread of the hue angle values from 150° to 215° (with the exception of one point where the hue angle is 127°). Therefore, the correlation between α_{org} and α values is less significant and the approximation of their dependence by a polynomial, as in [18], does not differ significantly from the linear one (Fig. 7, *left*) and has the following form:

$$\alpha_{org}(440) = -0.001 \alpha + 0.243; R = 0.70.$$

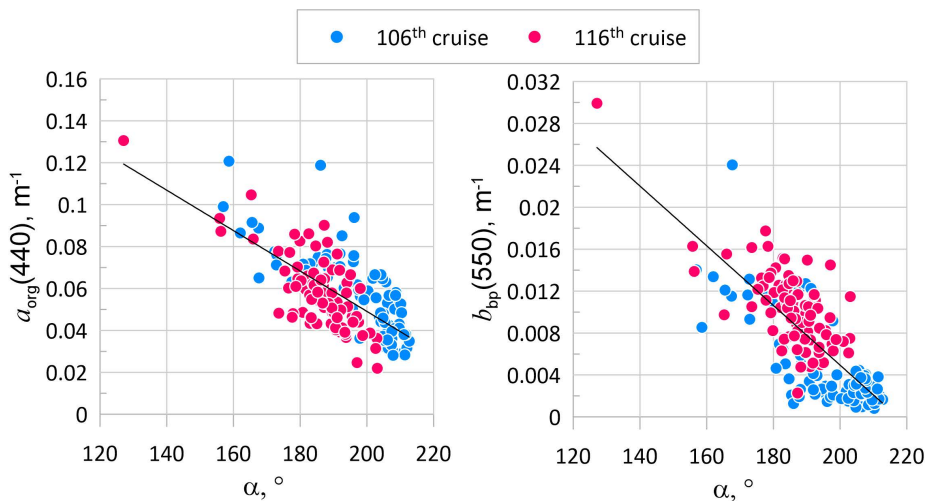


Fig. 7. Relationship between the hue angle and the absorption by dissolved organic matter (*left*) as well as the suspended particles backscattering (*right*)

There is also a correlation between the backscattering of suspended particles and the hue angle. It can be explained by several causes. Firstly, suspended organic matter not only absorbs, but also scatters light, i.e., the waters rich in organic matter

will have a higher suspended matter backscattering. In addition, coastal waters may contain increased amounts of dissolved organic matter and suspended minerals due to runoff from the land.

The approximation of relationship between backscattering by suspended particles b_{bp} and the hue angle α in the Black Sea waters is also presented in the form of a linear relationship (Fig. 7, *right*):

$$b_{bp}(550) = -2.8 \cdot 10^{-4}\alpha + 0.062; R = 0.77.$$

These empirical relationships can be used to calculate inherent optical characteristics in the Black Sea waters: absorption by dissolved organic matter and backscattering by suspended particles. In turn, the hue angle values can be calculated from optical data of the sea remote sensing if the data from contact measurements of the spectral reflectance coefficient are absent.

Conclusion

The measurement data of spectral reflectance coefficient of the water column and the Secchi disk depth obtained during the expeditions in the northern and northeastern parts of the Black Sea from 18 April 2019 to 13 May 2019 and from 22 April 2021 to 08 May 2021 were considered. The analysis of the reflectance coefficient variability and its color characteristics for similar spring periods of 2019 and 2021 revealed the following. All Rrs spectra had a similar shape characteristic of the Black Sea waters. In 2019, high Rrs variability was observed. The lowest values were recorded at the northwestern shelf and in the central deep-sea part of the test site. The increased values were observed in the coastal zones of Crimea and the Caucasus. In 2021, Rrs variability in the area under study was relatively low. There was practically no difference in values between the deep-sea and coastal parts. In general, the Rrs values and its color characteristics in 2021 were higher than in 2019. The values of the seawater color characteristics corresponded mainly to the blue-green color on the chromaticity diagram.

The previous weather conditions in 2019 were warmer and there was less precipitation than in 2021. In 2019, more typical distribution for the second half of spring was observed, while in 2021 the observed distribution indicated a continuing winter-spring development of phytoplankton communities, which was typical for the deep-sea part of the Black Sea in the years with cold winters.

Significant empirical relationships have been established between the Secchi disk depth and the spectral maximum of the reflectance coefficient, the dominant wavelength and color purity. A close correlation is observed between color purity and dominant wavelength. The obtained empirical relationships make it possible to classify Rrs spectra and simplify such approaches as, for example, cluster analysis.

To calculate inherent optical characteristics in the Black Sea waters, empirical relationships between the hue angle and the absorption by dissolved organic matter and backscattering by suspended particles have been obtained for the first time. The hue angle values can be calculated from the remote sensing data of the sea reflectance coefficient if contact measurement data are not available. In the future, it is planned to calculate the hue angle from satellite data using a regional atmospheric correction algorithm for the Black Sea and compare it with the hue angle values obtained in this work from contact measurements of spectral Rrs .

REFERENCES

1. Smith, T. and Guild, J., 1931. The C.I.E. Colorimetric Standards and Their Use. *Transactions of the Optical Society*, 33(3), pp. 73-134. doi:10.1088/1475-4878/33/3/301
2. Van der Woerd, H.J. and Wernand, M.R., 2015. True Colour Classification of Natural Waters with Medium-Spectral Resolution Satellites: SeaWiFS, MODIS, MERIS and OLCI. *Sensors*, 15(10), pp. 25663-25680. doi:10.3390/s151025663
3. Garaba, S.P., Friedrichs, A., Voß, D. and Zielinski, O., 2015. Classifying Natural Waters with the Forel-Ule Colour Index System: Results, Applications, Correlations and Crowdsourcing. *International Journal of Environmental Research and Public Health*, 12(12), pp. 16096-16109. doi:10.3390/ijerph121215044
4. Van der Woerd, H.J. and Wernand, M.R., 2018. Hue-Angle Product for Low to Medium Spatial Resolution Optical Satellite Sensors. *Remote Sensing*, 10(2), 180. doi:10.3390/rs10020180
5. Lee, M.E., Shybanov, E.B., Korchemkina, E.N. and Martynov, O.V., 2015. Determination of the Concentration of Seawater Components based on Upwelling Radiation Spectrum. *Physical Oceanography*, (6), pp. 15-30. doi:10.22449/1573-160X-2015-6-15-30
6. Korchemkina, E.N. and Mankovskaya, E.V., 2022. Relationships between Bio-Optical Parameters of the Black Sea Waters and Spectral Reflectance Coefficient in Spring 2019. *Fundamental and Applied Hydrophysics*, 15(3), pp. 53-64. doi:10.48612/fpg/47v1-8k56-g93n
7. Morel, A., 1974. Optical Properties of Pure Water and Pure Sea Water. In: N. G. Jerlov and E. S. Nielsen, eds., 1974. *Optical Aspects of Oceanography*. New York: Academic Press, pp. 1-24.
8. Smith, R.C. and Baker, K.S., 1981. Optical Properties of the Clearest Natural Waters (200–800 nm). *Applied Optics*, 20(2), pp. 177-184. doi:10.1364/AO.20.000177
9. Churilova, T., Suslin, V., Krivenko, O., Efimova, T., Moiseeva, N., Mukhanov, V. and Smirnova, L., 2017. Light Absorption by Phytoplankton in the Upper Mixed Layer of the Black Sea: Seasonality and Parametrization. *Frontiers in Marine Science*, 4, 90. doi:10.3389/fmars.2017.00090
10. Churilova, T., Moiseeva, N., Efimova, T., Suslin, V., Krivenko, O. and Zemlianskaia, E., 2017. Annual Variability in Light Absorption by Particles and Colored Dissolved Organic Matter in the Crimean Coastal Waters (the Black Sea). In: SPIE, 2017. *Proceedings of SPIE*. Vol. 10466: 23rd International Symposium on Atmospheric and Ocean Optics: Atmospheric Physics. Irkutsk: SPIE, 104664B. doi:10.1117/12.2288339
11. Mikaelyan, A.S., Chasovnikov, V.K., Kubryakov, A.A. and Stanichny, S.V., 2017. Phenology and Drivers of the Winter-Spring Phytoplankton Bloom in the Open Black Sea: The Application of Sverdrup's Hypothesis and Its Refinements. *Progress in Oceanography*, 151, pp. 163-176. doi:10.1016/j.poccean.2016.12.006
12. Finenko, Z.Z., Mansurova, I.M. and Suslin, V.V., 2022. Temporal Dynamics of Phytoplankton Biomass in the Surface Layer of the Black Sea According to Satellite Observations. *Oceanology*, 62(3), pp. 358-368. doi:10.1134/S0001437022030043
13. Mankovsky, V.I., 2017. Color Characteristics of Waters and Their Correlation with Secchi Depth. *Oceanology*, 57(5), pp. 611-614. doi:10.1134/S0001437017050101
14. Mankovsky, V.I., 2019. Influence of the Composition of Suspended Matter on the Secchi Disk Depth. *Atmospheric and Oceanic Optics*, 32(3), pp. 284-288. doi:10.1134/S1024856019030138
15. Man'kovsky, V.I. and Grinchenko, D.V., 2018. Suspended Matter and Its Composition from the Data on Light Scattering at the Large-Scale Polygon in the Northern Part of the Tropical Atlantic Ocean. *Physical Oceanography*, 25(3), pp. 235-246. doi:10.22449/1573-160X-2018-3-235-246
16. Man'kovskii, V.I., Tolkachenko, G.A., Shibanov, E.B., Martynov, O.V., Korchemkina, E.N., Yakovleva, D.V. and Kalinskii, I.A., 2010. Optical Characteristics of Coastal Waters and Atmosphere near the South Coast of the Crimea at the end of Summer 2008. *Physical Oceanography*, 20(3), pp. 207-230. doi:10.1007/s11110-010-9079-x

17. Woźniak, S.B., Darecki, M. and Sagan, S., 2019. Empirical Formulas for Estimating Backscattering and Absorption Coefficients in Complex Waters from Remote-Sensing Reflectance Spectra and Examples of Their Application. *Sensors*, 19(18), 4043. doi:10.3390/s19184043
18. Morel, A. and Prieur, L., 1977. Analysis of Variations in Ocean Color. *Limnology and Oceanography*, 22(4), pp. 709-722. doi:10.4319/lm.1977.22.4.0709

Submitted 24.03.2023; approved after review 04.05.2023;
accepted for publication 15.11.2023.

About the authors:

Elena N. Korchemkina, Senior Research Associate, Marine Hydrophysical Institute of RAS (2 Kapitanskaya Str., Sevastopol, 299011, Russian Federation), CSc (Phys.-Math.), **ORCID ID: 0000-0003-0526-4083**, **WoS ResearcherID: I-1595-2015**, **Scopus Author ID: 23004799100**, korchemkina@mhi-ras.ru

Ekaterina V. Mankovskaya, Senior Research Associate, Marine Hydrophysical Institute of RAS (2 Kapitanskaya Str., Sevastopol, 299011, Russian Federation), CSc (Tech.), **ORCID ID: 0000-0002-4086-1687**, **Scopus Author ID: 57192647961**, **WoS ResearcherID: AAB-5303-2019**, emankovskaya@mhi-ras.ru

Contribution of the co-authors:

Elena N. Korchemkina – carrying out experimental studies, processing measurement data, analysis and synthesis of the research results, editing and supplementing of the paper text

Ekaterina V. Mankovskaya – collecting information for research, processing measurement data, analysis and synthesis of the research results, formulation of conclusions, preparation of the paper text

The authors have read and approved the final manuscript.

The authors declare that they have no conflict of interest.

Original article

Interdecadal Variability of Large-Scale Atmospheric Circulation in the Atlantic-European Sector Conditioning Surface Temperature Anomalies in the Black, Barents and Norwegian Seas

A. A. Sizov, T. M. Bayankina , V. L. Pososhkov, A. V. Yurovskiy

Marine Hydrophysical Institute of RAS, Sevastopol, Russian Federation
 bayankina_t@mail.ru

Abstract

Purpose. The study is aimed at analyzing and assessing the interdecadal variability of winter hydrometeorological fields in the Atlantic-European sector during different phases of the Arctic and North Atlantic Oscillations indices.

Methods and results. The structure of positive (negative) anomalies of the geopotential height was analyzed based on the composite maps of geopotential height anomalies at levels H_{1000} and H_{50} , the North Atlantic Oscillation index was scrutinized using the data from the Climate Prediction Center archives, the sea surface temperature anomalies were surveyed applying the information from the Japan Oceanographic Data Center. The researches covered two periods: a decade of negative and a decade of positive values of the Arctic and North Atlantic Oscillations indices. During a decade of positive values of these indices, the Azores anticyclone and the Icelandic cyclone are intensified, while the Siberian anticyclone weakens. And, on the contrary, during a decade of negative values, the Siberian anticyclone strengthens, while the Azores anticyclone and the Icelandic cyclone wane. Atmospheric circulation in the Atlantic-European sector (the Western Europe subregion) is formed being affected by the Atlantic air masses, and in the Eastern Europe subregion – by the Azores anticyclone and the Siberian anticyclone spur. During a decade of positive phase of the Arctic and North Atlantic Oscillations, the Black Sea surface temperature decreases and becomes lower than the climatic, whereas that of the Barents and Norwegian seas – higher. During a decade of negative phase of the Arctic and North Atlantic Oscillations, the surface temperature of the Black Sea becomes higher, and that of the Barents and Norwegian seas – lower.

Conclusions. During different phases of the Arctic Oscillation, interdecadal variability in the polar vortex intensity affects the redistribution of atmospheric mass between the center of a polar vortex and its boundaries. The consequence of this phenomenon consists in strengthening (weakening) of the Azores, Siberian and Icelandic centers of atmospheric action as well as formation of the interdecadal variability of atmospheric circulation in the Atlantic-European sector. As a result, the pressure structures conditioning the anomalies in surface air and sea surface temperatures with opposite signs are formed in the subregions of the Atlantic-European sector.

Keywords: North Atlantic, hydrometeorological parameters, Black Sea, Barents Sea, Norwegian Sea, temperature anomaly, geopotential, North Atlantic Oscillation, Arctic Oscillation, interdecadal variability

Acknowledgments: The work was carried out within the framework of state assignment on theme FNNN-2024-0014 “Fundamental research of interaction processes in the ocean-atmosphere system which form variability of physical state of marine environment on different spatial-temporal scales”. The authors are grateful to E. I. Dyachkina for her assistance in selecting scientific literature.

For citation: Sizov, A.A., Bayankina, T.M., Pososhkov, V.L. and Yurovskiy, A.V., 2024. Interdecadal Variability of Large-Scale Atmospheric Circulation in the Atlantic-European Sector Conditioning Surface Temperature Anomalies in the Black, Barents and Norwegian Seas. *Physical Oceanography*, 31(1), pp. 18-32.

© 2024, A. A. Sizov, T. M. Bayankina, V. L. Pososhkov, A. V. Yurovskiy

© 2024, Physical Oceanography

Introduction

The main atmospheric circulation characteristics influencing weather conditions in Northern Europe are the North Atlantic Oscillation (NAO) and the Arctic Oscillation (AO). The NAO and the AO regulate the intensity of cyclonic and anticyclonic activity in the North Atlantic and Europe [1].

Works [2, 3] note that the AO is involved in the atmospheric mass redistribution between the Arctic and mid-latitudes from the earth's surface to the lower stratosphere and has close ties to the NAO. The correlation coefficient between the NAO and the AO is 0.95 [3]. A characteristic feature of the negative AO phase is high atmospheric pressure over the polar regions and low pressure in the middle latitudes (about 45°N). The picture is opposite with a positive value of the AO index [4–7]. It is shown in [5] that the AO is the dominant variability mode in the field of surface atmospheric pressure and in the field of geopotential heights in the Northern Hemisphere from 20°N to the North Pole. The variability of atmospheric processes is characterized by surface pressure anomalies of the same sign in the Arctic and anomalies of the opposite sign in mid-latitudes 40°–50°N.

A positive surface pressure anomaly is observed in northeast Asia and over Europe during the positive AO phase, and a negative anomaly is observed over Siberia, the Western Arctic and Greenland. An opposite distribution of surface pressure field anomalies is observed during the negative AO phase [5].

Annual NAO index values correlate well with sea surface temperature. The correlation between winter NAO index values and air temperature anomalies in Northern Europe is 0.7–0.8 [8].

In [8], the main features of the hydrometeorological fields of the North Atlantic in the winter months during different NAO phases were summarized based on an analysis of literary sources. The present paper shows that in the Atlantic-European sector, surface pressure and geopotential height at the H_{50} level in the Azores anticyclone and Icelandic cyclone change inphase in different NAO phases [8]. The Azores anticyclone strengthens and the Siberian anticyclone weakens during the positive NAO phase. At the same time, the anomaly of surface pressure and geopotential height in the Icelandic cyclone is negative, and in the Azores anticyclone it is positive [8]. The process of strengthening and weakening of these atmospheric action centers develops in the opposite direction during the negative NAO phase. As shown in [9, 10], this means for Eastern Europe that the Siberian anticyclone effect on the atmospheric circulation ¹ increases during the negative NAO phase.

It is known that the interdecadal variability of the NAO index phase occurs in antiphase with the variability of the North Atlantic (AMO index) surface temperature [11].

¹ Roshydromet, 2008. *Assessment Report on Climate Change and Its Consequences in Russian Federation*. Moscow: Roshydromet, 2008. Vol. 1: Climate Change. 227 p. Available at: <http://climate2008.igce.ru/v2008/htm/index00.htm> [Accessed: 09 January 2024] (in Russian).

The study is purposed at analyzing and assessing the interdecadal variability of winter hydrometeorological fields in the Atlantic-European sector during different phases of the Arctic and North Atlantic Oscillations indices.

Materials and methods

The work analyzed mean values of hydrometeorological characteristics for January – March from the archives of the Climate Prediction Center and the Japan Oceanographic Data Center.

The mean values of the NAO index, geopotential height anomalies (Monthly/Seasonal Maps and Composites: NCEP/NCAR Reanalysis and other datasets from NOAA Physical Sciences Laboratory) in the selected climate centers of the Azores (25°–40°N, 15°–45°W) and Siberian (5°–55°N, 85°–105°E) anticyclones and the Icelandic cyclone (60°–75°N, 15°–50°W) were retrieved from the Climate Prediction Center archive (https://ftp.cpc.ncep.noaa.gov/wd52dg/data/indices/tele_index.nh). Geopotential height anomalies were analyzed in the surface layer at levels H_{1000} and in the lower stratosphere H_{50} .

Surface temperature values in the Atlantic-European sector were accessed in the Japan Oceanographic Data Center (<https://ds.data.jma.go.jp/tcc/products/elnino/cobesst/cobe-sst.html>).

Results and discussion

Hydrometeorological processes in the Atlantic-European sector in different NAO phases in 1950–2020 were studied. It was noted in [8] that the negative NAO phase was observed in 1960–1970 and the positive – in 1980–1990. Fig. 1 shows the interannual variability of the mean NAO index value for January – March. Negative mean values of the NAO index were observed in 1960–1970, positive ones in 1980–2000 (Fig. 1).

Values of hydrometeorological characteristics averaged over ten-year time intervals were analyzed which made it possible to show the main differences in the values of these characteristics in the studied subregions of the Atlantic-European sector in the indicated decades.

To assess the extreme states of the winter spatial structure of hydrometeorological fields in the Atlantic-European sector, their variability was considered in two ten-year intervals: negative (1961–1970) and positive (1991–2000) NAO index values. The spatial structure of the geopotential height anomaly at the earth's surface (H_{1000}) and in the lower stratosphere (H_{50}) on the Eurasian continent was considered taking into account that the values of the NAO and AO (stratospheric polar vortex) indices are positive in winter months [7]. Geopotential height anomalies at these levels were calculated relative to the 1991–2020 climate series and are shown on composite maps during various NAO phases (Fig. 2).

The geopotential height anomalies near the earth's surface and in the lower stratosphere are similar in structure (Fig. 2) in the decade of negative and decade of positive values of the NAO index, which is consistent with the results of [2, 7].

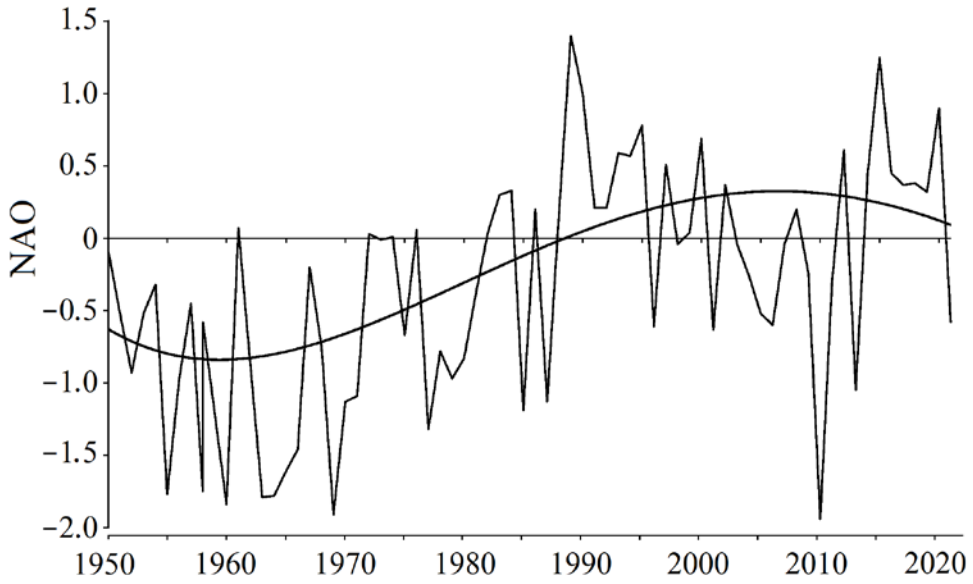


Fig. 1. Interannual variability of the NAO index average values for January – March (thin line) and polynomial trend line (thick line)

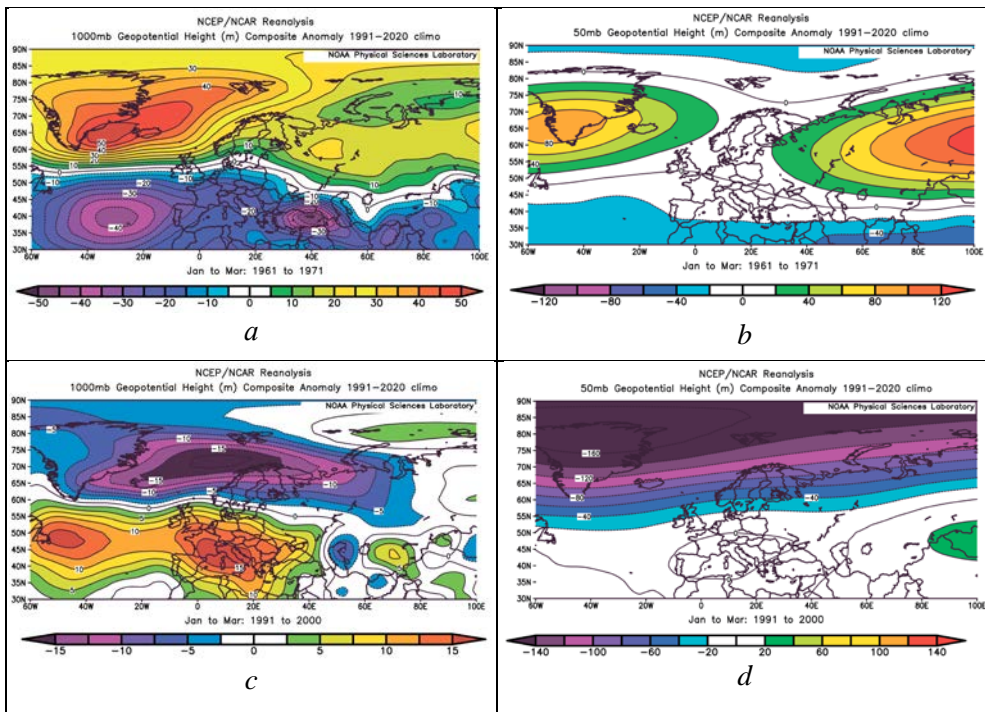


Fig. 2. Composite maps of the geopotential height anomalies at H_{1000} (a, c) and H_{50} (b, d) during the decade (1961–1970) of the NAO index negative phase (a, b) and the decade (1991–2000) of its positive phase (c, d)

In the decade of NAO index negative values (1961–1970), the positive geopotential height anomaly (H_{1000}) extended over the entire Arctic, eastern Europe and Siberia while its negative anomaly was located over Central and Southern Europe (south of 50°N). Fig. 2, *a* shows that in this decade two areas with maximum positive geopotential height anomalies were formed in the subregions of Greenland and Iceland (40–50 m) and in the region of the Siberian anticyclone (20 m). The positive maximum geopotential height anomaly over Greenland is well known as Greenland blocking [12]. According to [1], frequent winter blockings over the North Atlantic are observed in the NAO negative phase. The process of strengthening the Greenland blocking and weakening the Icelandic cyclone occurs simultaneously with the strengthening of the Siberian and weakening of the Azores anticyclone (Fig. 2, *a*). The negative geopotential height anomaly of 40 m occurred in the region of the climatic position of the Azores anticyclone. Another extreme negative anomaly of 30 m was localized near the southeastern part of the Black Sea.

Positive geopotential height anomalies in the subregions of Greenland and the Siberian anticyclone are clearly visible in the lower stratosphere at the H_{50} level. This is especially noticeable in the subregion of the Siberian anticyclone where positive geopotential height anomaly H_{50} exceeds corresponding anomaly H_{1000} by 6–7 times (Fig. 2, *b*).

Distribution features of the geopotential height anomaly (Fig. 2, *a, b*) lead to the provisional conclusion that these anomalies are well expressed in the atmosphere from the surface layer to the lower stratosphere in the decade of NAO index negative values.

In the decade of NAO index positive values (1991–2000), the Azores anticyclone intensified (Fig. 2, *c*) and the positive geopotential height anomaly was about 10 m in its climatic location subregion (near Newfoundland). At the same time, a second center of the Azores anticyclone with a positive geopotential height anomaly of 15 m is formed in the south of Central Europe (in the north of the Apennine Peninsula). The formation of two Azores anticyclone centers can be explained by the Icelandic cyclone intensification. In this decade, the negative geopotential height anomaly in the Icelandic anticyclone reached 15 m (Fig. 2, *c*), its pressure trough divided the Azores anticyclone into two cores. At the same time, the Icelandic cyclone (Fig. 2, *c*) extended its influence to the seas of the North European basin, including the Barents Sea. A stratospheric polar vortex with a negative geopotential height anomaly of 160 m is formed at high latitudes in the lower stratosphere (Fig. 2, *d*).

Assessment of the geopotential height anomaly value is approximate like all the above assessments, since it depends on the choice of climatic average. For the same reason, the geopotential height anomaly was close to zero in the subregion of the Azores anticyclone and the positive anomaly was 20 m in the subregion of the Siberian anticyclone. In this decade, the features of the vertical structure of the geopotential height anomaly in the Azores, Iceland and Siberian centers of atmospheric action were weakly expressed.

Distribution of geopotential height anomalies (Fig. 2) in the surface layer of the Eurasian region gives an idea of the way how the atmospheric circulation changes in the Atlantic-European sector in the decade of negative and decade

of positive values of the NAO index. Consequently, changes appear in the spatial distribution of large-scale anomalies of hydrometeorological fields.

Further, we studied the spatial distribution of the air temperature anomaly in the surface atmosphere layer in the Atlantic-European sector (Fig. 3)

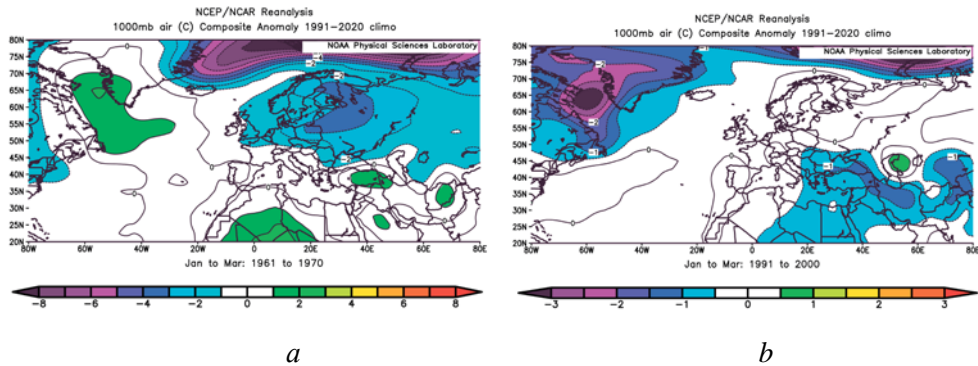


Fig. 3. Anomaly of surface air temperature in the Atlantic-European sector during the decades of negative (1961–1970) (*a*) and positive (1991–2000) (*b*) NAO index values

Distribution of the surface temperature anomaly in the Atlantic-European sector (Fig. 3) shows a good relationship with the distribution of the geopotential height anomaly (Fig. 2). Note that the geopotential height anomaly and atmospheric pressure are closely related [8].

The anticyclonic circulation of the surface atmosphere represented by a positive geopotential height anomaly at the H_{1000} level in the area between Greenland and Iceland “pumped” warm Atlantic air into the Labrador Sea region during the decade of NAO index negative values (1961–1970). A positive anomaly of surface air temperature was formed in this area. This is consistent with the results of [13]. Arctic air was “pumped” into the region of Scandinavia and northern Europe along the eastern periphery of the anticyclone near Greenland and Iceland (Fig. 2, *a*) which led to the formation of a negative anomaly of surface air temperature [13]. In subtropical latitudes (Fig. 3, *a*), the cyclonic circulation formed during the decade of NAO index negative values generated air temperatures in the Southern Europe regions that were close to the climatic.

In the decade of NAO index positive values (1991–2000), the surface air temperature anomaly in the Atlantic-European sector was negative (Fig. 3, *b*). With the strengthening of the Newfoundland core (Fig. 2, *c*), the Azores anticyclone “pumped” Arctic air into the Labrador Sea region forming a negative anomaly of surface air temperature in this area.

The western periphery of the Apennine core of the Azores anticyclone (Fig. 2, *c*) “pumped” Atlantic air into high latitudes forming there an air temperature close to the climatic. The eastern periphery of the Apennine core of the Azores anticyclone transported Arctic air to subtropical latitudes forming a negative anomaly of surface air temperature in this region (Fig. 3, *b*).

The pressure field in Western and Eastern Europe differed widely in the decade of negative and the decade of positive values of the NAO index (Fig. 2, *a*, *b*).

To identify differences in the structure of thermobaric characteristics in the European part, two subregions were selected: western (40° – 70° N, 10° W – 10° E) and eastern (50° – 70° N, 30° E – 50° E) ones. Fig. 4 shows surface pressure and air temperature variability in these subregions.

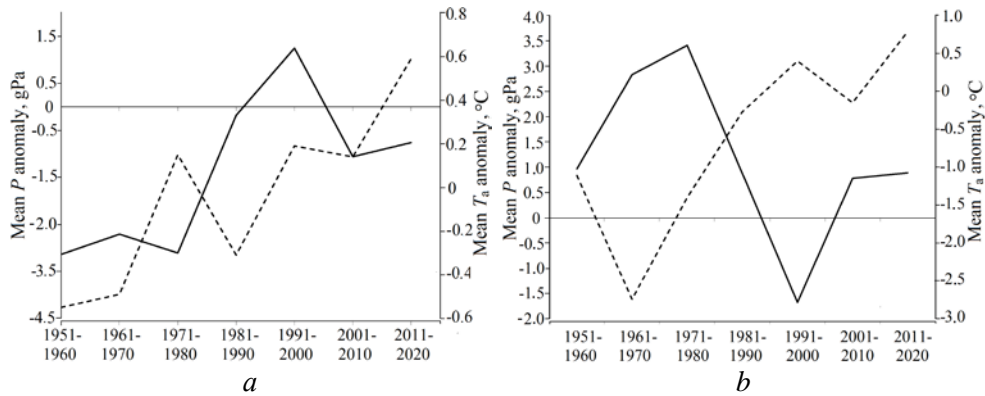


Fig. 4. Anomalies of surface pressure P' (solid line) and air temperature T_a (dashed line) in the western (a) and eastern (b) subregions

The western subregion was in the area of negative surface pressure anomaly (it corresponds to the area of negative geopotential height anomaly at the H_{1000} level in Fig. 2, a) in the decade of NAO index negative values (Fig. 4, a). The eastern subregion (Fig. 4, b) was located in the area of positive surface pressure anomaly (it corresponds to the area of positive geopotential height anomaly at the H_{1000} level in Fig. 2, a). Atmospheric processes in this subregion were influenced greatly by the Siberian anticyclone.

On the contrary, the western subregion (Fig. 4, a) was in the region of a positive surface pressure anomaly (positive geopotential height anomaly at H_{1000}) (Fig. 2, c) and the eastern subregion (Fig. 4, b) – in the area of negative surface pressure anomaly (negative geopotential height anomaly at H_{1000}) (Fig. 2, c) in the decade of NAO index positive values. Therefore, it can be said that the interdecadal variability of the surface pressure anomaly occurred in antiphase in these subregions.

The interdecadal variability of the air temperature anomaly in the western and eastern subregions reflects the thermal influence characteristics of the North Atlantic on the Eurasian continent. It was determined by the variability of the North Atlantic surface temperature anomaly (AMO index [14]) in the western subregion (Fig. 4, a) and it was influenced by processes determined by the Azores anticyclone and the Siberian anticyclone in the eastern subregion (Fig. 4, b).

A negative air temperature anomaly was formed during the Arctic air invasion with the weakening of the Azores and the strengthening of the Siberian anticyclone in the decade of NAO index negative values (Fig. 4, b).

The opposite process was observed in the decade of NAO index positive values (Fig. 4, b): the strengthening of the Azores and weakening of the Siberian anticyclone created a positive air temperature anomaly in the eastern subregion.

The surface thermobaric field in the Atlantic-European sector was manifested in surface pressure and air temperature anomalies in the subregions of the Black Sea

and the North European basin seas. Fig. 5 shows the interdecadal variability of the winter anomaly of these characteristics in the Norwegian and Barents Seas.

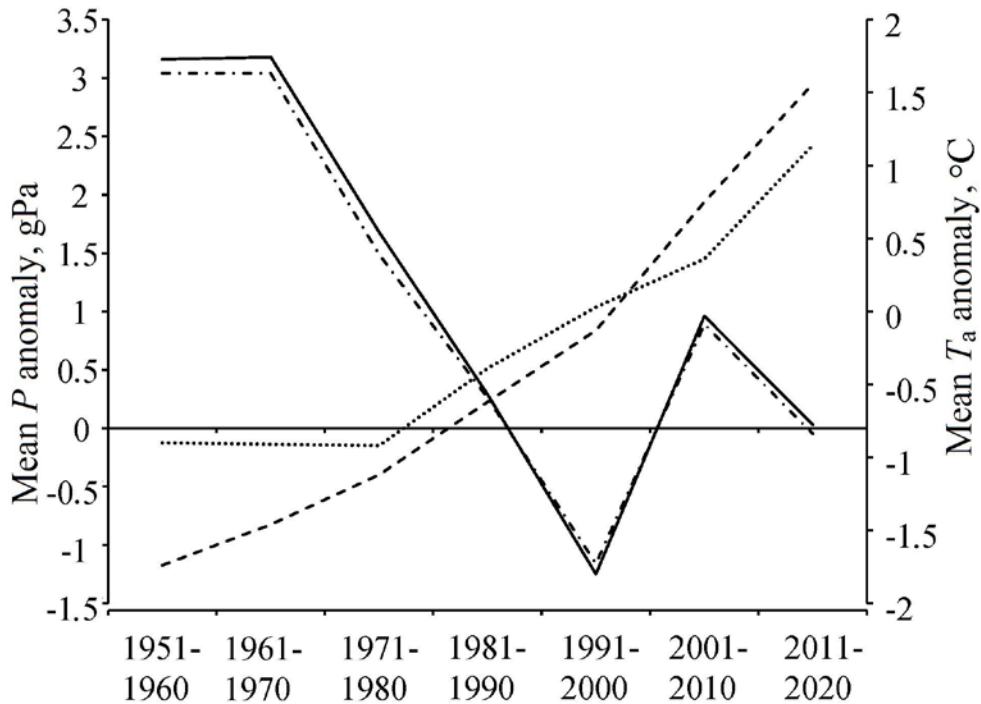


Fig. 5. Interdecadal variability of the atmospheric pressure anomaly P' in the Barents (dash-dotted line) and Norwegian (solid line) seas and the surface air temperature anomalies in the regions of the Barents (dotted line) and Norwegian (dashed line) seas

A positive anomaly of surface pressure was noted during the AO and NAO negative phase (1950–1970) with the developed Greenland blocking [7]. Anticyclonic atmospheric circulation conditions characterized by low air temperatures prevailed during these years over the Norwegian and Barents seas (Fig. 5).

A negative surface pressure anomaly which created cyclonic atmospheric circulation conditions supporting a positive surface air temperature anomaly prevailed in the region of these seas during the decades of the AO and NAO positive phase (1981–2020). The correlation between surface pressure anomalies and air temperature in the region of the Norwegian and Barents Seas is significant and equal to -0.68 .

The formation of the sea surface temperature anomaly occurred with the Atlantic water mass participation brought to the region by the Norwegian Current. Therefore, the interdecadal variability of the surface temperature anomaly of the Norwegian and Barents Seas was largely determined by the corresponding AMO index variability (the mean North Atlantic surface temperature anomaly for January – March).

The AMO index analogue – the mean North Atlantic surface temperature anomaly for January – March – was used to assess the interdecadal variability of the sea surface temperature anomaly. The water area determining this anomaly was limited to coordinates of 30°–60°N, 10°–55°W (Fig. 6).

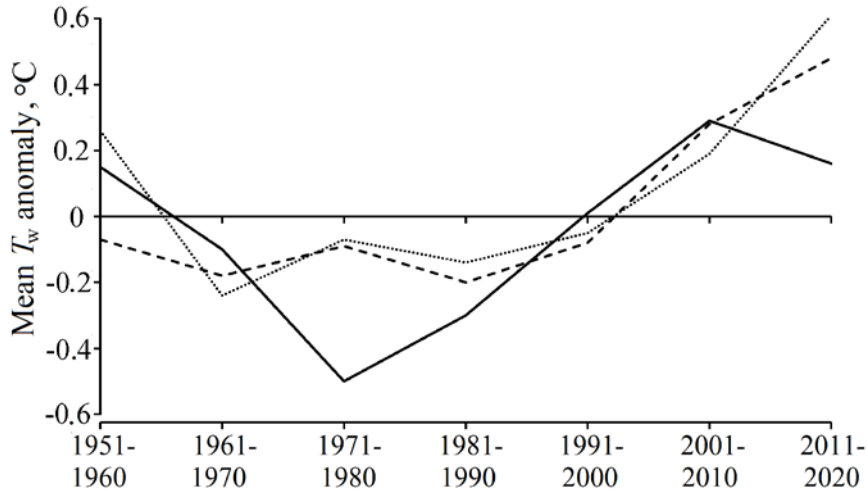


Fig. 6. Interdecadal variability of surface temperature anomaly of the North Atlantic (solid line) and surface temperature of the Norwegian (dashed line) and Barents (dotted line) seas

North Atlantic surface temperatures were below the climatic in 1960–1990 and above it in 1950 and 2000–2020 (Fig. 6). Corresponding anomalies in the surface temperature of the Norwegian and Barents seas were observed in the same decades. The correlation coefficient between the surface temperature anomaly of these seas and the surface temperature anomaly of the North Atlantic is significant and equal to 0.64. It can be assumed that the interdecadal variability in the surface temperature of the Norwegian and Barents Seas was determined mainly by the corresponding variability in the surface temperature of the North Atlantic.

The regions of the Norwegian and Barents Seas were characterized by anomalously high surface pressure in the decade of NAO index negative values (1961–1970) while the Black Sea region – by anomalously low surface pressure. The same antiphase in the distribution of the surface pressure anomaly was observed in the decade of NAO index positive values (1991–2000).

The Black Sea region and the regions of the Norwegian and Barents Seas differ as changes in the surface temperature anomaly of the Atlantic waters do not have a direct impact on the surface temperature formation of the Black Sea [15]. The main contribution to the formation of the surface temperature and Black Sea surface temperature anomalies is made by atmospheric circulation.

In the Black Sea region, cyclonic atmospheric circulation prevailed in the decade of NAO index negative values and anticyclonic circulation prevailed in the decade of NAO index positive values [15].

Fig. 7 shows interdecadal variability of surface air temperature, sea surface temperature and atmospheric pressure in the Black Sea. Atmospheric circulation is represented by the NAO index in this figure.

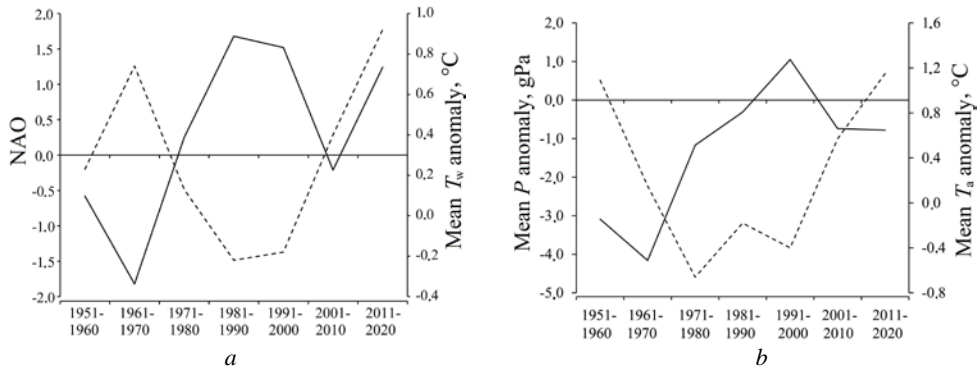


Fig. 7. Interdecadal variability of the NAO index (solid line) and the anomalies of sea surface temperature (dashed line) (a), surface pressure (solid line) and surface air temperature (dashed line) (b) of the Black Sea

Fig. 7 shows that the interdecadal variability of the surface pressure anomaly is consistent with the NAO index variability in the Black Sea region. The correlation coefficient between NAO and atmospheric pressure is 0.90. Accordingly, cyclonic atmospheric circulation conditions prevailed in the region and the sea surface temperature was above the climatic in the decade of NAO index negative values (1961–1970). Anticyclonic atmospheric circulation conditions prevailed in the region and the sea surface temperature was below the climatic in the decade of NAO index positive values (1980–2000).

The interdecadal variability of surface air temperature corresponds to the variability of the sea surface temperature anomaly with a correlation coefficient of 0.64. However, negative values of the surface temperature anomaly in the 1971–1980 and 1991–2000 decades confirm that surface air temperature is formed in the Black Sea region under the influence of the Arctic air intrusion.

Large-scale atmospheric circulation restructuring determined by the AO and NAO indices forms the main features of the surface pressure field structure in the Atlantic-European sector. The mutual influence of the Azores and the Siberian anticyclone on the pressure fields of these subregions is clearly visible in the correlations (Table).

Correlation coefficient between the NAO index and the surface pressure anomaly, hPa, in the western and eastern subregions of Europe

Parameter	P'_w	P'_E
NAO	0.78	-0.73
P'_w	–	-0.79
P'_E	-0.79	–

Note: P'_w is surface pressure anomaly in the western subregion of Europe; P'_E is surface pressure anomaly in the eastern subregion of Europe.

Surface pressure in the western subregion changes in phase with the NAO index, while in the eastern subregion it is in antiphase. Accordingly, surface pressure in the western subregion is higher than the climatic value in the decade of NAO positive values and lower in the decade of its negative values and vice versa in the eastern subregion.

Therefore, it is advisable to consider the spatial structure using composite maps of the surface temperature anomaly of the Norwegian, Barents and Black Seas in the decade of negative (1961–1970) and decade of positive (1991–2000) NAO index values (Figs. 8–10). Fig. 8 shows the values of the surface temperature anomaly of the Norwegian Sea in various NAO phases averaged over January – March.

During the decade of NAO index negative values (Fig. 8, *a*), a positive surface temperature anomaly in the Norwegian Sea was recorded in its southern part, approximately in the localization area of the Norwegian Current. A negative surface temperature anomaly was observed in the northern part of the sea, in the area where the Norwegian and Lofoten gyres are located.

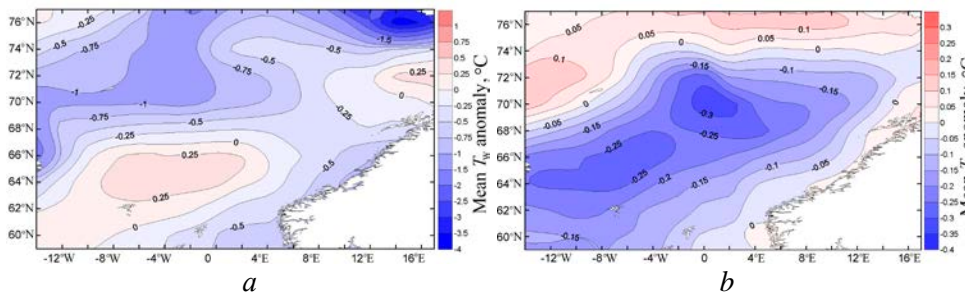


Fig. 8. Surface temperature anomaly in the Norwegian Sea during the decades of negative (*a*) and positive (*b*) values of the NAO index

The positive temperature anomaly shifted to the north of the Norwegian Sea while the negative one – to the south of the sea in the Norwegian Current area in the decade of NAO positive index values (Fig. 8, *b*). One of the reasons for the change in the sign of the surface temperature anomaly in the Norwegian Current could be an increase in the Atlantic water flow through the Faroe-Shetland Strait into the Polar Basin in the years of NAO index negative values [16, 17]. At the same time, the inflow of Atlantic waters into the Norwegian Sea through the Iceland-Faroe threshold and the Denmark Strait increased [18]. The pattern of currents in the Norwegian Sea [18] suggests that the Norwegian Current branch generated cyclonic and anticyclonic gyres in the Norwegian and Lofoten basins in the years of NAO index negative values. This could be the reason for the increase in the negative surface temperature anomaly in the Norwegian Basin and its decrease in the Lofoten Basin (Fig. 8, *a*). The weakening of the Atlantic waters inflow into the Norwegian Sea which is typical for a decade of NAO index positive values [16, 17] could be the reason for the change in the sign of the gyres in the Norwegian and Lofoten basins as a result of which the sign of the surface temperature anomaly in these areas changed (Fig. 8, *b*).

In the Barents Sea, a negative sea surface temperature anomaly with the coldest waters located in its southern and eastern regions was observed during the decade of NAO index negative values (Fig. 9, *a*). Colder waters occupied the eastern and western peripheries of the sea and warmer waters occupied the central part of the Barents Sea in the decade of NAO index positive values (Fig. 9, *b*).

It can be assumed that in this case the localization of areas with warmer and colder water was also determined by the existence of anticyclonic and cyclonic gyres in the Barents Sea region. Thus, it is known that a transformation of the thermohaline characteristics of water masses takes place in the eastern part of the Barents Sea [19]. As a result, a water mass with components of the Fram and Barents Sea branches of Atlantic water is formed [20].

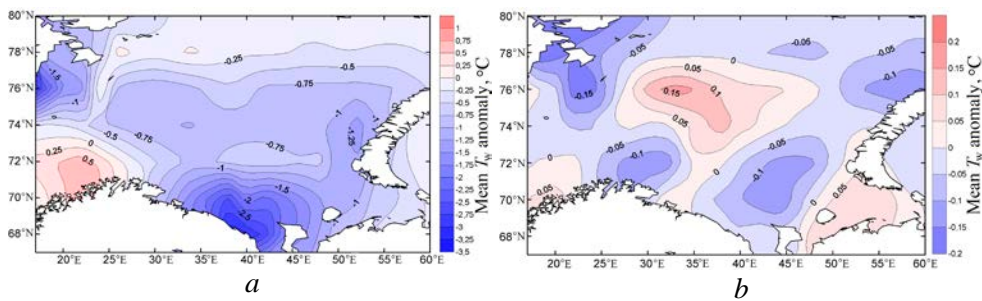


Fig. 9. Surface temperature anomaly in the Barents Sea during the decades of negative (*a*) and positive (*b*) values of the NAO index

Fig. 10 shows the spatial distribution of the Black Sea surface temperature anomaly in the decade of negative and decade of positive NAO index values.

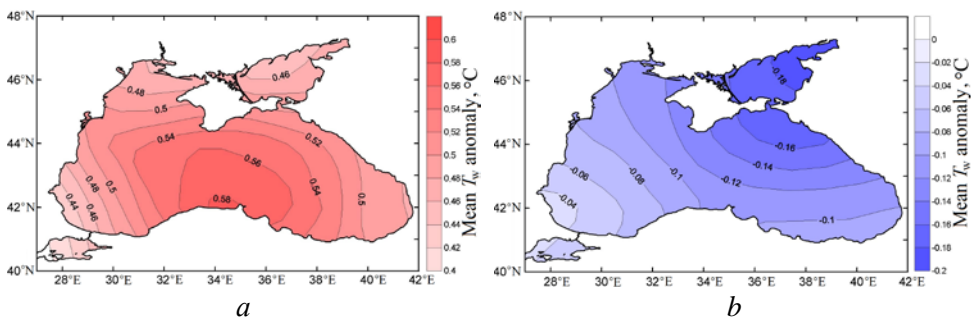


Fig. 10. Surface temperature anomaly of the Black Sea during the decades of negative (*a*) and positive (*b*) values of the NAO index

The surface temperature of the Black Sea is above the climatic in the years of NAO index negative values and cyclonic atmospheric circulation (Fig. 10, *a*) and below the climatic in the years of NAO index positive values with anticyclonic circulation (Fig. 10, *b*) which is consistent with the results given in [15].

Conclusion

1. Interdecadal variability of winter hydrometeorological characteristics in the Atlantic-European sector is regulated by atmospheric circulation. Its large-scale fluctuation is formed to a large extent by the polar vortex dynamics.

2. The Azores, Siberian and Icelandic centers of atmospheric action strengthen or weaken depending on the stage of polar vortex development (AO phase).

3. Local regions with different characteristics of atmospheric circulation are formed in the Atlantic-European sector. They create corresponding anomalies in surface pressure, air temperature and surface temperature in the subregions of Europe and the seas of the North European basin.

REFERENCES

1. Hurrell, J.W., 1995. Decadal Trends in the North Atlantic Oscillation: Regional Temperatures and Precipitation. *Science*, 269(5224), pp. 676-679. doi:10.1126/science.269.5224.676
2. Thompson, D.W.J. and Wallace, J.M., 1998. The Arctic Oscillation Signature in the Wintertime Geopotential Height and Temperature Fields. *Geophysical Research Letters*, 25(9), pp. 1297-1300. doi:10.1029/98GL00950
3. Deser, C., 2000. On the Teleconnectivity of the "Arctic Oscillation". *Geophysical Research Letters*, 27(6), pp. 779-782. doi:10.1029/1999GL010945
4. Kitoh, A., Koide, H., Kodera, K., Yukimoto, S. and Noda, A., 1996. Interannual Variability in the Stratospheric-Tropospheric Circulation in a Coupled Ocean-Atmosphere GCM. *Geophysical Research Letters*, 23(5), pp. 543-546. doi.org/10.1029/96GL00158
5. Overland, J.E., Adams, J.M. and Bond, N.A., 1999. Decadal Variability of the Aleutian Low and Its Relation to High-Latitude Circulation. *Journal of Climate*, 12(5), pp. 1542-1548. doi:10.1175/1520-0442(1999)012<1542:DVOTAL>2.0.CO;2
6. Greatbatch, R.J., 2000. The North Atlantic Oscillation. *Stochastic Environmental Research and Risk Assessment*, 14(4-5), pp. 213-242. doi:10.1007/s004770000047
7. Wanner, H., Brönnimann, S., Casty, C., Gyalistras, D., Luterbacher, J., Schmutz, C., Stephenson, D.B. and Xoplaki, E., 2001. North Atlantic Oscillation – Concepts and Studies. *Surveys in Geophysics*, 22(4), pp. 321-381. doi:10.1023/A:1014217317898
8. Nesterov, E.S., 2013. [*The North Atlantic Oscillation: Atmosphere and Ocean*]. Moscow: Triada Ltd, 144 p. (in Russian).
9. Popova, V.V. and Shmakina, A.B., 2003. Influence of the North Atlantic Oscillation on Multiyear Hydrological and Thermal Regime of Northern Eurasia. I. Statistical Analysis of Observational Data. *Russian Meteorology and Hydrology*, (5), pp. 47-56.
10. Semenov, E.K., Sokolikhina, N.N. and Tudrii, K.O., 2013. The Warm Winter in the Russian Arctic and Anomalous Cold in Europe. *Russian Meteorology and Hydrology*, 38(9), pp. 614-621. doi:10.3103/S1068373913090045
11. Semenov, V.A. and Cherenkova, E.A., 2018. Evaluation of the Atlantic Multidecadal Oscillation Impact on Large-Scale Atmospheric Circulation in the Atlantic Region in Summer. *Doklady Earth Sciences*, 478(2), pp. 263-267. doi:10.1134/S1028334X18020290
12. Li, Y., Ren, R., Cai, M. and Yu, Y., 2020. Climatological Features of Blocking Highs from the Perspective of Air Mass and Mass Transport. *International Journal of Climatology*, 40(2), pp. 782-794. doi:10.1002/joc.6238

13. Van Loon, H. and Rogers, J.C., 1978. The Seesaw in Winter Temperatures between Greenland and Northern Europe. Part 1: Greenland Description. *Monthly Weather Review*, 106(3), pp. 296-310. doi:10.1175/1520-0493(1978)106<0296:TSIWTB>2.0.CO;2
14. Enfield, D.B., Mestas-Nuñez, A.M. and Trimble, P.J., 2001. The Atlantic Multidecadal Oscillation and Its Relation to Rainfall and River Flows in the Continental U.S. *Geophysical Research Letters*, 28(10), pp. 2077-2080. doi:10.1029/2000GL012745
15. Sizov, A.A., Bayankina, T.M., Pososhkov, V.L. and Anisimov, A.E., 2022. Processes Determining Synchronous Interdecadal Variability of Surface Temperature in the Barents and Black Seas. *Physical Oceanography*, 29(3), pp. 257-270. doi:10.22449/1573-160X-2022-3-257-270
16. Dvoryaninov, G.S., Kubryakov, A.A., Sizov, A.A., Stanichny, S.V. and Shapiro, N.B., 2016. The North Atlantic Oscillation: A Dominant Factor in Variations of Oceanic Circulation Systems of the Atlantic Ocean. *Doklady Earth Sciences*, 466(1), pp. 100-104. doi:10.1134/S1028334X16010207
17. Mikhailova, N.V., Bayankina, T.M. and Sizov, A.A., 2021. Two Modes of Atmosphere–Ocean Interaction in the Atlantic Sector of the Arctic Basin. *Oceanology*, 61(4), pp. 443-449. doi:10.1134/S0001437021030097
18. Hughes, S.L., Holliday, N.P. and Gaillard, F., 2012. Variability in the ICES/NAFO Region between 1950 and 2009: Observations from the ICES Report on Ocean Climate. *ICES Journal of Marine Science*, 69(5), pp. 706-719. doi:10.1093/icesjms/fss044
19. Ashik, I.M., Ivanov, V.V., Kassens, H., Makhotin, M.S., Polyakov, I.V., Timokhov, L.A., Frolov, I.E. and Hoelemann, J.A., 2015. Major Results of Oceanographic Studies of the Arctic Ocean during the Last Decade. *Arctic and Antarctic Research*, 1(103), pp. 42-56 (in Russian).
20. Ivanov, V.V. and Aksenov, E.O., 2013. Atlantic Water Transformation in the Eastern Nansen Basin: Observations and Modelling. *Arctic and Antarctic Research*, 1(95), pp. 72-87 (in Russian).

Submitted 28.03.2023; approved after review 29.06.2023;
accepted for publication 15.11.2023

About the authors:

Anatoly A. Sizov, Senior Researcher, Marine Hydrophysical Institute of RAS (2 Kapitanskaya Str., Sevastopol, 299011, Russian Federation), CSc (Phys.-Math.), **WOS ResearcherID: S-1481-2019**, **ORCID ID: 0000-0001-9055-4768**, sizov_anatoliy@mail.ru

Tatiana M. Bayankina, Senior Researcher, Marine Hydrophysical Institute of RAS (2 Kapitanskaya Str., Sevastopol, 299011, Russian Federation), CSc (Geogr.), **WoS ResearcherID: G-2535-2019**, **ORCID ID: 0000-0002-7394-7110**, bayankina_t@mail.ru

Vladimir L. Pososhkov, Researcher, Marine Hydrophysical Institute of RAS (2 Kapitanskaya Str., Sevastopol, 299011, Russian Federation), **ORCID ID: 0000-0002-3891-2772**, vla_po@mail.ru

Alexander V. Yurovskiy, Researcher, Marine Hydrophysical Institute of RAS (2 Kapitanskaya Str., Sevastopol, 299011, Russian Federation), CSc (Geogr.), **ResearcherID: S-1551-2019**, a_yurovsky@mail.ru

Contribution of the co-authors:

Anatoly A. Sizov – general scientific supervision of the research; formulation of the goals and objectives; writing an article text; analysis of results and their interpretation; description of the research results; discussion of the research results; formulation of conclusions; critical text analysis

Tatiana M. Bayankina – review of literature on the research problem; editing the article text; analysis of research results; drawing graphs; participating in the discussion of the article materials; formulation of conclusions

Vladimir L. Pososhkov – collection of available materials on the research topic; data systematization; methodology; data visualization and presentation; construction of composite maps; participation in the discussion of article materials

Alexander V. Yurovskiy – collection of available materials on the research topic; data systematization; data analysis; methodology; software debugging for data processing; construction of composite maps; data visualization; participation in the discussion of article materials

The authors have read and approved the final manuscript.

The authors declare that they have no conflict of interest.

Original article

Formation of Large Anomalies in the Thermal Conditions of Waters on the Western and Eastern Shelf of the Sakhalin Island

T. A. Shatilina¹, V. V. Moroz^{2, ✉}, G. Sh. Tsitsiashvili³,
T. V. Radchenkova³

¹ Russian Federal Research Institute of Fisheries and Oceanography,
Pacific Branch of FSBSI VNIRO (TINRO), Vladivostok, Russian Federation

² V. I. Il'yichev Pacific Oceanological Institute, Far Eastern Branch of Russian Academy of Sciences,
Vladivostok, Russian Federation

³ Institute of Applied Mathematics, Far Eastern Branch of Russian Academy of Sciences,
Vladivostok, Russian Federation

✉ moroz@poi.dvo.ru

Abstract

Purpose. The study is aimed at identifying the mechanisms forming large anomalies in the water thermal conditions on the western and eastern shelf of Sakhalin Island being impacted by the atmospheric processes in spring-summer periods.

Methods and results. The data of coastal observation stations performed by the Hydrometeorological Centre of Russia in 1980–2021 permitted to study and assess the multi-year variability of water thermal regime in the fishery regions on the western and eastern Sakhalin shelf from May to August. The extreme fluctuations of monthly average thermal conditions of the water areas were revealed. The years known for formation of large negative and positive anomalies in the water thermal conditions were determined using the criterion analysis method. The fact that frequency of arising of large negative anomalies exceeds that of large positive ones was found. It was established that the mechanisms forming large anomalies were conditioned by the regional features of atmosphere circulation, i.e. by the abnormal changes in development and spreading of the atmosphere action centers (summer Far East depression, Okhotsk anticyclone and Hawaiian maximum). The cause-effect relations were determined.

Conclusions. In Sakhalin Island coastal regions, formation of large anomalies in the water thermal regime is conditioned by the abnormal changes of the baric fields structures in the regional atmosphere action centers, as well as by the changes in their local impact.

Keywords: Sakhalin Island shelf, large temperature anomalies, thermal regime, water dynamics, Sea of Japan, Sea of Okhotsk, atmosphere action centers

Acknowledgments: The work was carried out within the framework of state assignment of POI FEB RAS on theme No. 0211-2021-0008, state registration No. 121021700346-7, and state assignment of IAM FEB RAS No. 0075-01290-23-00. The authors are thankful to the software developers for the opportunity of using the data posted on the Global Meteorological Network and *JMA* websites, as well as to the reviewer for useful comments.

For citation: Shatilina, T.A., Moroz, V.V., Tsitsiashvili, G.Sh. and Radchenkova, T.V., 2024. Formation of Large Anomalies in the Thermal Conditions of Waters on the Western and Eastern Shelf of Sakhalin Island. *Physical Oceanography*, 31(1), pp. 33-45.

© 2024, T. A. Shatilina, V. V. Moroz, G. Sh. Tsitsiashvili, T. V. Radchenkova

© 2024, Physical Oceanography



Introduction

Currently, due to the increasing frequency of large anomalies of hydrometeorological phenomena in the backdrop of global warming, much attention is paid to the analysis of these anomalies [1–4].

The subject of this work is to study the features of large anomalies formation in the water thermal conditions on the western and eastern coasts of Sakhalin Island in summer. Water areas under consideration (Fig. 1) are characterized by complex hydrological conditions due to significant length of the island from the south to the north (about 1000 km between 46°N and 55°N). A set of factors that determine features of the area hydrological regime includes the presence of waters of various origins washing the western and eastern coasts of the island (warm Tsushima Current waters of the Sea of Japan and cold East-Sakhalin Current waters of the Sea of Okhotsk, respectively), redistribution of these waters by the system of coastal currents under conditions of indented coastline, as well as the monsoon nature of atmospheric processes with seasonal variations in wind direction [5].

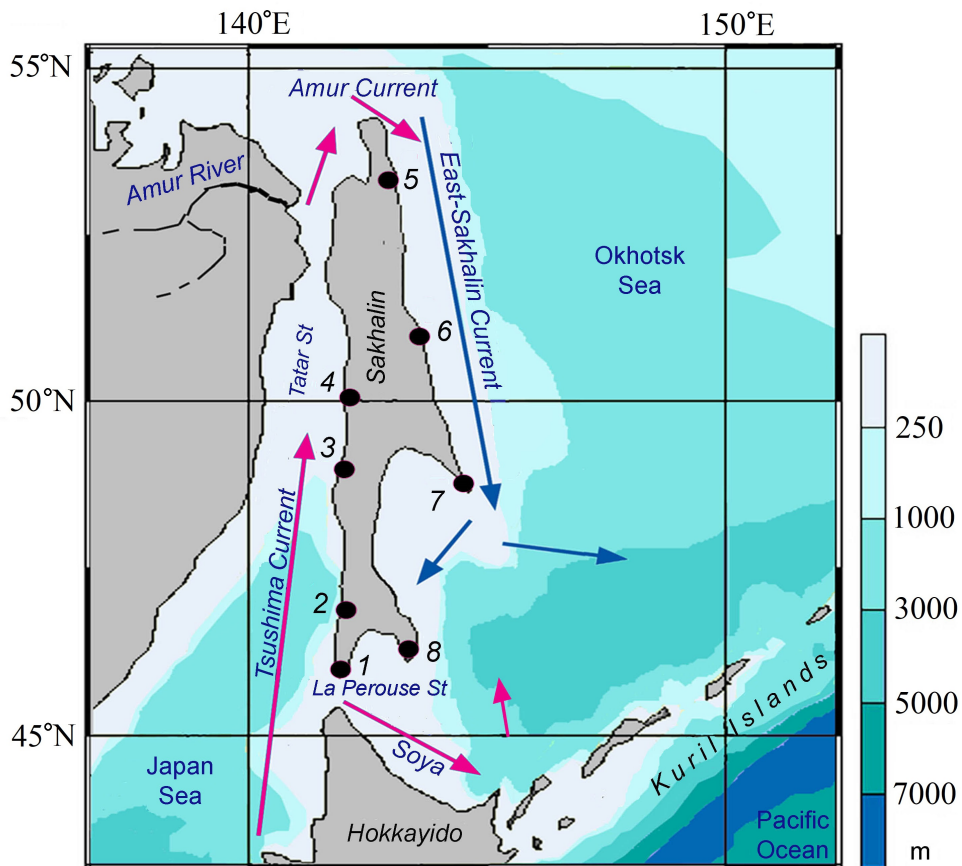


Fig. 1. Region under study. Location of the hydrometeorological stations (HMS): 1 – Cape Krilyon, 2 – Kholmok, 3 – Uglegorsk, 4 – Pilvo, 5 – Odoptu, 6 – Komrvo, 7 – Cape Terpeniya, 8 – Novikovo

At the same time, the Sakhalin Island waters are important fishery regions in the Far East seas with numerous catch. These are areas of high biological productivity, areas of reproduction of pink salmon which forms the basis of the Asian salmon catch. Its life cycle is largely determined by such an important factor as thermal conditions. However, abnormally low temperatures at the river mouths during the fry migration (May–June) can lead to its death, and extremely high temperatures near the coast affect migration and spawning (July–August) negatively. The formation of abnormally cold or warm thermal conditions in some years leads to the displacement of catch regions which causes difficulties in fishery forecasting [6, 7]. In this regard, the study of cause-effect relations and factors affecting the formation of anomalous thermal conditions in these waters is of particular importance.

In recent decades, the relationship between thermal regime variability during the summer fishing period and the development intensity of regional atmosphere action centers (AAC) has been assessed and their relationship has been identified in a number of areas in the Sea of Japan and the Sea of Okhotsk. The differences in the variability of baric fields in the years with thermal regime anomalies are shown [8, 9]. The approaches for identifying previous baric structures that affect the formation of anomalous conditions of water thermal regimes [10] were proposed.

At the same time, in the areas of the Sakhalin Island shelves of the Sea of Japan and the Sea of Okhotsk the causes for formation of anomalous thermal conditions in certain years are not clear enough. Questions about the formation mechanisms of large cold and warm thermal anomalies in these waters remain open. Identification of these mechanisms and assessment of cause-effect relations constituted the purpose of this study.

The following tasks were resolved under this study:

- research and assessment of interannual variability of the water thermal regime for the period from May to August on the western Sakhalin shelf – the zone affected by the waters of the warm Tsushima Current (HMS Kholmsk, HMS Ulegorsk, HMS Pilvo) and its branch in the Sea of Japan, the Soya Current (HMS Cape Crilyon), as well as on the eastern Sakhalin shelf (HMS Odoptu, HMS Komrvo, HMS Cape Terpeniya, HMS Novikovo) – the zone affected by cold waters of the East-Sakhalin Current (Fig. 1);

- identification of years with large anomalies of thermal conditions from May to August at each HMS;

- assessment of AAC role in the mechanisms forming large anomalies in the water thermal regimes taking into account the features of hydrological conditions in each region.

Data and methods

To study the long-term variability of thermal regime in the region coastal waters, water temperature observations from ESIMO electronic database (available at: <http://portal.esimo.ru/portal/>), RIHMI-WDC (available at: <http://meteo.ru>) at the HMS of the Hydrometeorological Centre of Russia for 1980–2021 were used.

To analyze thermal conditions, we used the data on the sea surface temperature in the nodes of $0.25 \times 0.25^\circ$ regular grid for 1980–2021 from the archives of

the Japan Meteorological Agency (JMA) (http://ds.data.jma.go.jp/gmd/goos/data/rrtdb/jma-pro/cobe_sst_glb_M.html).

The long-term variability of atmospheric circulation of the second natural synoptic region (2 n.s.r.) was analyzed. We used the reanalysis archive data (NCEP/NCAR Reanalysis Monthly Means and Other Derived Variables) of surface atmospheric pressure (P_0) and geopotential (H_{500}) in the nodes of $2.5 \times 2.5^\circ$ regular grid for 1980–2021. We also used the surface pressure (P_0) and H_{500} geopotential maps for 2000–2021 compiled by JMA to analyze baric fields.

Anomalies (deviations from long-term average values) of surface pressure P_0 and geopotential H_{500} were applied when assessing the interannual variability of AAC development intensity. To assess the variability of thermal conditions, water temperature anomalies (deviations of monthly averages from long-term averages) were used. World Meteorological Organization recommends calculating climatological standard norms as average data for the closest 30-year reference period to the current time ending with the year with the last digit 0 [11]. Monthly average anomalies of all parameters applied in the work were calculated concerning the climate norm for the period 1991–2020.

For calculating large water temperature anomalies, we used the method outlined in [12]. The criterion for the occurrence of such an anomaly (T_w) is the temperature deviation from an average value by 1.2σ , where σ is standard deviation. Five groups of anomalies were distinguished according to their magnitude: extremely low ($T_w \leq -1.2\sigma$); low ($-1.2\sigma < T_w < -0.4\sigma$); average ($-0.4\sigma \leq T_w \leq 0.4\sigma$); high ($0.4\sigma < T_w < 1.2\sigma$); extremely high ($T_w \geq 1.2\sigma$). Calculations were carried out for all water temperature intervals. The paper presents the results of calculating large anomalies at each HMS for May, June, July, August in 1980–2012.

The frequency (f) of exceeding the value of 1.2σ was also calculated as the ratio of the number of large water temperature anomalies to the series length. This frequency is a probabilistic-statistical assessment of a time series [13]. We were interested in the probability of exceeding the value of 1.2σ . In probability theory, such a value is also called the tail of distribution. The frequency of 1.2σ level excess can be considered as an empirical assessment of the tail of distribution.

During the analysis of regional time series of climate parameters, when large fluctuations for local areas are revealed, it is necessary to refine the trend assessments. We assessed trend significance by the relation a/s , where a is linear trend coefficient of the time series of water temperature variability, s is residual variability (residual variance square root¹). The relation a/s characterizes statistical significance of the results at a fixed series length with a specified critical value corresponding to the accepted significance level. Applying the Student's t-test, this relation makes it possible to determine the probability with which the hypothesis of linear trend coefficient equality to zero is accepted (or not accepted) [14]. The coefficient critical value is 0.04 for a 95% significance level with a series duration of 30 years. The statistical assessments we used are featured by a more accurate indication of the residual variability s which is not affected by inaccuracies in determining the linear trend coefficient a [15].

¹Borovkov, A.A., 1984. *Mathematical Statistics. Additional Chapters*. Moscow: Nauka, 144 p. (in Russian).

Variability of the water thermal regime

Assessments of interannual variability of water temperature anomalies carried out for all HMS (except for HMS Komrvo due to an incomplete data series) show that a predominant upward trend indicates no significant trends in anomalies during the period under study. This is explained by high values of residual variability (fluctuations) both on the western and eastern shelves (Fig. 2, Table 1).

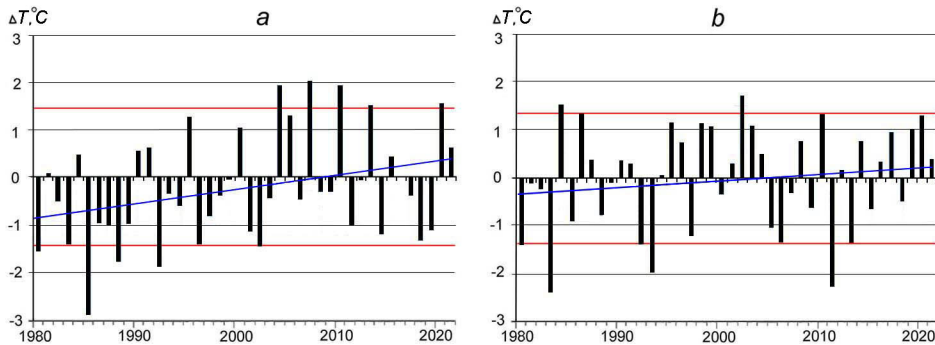


Fig. 2. Interannual variability of water temperature anomalies in the western, HMS Kholmsk (*a*), and eastern, HMS Cape Terpeniya (*b*), areas of the Sakhalin shelf (blue lines denote the linear trends, red ones – the criteria of large anomalies)

Table 1

Assessments of variability of water temperature anomalies at HMS in 1980–2021

HMS	Significance of the trend a/s				Residual variability s			
	May	June	July	August	May	June	July	August
Krilyon	0.03	0.03	0.02	0.03	0.90	0.96	1.06	1.07
Kholmsk	0.03	0.03	0.03	0.03	1.01	1.07	1.52	1.41
Ulegorsk	0	0	0	0.01	0.94	1.07	1.42	1.44
Pilvo	0.02	0	0.01	0.03	0.82	1.22	1.09	1.22
Odoptu	0.02	0	0.01	0	0.82	1.47	1.18	1.59
Terpeniya	0.02	0.01	0.01	0	1.04	1.02	1.20	1.14
Novikovo	0.01	0.01	0.02	0.02	1.26	1.59	1.35	1.50

According to these assessments, the greatest fluctuations are observed on the western shelf of the island affected by the warm Tsushima Current at HMS Kholmsk in July. In some years, the northern branch of the current reaches the northern Tatar Strait part – up to HMS Ulegorsk and further to HMS Pilvo [9, 16, 17]. Year-to-year variation in the distribution of the Tsushima Current waters determines changes in the thermal conditions of the water area off the west coast.

On the eastern shelf, at HMS Odoptu the greatest variability is observed in August, at HMS Novikovo – in June and August. HMS Odoptu is located in the north of the eastern shelf. Long-term variations of water thermal regime here are determined by the interaction of waters of different origins – warm waters of the Amur Current and cold waters of the East-Sakhalin Current (Fig. 1) [18].

In July – August, southerly winds weaken the East-Sakhalin Current during the summer monsoon development, but upwelling which often occurs under effect of prevailing southeasterly winds off the east coast (HMS Komrvo area) largely determines the cold thermal regime of the waters here. The upwelling zone is often observed in July–August in the eastern shelf central zone northwards of Cape Terpeniya (HMS Cape Terpeniya); it also determines significant fluctuations here. At the southeastern shelf of the island (HMS Novikovo), water thermal regime is determined by the variability of the anticyclonic circulation component flows in the southern part of the Sea of Okhotsk including cold waters of the East-Sakhalin Current and the intrusions of transformed warm water jets of the Soya Current [19, 20]. The wind effect directions and water dynamics in the area of the Sakhalin eastern coast are important factors determining variations in the water area temperature regime and the formation of significant anomalies.

To identify years in which large water temperature anomalies were observed, criterion values were calculated for each HMS (Table 2).

Table 2

**Criterion of water temperature large anomaly (°C) at HMS
in 1980–2021**

Station	May	June	July	August
Krilyon	±1.18	±1.27	±1.35	±1.42
Kholmok	±1.31	±1.38	±1.94	±1.82
Ulegorsk	±1.15	±1.30	±1.72	±1.76
Pilvo	±1.03	±1.49	±1.36	±1.56
Odoptu	±1.05	±1.80	±1.47	±1.96
Komrvo	–	±0.98	–	–
Terpeniya	±1.29	±1.27	±1.49	±1.40
Novikovo	±1.57	±1.96	±1.71	±1.91

The calculations demonstrate that the values of the large anomaly criterion are different for each station. The highest values are observed in July and August which is consistent with an increase in residual variability (Table 1).

Taking into account the assessments, we identified the years in which negative and positive large water temperature anomalies exceeding the criterion values were formed. Also, the frequency of arising of large anomalies in each month was determined (Fig. 3).

According to the calculation results presented in Fig. 3, the frequency of arising of large negative anomalies in water temperature prevails at most stations of Sakhalin Island in May – August 1980–2021. It should be noted that the risk of severe cold snaps is especially important in May–June, when the salmon fry migrate to coastal areas.

In May, the highest frequency of arising of negative anomalies is observed at the western shelf HMS while its peak is noted at HMS Ulegorsk. However,

the frequency of occurrence of positive water temperature anomalies exceeds the one of negative anomalies at HMS Kholmsk in May.

In June, the frequency of arising of negative water temperature anomalies exceeds the one of positive anomalies both at the western and eastern coasts. At the same time, the greatest frequency increase of positive anomalies is noted at HMS Pilvo (western shelf) and HMS Odoptu (northeastern shelf).

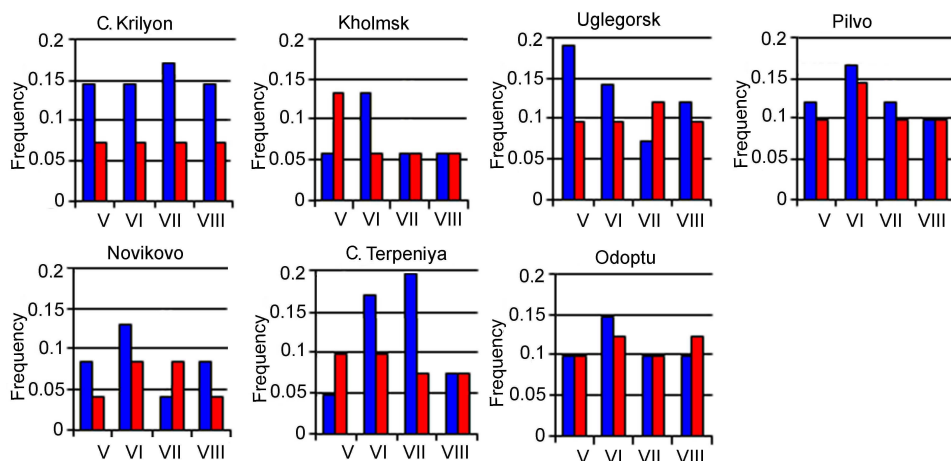


Fig. 3. Frequency of arising of strong negative (blue color) and positive (red color) anomalies of water temperature at HMS in May – August 1980–2021

In July, the highest frequency of arising of negative anomalies is observed at the stations located on capes – HMS Cape Crilyon and HMS Cape Terpeniya. The frequency of arising of positive anomalies is the highest at HMS Ulegorsk. It exceeds the frequency of arising of negative anomalies at this station. An excess of the frequency of arising of positive anomalies over the one of negative anomalies also takes place at HMS Novikovo.

In August, high frequency of negative anomalies remains at HMS Cape Crilyon. The highest frequency of arising of positive anomalies is observed at HMS Odoptu where it exceeds the one of negative anomalies.

The analysis shows that thermal regime characterized by arising of large water temperature anomalies in May – August is observed at the HMS of both western and eastern shelves.

As noted above, variability of the water area temperature regime in spring-summer period and formation of significant positive or negative anomalies are determined by the features of hydrological conditions in the west and east of the island. However, in some years, thermal regimes characterized by the formation of large anomalies of only one sign are observed in a number of HMS of both regions.

Thus, the thermal regime characterized by negative water temperature anomalies was observed on the western and eastern shelves of the island during

the period under study in May 1980, 2005, June 1983, 2011, July 1988, 1997, August 1981, 1992, 2002; positive anomalies – in May 1995, 2002, 2019, June 2010, July 1990, 2013, 2021, August 1995, 2000, 2006.

Formation of thermal conditions with large anomalies of the same sign on both coasts of the island in some years is, apparently, the result of impact of one factor – the atmospheric effect. In this regard, it is very important to determine the mechanisms of this effect.

Mechanisms of large anomalies formation

As provided at this stage, the atmospheric circulation and transport of air masses over the region under study during the summer monsoon (with characteristic southerly winds) are determined by the seasonal AAC – the Okhotsk High (OH) formed over the Sea of Okhotsk in the surface field and the cold Troposphere Low in the middle troposphere, as well as the Summer Far East Low (SFEL) as a part of the extensive Asiatic Low directed towards the Amur region. On the ocean side, atmospheric circulation is associated with the North Pacific high-pressure zone development – the Hawaiian High (HH). At the same time, the development intensity of regional AAC varies year after year. In addition, a variability in the position of these atmospheric baric formations and a corresponding change in their local impact are observed [8, 9].

Fig. 4 shows the examples of specific monthly average baric fields in May – August during the years of formation of thermal regimes characterized by large cold (Fig. 4, *a – d*) and warm (Fig. 4, *e – h*) thermal water anomalies in the studied coastal areas of Sakhalin Island.

The analysis of atmospheric fields structure shows that extreme cooling in the island coastal waters is observed in such baric situations when the Troposphere Low marked on the AT_{500} absolute topography maps is directed towards the southwest of the Sea of Okhotsk in high-altitude fields. The formation of centers with extremely low values of geopotential anomalies H_{500} is observed in the depression delta above the study area. In these centers, cold air accumulates at the downward flows near the ground and negative water temperature anomalies are formed. In turn, the OH localization in the northeast and east of the Sea of Okhotsk and the SFEL displacement to the west (Fig. 4, *a, c, d*) contribute to the influx of cold air masses from the northeast in the surface field.

In case of OH absence (Fig. 4, *b*) during significant SFEL development from the area of which cyclones move towards the Sea of Okhotsk along the southern trajectories, cold air masses are also transported to the island area in the rear part of the cyclones from the northwest. This transport supports the cold waters flow of the East-Sakhalin Current [21] and upwelling on the eastern shelf [22, 23] but prevents the development of the warm Tsushima Current and its branch, the Soya Current, in the southwest of the Sea of Okhotsk [9, 17] which determines the arising of negative water temperature anomalies along the entire coast in combination with the center of cold air masses forming here.

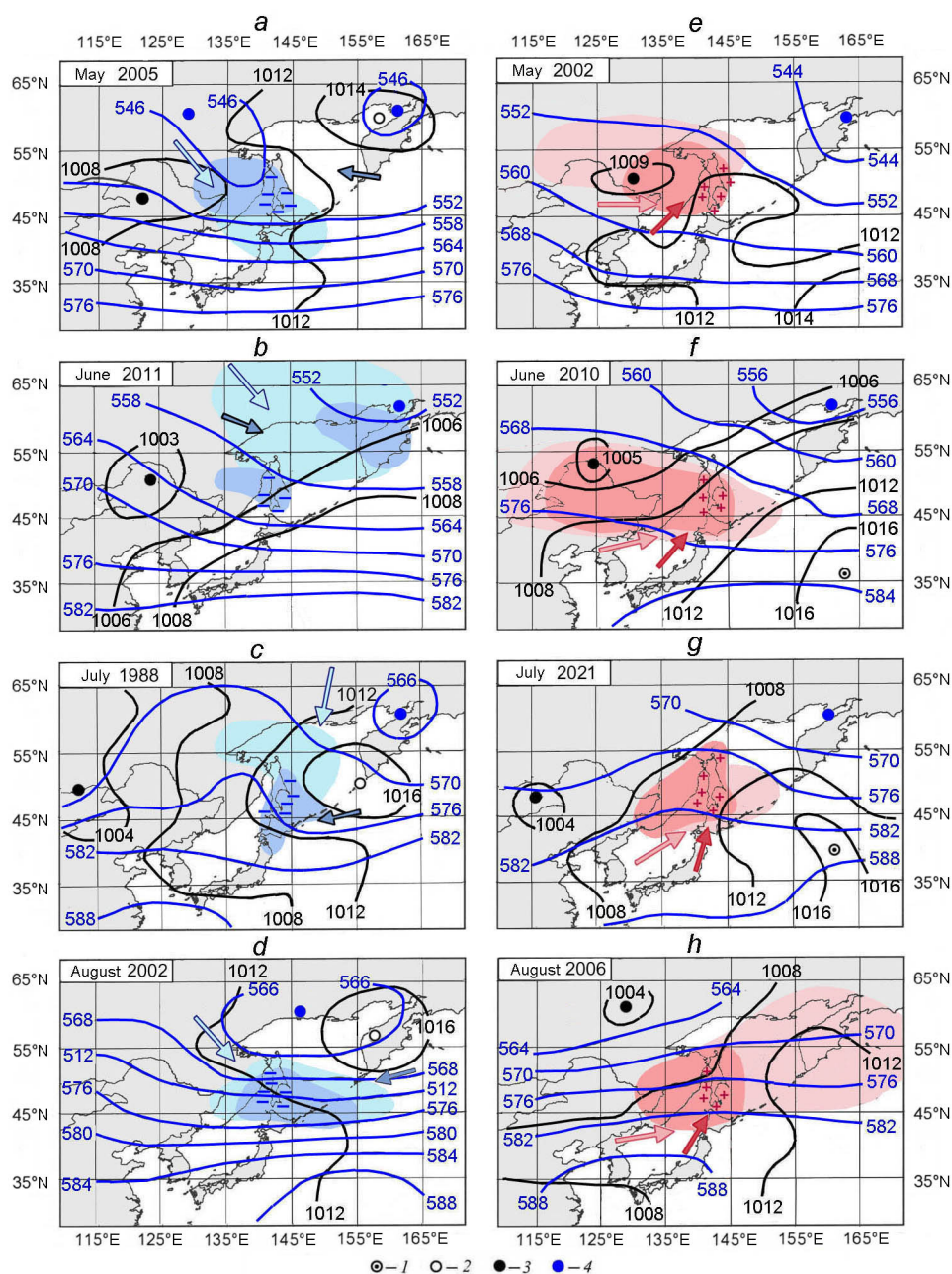


Fig. 4. Typical structures of the surface baric fields P_0 (black isobars, hPa) and geopotential H_{500} (blue isohypses, hPa) in the yeas of formation of large negative (*a – d*) and positive (*e – h*) water temperature anomalies. 1 – Hawaiian High, 2 – Okhotsk High, 3 – Summer Far East Low, 4 – Troposphere Low. Light blue and pink arrows denote the direction of basic motion of the cold and warm air masses in the mid troposphere, blue and red ones – the motion direction in the near land layer; signs “-” and “+” show the negative and positive anomalies of water temperature; light blue color marks the centers of negative anomalies of geopotential H_{500} and pink color – the centers of positive anomalies of geopotential H_{500} ; blue and red colors show the centers of abnormally low and high air temperature, respectively

The formation of extremely warm regimes is due to the development of the HH western branch. In years when as early as May (Fig. 4, *e*) the study area is affected by the tropospheric ridge, localization of an extreme center of H_{500} geopotential positive values is observed above Sakhalin Island. We indicate an extreme center of positive air temperature anomalies in the surface field and positive water temperature anomalies in the water area. With the strengthening of the HH ridge and its propagation to the Seas of Japan and Okhotsk (Fig. 4, *f, g*), the area with extreme values of geopotential H_{500} is located above the Primorye coast, the Tatar Strait, and Sakhalin Island. An intense influx of warm air masses takes place along the western periphery of the HH. Intensification of southerly winds occurs as well. In the case when the SFEL displaced towards the north (Fig. 4, *h*), its interaction with the HH front part ensures the intrusion of warm air masses from the south which also contributes to the formation of positive anomalies in the island water areas. At southern and southwestern transport in the atmosphere, the intensity of the warm Tsushima Current increases. According to instrumental observations, the propagation of current to the Tatar Strait northern zone [16, 17] is noted. Active development of its branch – the Soya Current [19, 20] – and weakening of the cold East-Sakhalin Current [21] which ensures the formation of large positive anomalies in water temperature in combination with the thermal atmospheric impact are also observed.

Thus, when analyzing baric situations during the years when large cold or warm water temperature anomalies are formed on the Sakhalin Island shelf, differences in the structure of atmospheric fields were identified. As a result of different local thermal atmospheric impact on the underlying surface, differences in the mechanisms forming cold and warm thermal conditions were identified. At the same time, a dynamic atmospheric effect takes place contributing to changes in the near-island water circulation which together determines the formation of large temperature anomalies in the water area.

Conclusion

Assessment of interannual variability of the water thermal regime condition for the period from May to August 1980–2021 revealed no significant upward trend in the water temperature time series at a predominant growth tendency in the water area of the Sakhalin Island western and eastern shelves during the warm period. This is explained by high values of residual variability (fluctuations) on both western and eastern shelves.

The greatest fluctuations in water temperature anomalies are observed in July and August. The frequency of arising of large negative anomalies in the thermal regime condition exceeds the frequency of arising of positive ones both on the western and eastern shelves of the island.

Considering the calculated criteria for temperature anomalies, years with large negative and positive anomalies in the water thermal regime condition were identified. It was revealed that in some years we observed the occurrence of large anomalies of the same sign at a number of stations in both regions under different hydrological conditions on the western and eastern shelves of the island. Formative cause-effect relations are identified. The mechanisms forming large water temperature anomalies in the region associated with the position variability and intensity development of seasonal regional AAC were established. It is shown that

anomalously cold thermal conditions are formed when a center of decrease of geopotential H_{500} and area of abnormally low surface air temperature are observed over Sakhalin Island. Such extreme zones are caused by the OH intensification or the passage of cyclones along the southern trajectories during the SFEL development. In the years known for large positive anomalies in water temperature, we observe the opposite pattern when a hotspot of extremely elevated H_{500} geopotential values and an area of abnormally high surface air temperatures above Sakhalin Island are located. Such conditions are associated with an increase in the HH warming effect and a corresponding change in the air masses transport. Anomalous variations in the baric structure of atmospheric fields causing the accumulation of abnormally cold or warm air masses in individual centers over the entire study area determine the formation of large temperature anomalies in the waters of the Sakhalin Island western and eastern shelves.

The results of the performed studies can be used for assessing extremeness of thermal environmental conditions during the catch, as well as in predictive models.

REFERENCES

1. Byshev, V.I., Neiman, V.G., Ponomarev, V.I., Romanov, Yu.A., Serykh, I.V. and Tsurikova, T.V., 2014. The Influence of Global Atmospheric Oscillation on Formation of Climate Anomalies in the Russian Far East. *Doklady Earth Sciences*, 458(1), pp. 1116-1120. doi:10.1134/S1028334X14090025
2. Rostov, I.D., Dmitrieva, E.V., Rudykh, N.I. and Vorontsov, A.A., 2020. Climatic Changes in Thermal Conditions of Marginal Seas in the Western Pacific. *Russian Meteorology and Hydrology*, 45(3), pp. 169-178. doi:10.3103/S1068373920030048
3. Jiang, X., Li, Y., Yang, S. and Wu, R., 2011. Interannual and Interdecadal Variations of the South Asian and Western Pacific Subtropical Highs and Their Relationships with Asian-Pacific Summer Climate. *Meteorology and Atmospheric Physics*, 113(3-4), pp. 171-180. doi:10.1007/s00703-011-0146-8
4. Jung, H.-K., Rahman, S.M.M., Choi, H.-C., Park, J.-M. and Lee, C.-I., 2021. Recent Trends in Oceanic Conditions in the Western Part of East/Japan Sea: An Analysis of Climate Regime Shift that Occurred after the Late 1990s. *Journal of Marine Science and Engineering*, 9(11), 1225. doi:10.3390/jmse9111225
5. Glukhovskiy, B.Kh., Goptarev, N.P. and Terziev, F.S., eds., 1998. *Hydrometeorology and Hydrochemistry of the Seas in the USSR. Vol. 9. The Okhotsk Sea. Iss. 1. Hydrometeorological Conditions*. Saint Petersburg: Gidrometeoizdat, 342 p. (in Russian).
6. Shuntov, V.P., Temnykh, O.S. and Naydenko, S.V., 2019. Once Again on Factors Limiting the Number of Pacific Salmon (*Oncorhynchus* spp., fam. Salmonidae) during the Oceanic Period of Their Life. *Izvestiya TINRO*, 196(1), pp. 3-22. doi:10.26428/1606-9919-2019-196-3-22 (in Russian).
7. Kaev, A.M., 2018. A Decrease in the Pink Salmon (*Oncorhynchus Gorbuscha*) Abundance in the Sakhalin-Kuril Region under the Effects of Extreme Environmental Factors. *Russian Journal of Marine Biology*, 44(7), pp. 540-548. doi:10.1134/S1063074018070039
8. Shatilina, T.A., Tsitsiashvili, G.Sh. and Radchenkova, T.V., 2019. Features of the Summer Atmospheric Force Centers Variability over the Far East and Climatic Extremes in the Period 1980–2017. *Proceedings of the Russian State Hydrometeorological University*, (56), pp. 61-80. doi:10.33933/2074-2762-2019-56-61-80 (in Russian).
9. Moroz, V.V., Shatilina, T.A. and Rudykh, N.I., 2021. The Abnormally Thermal Regime Forming in the North Part of the Tatar Strait and Amur Liman under the Influence of Atmosphere Processes. *Vestnik of the Far East Branch of the Russian Academy of Sciences*, (6), pp. 101-110. doi:10.37102/0869-7698_2021_220_06_10 (in Russian).

10. Shatilina, T.A., Tsitsiashvili, G.Sh. and Radchenkova, T.V., 2021. Application of Interval Approach to Pattern Recognition for Identification of Preceding Baric Structures that Determine Extreme Thermal Modes in the South-Kuril Area in Summer. *Izvestiya TINRO*, 201(2), pp. 470-483. doi:10.26428/1606-9919-2021-201-470-483 (in Russian).
11. Korshunova, N.N. and Shvets, N.V., 2014. The Change in Major Climate Parameter Standards over the Russian Area for the Past Decades. In: World Data Center, 2014. *Trudy VNIIGMI-MTsD = Proceedings of All-Russian Research Institute of Hydrometeorological Information – World Data Center*. Obninsk: World Data Center. Vol. 178, pp. 11-24 (in Russian).
12. Spichkin, V.A., 1987. [Determination of the Criterion for a Major Anomaly]. In: A. A. Kirillov and V. A. Spichkin, 1987. *Proceedings of AARI*. Leningrad: Gidrometeoizdat. Vol. 402, pp. 15-20 (in Russian).
13. Embrechts, P., Klüppelberg, C. and Mikosch, T., 1997. *Modelling Extremal Events for Insurance and Finance*. Stochastic Modelling and Applied Probability, vol. 33. Berlin: Springer. Chapter 1, pp. 3-19. doi:10.1007/978-3-642-33483-2
14. Shitikov, V.K., Rozenberg, G.S. and Zinchenko, T.D., 2003. *Quantitative Hydroecology: Methods of System Identification*. Tolyatti: Samara Scientific Centre of RAS, 463 p. (in Russian).
15. Tsitsiashvili, G.Sh., 2008. Variations Estimates. *Far Eastern Mathematical Journal*, 8(2), pp. 229-234 (in Russian).
16. Djakov, B.S., 2006. Year-to-Year Variability of Water Circulation in the Tatar Strait in Summer. *Izvestiya TINRO*, 144, pp. 281-299 (in Russian).
17. Pishchal'nik, V.M., Arkhipkin, V.S. and Leonov, A.V., 2010. On Water Circulation in Tatar Strait. *Water Resources*, 37(6), pp. 759-772. doi:10.1134/S0097807810060035
18. Zhabin, I.A. and Luk'yanova, N.B., 2022. Impact of the Wind-Driven Upwelling and Amur River Discharge on the Thermohaline Water Structure off the Northeastern Coast of Sakhalin. *Russian Meteorology and Hydrology*, 47(9), pp. 660-667. doi:10.3103/S1068373922090035
19. Fukamachi, Y., Ohshima, K.I., Ebuchi, N., Bando, T., Ono, K. and Sano, M., 2010. Volume Transport in the Soya Strait during 2006–2008. *Journal of Oceanography*, 66(5), pp. 685-696. doi:10.1007/s10872-010-0056-2
20. Uchimoto, K., Mitsudera, H., Ebuchi, N. and Miyazawa, Y., 2007. Anticyclonic Eddy Caused by the Soya Warm Current in an Okhotsk OGCM. *Journal of Oceanography*, 63(3), pp. 379-391. doi:10.1007/s10872-007-0036-3
21. Andreev, A.G., 2017. Mesoscale Circulation in the East Sakhalin Current Region (Okhotsk Sea). *Issledovanie Zemli iz Kosmosa*, (2), pp. 3-12. doi:10.7868/S0205961417010031 (in Russian).
22. Zhabin, I.A. and Dmitrieva, E.V., 2021. Seasonal and Interannual Variability of Wind-Driven Upwelling along Eastern Sakhalin Island Coast Based on the QuikSCAT/SeaWinds Scatterometer Data. *Izvestiya, Atmospheric and Oceanic Physics*, 57(12), pp. 1680-1689. doi:10.1134/S000143382112029X
23. Shevchenko, G.V. and Kirillov, K.V., 2017. Water Temperature Variations off the Sakhalin Coast from the Data of Instrumental Observations. *Russian Meteorology and Hydrology*, 42(3), pp. 189-197. doi:10.3103/S1068373917030062

Submitted 23.06.2023; approved after review 25.07.2023;
accepted for publication 15.11.2023.

About the authors:

Tatyana A. Shatilina, Leading Research Associate, Laboratory of Fishing Oceanology, Russian Federal Research Institute of Fisheries and Oceanography, Pacific Branch of VNIRO (TINRO), (4 Shevchenko Alley, Vladivostok, 690091, Russian Federation), CSc (Geogr.), **Scopus Author ID: 6505548902**, **ORCID ID: 0009-0005-7954-9745**, tatyana.shatilina@tinro.ru

Valentina V. Moroz, Senior Research Associate, Laboratory of Informatics and Ocean Monitoring, V. I. Il'yichev Pacific Oceanological Institute, Far Eastern Branch of Russian Academy of Sciences (43 Baltiyskaya Str., Vladivostok, 690041, Russian Federation), CSc (Geogr.), **Scopus**

Author ID: 7102508049, ORCID ID: 0000-0001-5937-4080, Researcher ID: K-1520-2018,
moroz@poi.dvo.ru

Guram Sh. Tsitsiashvili, Chief Research Associate, Institute of Applied Mathematics, Far Eastern Branch of Russian Academy of Sciences (7 Radio Str., Vladivostok, 690041, Russian Federation), DSc (Phys.-Math.), Professor, **Scopus Author ID: 35605421700, ORCID ID: 0000-0003-2600-0474**, guram@iam.dvo.ru

Tatyana V. Radchenkova, Engineer-Researcher, Institute of Applied Mathematics, Far Eastern Branch of Russian Academy of Sciences (7 Radio Str., Vladivostok, 690041, Russian Federation), **ORCID ID: 0000-0003-2287-975X**, tarad@yandex.ru

Contribution of the co-authors:

Tatyana A. Shatilina – purpose of paper, collection and processing of meteorological data, data analysis, result interpretation

Valentina V. Moroz – paper structure development, collection and processing of oceanographic data, data analysis, drawing design, references, writing of the paper text

Guram Sh. Tsitsiashvili – creation of original algorithms for calculation, interpretation of results, suggestion of algorithms for calculation

Tatyana V. Radchenkova – creation of calculation programs, calculations

The authors have read and approved the final manuscript.

The authors declare that they have no conflict of interest.

Original article

Variability of Decadal Horizontal Thermohaline Gradients on the Surface of the Barents Sea during Summer Season in 1993–2022

A. A. Konik¹ ✉, O. A. Atadzhanova^{1, 2}

¹ *Shirshov Institute of Oceanology of RAS, Moscow, Russian Federation*

² *Marine Hydrophysical Institute of RAS, Sevastopol, Russian Federation*

✉ konikrshu@gmail.com

Abstract

Purpose. The paper is aimed at comparative analysis of the decadal horizontal gradients of thermohaline fields in the Barents Sea during the summer periods in 1993–2022 derived from the reanalysis and satellite measurements with the aim to select the most suitable data array for studying the surface manifestations of frontal zones.

Methods and Results. The fields of decadal and background thermohaline gradients on the Barents Sea surface were calculated for the summer periods in 1993–2022 based on the monthly mean temperature data from GHRSSST OSTIA, MODIS/Aqua, and VIIRS/Suomi NPP, as well as on the monthly mean temperature and salinity data from CMEMS GLORYS12V1 and MERCATOR PSY4QV3R1. The quantitative estimates of temperature and salinity gradients were obtained for certain decades using different data arrays, and a comparative analysis of these estimates was performed along with a description of the physical and geographical characteristics of frontal zones. Maximum thermohaline gradients on the surface were observed in July. Based on the data from all the sources, the background horizontal thermal gradient has been increasing over three decades. During a summer period, the Polar Frontal Zone was identified on the surface of the Barents Sea in all the data arrays, whereas the Coastal and Arctic Frontal Zones were observed in the salinity field based on the CMEMS GLORYS12V1 and MERCATOR PSY4QV3R1 data.

Conclusions. The difference between the calculated estimates of horizontal temperature gradient can exceed 0.01°C/km that is comparable to the magnitude of the average climate gradient in the Barents Sea. The thermal gradient values obtained from the CMEMS GLORYS12V1 and MERCATOR PSY4QV3R1 reanalysis data are the closest to this estimate. This fact makes it possible to classify these data arrays as the most preferable ones for the analysis of the surface manifestations of frontal zones in the Barents Sea.

Keywords: frontal zones, temperature gradient, satellite data, reanalysis, Barents Sea, sea surface temperature

Acknowledgements: The work was carried within the framework of state assignments No. FMWE-2024-0028 (IO RAS) and No. FNNN-2024-0017 (MHI RAS).

For citation: Konik, A.A. and Atadzhanova, O.A., 2024. Variability of Decadal Horizontal Thermohaline Gradients on the Surface of the Barents Sea during Summer Season in 1993–2022. *Physical Oceanography*, 31(1), pp. 46-58.

© 2024, A. A. Konik, O. A. Atadzhanova

© 2024, Physical Oceanography

Introduction

Frontal zones in the seas and oceans represent a complex geophysical phenomenon that affects the formation of small eddy structures and internal waves as well as the variability of biogeochemical cycles [1–3]. Baing formed at the boundary of areas where waters with different hydrological characteristics



interact, frontal zones are distinguished by their complex internal structure and dynamics.

One of the most significant problems associated with frontal zones in the World Ocean is the methodology of their determination. According to the work ¹, frontal zone is a region of sharpened spatial gradients of thermodynamic characteristics compared to the average uniform distribution between steadily existing extrema, and the main frontal section (front) inside the frontal zone is the surface inside it which coincides with the maximum gradient surface of the characteristic.

There is a large variety of works [4–8] studying the spatial variability and features of frontal zones based on *in situ* data, satellite measurements or reanalysis using various methods and approaches. Taken together, most of these studies are united by a single criterion for determining the frontal zone for the World Ocean ¹ – a tenfold excess of the gradient of hydrophysical parameters over the background (mean value of the gradient over space). At the same time, compared to other parts of the World Ocean, the Arctic seas represent a relatively inert system for most period of the year which leads to a much smaller value of primarily horizontal hydrophysical gradients and complicates the process of identifying frontal zones.

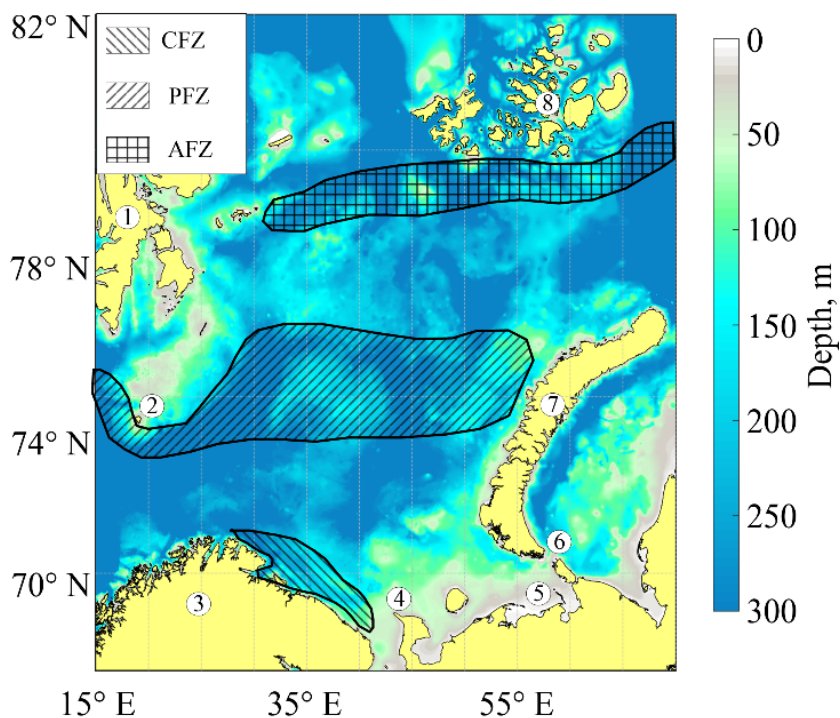


Fig. 1. Composite scheme of large-scale frontal zones in the Barents Sea based on [4–10]: 1 – Svalbard; 2 – Bear Island; 3 – Scandinavian Peninsula; 4 – Kanin Nos; 5 – Pechora Sea; 6 – Kara Gate; 7 – Novaya Zemlya; 8 – Franz Josef Land. CFZ – Coastal Frontal Zone; PFZ – Polar Frontal Zone; AFZ – Arctic Frontal Zone

¹ Fedorov, K.N., 1983. *The Physical Nature and Structure of Oceanic Fronts*. New York: Springer, 333 p.

The Barents Sea (Fig. 1) belongs to the Arctic Ocean basin and is characterized by a complex system of surface and subsurface frontal zones combined into the largest Coastal, Polar and Arctic Frontal Zones [5, 9–11]. These frontal zones are an important part of the Barents Sea hydrological regime affecting its thermohaline characteristics, ice conditions and distribution of nutrients [4, 8]. According to the general concept accepted by a large number of researchers (see work ² and [7, 8]), it is sufficient for the hydrophysical feature gradient to exceed its background value twice to determine the frontal zone on the Barents Sea surface. A number of works [5, 7–8] give estimates of the value of the Barents Sea background gradient on the basis of which the criterion for recording the position and features of frontal zones is then determined. Such estimates can vary within 0.005–0.01 °C/km for temperature and 0.005 PSU/km for salinity. However, hydrological features of the sea (negative water temperature, ice cover) and climate changes [12–14] affect thermohaline fields which ultimately affects the value of the background horizontal gradient and leads to the need to refine its assessments.

Determining the background horizontal gradient of the Barents Sea therefore currently remains an urgent problem which solution would help to improve the quality of assessment of the frontal zones variability in this region. Thus, the main purpose of this work is a comparative analysis of horizontal gradients of thermohaline fields in the Barents Sea calculated over decades from 1993 to 2022 for summer periods using satellite and model (reanalysis, forecast and assimilation) data.

Data and methods

To calculate the gradients, various reanalysis and satellite measurement data on the temperature and salinity of the Barents Sea were used with a spatial step of latitude and longitude from 4 to 25 km for June–August periods over three decades from 1993 to 2022. Fig. 2 shows clearly the difference in the grid scales that are included in each of the data arrays used.

Thermal characteristics were analyzed using L3 processing level monthly mean sea surface temperature (SST) data (<http://oceancolor.gsfc.nasa.gov>) obtained from visible and infrared surveys with a spatial resolution of 0.05° by MODIS (Moderate Resolution Imaging Spectroradiometer) satellite spectroradiometer installed on board Aqua satellite for warm periods of 2003–2022 and VIIRS (Visible Infrared Imaging Radiometer Suite) radiometer on board Suomi NPP for 2013–2022 [15].

GHRSSST OSTIA product (The Group for High Resolution Sea Surface Temperature Operational Sea Surface Temperature and Sea Ice Analysis) contains data fields averaged using optimal interpolation on a global grid with a resolution of 0.054° in latitude and longitude [16]. GHRSSST OSTIA is based on satellite SST data from high-resolution sensors (AVHRR, AMSR-E and AATSR) and data from buoys. The daily OSTIA data for June–August 2013–2022 previously averaged to a monthly interval were used for the calculations.

² Ozhigin, V.K., Ivshin, V.A., Trofimov, A.G., Karsakov, A.L. and Antsiferov, M.Yu., 2016. *The Barents Sea Water: Structure, Circulation, Variability*. Murmansk: PINRO, 260 p. (in Russian).

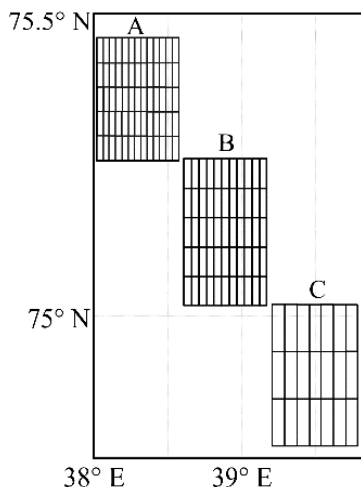


Fig. 2. Schematic representation of grids for each data array: a – MODIS/Aqua and VIIRS/Suomi NPP; b – GHRSSST OSTIA; c – GLORYS12v1 and PSY4QV3R1

The Global Ocean Physics Reanalysis³ product (CMEMS GLORYS12v1) contains monthly and daily average hydrophysical fields with global coverage at a resolution of 0.083° in longitude and latitude for 50 horizons. The model component of GLORYS12v1 is the ECMWF (European Center for Medium-Range Weather Forecasts) ERA-Interim reanalysis system which uses a Kalman filter to assimilate [17] data on temperature, salinity, currents, sea level and ice surface. To calculate horizontal gradients, monthly averages of surface water temperature and salinity for the summer period from June to August 1993–2020 were used.

A product based on a predictive model was also used. Global Ocean $1/12^\circ$ Physics Analysis and Forecast updated Daily⁴ (MERCATOR PSY4QV3R1) is a CMEMS GLORYS12v1 continuation. It provides simulation of mean daily hydrophysical fields for the entire World Ocean with a resolution of 0.083° . MERCATOR PSY4QV3R1 contains daily data on sea level, salinity, temperature, mixed layer depth and ice extent. MERCATOR PSY4QV3R1 contains the NEMO numerical model [18] with 50 unevenly spaced horizons for most hydrophysical characteristics. Monthly average data on surface water temperature and salinity for the periods from June to August 2021–2022 were used within the study.

The quality of the satellite data used depends both on the type of sounding systems and on the state of the surface waters of the considered water area. The error of the satellite data used in the work (VIIRS/Suomi NPP and MODIS/Aqua) on SST does not exceed 0.15°C , while the reanalysis data error (GHRSSST OSTIA, CMEMS GLORYS12v1 and MERCATOR PSY4QV3R1) is 0.1°C . The reanalysis data error (CMEMS GLORYS12v1 and MERCATOR PSY4QV3R1) on surface salinity is on average less than 0.1 PSU.

Surface decadal gradient fields were calculated identically for all data arrays. The first stage included monthly averaging of temperature and salinity fields for each decade. The second stage consisted of calculating horizontal gradients of temperature and salinity according to a method repeatedly tested for the Barents Sea [8, 19]. At the third stage, the module of the ten-year horizontal gradient was determined. First, the step along the parallel and meridian in kilometers was

³ Global Ocean Physics Analysis and Forecast. *E.U. Copernicus Marine Service Information (CMEMS). Marine Data Store (MDS)*. doi:10.48670/moi-00016

⁴ Global Ocean Physics Reanalysis. *E.U. Copernicus Marine Service Information (CMEMS). Marine Data Store (MDS)*. doi:10.48670/moi-00021

calculated, then the zonal and meridional components of the gradient were calculated for each grid node. The final ten-year module of the horizontal gradient was calculated as the sum square root of the squares of zonal and meridional components.

Research results

Temperature gradients from MODIS/Aqua and VIIRS/Suomi NPP data.

Fig. 3 shows maps of the surface distribution of horizontal temperature gradients based on satellite data for July 1993–2022.

According to MODIS/Aqua data, in June the maximum thermal gradient reaching 0.03–0.04 °C/km is observed in the central and western Barents Sea near the Svalbard and Bear Island. In the first decade (2003–2012), in June, the main frontal section of the Polar Frontal Zone can be observed throughout the central Barents Sea, while from 2013 to 2022 – only in the western part of the sea in the region of 15°–35°E. At the same time, in the southern part of the sea, the values of thermal horizontal gradients are not large and average 0.01–0.015 °C/km, and the front in the Coastal Frontal Zone is not traced. From 2013 to 2022, more pronounced surface gradients are observed in the north of the sea. Its values on average reach 0.02–0.03 °C/km, which correlates with the ten-year position of the Arctic Frontal Zone [11]. Two decades of June showed the temperature gradient of 0.03–0.04 °C/km in the Pechora Sea. The maximum temperature gradient is observed in July. In both decades (see Fig. 3, *a, b*), maximum values of 0.03–0.05 °C/km are recorded around Bear Island and in the Pechora Sea. In August, thermal gradient decrease is observed over the first and second decades. Thus, this is reflected in the Polar Frontal Zone with its main frontal section appearing to the south of Bear Island and further in the central Barents Sea in 2003–2012, while in 2013–2022 in the area 20°–45°E its position is difficult to track. In addition, in August 2003–2012 near the Scandinavian Peninsula coast a strip of large thermal gradient values (> 0.03 °C/km) is observed, which correlates with the Coastal Front position, and in the Pechora Sea individual areas with a thermal gradient not exceeding 0.05 °C/km are registered. A comparative analysis by decade shows that the maximum surface temperature gradients are recorded in July 2003–2012 according to MODIS/Aqua data. The mean value of the horizontal thermal temperature gradient in the Barents Sea has decreased by 0.01 °C/km over the past two decades.

Analysis of VIIRS/Suomi NPP satellite products for 2013–2022 showed the correlation of thermal gradient value according to data from this database with its values from MODIS/Aqua array. Fig. 3, *c* gives a map for July as an example. Thus, the Polar Frontal Zone appears also in the area of Bear Island only, where the SST gradient value from June to August varies within 0.04–0.05 °C/km, and in the Pechora Sea its value of 0.03–0.04 °C/km for the warm season is comparable to the SST gradient value according to MODIS/Aqua data. At the same time, separate high-gradient areas that can be attributed to the Arctic Frontal Zone are observed near the Novaya Zemlya and the Franz Josef Land. Position of the Coastal Frontal Zone for 2013–2022 is not traceable according to SST data.

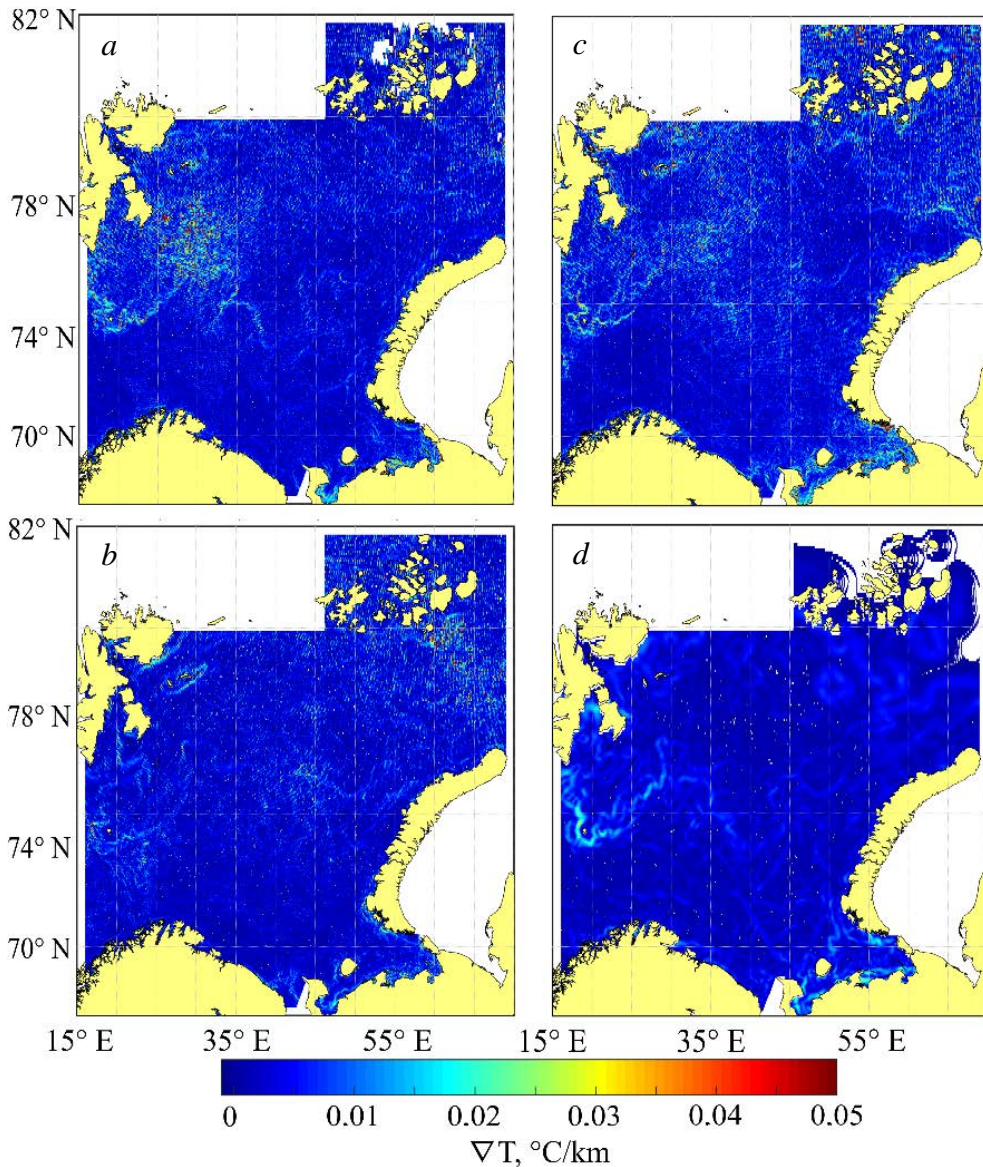


Fig. 3. Distribution of decadal horizontal temperature gradients in the Barents Sea in July based on the satellite data: *a* – MODIS/Aqua, 2003–2012; *b* – MODIS/Aqua, 2013–2022; *c* – VIIRS/Suomi NPP, 2013–2022; *d* – GHRSSST OSTIA, 2013–2022

Temperature gradients according to GHRSSST OSTIA data. According to GHRSSST OSTIA data, the maximum value of the temperature gradient in summer in the Barents Sea does not exceed 0.03 °C/km. Such gradients are most often observed in June and July (see Fig. 3, *d*); in August their magnitude decreases. High-gradient areas can be observed in the Polar Frontal Zone and the Pechora Sea. According to GHRSSST OSTIA data, the position of the main front of the Polar Frontal Zone is more pronounced than according to satellite data, especially near the Svalbard and Bear Island. In addition, the Arctic Frontal Zone is traced in

the northern Barents Sea, where the gradient can reach 0.025 °C/km. In the southern part of the sea, the gradient value does not exceed 0.01 °C/km. It is worth noting that according to OSTIA data, in July the Coastal Front can be traced with a gradient not exceeding 0.02 °C/km. In general, the surface gradient values from GHR SST OSTIA reanalysis data are lower by 0.02 °C/km than those from MODIS/Aqua and VIIRS/Suomi NPP satellite data.

Temperature and salinity gradients from CMEMS GLORYS12v1 and MERCATOR PSY4QV3R1 data. Fig. 4 shows maps of the surface distribution of horizontal temperature gradients according to reanalysis data for July 1993–2022.

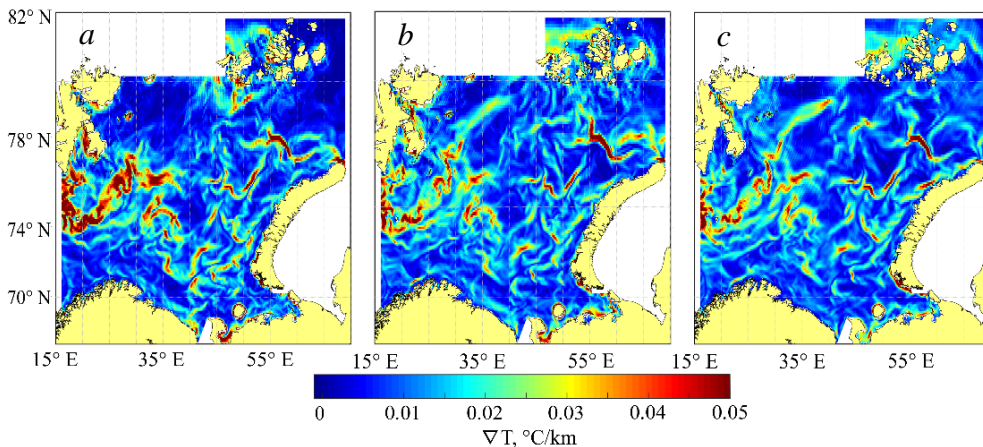


Fig. 4. Distribution of decadal horizontal temperature gradients in the Barents Sea in July based on the reanalysis data: *a* – CMEMS GLORYS12v1, 1993–2002; *b* – CMEMS GLORYS12v1, 2003–2012; *c* – CMEMS GLORYS12v1 and MERCATOR PSY4QV3R1, 2013–2022

According to CMEMS GLORYS12v1 and MERCATOR PSY4QV3R1 reanalysis data, in all the months high-gradient zones (> 0.07 °C/km) corresponding to the quasi-stationary western part of the Polar Frontal Zone are observed.

A comparison of SST gradient fields in June over three decades showed that the areas of maximum gradients almost coincided. The eastern part of the Polar Frontal Zone is less pronounced in the first decade (smaller gradients) than in the other two. June 2003–2012 is characterized by high gradient values near the Franz Josef Land. In July, in each decade (see Fig. 4), maximum Polar Frontal Zone gradients (> 0.07 °C/km) are also clearly visible. The western part of the frontal zone is clearly expressed in July 2013–2022, while the values of the gradients in its eastern part do not change significantly. Unlike June, in July high-gradient (> 0.07 °C/km) areas are observed already near the Kara Gate and in the Pechora Sea, where maximum gradients are also observed in the third decade. In August, for all three decades, the maximum values of surface temperature gradients (> 0.07 °C/km) are observed in the western and eastern parts of the Polar Frontal Zone. The areas near the northern part of the Novaya Zemlya, the Svalbard and

the Franz Josef Land are worth noting individually as there the thermal gradient magnitude has increased significantly compared to other months.

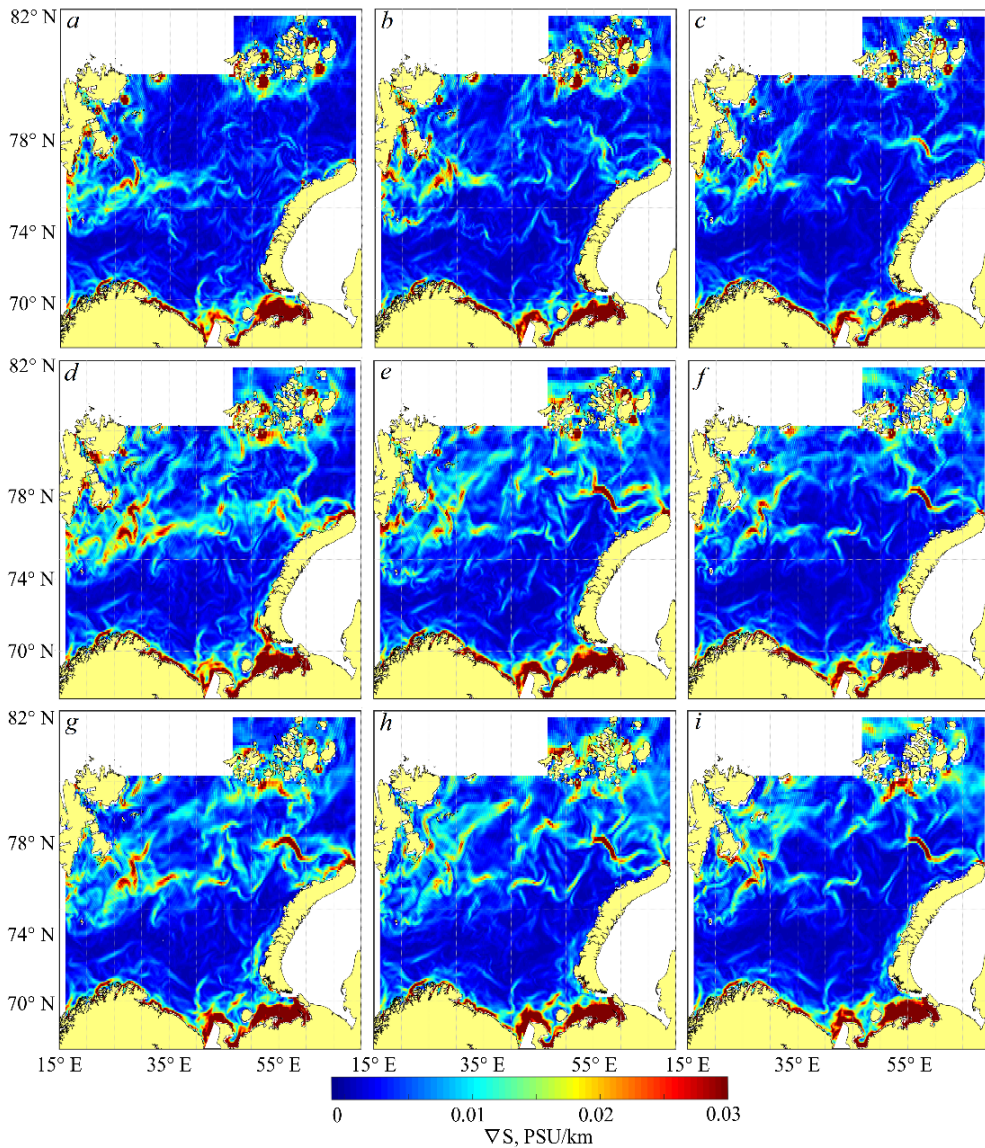


Fig. 5. Distribution of decadal horizontal salinity gradients in the Barents Sea based on the CMEMS GLORYS12v1 and MERCATOR PSY4QV3R1 data: in June (*a, b, c*), in July (*d, e, f*), in August (*g, h, i*), 1993–2002 (*a, d, g*), 2003–2012 (*b, e, h*), 2013–2022 (*c, f, i*)

Analysis of summer SST data for three decades showed that in the field of temperature gradients the Polar Frontal Zone and the frontal zone in the Pechora Sea were best identified, and maxima (up to 0.15 °C/km) were most often observed in the third decade. It is also worth noting that the Coastal Frontal Zone on the surface

for 1993–2022 could not be identified according to CMEMS GLORYS12v1 and MERCATOR PSY4QV3R1 data.

Fig. 5 shows maps of the horizontal distribution of the salinity gradient according to CMEMS GLORYS12v1 and MERCATOR PSY4QV3R1 reanalysis data. There is no significant variability in the characteristics over all three months under study. In June, small high-gradient areas (> 0.03 PSU/km) are observed in the western part of the Polar and Coastal Frontal Zones, near the shores of the Svalbard and the Franz Josef Land. Maximum haline gradients (> 0.07 PSU/km) are recorded in the Pechora Sea. In July 2003–2012, gradients are minimal (> 0.02 PSU/km) in contrast to other decades, especially in the western part of the Polar Frontal Zone and in the Kanin Nos region. The gradient values in the Pechora Sea and in the region of the Coastal Frontal Zone are close. In August, the trends of July continue – in the second decade, the western region of the Polar Frontal Zone is less pronounced than in the first and third ones; maxima are observed in the Pechora Sea and in the region of the Coastal Frontal Zone.

Comparative analysis of thermohaline gradients in the Barents Sea.

The table below presents quantitative estimates of the spatially mean temperature and salinity gradient variability in the summer seasons for three decades under consideration.

Horizontal gradient of temperature and salinity in the Barents Sea in 1993–2022

Data source	1993–2002			2003–2012			2013–2022		
	June	July	August	June	July	August	June	July	August
∇S , PSU/km									
CMEMS GLORYS12v1	0.008	0.010	0.009	0.008	0.009	0.009	0.007	0.009	0.008
MERCATOR PSY4QV3R1									
∇T , °C/km									
CMEMS GLORYS12v1	0.013	0.014	0.013	0.014	0.014	0.013	0.014	0.014	0.014
MERCATOR PSY4QV3R1									
MODIS/Aqua	–	–	–	0.005	0.005	0.004	0.006	0.005	0.004
VIIRS/Suomi NPP	–	–	–	–	–	–	0.006	0.006	0.005
GHRSSST OSTIA	–	–	–	–	–	–	0.002	0.003	0.003

The obtained estimates show that the data source affects the magnitude of the area-averaged decadal surface gradient significantly. According to CMEMS GLORYS12v1 and MERCATOR PSY4QV3R1 data, the maximum values of the background thermal gradient (> 0.014 °C/km) are observed in the first decade in July, and the minimum values are observed in the third decade in June (0.003 °C/km) according to GHRSSST OSTIA. The temperature gradient value according to satellite measurements is on average 0.005 °C/km lower than according to the reanalysis results. The difference among the estimates of the background gradient based on the data used in this paper can be more than 0.01 °C/km which is comparable to the value of the mean climate gradient in the Barents Sea ¹. At the same time, the smallest difference was recorded between the background decadal gradients calculated using CMEMS GLORYS12v1 and MERCATOR PSY4QV3R1 data, and the climatic temperature gradient from work ¹, which permits to classify these arrays of satellite measurements as the most preferred data source for analyzing the surface manifestations of the Barents Sea frontal zones on climatic time scales. According to CMEMS GLORYS12v1 and MERCATOR PSY4QV3R1 data, the maximum values of salinity gradients are recorded in the first decade in July (0.1 PSU/km), and the minimum ones – in the third decade in July (< 0.08 PSU/km).

The interdecadal variability analysis of the data from all sources showed a slight increase of the background horizontal thermal gradient over three decades. This situation results from the changes in the Atlantic water transport volume which can be associated with a record warm period observed in the Barents Sea in the last decade [20]. The thermal gradient increase in the Barents Sea is monitored in July as a result of surface currents weakening and pycnocline formation leading to significant instability in the surface layer [21]. August is characterized by a temperature gradient decrease associated with a decrease in the number of heterogeneity areas as a result of an increase in temperature to a seasonal maximum and stable stratification in the Barents Sea.

The magnitude of surface salinity gradients has significantly decreased over the past three decades, with a maximum recorded in July. Such interdecadal variability can appear from the reduction of ice cover in the Barents Sea [22, 23] which affects the intensity of interaction between the ocean and the atmosphere and, ultimately, the magnitude of the surface horizontal gradient of not only salinity, but also temperature. It is important to note that the significant difference in the values of thermohaline gradients obtained from different arrays data could be influenced by hydrometeorological (cloudiness, wind) and ice processes which were not taken into account in the present study.

Conclusion

Based on a set of reanalysis data and satellite measurements, a comparative analysis of horizontal decadal gradients of thermohaline fields in the Barents Sea was carried out for the summer period of 1993–2022. Analysis of surface gradients

showed a high degree of variability in space and time, both within the warm season and between decades.

In all summer months and in all data sets, the position of the large-scale Polar Frontal Zone is observed on the surface. According to CMEMS GLORYS12v1 and MERCATOR PSY4QV3R1 data, it is possible to determine the position of the Coastal and Arctic Frontal Zones in July and August. It has been established that according to data from all presented arrays the maximum background gradients on the Barents Sea surface are recorded in July (0.014 °C/km and 0.01 PSU/km), and in August the magnitude of the gradients decreases. It is shown that increased Atlantic water transport and decreased ice cover in the Barents Sea can be the main factors in increasing the background thermal gradient and decreasing the salinity gradient.

The difference between the calculated estimates of background horizontal temperature gradients can reach more than 0.01 °C/km, which is comparable to the value of the mean climatic temperature gradient in the Barents Sea. The thermal gradient value is closest to this value according to data from CMEMS GLORYS12v1 and MERCATOR PSY4QV3R1 data which could potentially be the most preferable tool for determining and analyzing long-term variability of the surface manifestations of frontal zones in the Barents Sea.

Thus, the choice of data source from various reanalysis arrays or satellite measurements for calculations can have a significant impact on the resulting value of the horizontal gradient of temperature and salinity which should be taken into consideration when obtaining the final estimate of the background gradient.

REFERENCES

1. Johannessen, O.M., Johannessen, J.A., Svendsen, E., Shuchman, R.A., Campbell, W.J. and Josberger, E., 1987. Ice-Edge Eddies in the Fram Strait Marginal Ice Zone. *Science*, 236(4800), pp. 427-429. doi:10.1126/science.236.4800.427
2. Small, R.J., deSzoeko, S.P., Xie, S.P., O'Neill, L., Seo, H., Song, Q., Cornillon, P., Spall, M. and Minobe, S., 2008. Air-Sea Interaction over Ocean Fronts and Eddies. *Dynamics of Atmospheres and Oceans*, 45(3-4), pp. 274-319. doi:10.1016/j.dynatmoce.2008.01.001
3. Boeckel, B. and Baumann, K.-H., 2008. Vertical and Lateral Variations in Coccolithophore Community Structure across the Subtropical Frontal Zone in the South Atlantic Ocean. *Marine Micropaleontology*, 67(3-4), pp. 255-273. doi:10.1016/j.marmicro.2008.01.014
4. Våge, S., Basedow, S.L., Tande, K.S. and Zhou, M., 2014. Physical Structure of the Barents Sea Polar Front near Storbanken in August 2007. *Journal of Marine Systems*, 130, pp. 256-262. doi:10.1016/j.jmarsys.2011.11.019
5. Oziel, L., Sirven, J. and Gascard, J.-C., 2016. The Barents Sea Frontal Zones and Water Masses Variability (1980–2011). *Ocean Science*, 12(1), pp. 169-184. doi:10.5194/os-12-169-2016
6. Atadzhanova, O.A., Zimin, A.V., Svergun, E.I. and Konik, A.A., 2018. Submesoscale Eddy Structures and Frontal Dynamics in the Barents Sea. *Physical Oceanography*, 25(3), pp. 220-228. doi:10.22449/1573-160X-2018-3-220-228
7. Artamonov, Yu.V., Skripaleva, E.A. and Fedirko, A.V., 2019. Seasonal Variability of Temperature Fronts on the Barents Sea Surface. *Russian Meteorology and Hydrology*, 44(1), pp. 53-61. doi:10.3103/S1068373919010060

8. Ivshin, V.A., Trofimov, A.G. and Titov, O.V., 2019. Barents Sea Thermal Frontal Zones in 1960–2017: Variability, Weakening, Shifting. *ICES Journal of Marine Science*, 76(suppl. 1), pp. i3-i9. doi:10.1093/icesjms/fsz159
9. Moiseev, D.V., Zaporozhtsev, I.F., Maximovskaya, T.M. and Dukhno, G.N., 2019. Identification of Frontal Zones Position on the Surface of the Barents Sea According to in Situ and Remote Sensing Data (2008-2018). *Arctic: Ecology and Economy*, (2), pp. 48-63. doi:10.25283/2223-4594-2019-2-48-63 (in Russian).
10. Konik, A.A., Zimin, A.V. and Kozlov, E.I., 2021. Spatial and Temporal Variability of the Polar Frontal Zone Characteristics in the Barents Sea in the First Two Decades of the XXI Century. *Fundamental and Applied Hydrophysics*, 14(4), pp. 39-51. doi:10.7868/S2073667321040043 (in Russian).
11. Konik, A.A. and Zimin, A.V., 2022. Variability of the Arctic Frontal Zone Characteristics in the Barents and Kara Seas in the First Two Decades of the XXI Century. *Physical Oceanography*, 29(6), pp. 659-673. doi:10.22449/1573-160X-2022-6-659-673
12. Callaghan, T.V., Bergholm, F., Christensen, T.R., Jonasson, C., Kokfelt, U. and Johansson, M., 2010. A New Climate Era in the Sub-Arctic: Accelerating Climate Changes and Multiple Impacts. *Geophysical Research Letters*, 37(14), L14705. doi:10.1029/2009GL042064
13. Overland, J.E., Wang, M., Walsh, J.E. and Stroeve, J.C., 2014. Future Arctic Climate Changes: Adaptation and Mitigation Time Scales. *Earth's Future*, 2(2), pp. 68-74. doi:10.1002/2013ef000162
14. Yamanouchi, T. and Takata, K., 2020. Rapid Change of the Arctic Climate System and Its Global Influences – Overview of GRENE Arctic Climate Change Research Project (2011–2016). *Polar Science*, 25, 100548. doi:10.1016/j.polar.2020.100548
15. Liu, Y. and Minnett, P.J., 2016. Sampling Errors in Satellite-Derived Infrared Sea-Surface Temperatures. Part I: Global and Regional MODIS Fields. *Remote Sensing of Environment*, 177, pp. 48-64. doi:10.1016/j.rse.2016.02.026
16. Stark, J.D., Donlon, C.J., Martin, M.J. and McCulloch, M.E., 2007. OSTIA: An Operational, High Resolution, Real Time, Global Sea Surface Temperature Analysis System. In: *OCEANS 2007 – Europe*. Aberdeen, UK: IEEE, pp. 1-4. doi:10.1109/oceans.2007.4302251
17. Poli, P., Healy, S.B. and Dee, D.P., 2010. Assimilation of Global Positioning System Radio Occultation Data in the ECMWF ERA-Interim Reanalysis. *Quarterly Journal of the Royal Meteorological Society*, 136(653), pp. 1972-1990. doi:10.1002/qj.722
18. Mathiot, P., Jenkins, A., Harris, C. and Madec, G., 2017. Explicit Representation and Parametrised Impacts of under Ice Shelf Seas in the z* Coordinate Ocean Model NEMO 3.6. *Geoscientific Model Development*, 10(7), pp. 2849-2874. doi:10.5194/gmd-10-2849-2017
19. Chvilev, S.V., 1991. Frontal Zones in the Barents Sea. *Meteorologiya i Gidrologiya*, (11), pp. 103-110 (in Russian).
20. Trofimov, A.G., Karsakov, A.L. and Ivshin, V.A., 2018. Climate Changes in the Barents Sea over the Last Half Century. *Trudy VNIRO*, 173, pp. 79-91 (in Russian).
21. Pnyushkov, A.V., 2008. The Investigations of Barents Sea Water Circulation Structure. *Arctic and Antarctic Research*, (1), pp. 27-37 (in Russian).
22. Zhichkin, A.P., 2012. Climatic Variations of Ice Conditions in Different Regions of the Barents Sea. *Russian Meteorology and Hydrology*, 37, pp. 624-630. doi:10.3103/S1068373912090063
23. Ivanov, V.V., Arkhipkin, V.S., Lemeshko, Ye.M., Myslenkov, S.A., Smirnov, A.V., Surkova, G.V., Tuzov, F.K., Chechin, D.G. and Shestakova, A.A., 2022. Changes in Hydrometeorological Conditions in the Barents Sea as an Indicator of Climatic Trends in the Eurasian Arctic in the 21st Century. *Vestnik Moskovskogo Universiteta. Seriya 5, Geografiya*, 1, pp. 13-25 (in Russian).

About the authors:

Alexandr A. Konik, Junior Research Associate, Shirshov Institute of Oceanology of RAS (30, 1st line of Vasilievsky Island, St. Petersburg, 199004, Russian Federation); CSc (Geogr.), **WoS ResearcherID:** AAB-7195-2020, **ORCID ID:** 0000-0002-2089-158X, **Scopus Author ID:** 57203864647, konikrshu@gmail.com

Oksana A. Atadzhanova, Senior Research Associate, Shirshov Institute of Oceanology of RAS (30, 1st line of Vasilievsky Island, St. Petersburg, 199004, Russian Federation); DSc (Geogr.), **WoS ResearcherID:** R-7835-2018, **Scopus Author ID:** 57188718743, oksanam07@list.ru

Submitted 04.08.2023; approved after review 29.08.2023;
accepted for publication 15.11.2023.

Contribution of the co-authors:

Alexandr A. Konik – data collection and systematization, selection and analysis of literature, preparation of the text of the article, creating figures

Oksana A. Atadzhanova – selection and analysis of literature, text analysis and verification

The authors have read and approved the final manuscript.

The authors declare that they have no conflict of interest.

Original article

Variance of Short-Period Sea Level Oscillations in the Black Sea: Seasonal and Interannual Variations

I. P. Medvedev

Shirshov Institute of Oceanology of RAS, Moscow, Russian Federation
✉ patamates@gmail.com

Abstract

Purpose. The study is aimed at investigating the peculiarities of seasonal and interannual variations of the variance of short-period sea level oscillations in the Black Sea.

Methods and Results. The peculiarities of changes in the variance (energy) of synoptic (2–30 days) and mesoscale (2 h – 2 days) sea level oscillations in the Black Sea were studied based on the analyses of long-term sea level observation series. The results of spectral analysis made it possible to find out that on the eastern coast of the Black Sea, the spectral density of sea level oscillations increases from summer to winter and decreases from winter to summer within the frequency range of 0.1–0.8 cycles/day. As for the northwestern and Crimean coasts, the spectral density is practically the same in autumn and winter, further it decreases in spring and summer. The interannual changes of the variance of synoptic oscillations on the eastern sea coast are characterized by a negative trend achieving $-0.25 \text{ cm}^2/\text{year}$ in Batumi and $-0.41 \text{ cm}^2/\text{year}$ in Poti. The variance of mesoscale sea level oscillations has negative trends with the rates from $-0.21 \dots -0.24 \text{ cm}^2/\text{year}$ in Odessa and Nikolaev to $-0.13 \text{ cm}^2/\text{year}$ in Gelendzhik.

Conclusions. The variance of short-period sea level oscillations in the Black Sea increases from summer to winter and decreases from winter to summer that is related to the intensification of cyclonic activity in the atmosphere during autumn and winter. A local seasonal decrease in the variance of sea level oscillations is observed in the estuaries of large rivers in winter due to the developed ice cover preventing the formation of wind surges and seiches. At that, the higher the oscillation frequency, the stronger the ice cover influence.

Keywords: sea level oscillations, Black Sea, synoptic variability, spectrum, variance

Acknowledgements: The research was carried out within the framework of a state assignment of IO RAS (theme No. FMWE-2024-0018).

For citation: Medvedev, I.P., 2024. Variance of Short-Period Sea Level Oscillations in the Black Sea: Seasonal and Interannual Variations. *Physical Oceanography*, 31(1), pp. 59-70

© 2024, I. P. Medvedev

© 2024, Physical Oceanography

Introduction

The Black Sea is one of the most isolated seas of the World Ocean. Short-period sea level oscillations from adjacent basins (the Mediterranean, Aegean, and Marmara seas) hardly ever pass into the Black Sea due to the narrowness and shallowness of the Bosphorus and Dardanelles straits. As a result, short-period oscillations are formed directly inside the sea under the effect of atmospheric processes of a natural synoptic period¹.

¹ German, V.Kh. and Levikov S.P., 1988. [*Probabilistic Analysis and Modeling of the Sea Level Oscillations*]. Leningrad: Gidrometeoizdat, 231 p. (in Russian).



Tides make the maximum energy contribution, about 85–90%, to the total variance of sea level oscillations in the marginal seas that freely communicate with the open ocean [1]. The tides from adjacent waters also do not penetrate into the Black Sea due to the narrowness of the straits. The sea forms its own tide which is the reaction of the basin water mass to the direct effect of tidal forces [2–4]. The maximum tidal range in the Black Sea varies from 1 cm near the Crimean Peninsula to 18–19 cm in the Dnieper-Bug Estuary and Karkinitzky Bay [3]. The contribution of tides to the total variance of the Black Sea level oscillations varies from 0.3% in Sevastopol to 6% in Batumi [5].

Synoptic (2–30 days) and mesoscale (2 h – 2 days) ranges of the sea level oscillation periods were identified in [5, 6] based on the classification². Synoptic and mesoscale sea level oscillations in the Black Sea are formed mainly under the effect of meteorological factors (atmospheric pressure and wind) [7–9]. In the mesoscale range of periods, dynamic processes are formed under the influence of buoyancy force and the Earth rotation around its axis. The main types of the Black Sea level oscillations in this range of periods are seiches, storm surges, and tides^{1,3,4}[5, 7, 10]. The effect of buoyancy forces decreases with an increasing period of oscillations in the synoptic variability range and the sea dynamics is determined by the Earth rotation around its axis and the unevenness of this rotation with latitude (β -effect). The main class of motions in this case is planetary Rossby waves [8]. Barotropic waves predominate in the short-period part of the sea synoptic variability, baroclinic waves – in the long-period part and eddy movements (synoptic eddies) – in the interval between them [8].

If in the mesoscale range of the Black Sea level variability one can identify stable peaks related to seiches and tides [10], in the synoptic variability range individual peaks are weakly expressed. A summary table of estimates of oscillation periods in the synoptic and mesoscale ranges obtained by various authors is presented in [8]. A dominant stable peak in the synoptic range is a wide increase in spectral density over periods of 14–16 days characteristic of the steep Crimean and Caucasian coasts [5, 11, 12]. It was demonstrated in [13] that these were coastal trapped Kelvin waves propagating counterclockwise at 2.3–2.6 m/s velocity and having characteristic heights of up to 10–20 cm.

The spectrum evolution of the Black Sea level oscillations with an increase in the frequency of oscillations in various variability ranges from 2 hours to 10 years, as well as variance spatial distribution features of the Black Sea level oscillations in five different frequency ranges were studied in [5] based on long-term series of observations at 23 coastal stations. The synoptic and mesoscale sea level oscillations demonstrate significant unevenness of variance distribution over the water area. The highest values are observed in the shallow northwestern part of the Black Sea. They are due to the surface wind effect. If the variance of seasonal and interannual

² Monin, A., Kamenkovich, V. and Kort, V., 1977. *Variability of the Oceans*. London: John Wiley & Sons Ltd, 241 p.

³ Blatov, A.S., Bulgakov, N.P., Ivanov, V.A., Kosarev, A.N. and Tuzhilkin, V.S., 1984. *Variability of the Black Sea Hydrophysical Fields*. Leningrad: Gidrometeoizdat, 240 p. (in Russian).

⁴ Arkhipkin, V.S., Ivanov, V.A. and Nikolaenko, E.G., 1989. Modeling of Barotropic Seiches in Southern Seas. In: A. S. Sarkisyan, ed., 1989. *Modeling of Hydrophysical Processes and Fields in Closed Basins and Seas*. Moscow: Nauka, pp. 104-117 (in Russian).

sea level oscillations exceeds the variance of synoptic sea level oscillations by approximately 1.5–2 times at stations of the Caucasian coast of the Black Sea (Tuapse, Poti, Batumi) and near the Crimean coast (Sevastopol), then a synoptic component contributes the most to the total sea level variance in the northwestern part. In [11], V.A. Ivanov and V.P. Yastreb assessed the energy characteristics of various types of the Black Sea level oscillations at three points: Poti, Tuapse, and Feodosia based on hourly series. Synoptic variability contribution to the total variance of sea level variations according to [11, 14] is 5–13 times greater than the contribution of mesoscale oscillations.

The above-described studies [5] were continued in this work. The purpose is studying the features of seasonal and interannual variability of the variance of short-period oscillations in the Black Sea level. Qualitative and quantitative estimates of this variability were obtained based on long series of observations.

Materials and methods

Long series of hourly observations of the sea level oscillations at 12 coastal stations from [5] were used for the analysis. Fig. 1 demonstrates the geographical location of the stations in question, which is the post-Soviet coast of the Black Sea (the coast of Russia, Ukraine and Georgia). The data duration varied greatly from station to station, ranging from 3 to 38 years (Table 1).

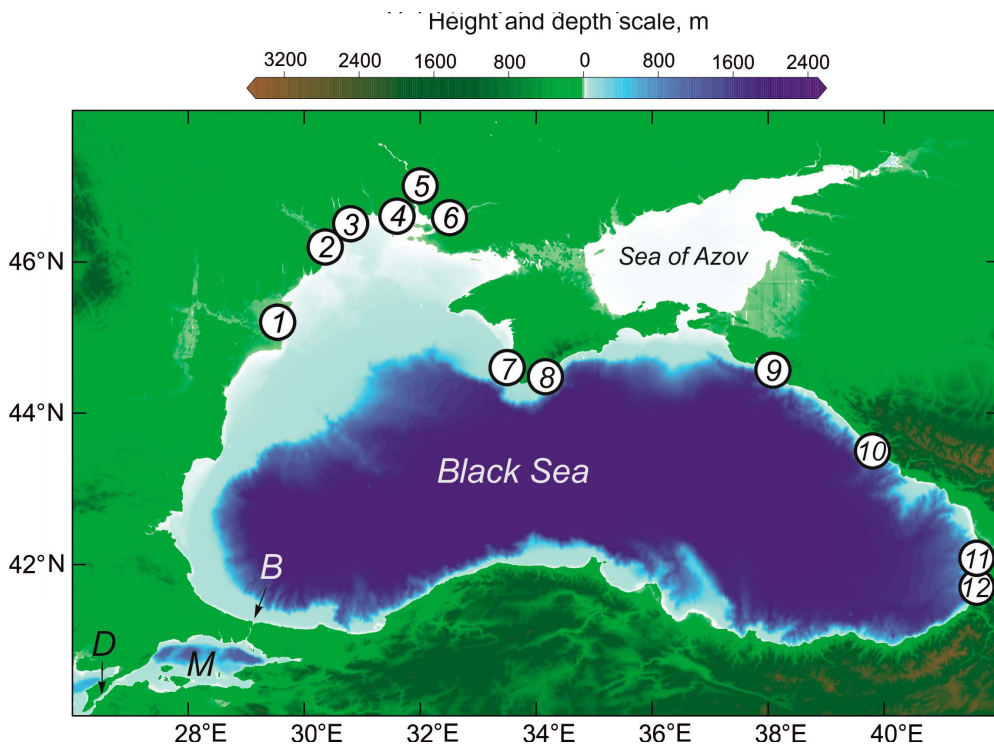


Fig. 1. Location of the coastal tide gauges whose data were used in the study: 1–12 are station numbers. Other designations: *M* is the Sea of Marmara, *B* is the Bosphorus, *D* is the Dardanelles

Information on the stations in the Black Sea whose observation series were used

Station No.	Station	Coordinates		Period, years
		°N	°E	
1	Bolshoe	42.5	29.7	1977–1984
2	Belgorod-Dnestrovsky	46.2	30.4	1977–1995
3	Odessa	46.5	30.8	1977–1995
4	Ochakov	46.6	31.6	1977–1995
5	Nikolaev	47.0	32.0	1977–1995
6	Kasperovka	46.6	32.3	1977–1995
7	Sevastopol	44.6	33.5	1977–1995
8	Yalta	44.5	34.2	1977–1995
9	Gelendzhik	44.6	38.1	1977–1992
10	Sochi	43.5	39.8	1977–2014
11	Poti	42.1	41.6	1977–1991
12	Batumi	41.7	41.6	1977–1991

Results and discussion

Seasonal variations in the spectrum of Black Sea level oscillations

The spectral density of sea level oscillations steadily decreases with increasing frequency f of oscillations according to the law f^{-2} , i.e., it corresponds to “red noise” (Fig. 2). Disturbances in the continuous decay of the spectrum are caused primarily by two main factors: 1) tidal components and 2) frequency-selective properties of the basin. Tides manifest themselves as sharp spectral peaks at fixed diurnal and semidiurnal frequencies (D and SD in Fig. 2). Sea level variations caused by variable air pressure and wind are mainly in the nature of random noise and have a spectrum in the form of a continuous function of frequency (continuum). The nature of the continuous part of the spectrum changes depending on the frequency-selective properties of the entire sea and the water area of its individual parts (gulfs and bays). Local “humps” of a continuous spectrum are formed near the resonant frequencies, where the energy of natural oscillations of the basin level (seiches) is concentrated.

The nature of seasonal variability of the spectra varies greatly depending on the frequency. In the low-frequency range (< 0.8 cycle/day), a significant difference in the energy of the winter and summer spectra is observed. The eastern coast of the sea (Batumi and Sochi) is characterized by an increase in spectral density from summer to winter and a decrease from winter to summer. Moreover, in autumn and spring seasons the spectra have a similar energy level. For the northwestern (Ochakov, Odessa, and Bolshoe) and Crimean coasts, the spectral density in autumn and winter is almost the same further decreasing in spring and summer. At the stations Nikolaev, Kasperovka, and Belgorod-Dnestrovsky, located in the estuaries of large rivers (the Southern Bug, Dnieper, and Dniester, respectively), the spectral density in winter, autumn and spring has similar values. The increase in spectral density in the autumn-winter period is associated with the intensification of cyclonic activity in the atmosphere. Such winter intensification is not observed in the estuaries of large rivers apparently due to the ice cover, which partially dampens synoptic oscillations of sea level.

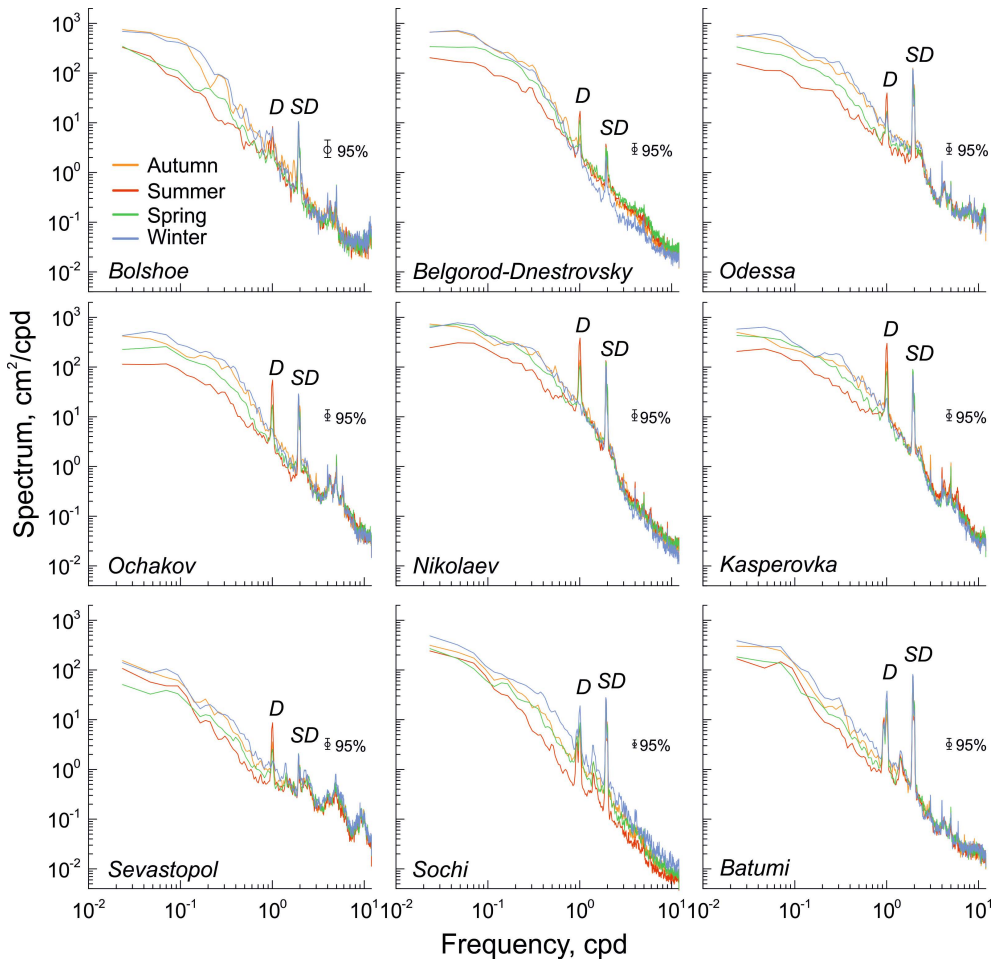


Fig. 2. Seasonal spectra of the sea level oscillations at nine stations in the Black Sea

In the high-frequency region of the spectrum (> 1.2 cycle/day), the level of spectral density varies slightly depending on the season at almost all the stations under consideration. The exception is the spectra for the Sochi, where seasonal variability of high-frequency oscillations repeats the feature characteristic of the low-frequency spectrum region of this station – intensification in winter. At stations located in the estuaries of large rivers (Nikolaev, Kasperovka and Belgorod-Dnestrovsky), the energy of high-frequency sea level oscillations in winter is even slightly inferior to the spectral density characteristic of other seasons of the year. This is probably due to the development of ice cover in the winter season [15] which prevents formation of the sea level oscillations of wind origin (surges and seiches) in the estuaries.

In Fig. 2, special attention should be paid to radiational (thermal) tidal spectral peaks at frequencies of 1 cycle/day and multiple frequencies. Radiational tides are movements of water directly or indirectly associated with solar radiation [3, 10]. They are formed under the combined effect of various periodic factors: diurnal

oscillations of water and air temperatures, atmospheric tides, and breeze winds. The detailed information about the features of radiational and gravitational tides in the Black Sea is given in [3].

The diurnal peaks in Fig. 2 apparently have a significant contribution from the radiation component. As a result, the peak with a frequency of 1 cycle/day varies greatly throughout the year: in winter it is the weakest and at some stations (Ochakov, Nikolaev, Sevastopol) it is even absent. In summer, this peak reaches maximum energy values even exceeding the semi-diurnal tidal peak at Ochakov, Nikolaev, and Kasperovka. It should be noted that seasonal variability of the diurnal peak at most stations is in antiphase to the nature of the seasonal variability of the spectrum continuous part in the frequency range of 0.2–2 cycle/day.

These features of spectrum seasonal variability confirm the hypothesis about the breeze origin of these diurnal spectral peaks [3, 10]. On the northern coast of the Black Sea, breeze winds are observed from April to October [16]. The highest frequency of breezes is observed on the southern coast of Crimea – on average more than 50 days/year, in some places up to 190 days/year (Yalta) [16]. At the Caucasian coast, the frequency of breezes increases from north to south from 18 to 50 days/year [16]. According to [17], the energy of diurnal sea level oscillations off the coast of Bulgaria in summer is 3–4 times greater than in winter. In [18] it was demonstrated that the breeze wind off the coast of Bulgaria causes diurnal sea level oscillations of about 3–4 cm amplitude, while the influence of water temperature diurnal variations on the sea level variation is negligible. The semi-diurnal spectral peak in Fig. 2 has an astronomical tidal origin [3], as a result of which it does not undergo any special variations from season to season.

Seasonal changes in the variance of synoptic level oscillations

To quantify the seasonal variability of energy of short-period sea level oscillations in the Black Sea, we calculated the spectra for each monthly series of hourly observations and variance values were obtained in various frequency ranges. Residual (non-tidal) series of sea level variations were applied for calculations. They were obtained by subtracting from the original series the sea level variations of tidal oscillations, calculated using harmonic analysis by the least squares method [3]. The main attention was paid to the synoptic range with oscillation periods from 2 days to one month, as well as the mesoscale range with oscillation periods from 2 hours to 2 days. The variance for the selected ranges can be estimated as $\sigma^2 = \Delta f \sum S(f_i)$, where Δf is spectral frequency resolution, and i varies within specified limits. Next, the median, lower (first) and upper (third) quartiles (25th and 75th percentiles, respectively) were calculated for each month. The edges of a statistically significant sample (the ends of the whiskers) were determined by the difference between the first quartile and one and a half interquartile distances (in the case of the lower one) and the sum of the third quartile and one and a half interquartile distances (in the case of the upper one). The interquartile distance (interquartile range, *IQR*) is defined as the difference between the values of the third and the first quartiles.

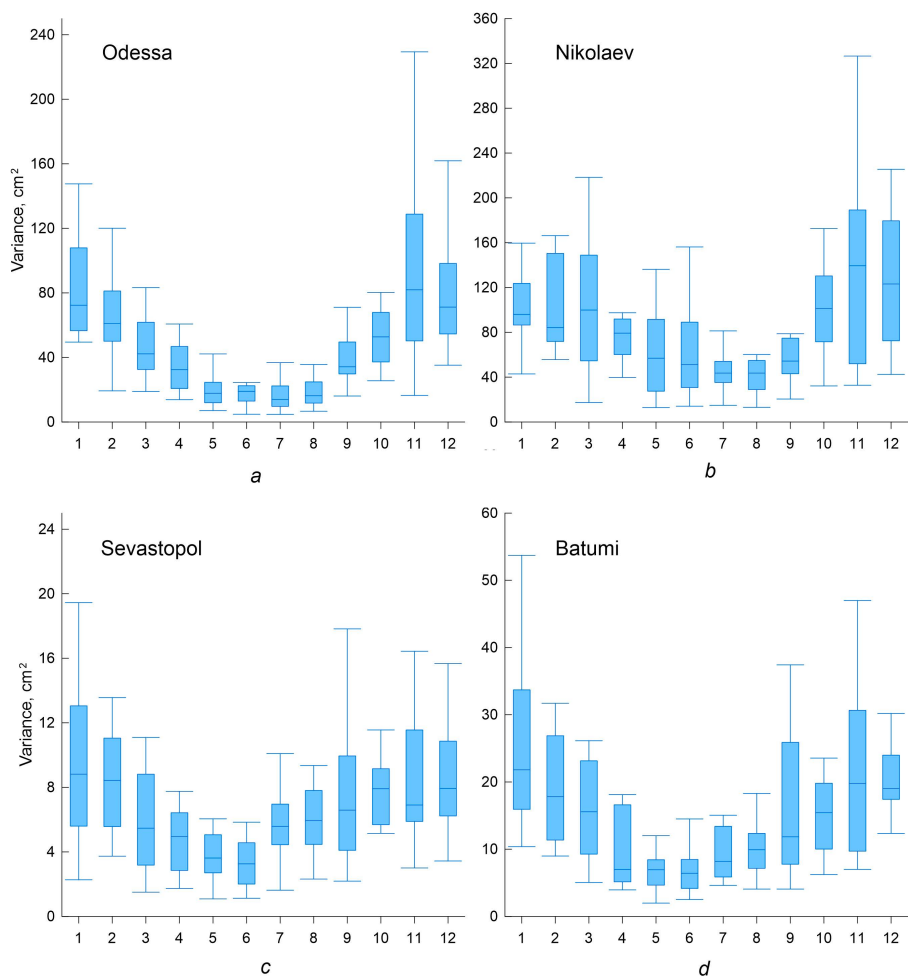


Fig. 3. Box plots of seasonal variations of the variance of synoptic sea level oscillations at the stations Odessa (*a*), Nikolaev (*b*), Sevastopol (*c*), and Batumi (*d*)

In Fig. 3 the calculated box plots (“boxes with whiskers”) of variance estimates of synoptic sea level oscillations for Odessa, Nikolaev, Sevastopol, and Batumi stations are given. All four stations are characterized by high variance values in the autumn-winter period and lower ones in the summer. Moreover, in the deep-water parts of the sea (Sevastopol and Batumi) the minimum variance is observed from May to June, in Odessa this period is wider – from May to August and in Nikolaev it shifts towards the end of summer – from July to August. The interannual spread of variance estimates from November to January is also significantly higher than in other months. In the northwestern part of the sea (Fig. 3, *a, b*), the maximum median value of the variance, as well as the spread of extreme values, reaches its maximum in November. In Nikolaev, the river runoff influence, which increases the spread of variance estimates in May – June, is likely to be felt. In Sevastopol and Batumi, the maximum median values are observed in January (Fig. 3, *c, d*).

In September, these stations demonstrate local increase in both the median estimate and the spread.

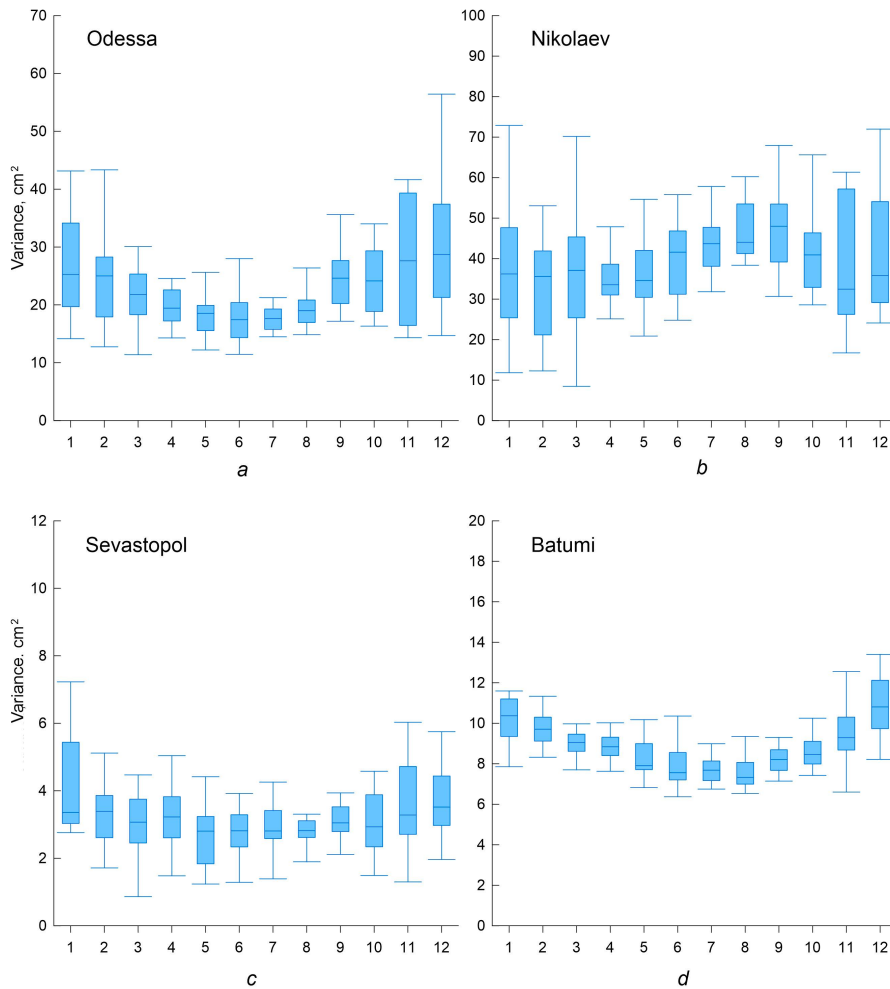


Fig. 4. Box plots of seasonal variations of the variance of mesoscale sea level oscillations at the stations Odessa (a), Nikolaev (b), Sevastopol (c), and Batumi (d)

The mesoscale variability range is characterized by different box plots of variance estimates of sea level oscillations (Fig. 4). The maximum values are observed in autumn and winter. The minimum values of the median variance in Odessa, Sevastopol, and Batumi are typical for May – August. In Nikolaev, the lowest variance values are observed in April, May, and November. The spread of variance values at three stations (Fig. 4, a, c, d) decreases from winter to summer and increases from summer to winter. Nikolaev is characterized by atypical histograms with an increase in median variance values from May to September followed by a decrease in the median and an increase in variance by November – December.

The cause of this effect is probably the interannual variability of the ice cover. In years with maximum duration of the ice cover, the variance values of mesoscale sea level oscillations are lower compared to the summer months. For example, this is illustrated by the lower whiskers from November to March in the diagrams in Nikolaev (Fig. 3, *b*). Due to the fact that prolonged ice cover in the Bug Estuary is observed almost every year [15], the median variance values in November – December are also lower than in other months. Winters with weak ice cover are characterized by an increase in the variance of mesoscale oscillations caused by cyclonic activity, as evidenced by the maximum values of the diagrams for the winter months (upper whiskers).

Interannual variations in the variance of short-period level oscillations

As was shown in the previous section, variance estimates for individual months vary from year to year. To analyze the interannual variability of the variance of short-period sea level oscillations, average annual values were calculated. Fig. 5 demonstrates the annual variance of synoptic (*a*) and mesoscale (*b*) sea level oscillations. The coefficient of variation (c_v), reflecting the variability degree of σ_{syn}^2 values in relation to the average sample value, ranged from 0.17 for the Nikolaev to 0.29 for the Gelendzhik. Interannual variations in σ_{syn}^2 on the eastern coast of the sea are characterized by a negative trend of up to $-0.25 \text{ cm}^2/\text{year}$ in Batumi and $-0.41 \text{ cm}^2/\text{year}$ in Poti, which is proportional to σ_{syn}^2 decrease by 1.3 and 1.8% per year from the average value, respectively (Fig. 5, *a*). For the Crimean and northwestern coasts of the sea there isn't a clearly defined trend, but in Nikolaev there is already a weak trend towards an increase in σ_{syn}^2 from 1977 to 1995 at a rate of $0.46 \text{ cm}^2/\text{year}$ (0.44%).

The variance values of mesoscale oscillations σ_{mes}^2 at some stations also vary significantly from year to year (Fig. 5, *b*). The coefficient of variation for Sevastopol, Gelendzhik, and Poti is 0.22, 0.30 and 0.18, respectively. For Yalta, Odessa, Nikolaev c_v decreases to 0.13–0.16. In Batumi c_v is 0.04, which reflects weak interannual variability of σ_{mes}^2 values. Thus, two nearby stations (Batumi and Poti) have different patterns of interannual σ_{mes}^2 variations (Fig. 5, *b*). Moreover, if in Batumi no significant trends in σ_{mes}^2 variations were identified, in Poti a negative trend at a rate of $-0.09 \text{ cm}^2/\text{year}$ (1.4%) was observed. In Gelendzhik, the nature of interannual variations is different, but the rate of σ_{mes}^2 decrease is even higher than in Poti ($-0.13 \text{ cm}^2/\text{year}$ (3.7%)). For the Crimean coast, pronounced trends in interannual variability are absent. Moreover, in Sevastopol and Yalta σ_{mes}^2 interannual variations occur in antiphase. In Odessa and Nikolaev, we observed a similar pattern of interannual variability with a weak negative trend ($-0.21 \dots -0.24 \text{ cm}^2/\text{year}$; 0.6–0.9%) in σ_{mes}^2 values.

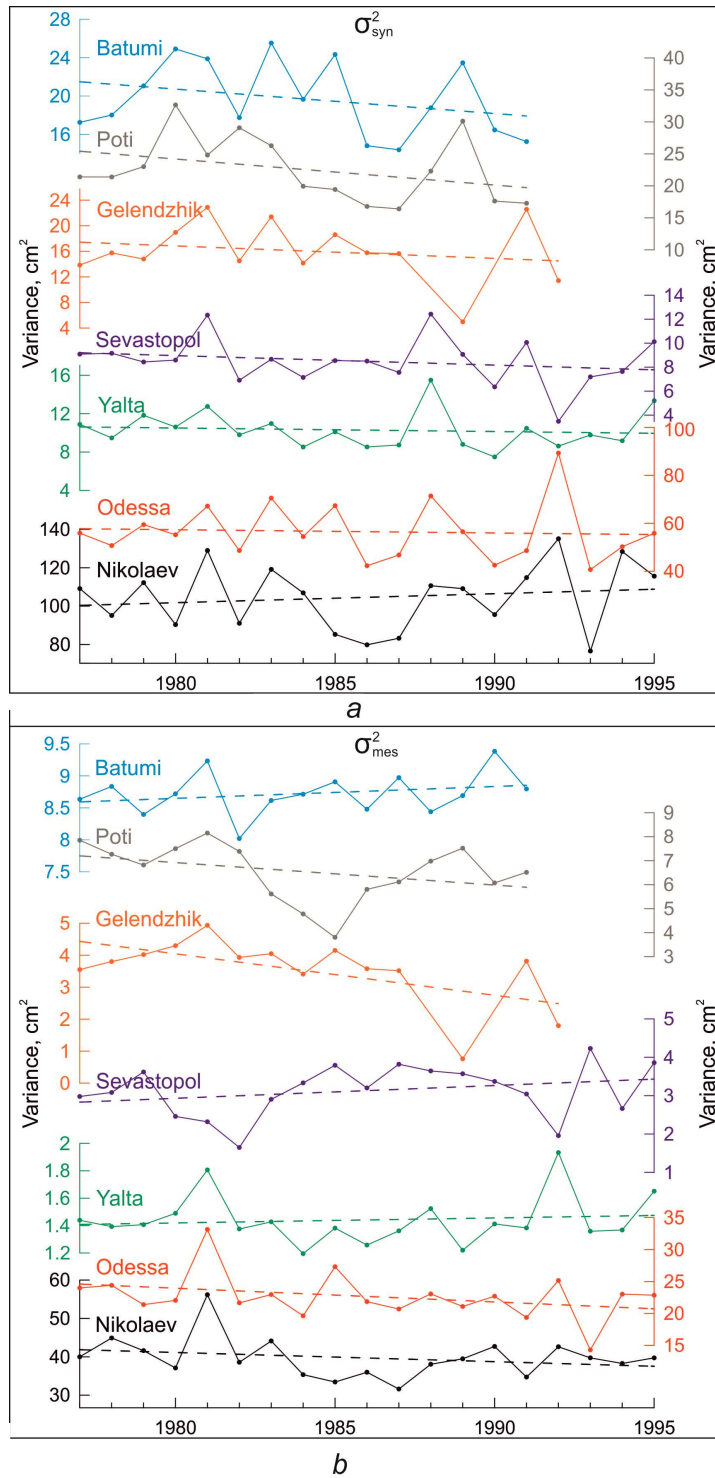


Fig. 5. Interannual changes of variance of the synoptic (a) and mesoscale (b) Black Sea level oscillations at the stations Batumi, Poti, Gelendzhik, Sevastopol, Yalta, Odessa, and Nikolaev. The dashed line shows long-term linear trends

Conclusions

The long-term series of sea level observations made it possible to study the features of variance (energy) changes of the Black Sea level oscillations. Based on the results of spectral analysis, this work provided quantitative and qualitative characteristics of seasonal and interannual sea level variability in various physical and geographical conditions.

On the eastern coast of the Black Sea, the spectral density of sea level oscillations increases from summer to winter and decreases from winter to summer within the frequency range of 0.1–0.8 cycle/day. For the northwestern (Ochakov, Odessa, and Bolshoe) and Crimean coasts, the spectral density level in autumn and winter is almost the same, further decreasing in spring and summer. These features of seasonal variability in the spectrum of sea level oscillations are associated with the intensification of cyclonic activity in the atmosphere in the autumn-winter period.

In the estuaries of large rivers (for example, Nikolaev, Kasperovka, and Belgorod-Dnestrovsky stations), developed ice cover in winter prevents the formation of wind-induced oscillations in sea level (surges and seiches) due to which spectral energy decreases. Moreover, the higher the frequency, the more important the role played by the ice cover. Thus, in the synoptic frequency range in these sea areas, the spectral density level in winter is close to the autumn and spring values and in the mesoscale frequency range it is even lower.

The pronounced diurnal spectral peak is of radiational (thermal) tidal origin, in contrast to the semi-diurnal peak associated with classical astronomical tides. Apparently, the main factor affecting the formation of this peak is breeze winds. As a result, the diurnal peak is weakly distinguished in the winter season and reaches its maximum energy values in summer when the breeze circulation is most developed.

The variance values of sea level oscillations vary both from month to month and from year to year. To analyze the interannual variability of the variance of short-period sea level oscillations, average annual values were calculated. Interannual changes in the variance of synoptic oscillations on the eastern coast of the sea are characterized by a negative trend of up to $-0.25 \text{ cm}^2/\text{year}$ in Batumi and $-0.41 \text{ cm}^2/\text{year}$ in Poti, which is 1.3 and 1.8% of the average value, respectively. The variance of mesoscale sea level oscillations has negative trends with rates from $-0.21 \dots -0.24 \text{ cm}^2/\text{year}$ (0.6–0.9%) in Odessa and Nikolaev to $-0.13 \text{ cm}^2/\text{year}$ (3.7%) in Gelendzhik.

Based on the obtained results, the seasonal and interannual variability of energy of the Black Sea level oscillations was assessed. In the case of a mesoscale range of periods, these estimates reflect the variability of sea level oscillations of wind origin, primarily surge phenomena and seiches.

REFERENCES

1. Wunsch, C., 1972. Bermuda Sea Level in Relation to Tides, Weather, and Baroclinic Fluctuations. *Reviews of Geophysics*, 10(1), pp. 1-49. doi:10.1029/RG010i001p00001
2. Medvedev, I.P., Rabinovich, A.B. and Kulikov, E.A., 2016. Tides in Three Enclosed Basins: the Baltic, Black, and Caspian Seas. *Frontiers in Marine Science*, 3, 46. doi:10.3389/fmars.2016.00046

3. Medvedev, I.P., 2018. Tides in the Black Sea: Observations and Numerical Modelling. *Pure and Applied Geophysics*, 175(6), pp. 1951-1969. doi:10.1007/s00024-018-1878-x
4. Ferrarin, C., Bellaifiore, D., Sannino, G., Bajo, M. and Umgiesser, G., 2018. Tidal Dynamics in the Inter-Connected Mediterranean, Marmara, Black and Azov Seas. *Progress in Oceanography*, 161, pp. 102-115. doi:10.1016/j.pocean.2018.02.006
5. Medvedev, I.P., 2018. Analysis of Variance of the Black Sea Level Oscillations in a Wide Range of Frequencies. *Physical Oceanography*, 25(6), pp. 448-458. doi:10.22449/1573-160X-2018-6-448-458
6. Medvedev, I.P., 2015. Formation of the Baltic Sea Level Spectrum. *Doklady Earth Sciences*, 463(1), pp. 760-764. doi:10.1134/S1028334X1507020X
7. Ivanov, V.A. and Yankovskiy, A.E., 1992. [*Long-Wave Motion in the Black Sea*]. Kiev: Naukova Dumka, 110 p. (in Russian).
8. Ivanov, V.A. and Belokopytov, V.N., 2013. *Oceanography of Black Sea*. Sevastopol: ECOSI-Gidrofizika, 210 p.
9. Medvedev, I.P., 2022. Numerical Modeling of Meteorological Sea Level Oscillations in the Black Sea. *Oceanology*, 62(4), pp. 471-481. doi:10.1134/S0001437022040087
10. Medvedev, I.P. and Kulikov, E.A., 2016. Spectrum of Mesoscale Sea Level Oscillations in the Northern Black Sea: Tides, Seiches, and Inertial Oscillations. *Oceanology*, 56(1), pp. 6-13. doi:10.1134/S0001437016010094
11. Ivanov, V.A. and Yastreb, V.P., 1989. Fluctuations of the Black Sea Level. *Water Resources*, 16(2), pp. 173-179.
12. Stanev, E.V., Grashorn, S. and Zhang, Y.J., 2017. Cascading Ocean Basins: Numerical Simulations of the Circulation and Interbasin Exchange in the Azov-Black-Marmara-Mediterranean Seas System. *Ocean Dynamics*, 67(8), pp. 1003-1025. doi:10.1007/s10236-017-1071-2
13. Aydın, M. and Beşiktepe, Ş.T., 2022. Mechanism of Generation and Propagation Characteristics of Coastal Trapped Waves in the Black Sea. *Ocean Science*, 18(4), pp. 1081-1091. doi:10.5194/os-18-1081-2022
14. Goryachkin, Yu.N. and Ivanov, V.A., 2006. *Black Sea Level: Past, Present, Future*. Sevastopol: ECOSI-Gidrofizika, 210 p. (in Russian).
15. Ilyin, Yu.P., Repetin, L.N., Belokopytov, V.N., Goryachkin, Yu.N., Dyakov, N.N., Kubryakov, A.A. and Stanichny, S.V., 2012. *Hydrometeorological Conditions of the Ukrainian Seas. Vol. 2. The Black Sea*. Sevastopol: ECOSI-Gidrofizika, 421 p. (in Russian).
16. Fomicheva, L.A., Rabinovich, A.B. and Demidov, A.N., 1991. [Sea Level]. In: E. N. Altman and A. I. Simonov, eds., 1991. *Hydrometeorology and Hydrochemistry of Seas in the USSR. Vol. IV. Black Sea. Issue 1. Hydrometeorological Conditions*. Leningrad: Gidrometeoizdat, pp. 329-354 (in Russian).
17. Mungov, G., 1981. [Study of Sea Level Fluctuations along the Bulgarian Coast in a Medium-Scale Frequency Range]. *Hidrologija i Meteorologija*, 30(2), pp. 20-32 (in Bulgarian).
18. Krasteva, E., 1981. Diurnal Amplitudes of the Black Sea Level near Varna and Burgas. *Problems of Geography*, 2, pp. 15-24 (in Bulgarian).

About the author:

Igor P. Medvedev, Leading Research Associate, Tsunami Laboratory, Shirshov Institute of Oceanology of RAS (36 Nakhimovsky ave, Moscow, 117997, Russian Federation), CSc (Phys.-Math.), **ORCID ID: 0000-0003-0748-0062**, **Scopus Author ID: 55656381400**, **Researcher ID: L-6118-2013**, patamates@gmail.com

The author has read and approved the final manuscript.

The author declares that he has no conflict of interest.

Ratio between Trough and Crest of Surface Waves in the Coastal Zone of the Black Sea

A. S. Zapevalov ✉, A. V. Garmashov

Marine Hydrophysical Institute of RAS, Sevastopol, Russian Federation
✉ sevzepter@mail.ru

Abstract

Purpose. The work is aimed at analyzing variability of the ratio between trough and crest of the sea surface waves, as well as the relationship of this ratio with the skewness of sea surface elevations.

Methods and results. The analysis is based on the wave measurements performed from the stationary oceanographic platform located near the Southern Coast of Crimea in the Black Sea. The depth at the place where the platform is installed is about 30 m. The analyzed data array totals 17,083 twenty-minute measurement sessions. The freak waves were identified by the abnormality index AI equal to the ratio between the maximum wave height per session and the significant wave height. The freak waves with index $AI > 2$ were observed in 562 measurement sessions. This corresponds to a probability of their occurrence equal to 3.3%. The AI values range from 1.16 to 2.79. The ratio between the trough Th of the highest wave and its crest Cr is in the range $0.37 < Th/Cr < 1.47$, at that the average value is 0.79.

Conclusions. Statistical characteristics of the waves revealed in the presence of freak waves differ noticeably from those obtained at $AI < 2$. In the situations when $AI < 2$, the probability of an event when the trough Th of the highest wave exceeds its crest Cr is 10.9%. The event with $Th/Cr > 1$ does not occur if $AI < 1.4$. When there are waves satisfying condition $AI > 2$, the probability of an event $Th/Cr > 1$ is 19.4%. It is shown that condition $Th/Cr > 1$ is not necessary for arising of a negative skewness of sea surface elevations. The probability of skewness large deviations from a zero value both towards positive values and towards negative ones, is higher at $AI > 2$ than at $AI < 2$. The statistical relationship between the skewness and the Th/Cr ratio is observed only for freak waves.

Keywords: sea surface, freak wave, abnormality index, skewness, Black Sea

Acknowledgments: The study was carried out within the framework of state assignment on theme FNNN-2021-0004 “Fundamental studies of oceanological processes which determine state and evolution of marine environment influenced by natural and anthropogenic factors, based on observation and modeling methods”.

For citation: Zapevalov, A.S. and Garmashov, A.V., 2024. Ratio between Trough and Crest of Surface Waves in the Coastal Zone of the Black Sea. *Physical Oceanography*, 31(1), pp. 71-78.

© 2024, A. S. Zapevalov, A. V. Garmashov

© 2024, Physical Oceanography

Introduction

In the classical representation, sea surface waves have a trochoidal form with a pointed crest and a flat trough. Waves of this form correspond to the positive skewness of surface elevations. Work [1] published in 1963 shows that in the case when sea surface structure is formed by free undamped waves, the skewness is always positive. Currently, several types of models are applied to describe the distribution of weakly nonlinear wave field: those constructed on the basis of the Stokes expansion [2, 3] and those in which the cumulants of sea surface elevations



are described by multidimensional integrals of wave spectra [4, 5]. The skewness determined within the framework of these models is always positive as well.

At the same time, numerous measurements carried out in the various World Ocean regions indicate the situations when the skewness of sea surface elevations is negative [6–10]. A possible cause why weakly nonlinear random wave models do not describe these situations lies in the fact that they are constructed for a statistically homogeneous field in which nonlinearity manifests itself in the form of minor corrections [3]. A real wave field includes mechanisms leading to local effects that cannot be considered weakly nonlinear ones. In particular, these are freak waves [11] the presence of which shows significant deviations of skewness and kurtosis from zero values. Skewness can reach a value of -0.4 , kurtosis can exceed one [7, 8].

Several forms of freak waves [12, 13] with different ratios of crest and trough are distinguished, including the waves in which trough is greater than crest. The presence of such waves should lead to a shift in the skewness of sea surface elevations towards negative values.

This work is purposed at analyzing the variability of the ratio between trough and crest of the surface waves, as well as the relationship of this ratio with the skewness of sea surface elevations.

Equipment and measurement conditions. Studies of the field of sea surface waves were carried out at a stationary oceanographic platform located in the Black Sea coastal part off the Southern Coast of Crimea. Measuring equipment, as well as the features of carrying out measurements from a stationary oceanographic platform, are described in [9, 14–16]. The sea depth at the place where the platform was located is ~ 30 m. For typical Black Sea waves, the indicated depth corresponds to deepwater conditions.

Measurements were carried out from May 2018 to January 2019 with several short breaks. For statistical analysis, continuous measurements were divided into sessions lasting 20 minutes each, from which the characteristics of the waves were determined.

Trough/crest ratio. The abnormality index (AI) is applied to identify freak waves [17–19]

$$AI = H_{\max} / H_s,$$

where H_{\max} is maximum wave height during the measurement session; H_s is significant wave height equal to $1/3$ of the average height of the highest waves. It is generally accepted that the waves with a height that exceeds significant wave height more than twice are freak waves, i.e. those waves for which $AI > 2$.

Another less common criterion for identifying freak waves is based on the ratio [20]

$$CI = Cr / H_s,$$

where Cr is height of the maximum wave crest. Waves with CI exceeding the critical value, which is set equal to 1.2, 1.25 or 1.3, are considered freak waves. The relationship between AI and CI parameters was analyzed in [19]. It was shown that the application of CI criterion resulted in an underestimation of the number of

situations when freak waves are observed, compared to the estimate obtained using the criterion $AI > 2$. Discrepancy is due to existence of freak waves crest of which is less than trough.

The data array analyzed in this work consisted of 17,083 measurement sessions. Freak waves (according to criterion $AI > 2$) were recorded in 562 sessions. This corresponds to the probability of their occurrence equal to 3.3%. For comparison, we point out that during the measurements off the western Black Sea coast of Turkey (12.5 m depth), the probability of freak waves occurrence was 2.6% [8].

The data array was obtained at wind speeds W_{10} from calm (conditionally 0 m/s) to 26 m/s with an average speed of 5.6 m/s over the entire measurement period. Here, the wind speed W_{10} is normalized to a horizon of 10 m. Significant wave heights during this period varied in the range of 0.04–2.27 m with an average value of 0.55 m/s. Variation of W_{10} and H_s occurred in almost the same ranges in situations when freak waves were observed: W_{10} varied in the range of 0–21.5 m/s with an average value of 5.4 m/s; H_s – in the range of 0.06–2.1 m with an average value of 0.52 m.

Three forms of freak waves can be distinguished according to the classification proposed in [13]. The form in which crest Cr is one and a half times greater than trough Th is positive. The form when $Th/Cr > 1.5$ is negative. The third form is intermediate. The probability of occurrence of these three forms was 63, 17.5 and 19.5%, respectively. The second form waves were not observed in our measurements; the maximum Th/Cr ratio is 1.47. It can be assumed that large Th/Cr values are due to the fact that wave measurement data were analyzed in [13] at shallow depths (2.7 m) where high nonlinearity caused by the interaction of surface waves with the bottom takes place.

According to measurements carried out from the stationary oceanographic platform, as well as according to previous studies, freak waves with $Th/Cr < 1$ predominate. Th/Cr ratio ranges from 0.37 to 1.47, with an average value of 0.79. In situations when $AI > 2$, the probability of occurrence of waves with $Th/Cr < 1$ was 19.4%. The probability that $Th/Cr > 1$ (calculated for the conditions when freak waves are not observed) was 10.9%, average probability for the ensemble of all situations is 11.3%. Fig. 1 shows Th/Cr dependence on the abnormality index.

Fig. 2 shows conditional probability of event $P(Th/Cr > 1 | AI < AI_0)$, at which $Th/Cr > 1$ if the abnormality index does not exceed a certain critical value AI_0 . It can be seen that the event $Th/Cr > 1$ does not occur if $AI < AI_0 = 1.4$. The conditional probability was constructed for a wave measurement data set in which AI parameter varied within 1.16 and 2.79.

Conditional probability $P(Th/Cr > 1 | AI < AI_0)$ increases rapidly in $AI < 2$ region and varies slightly when $AI > 2$. Based on Fig. 2, it can be assumed that the statistical characteristics of waves in the presence of freak waves differ from the statistical characteristics in cases when they are not observed. We provide other evidence of the validity of this assumption below.

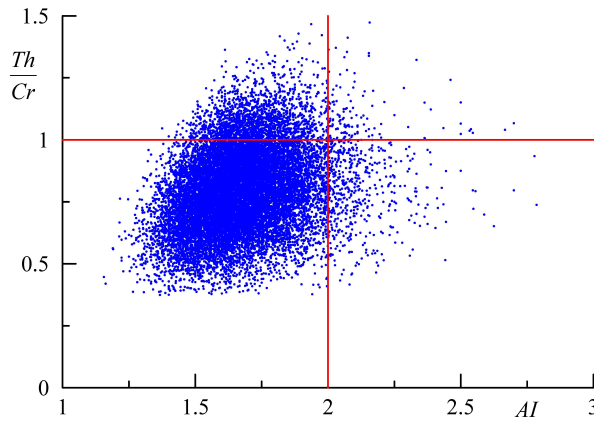


Fig. 1. Dependence of the ratio between trough and crest Th/Cr on the abnormality index AI

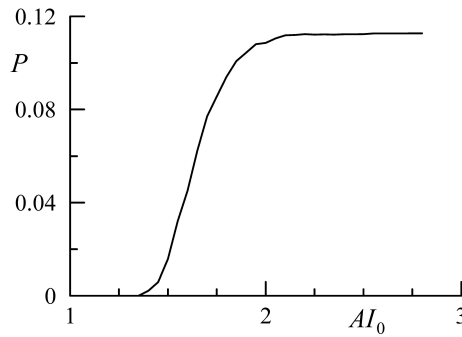


Fig. 2. Conditional probability $P(Th/Cr > 1 | AI < AI_0)$

Skewness. One of the main criteria for the nonlinearity of the field of sea surface waves is the deviation of statistical moments from the values corresponding to the Gaussian distribution [10, 21]. Assuming that the mean value of sea surface elevation is zero, the skewness A of sea surface elevations can be defined as

$$A = \mu_3 / \mu_2^{1.5},$$

where $\mu_n = \langle \xi^n \rangle$ is statistical moment of order n ; ξ is surface elevation; symbol $\langle \dots \rangle$ means averaging.

It is natural to assume that the occurrence of negative skewness values is statistically related to the ratio Th/Cr . Let us consider two arrays of wave measurement data. The first array includes all data, the second – only the data obtained in the presence of freak waves. If the analysis is carried out for the entire range of AI variations, then the relationship between A and Th/Cr is not observed (Fig. 3, *a*) and correlation coefficient ρ between these parameters is equal to -0.1 .

Statistical relationship between A and Th/Cr occurs only when $AI > 2$ (Fig. 3, *b*) and correlation coefficient is $\rho = -0.42$ for the second data array.

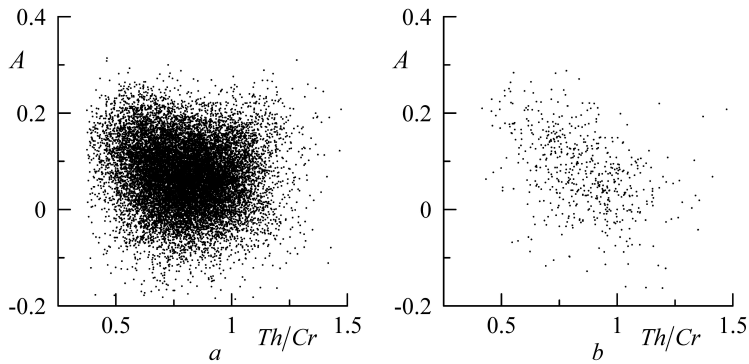


Fig. 3. Dependence of skewness A on the ratio between trough and crest Th/Cr : *a* – within the entire range of AI variation; *b* – at $AI > 2$

It is noteworthy that negative skewness values can occur when two conditions are simultaneously satisfied, $Th/Cr < 1$ and $AI < 2$.

Let us consider two groups of skewness estimates. Estimates A_{fw} were obtained when freak waves were observed ($AI > 2$), estimates A_0 – when freak waves were absent ($AI < 2$). Fig. 4 demonstrates the probability density functions of estimates A_{fw} and A_0 (we denote them as $P_A(A_{fw})$ and $P_A(A_0)$, respectively), as well as the ratio $P_A(A_{fw})/P_A(A_0)$. Probability density functions were calculated as histograms normalized by the sample length and the width of interval within which the skewness estimates fell. The probability of large skewness deviations from zero value at $AI > 2$ is higher than at $AI < 2$. This applies to deviations towards both positive and negative values.

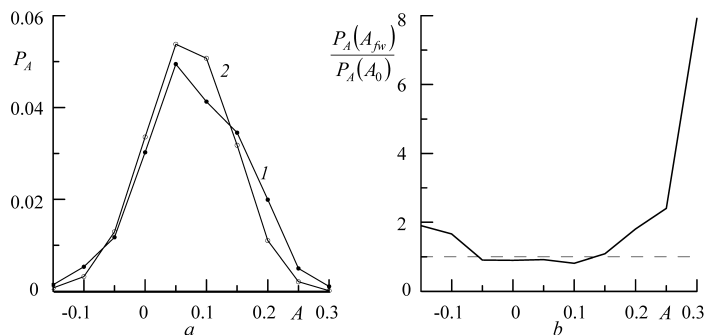


Fig. 4. Changes in the distribution of skewness of surface elevations in the presence of abnormal waves: *a* – probability density functions of skewness, curve 1 – $P_A(A_{fw})$, curve 2 – $P_A(A_0)$; *b* – ratio $P_A(A_{fw})/P_A(A_0)$

Average values calculated for two groups of skewness assessments are close: $\langle A_{fw} \rangle = 0.079$ and $\langle A_0 \rangle = 0.072$.

Conclusion. The probability of occurrence of freak waves (according to criterion $AI > 2$) in the Black Sea off the Southern Coast of Crimea when the deep water condition is satisfied is 3.3%. It is shown that statistical characteristics of the waves revealed in the presence of freak waves differ noticeably from those obtained at $AI < 2$. It was found that the probability of event when trough depth Th of the highest wave exceeds the height of its crest Cr is 10.9%. The probability of $Th/Cr > 1$ event was 19.4% with the occurrence of waves with abnormality index $AI > 2$. The event $Th/Cr > 1$ does not occur if $AI < 1.4$.

The probability of large skewness deviations from zero towards both positive and negative values for $AI > 2$ is higher than for $AI < 2$. The condition $Th/Cr > 1$ is not necessary for arising of negative skewness of sea surface elevations. Negative skewness values can be observed when two conditions are satisfied simultaneously: $Th/Cr < 1$ and $AI < 2$. Statistical relationship between skewness and Th/Cr ratio is observed only when $AI > 2$.

REFERENCES

1. Longuet-Higgins, M.S., 1963. The Effect of Non-Linearities on Statistical Distributions in the Theory of Sea Waves. *Journal of Fluid Mechanics*, 17(3), pp. 459-480. doi:10.1017/S0022112063001452
2. Hou, Y., Song, G., Zhao, X., Song, J. and Zheng Q., 2006. Statistical Distribution of Nonlinear Random Water Wave Surface Elevation. *Chinese Journal of Oceanology and Limnology*, 24(1), pp. 1-5. doi:10.1007/BF02842767
3. Tayfun, M.A. and Alkhalidi, M.A., 2016. Distribution of Surface Elevations in Nonlinear Seas. In: OTC, 2016. *Offshore Technology Conference Asia: Proceedings*. Kuala Lumpur, Malaysia. OTC-26436-MS. doi:10.4043/26436-MS
4. Janssen, P.A.E.M., 2003. Nonlinear Four-Wave Interactions and Freak Waves. *Journal of Physical Oceanography*, 33(4), pp. 863-884. doi.org/10.1175/1520-0485(2003)33<863:NFIAPW>2.0.CO;2
5. Annenkov, S.Y. and Shrira, V.I., 2014. Evaluation of Skewness and Kurtosis of Wind Waves Parameterized by JONSWAP Spectra. *Journal of Physical Oceanography*, 44(6), pp. 1582-1594. doi:10.1175/JPO-D-13-0218.1
6. Jha, A.K. and Winterstein, S.R., 2000. Nonlinear Random Ocean Waves: Prediction and Comparison with Data. In: ASME, 2000. *Proceedings of the 19th International Offshore Mechanics and Arctic Engineering Symposium*. New Orleans, USA. Paper No. 00-6125.
7. Guedes Soares, C., Cherneva, Z. and Antão, E.M., 2004. Steepness and Asymmetry of the Largest Waves in Storm Sea States. *Ocean Engineering*, 31(8-9), pp. 1147-1167. doi:10.1016/j.oceaneng.2003.10.014
8. Bilyay, E., Ozbahceci, B.O. and Yalciner, A.C., 2011. Extreme Waves at Filyos, Southern Black Sea. *Natural Hazards and Earth System Sciences*, 11(3), pp. 659-666. doi:10.5194/nhess-11-659-2011

9. Zapevalov, A.S. and Garmashov, A.V., 2021. Skewness and Kurtosis of the Surface Wave in the Coastal Zone of the Black Sea. *Physical Oceanography*, 28(4), pp. 414-425. doi:10.22449/1573-160X-2021-4-414-425
10. Zapevalov, A.S. and Garmashov, A.V., 2022. The Appearance of Negative Values of the Skewness of Sea-Surface Waves. *Izvestiya, Atmospheric and Oceanic Physics*, 58(3), pp. 263-269. doi:10.1134/s0001433822030136
11. Kharif, C., Pelinovsky, E. and Slunyaev, A., 2009. *Rogue Waves in the Ocean*. Advances in Geophysical and Environmental Mechanics and Mathematics. Berlin; Heidelberg: Springer, 216 p. doi:10.1007/978-3-540-88419-4
12. Glejtin, J., Kumar, V.S., Nair, T.B., Singh, J. and Nherakkol, A., 2014. Freak Waves off Ratnagiri, West Coast of India. *Indian Journal of Geo-Marine Sciences*, 43(7), pp. 1339-1342.
13. Didenkulova, I. and Anderson, C., 2010. Freak Waves of Different Types in the Coastal Zone of the Baltic Sea. *Natural Hazards and Earth System Sciences*, 10(9), pp. 2021-2029. doi:10.5194/nhess-10-2021-2010
14. Toloknov, Yu.N. and Korovushkin, A.I., 2010. The System of Collecting Hydrometeorological Information. In: MHI, 2010. *Monitoring Systems of Environment*. Sevastopol: ECOSI-Gidrofizika. Iss. 13, pp. 50-53 (in Russian).
15. Solov'ev, Yu.P. and Ivanov, V.A., 2007. Preliminary Results of Measurements of Atmospheric Turbulence over the Sea. *Physical Oceanography*, 17(3), pp. 154-172. doi:10.1007/s11110-007-0013-9
16. Efimov, V.V. and Komarovskaya, O.I., 2019. Disturbances in the Wind Speed Fields due to the Crimean Mountains. *Physical Oceanography*, 26(2), pp. 123-134. doi:10.22449/1573-160X-2019-2-123-134
17. Ivanov, V.A., Dulov, V.A., Kuznetsov, S.Yu., Dotsenko, S.F., Shokurov, M.V., Saprykina, Ya.V., Malinovsky, V.V. and Polnikov, V.G., 2012. Risk Assessment of Encountering Killer Waves in the Black Sea. *Geography, Environment, Sustainability*, 5(1), pp. 84-111. doi:10.24057/2071-9388-2012-5-1-84-111
18. Tao, A.-F., Peng, J., Zheng, J.-H., Wang, Y. and Wu, Y.-Q., 2015. Discussions on the Occurrence Probabilities of Observed Freak Waves. *Journal of Marine Science and Technology*, 23(6), pp. 923-928. doi:10.6119/JMST-015-0610-10
19. Zapevalov, A.S. and Garmashov, A.V., 2022. Probability of the Appearance of Abnormal Waves in the Coastal Zone of the Black Sea at the Southern Coast of Crimea. *Ecological Safety of the Coastal and Shelf Zones of Sea*, (3), pp. 6-15. doi:10.22449/2413-5577-2022-3-6-15
20. Luxmoore, J.F., Ilic, S. and Mori, N., 2019. On Kurtosis and Extreme Waves in Crossing Directional Seas: A Laboratory Experiment. *Journal of Fluid Mechanics*, 876, pp. 792-817. doi:10.1017/jfm.2019.575
21. Fedele, F., Brennan, J., Ponce De León, S., Dudley, J. and Dias, F., 2016. Real World Ocean Rogue Waves Explained without the Modulational Instability. *Scientific Reports*, 6(1), 27715. doi:10.1038/srep27715

Submitted 10.01.2023; approved after review 02.07.2023;
accepted for publication 15.11.2023.

About the authors:

Aleksandr S. Zapevalov, Chief Research Associate, Marine Hydrophysical Institute of RAS (2 Kapitanskaya Str., Sevastopol, 299011, Russian Federation), DSc (Phys.-Math.), **ORCID ID: 0000-0001-9942-2796**, **Scopus Author ID: 7004433476**, **WoS ResearcherID: V-7880-2017**, sevzepter@mail.ru

Anton V. Garmashov, Senior Research Associate, Marine Hydrophysical Institute of RAS (2 Kapitanskaya Str., Sevastopol, 299011, Russian Federation), CSc (Geogr.), **Scopus Author ID: 54924806400**, **WoS ResearcherID: P-4155-2017**, ant.gar@mail.ru

Contribution of the co-authors:

Aleksandr S. Zapevalov – formulation of goals and objectives of the study; review of literature on the research problem; analysis of measurement data; writing of the article text

Anton V. Garmashov – processing and description of measurement results; analysis and synthesis of research results; statistical analysis; addition to the article text

The authors have read and approved the final manuscript.

The authors declare that they have no conflict of interest.

Major Ion Composition of Waters in the Kerch Strait and the Adjacent Areas

N. Yu. Andrulionis , I. B. Zavialov, S. A. Rozhdestvenskiy

Shirshov Institute of Oceanology of RAS, Moscow, Russian Federation

 *natalya@ocean.ru*

Abstract

Purpose. The work is purposed at studying the influence of water exchange processes between the Black and Azov seas upon the characteristics of major ion composition (MIC) and other hydrochemical indicators of the Kerch Strait waters, as well as the impact of changes in the relative content of major ions of water salt composition upon the accuracy in determining salinity values. The MIC transformation during mixing of the sea surface waters and the Taman Bay ones in the Kerch Strait is investigated. The errors in calculating salinity by the standard methods are assessed for the Kerch Strait, the northeastern Black Sea and the Taman Bay waters.

Methods and Results. The concentrations of major ions determining MIC in the Kerch Strait, Black Sea and Taman Bay surface waters in 2019–2023 were defined by the potentiometric titration method. The water salinity values were obtained in four different ways.

Conclusions. It was established that the salinity value ~ 18.66 calculated by a sum of the major ions corresponds to the surface waters in the northeastern part of the Black Sea, that conforms to the practical salinity value ~ 18.10 calculated using the CTD probe data. On the average, MIC of these waters is characterized by the following relative content of major ions: $\text{Cl}^- = 54.1\%$, $\text{SO}_4^{2-} = 8.2\%$, $\text{HCO}_3^- = 1\%$, $\text{Na}^+ = 30.8\%$, $\text{K}^+ = 1.3\%$, $\text{Ca}^{2+} = 1.3\%$ and $\text{Mg}^{2+} = 3.4\%$. It is shown that the Kerch Strait waters, even in case of their similar salinity, can have different ratios of the major ions characterized by high spatial and temporal variability which, in its turn, is subjected to a significant impact of the waters inflowing from the shallow Taman Bay. The largest differences were between the sum of major ions and the practical salinity. For the Kerch Strait waters, the differences averaged $\sim 2.5\%$. The ionic variations contributed to underestimating the practical salinity values calculated for all the waters under study. In calculating salinity using the chlorine coefficient, the deviations from the sum of ions constituted $\sim 2\%$, whereas those obtained using the TEOS-10 equations – $\sim 1\%$.

Keywords: Kerch Strait, Black Sea, Taman Bay, Sea of Azov, determination of salinity, salinity, major ion composition, major ions, water exchange

Acknowledgments: The research was carried out with the support of Russian Science Foundation, grant No. 21-17-00191. The authors are grateful to all the participants of the expeditions in the Black Sea and the Kerch Strait in 2019–2023. Special thanks to Ph.D. G. A. Kolyuchkina, as well as to the employees of the Laboratory of Ecology of Coastal Bottom Communities (IO, RAS) and the participants of the expeditions in 2021 for delivery of the samples from the Taman Bay.

For citation: Andrulionis, N.Yu., Zavialov, I.B. and Rozhdestvenskiy, S.A., 2024. Major Ion Composition of Waters in the Kerch Strait and the Adjacent Areas. *Physical Oceanography*, 31(1), pp. 79-98.

© 2024, N. Yu. Andrulionis, I. B. Zavialov, S. A. Rozhdestvenskiy

© 2024, Physical Oceanography

Introduction

The Kerch Strait is a part of the Sea of Azov connecting it with the Black Sea. The western coast of the strait is the Kerch Peninsula of Crimea, the eastern one is the Taman Peninsula. The width of the strait is 4.5–15 km, the greatest depth is 18 m. The strait plays an important role in formation of the hydrological and



hydrochemical regime of the Azov-Black Sea basin. It is one of the main fishing areas and an important shipping route [1]. The main factors influencing salt composition of the Kerch Strait waters are seasonality of the continental runoff and precipitation inflow, water inflow from the estuaries and lagoons surrounding the sea bays, as well as water exchange with the Black Sea and the Sea of Azov. Complex water formation processes in the Kerch Strait result in the salinity values that vary within a fairly wide range of 9.5–19 and ionic variations lead to errors (up to 3%) in its determination [2, 3].

The scientific stage of studying the hydrochemical characteristics of the Black Sea waters started in 1890, of the Sea of Azov – in 1873 [1, 4], and their comprehensive study in our country began in the 1920s. Basic knowledge of hydrochemistry of the Black Sea and the Sea of Azov is presented in the works^{1, 2, 3}. In the 1970s and 1980s, the processes of hydrogen sulfide production and oxidation, organic carbon production and consumption, etc., were intensively studied. In the literature, as a rule, one can find the results of studies of individual elements of the major ion composition (MIC) of the Black Sea waters¹ [1, 5, 6] and the Sea of Azov waters [4]. To date, the carbonate system of the Black Sea has been well studied; a number of works [1, 7–11] are devoted to describing the research results. Some hydrochemical characteristics of the Sea of Azov waters are given in the works^{4, 5} [12–15]. Unfortunately, the authors were unable to find any published data on the main ion concentrations in the chemical composition of the Sea of Azov, Kerch Strait and Taman Bay waters.

The changes in hydrochemical properties of the Sea of Azov and the Black Sea are inevitable in the era of global climate change expressed in an increase in the maximum monthly average summer temperatures and minimum winter temperatures, a decrease in ice concentration in the Sea of Azov, as well as an anthropogenic load increase on its basin water resources. These changes lead to a decrease in the incoming part of the freshwater balance and an increase in salinity, water pollution, changes in their biocenoses – the species composition of hydrobionts and productivity of individual components of hydroecosystems [16–20].

The Sea of Azov water balance is regulated by the river flow (~ 50% of the balance), the inflow of the Black Sea waters through the Kerch Strait, water exchange with Lake Sivash, precipitation and evaporation⁴. Due to a large supply of fresh water mainly from the Don and Kuban rivers and a limited water exchange

¹ Skopintsev, B.A., 1975. [*Formation of the Modern Chemical Composition of the Black Sea Waters*]. Leningrad: Gidrometeoizdat, 336 p. (in Russian).

² Knipovich, N.M., 1932. [Hydrological Research in the Sea of Azov]. In: *Proceedings of the Azov and Black Sea Scientific and Fishery Expedition*. Zagorsk, iss. 5, pp. 3-97 (in Russian).

³ Knipovich, N.M. and Bregman, G.R., eds., 1936. [*Hydrological Directory of the Seas of the USSR*]. Vol. 3: *The Sea of Azov*. Leningrad; Moscow. Iss. 1, 222 p. (in Russian).

⁴ Bronfman, A.M., Dubinina, V.G. and Makarova, G.D., 1979. [*Hydrological and Hydrochemical Foundations of the Productivity of the Sea of Azov*]. Moscow: Pischevaya Promyshlennost, 288 p. (in Russian).

⁵ Matishov, G., Matishov, D., Gargopa, G., Dashkevich, L., Berdnikov, S., Kulygin, V., Arkhipova, O., Chikin, A., Shabas, I. [et al.], 2008. *Climatic Atlas of the Sea of Azov 2008*. Washington: United States Government Publishing Office, 148 p. Available at: <https://repository.library.noaa.gov/view/noaa/1135> [Accessed: 17 January 2024].

with the Black Sea, the hydrochemical properties of individual parts of the Sea of Azov vary significantly. Early studies showed that salinity in the main part of the sea during 1952–2007 varied in the range of 10–12, in the central part– in the range of 11–12.5, in the Taganrog Bay – in the range of 1–9 [21, 22]. Historically, the Kerch Strait waters have a large variability in salinity – from 9.5 to 19⁴ [2, 4, 23].

The development of agriculture, especially irrigation farming, causes the flow of large amounts of chlorine salts, sulfates, metals, biogenic and organic substances into the rivers and, consequently, into the Sea of Azov with return waters. This, along with a river flow reduction, affects the increase in the overall mineralization of river and sea waters, which determines the sea ecosystem and human economic activity in the water area. The increase in salinity leads to water stratification with oxygen deficiency, which increases the risk of death of aquatic organisms, reduces the level of primary production of organic matter and also decreases the sea water self-purification rate^{4, 6} [12, 14, 18, 21, 24, 25]. The increasing runoff of sulfates from year to year creates preconditions for hydrogen sulfide pollution of sea waters⁴ [4, 15, 16]. For the recent years of the Don low-water period, the Sea of Azov salinity reached the values of > 14 [25]. Although its salinity has been studied since the end of the 19th century, the study of the dynamics and the forecast of changes in its regime are still relevant.

The Kerch Strait waters are transformed Azov-Black Sea water masses; some historical hydrochemical characteristics of them (before 1981) are given in [4]. The principal factors influencing MIC formation of the Kerch Strait waters are seasonality of continental runoff and precipitation inflow, water inflow from the bays, as well as water exchange with the Black and Azov seas. Complex processes of MIC formation of Kerch waters lead to the hydrochemical compositional anomalies causing errors (up to 3%) when determining salinity with standard methods (calculations based on electrical conductivity and chlorinity). Kerch waters differ from ocean waters in a lower content of chlorides and a higher content of sulfates and hydrocarbonates [3].

The Taman Bay is a separate part of the Kerch Strait. It is located on its eastern shore between the Chushka and Tuzla spits and protrudes into the mainland for 16 km. It has an average depth of 5 m and a width at the entrance to the sea of 8 km⁷. Some hydrochemical characteristics of the Taman Bay waters are given in [16]. The bay is adjacent directly to the Kerch Strait and its influence on the Kerch water properties can be significant.

The Black Sea is a meromictic water body with a clearly defined two-layer water column structure with oxygen and anaerobic layers [26]. The hydrochemical and thermohaline properties of the upper layer depend on river runoff (~ 1000 rivers) and interaction with the atmosphere on various time scales. The properties of the lower layer depend on the influence of the Marmara (Mediterranean) waters coming with the Lower Bosphorus current, as well as on vertical exchange processes.

⁶ Dobrovolsky, A.D. and Zalogin, B.S., 1982. *Seas of the USSR*. Moscow: Moscow State University, 192 p. (in Russian).

⁷ Lotyshev, I.P., 2006. [*Geography of Kuban: Encyclopedic Dictionary*]. Maykop: Afisha, 527 p. (in Russian).

In the coastal zone and in the Kerch Strait, the surface water layer is characterized by lower salinity compared to deeper layers with increased horizontal salinity gradients. The salinity of surface waters in the central Black Sea is assumed to be 17.85–18.40 and on the northwestern shelf 14–16 (up to 17.90) (based on calculations using electrical conductivity [22]) [27].

Numerous studies of the complex hydrochemical structures of the Black Sea and the Sea of Azov attest to their significant differences from similar World Ocean structures. The most important physical characteristics, such as salinity and density, as well as their determination accuracy by indirect methods, depend on ionic variations. A possibility of accurate salinity calculation from electrical conductivity is determined by the constancy of the relative ion-salt composition of sea water and its violation leads to errors [27–29]. It was previously noted that ionic composition variations, even at the same chlorinity values, can cause differences in electrical conductivity values [4]. In 1970s, these differences in the Black and Azov waters served as the basis for the development of relationships for a more accurate calculation of salinity using the chlorine coefficient [4, 6].

Knowledge of the content and distribution of MIC components in the water mixing area will expand understanding of the processes of their formation and transport in the Kerch Strait. The need for comprehensive analysis of the characteristics of sea waters and the monitoring system development is especially relevant today in the context of climate change and increasing anthropogenic load on water resources. The knowledge gained can help in finding optimal solutions for their operation, developing technologies for hydrochemical process and water dynamics simulation in the strait. The present paper is aimed at studying MIC of the Kerch Strait waters and adjacent waters of the Black Sea and the Sea of Azov and the Taman Bay and their water exchange, as well as at estimating the influence of ionic variations in salt composition on the accuracy of determining water salinity in the areas under consideration.

Materials and methods

Location of stations. The sampling from the surface water layer was carried out on board R/V *Ashamba* and during coastal expeditions to the Kerch Strait, the Taman Bay, the northeastern part of the Black Sea and the southern part of the Azov Sea.

The water samples from the Kerch Strait were obtained on board R/V *Ashamba* in 2019–2023, from the Black Sea – along the route from the Blue Bay (Gelendzhik) to the Kerch Strait at a distance of up to 10 km from the coast on 21 September 2022 (2022 BSA stage).

During coastal expeditions, water samples were obtained in the following areas: in the Kerch Strait on 15–16 December 2021 (from Kerch to Yakovenkovo village) (published in [3]); in April, July and November 2021 – in the coastal area near the Chushka Spit (Port Kavkaz area) and in different areas of the Taman Bay, including the lagoon adjacent to the bay; in the Black Sea on 29 September 2022 (from Anapa to Sochi, Lazarevskoe microdistrict and near Sevastopol (2022 BSC stage)); in the Temryuk Gulf of the Sea of Azov on 10 October 2020 (in the area of Golubitskaya village).

Table 1

Characteristics of stations and dates of water sampling

Date of sampling	Water area	Station (location of sampling)	Station coordinates	
			°N	°E
01 May 2019	Kerch Strait – Feodosia Bay	0	45.089490	35.520194
		1a	44.987528	35.835800
		6	45.012694	36.209528
		24	45.291056	36.461444
		31	45.183333	36.592972
03–04 September 2019		12	45.071708	36.461732
		17	45.103928	36.482090
		20	45.119100	36.555908
		23	45.135783	36.623403
		24	45.288658	36.457697
		28	45.223365	36.535535
		31	45.182142	36.589330
01 July 2020		6	45.016460	36.215190
		1b	45.100560	36.468800
		23	45.132810	36.623840
		24	45.291690	36.460600
		30	45.193770	36.567890
		31	45.178270	36.583490
		32	45.034790	36.740890
		36	45.099130	36.741730
		41	45.066560	36.998340
15–16 December 2021	Kerch Strait	1	45.349800	36.476900
		2	45.301800	36.460700
		3	45.271700	36.437500
		4	45.244200	36.421200
		5	45.219800	36.405700
		6	45.229700	36.413600
		7	45.178100	36.405900
		8	45.166400	36.410700
		9	45.059200	36.327143
29 September 2022		1N	45.349607	36.47619
		4N	45.1572039	36.554363
		9N	45.128749	36.546070
		10N	45.1240664	36.638590
21 March 2023		10	45.1240664	36.638590
		10N	45.07516	36.625380
10 October 2020		PK	45.34686	36.683314
06 April 2021		(Chushka Spit, near	45.352445	36.696216
21 November 2021		Port Kavkaz)	45.347494	36.682850
10 October 2020		GV (Golubitskaya village)	45.323314	37.27490
06 April 2021		(Chushka Spit, near	45.351600	36.699305
21 November 2021		Dinskoy Bay)	45.353811	36.702750
06 April 2021		P (Primorskiy)	45.270794	36.912798
06 July 2021	Taman Bay of the Kerch Strait		45.270998	36.916198
21 November 2021			45.269542	36.909351
06 July 2021		S (Sennyoy)	45.279813	36.976939
21 November 2021		T (Taman)	45.221259	36.700954
06 July 2021		LP (Lagoon in the Primorskiy)	45.25393	36.898338
21 November 2021			45.253797	36.896663

Continuation of the Table 1				
Date of sampling	Water area	Station (location of sampling)	Station coordinates	
			°N	°E
21 September 2022	Black Sea, the BSA stage (Blue Bay – Kerch Strait)	1	44.57105	37.966255
		2	44.622805	37.773119
		3	44.660862	37.578031
		4	44.739155	37.393548
		5	44.854028	37.309866
		6	44.908118	37.309154
		7	44.940812	37.13572
		8	44.964315	36.950363
		9	44.997965	36.750853
		10	45.06947	36.563719
		11	45.206595	36.463493
29 September 2022	Black Sea, the BSC stage (Anapa – Lazarevskoe)	A (Anapa)	44.89789	37.306041
		N (Novorossiysk)	44.73275	37.783855
		S (Sevastopol)	44.615857	33.521145
		BB (Gelendzhik, Blue Bay)	44.576505	37.977587
		G (Gelendzhik Bay)	44.576335	38.024019
		AO (Arkhipo-Osipovka)	44.357138	38.526734
		T (Tuapse)	44.0942	39.072294
L (Sochi, Lazarevskoe)	43.909438	39.322485		

In total, 36 samples from the Kerch Strait were analyzed within the period of 2019–2023, 10 – from the Taman Bay, 21 – from the Black Sea and 1 – from the Sea of Azov. The location, station numbers, their coordinates and sampling dates are given in Table. 1, the location of stations on the map is shown in Fig. 1.

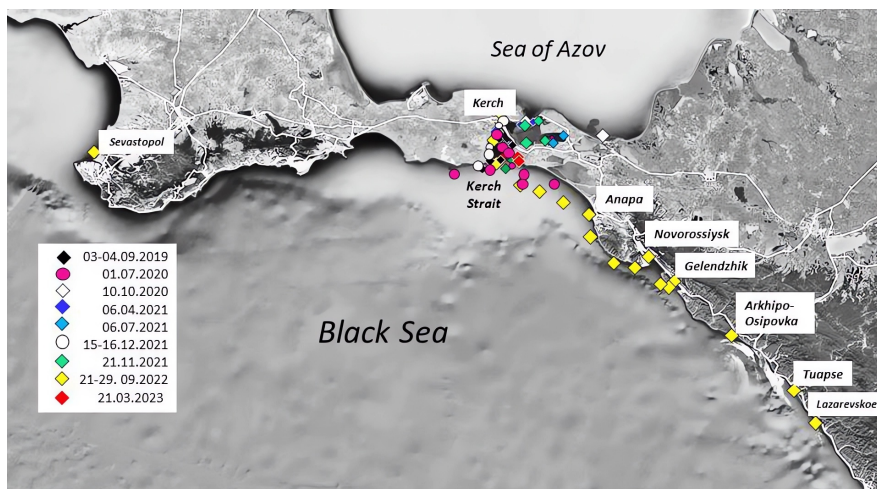


Fig. 1. Location of the sampling stations in 2019–2023 on the map (taken from *Google Earth Pro*)

During collection, water samples were placed in sealed containers volumed 0.5 and 1 l and delivered to the laboratory within several days for subsequent analysis. After determination of total alkalinity (AT), total dissolved inorganic carbon (T_{CO_2})

and pH, samples were filtered through a GF/F Whatman 0.7 μm membrane filter to remove mineral and organic suspended matter, placed in 250–300 ml glass containers, stored in a refrigerator at 4 $^{\circ}\text{C}$ and removed as needed during the analytical period.

Ion-salt composition study. Concentrations of the major ions of the salt composition (Cl^- , SO_4^{2-} , HCO_3^- , Na^+ , K^+ , Ca^{2+} , Mg^{2+}), expressed in g/kg, total alkalinity (*AT*) (in mmol/kg) and pH of waters of the studied samples were determined in the laboratory of the Institute of Oceanology of RAS in accordance with the methods originally selected for the analysis of hypersaline waters and described in [30], but taking into account the Black Sea water salinity. Similar determinations of major ion concentrations and densities were also carried out on *IAPSO* standard seawater (SSW) samples, specially intended for instrument calibration and verification of salinity measurements [31]. Comparison of the obtained results with literature data showed good convergence. Determination of concentrations of the main ions in the composition of the studied samples made it possible to obtain the most accurate values of the surface water salinity of the Kerch Strait and its water areas, to calculate the relative content of ions in the water compositions and the sulfate-chlorine ratio ($\text{SO}_4^{2-}/\text{Cl}^-$) and to determine salinity using the chlorine coefficient. Salinity was calculated by the sum of the major ions. Relative contribution of ions to the total mineralization of the studied water samples is given and analyzed in the present paper.

Deionized water (electrical conductivity $< 0.2 \mu\text{S}/\text{cm}$) was used to prepare reagent solutions and dilute samples. The analyzed sample mass was measured by weighing on Ohaus AX 423 laboratory analytical balance (USA) of the first accuracy class with an error of $\pm 0.005 \text{ g}$.

Density (σ_t) determination. Water density of the studied samples was measured in the laboratory of the Institute of Oceanology of RAS, using Anton Paar DMA 5000M precision density meter (Austria) at *in situ* temperature and atmospheric pressure. The instrument was calibrated according to the instructions. The error in measuring water density was $\pm 10^{-5} \text{ g}/\text{cm}^3$. The standard deviation when measuring the density of the studied samples with a density meter did not exceed $0.02 \text{ kg}/\text{m}^3$. The density data are presented in conventional density units (kg/m^3).

Salinity determination. Salinity was calculated in several ways: according to the CTD probe data (SeaBird 19plus until 2021 and CastAway since 2021), practical salinity (*SP*) was obtained based on electrical conductivity (only for the Kerch Strait waters); using the chlorine coefficient (S_{Cl}) from the ratio given in [6]; using the sum of major ions (*SS*) and density values (SA_{ρ}) from the TEOS-10 equation (<http://www.TEOS-10.org>, <https://www.teos-10.org/software.htm>). The results of similar studies for the Kerch Strait waters are given in [3]. The accuracy of the aforementioned methods for salinity calculation is given in the work ⁸. Salinity determination depends on the equipment error degree and the following methods:

⁸ Millero, F.J., 2013. *Chemical Oceanography*. Boca Raton: CRC Press, 591 p. <https://doi.org/10.1201/b14753>

- using density values up to $\pm 3 \cdot 10^{-5}$ g/cm³, which is equivalent to a salinity error of $\pm 0.4 \cdot 10^{-2}$;
- using chlorinity $0.2 \cdot 10^{-2}$ g/kg;
- using electrical conductivity $\pm 0.1 \cdot 10^{-2}$ μ S/cm;
- using a sum of major ions of $0.1 \cdot 10^{-1}$ g/kg.

Studying the SSW ion composition in the laboratory of the Institute of Oceanology of RAS and comparing the salinity obtained by the sum of ions with the reference salinity from [31], we found that the salinity exceeded our calculated one by 0.3%. For surface water samples of the Black Sea with a salinity of 18, this is equivalent to 0.05.

Practical salinity was calculated only for the Kerch Strait waters, since CTD probing was carried out only in this area.

Results

The results of hydrochemical studies of water samples from the Kerch Strait, the Taman Bay, as well as from the northeastern part of the Black Sea in 2019–2023 are given in Table 2.

Table 2

Hydrochemical characteristics of water samples from the Kerch Strait and adjacent waters of the Black Sea and the Taman Bay obtained in 2019–2023

Station	Date	pH	AT, mmol/kg	Salinity				Anions, %			Cations, %			
				SP	SS	S _{Cl}	S _{A_p}	Cl ⁻	SO ₄ ²⁻	HCO ₃	Na ⁺	K ⁺	Ca ²⁺	Mg ²⁺
<i>Kerch Strait – Feodosia Bay</i>														
0	01.05.20 19	8.13	3.21	–	18.24	17.69	17.92	53.49	7.56	0.98	31.99	1.08	1.26	3.64
1a		8.17	2.94	17.09	17.69	17.06	17.23	53.21	7.97	0.92	31.75	1.24	1.23	3.69
6		8.08	2.99	17.43	18.01	17.44	17.43	53.41	7.67	0.93	31.84	1.22	1.26	3.67
24		8.05	2.64	14.71	15.25	14.63	15.00	52.91	8.33	0.97	31.74	1.11	1.30	3.65
31		8.11	2.91	18.05	18.62	18.01	18.16	53.37	7.84	0.87	31.93	1.10	1.30	3.59
-		8.11	2.94	16.82	17.56	16.97	17.15	53.28	7.87	0.93	31.85	1.15	1.27	3.65
-		0.04	0.19	1.27	1.19	1.21	1.12	0.11	0.16	0.04	0.09	0.07	0.02	0.04
<i>Kerch Strait</i>														
12	01– 08.09. 2019	8.25	2.69	18.30	19.04	18.46	18.50	53.47	8.51	0.93	31.10	1.27	1.24	3.49
17		8.34	2.95	18.30	19.01	18.43	18.43	53.56	8.39	0.96	31.13	1.29	1.27	3.40
20		8.42	3.07	18.25	18.84	18.46	18.32	53.88	7.98	0.97	31.05	1.26	1.27	3.58
23		8.26	3.00	18.15	18.94	18.40	18.34	53.54	8.32	0.95	31.03	1.30	1.33	3.53
24		8.17	2.86	18.15	18.76	18.39	18.27	53.62	8.26	0.96	31.05	1.26	1.29	3.56
28		8.21	2.89	18.20	18.85	18.24	17.68	53.80	8.09	0.96	31.04	1.27	1.20	3.64
31		8.21	2.3	18.15	18.90	18.39	18.23	53.40	8.55	0.94	31.07	1.27	1.24	3.54
-		8.26	2.90	18.21	18.91	18.39	18.25	53.61	8.30	0.95	31.07	1.27	1.26	3.53
-		0.08	0.11	0.06	0.09	0.07	0.25	0.16	0.19	0.01	0.03	0.01	0.04	0.07
6	20.07. 2020	8.29	2.89	17.90	18.42	17.98	18.04	53.95	8.40	0.98	30.74	1.29	1.24	3.41
16		8.29	2.90	17.81	18.34	17.89	17.88	53.79	8.48	0.98	30.93	1.20	1.42	3.20
23		8.19	3.06	17.92	18.36	18.00	17.94	54.09	8.25	0.98	30.80	1.19	1.29	3.39
24		8.22	2.99	18.05	18.40	18.14	17.99	54.30	8.00	0.99	30.84	1.20	1.30	3.37
30		8.13	2.92	17.86	18.35	17.94	17.98	53.89	8.42	0.99	30.67	1.37	1.29	3.38
31		8.14	2.89	17.84	18.20	17.92	17.91	53.70	8.63	0.98	30.54	1.41	1.35	3.38
32		8.14	2.95	17.85	18.38	17.93	18.19	53.91	8.37	1.00	30.56	1.49	1.25	3.42
36		8.18	2.90	17.86	18.25	17.94	17.91	54.12	8.12	1.00	30.56	1.51	1.26	3.42
41		8.24	2.87	17.72	18.12	17.80	17.78	54.11	8.13	1.00	30.57	1.53	1.25	3.41
-		8.20	2.93	18.31	17.87	17.95	17.96	53.99	8.31	0.99	30.69	1.36	1.29	3.38
-	0.06	0.06	0.10	0.08	0.09	0.11	0.18	0.19	0.01	0.13	0.13	0.06	0.06	

Continuation of the Table 2

Station	Date	pH	AT, mmol/kg	Salinity				Anions, %			Cations, %				
				SP	SS	S _{Cl}	S _{A_p}	Cl ⁻	SO ₄ ²⁻	HCO ₃ ⁻	Na ⁺	K ⁺	Ca ²⁺	Mg ²⁺	
9	15- 16.12. 2021	8.27	2.89	16.8	17.19	16.8	17.1	53.88	8.58	0.96	30.40	1.28	1.38	3.61	
8		8.26	2.36	15.89	16.3	15.82	16.11	53.54	9.10	0.86	30.43	1.22	1.25	3.70	
7		8.16	2.47	15.86	16.23	15.77	16.17	53.57	8.97	0.88	30.26	1.40	1.35	3.64	
6		8.22	2.52	15.94	16.34	15.85	16.2	53.62	8.97	0.86	30.32	1.32	1.34	3.66	
5		8.19	2.47	15.87	16.28	15.83	16.06	53.52	9.08	0.88	30.26	1.34	1.30	3.71	
4		8.25	2.50	16.00	16.37	15.9	16.29	53.59	9.00	0.86	30.41	1.27	1.30	3.64	
3		8.21	2.46	16.06	16.41	15.93	16.25	53.54	9.04	0.86	30.29	1.40	1.30	3.65	
2		8.38	2.37	15.8	16.22	15.66	16.16	53.24	9.41	0.83	30.32	1.34	1.28	3.67	
1		8.17	2.49	16.04	16.38	15.91	16.22	53.59	8.98	0.87	30.35	1.32	1.34	3.63	
-			8.23	2.5	16.03	16.41	15.94	16.28	53.57	9.01	0.87	30.34	1.32	1.32	3.66
-		0.06	0.14	0.28	0.28	0.31	0.3	0.15	0.20	0.03	0.06	0.06	0.04	0.03	
1N	29.09. 2022	8.00	2.65	-	18.01	17.68	17.98	54.16	8.03	0.92	31.31	1.25	1.21	3.10	
4N		8.03	3.01	18.58	18.86	18.66	18.71	54.57	7.77	0.91	30.70	1.31	1.36	3.44	
9N		8.13	3.13	18.57	18.81	18.61	18.77	54.57	7.55	0.97	31.23	1.32	1.21	3.19	
10N		8.06	3.21	18.53	18.98	18.7	18.88	54.34	7.77	0.98	31.36	1.26	1.20	3.16	
-			8.06	3	18.56	18.67	18.41	18.59	54.41	7.78	0.94	31.15	1.29	1.25	3.22
-			0.05	0.22	0.02	0.39	0.42	0.35	0.17	0.17	0.03	0.26	0.03	0.07	0.13
10	21.03. 2023	8.15	2.66	17.28	17.55	17.3	17.66	54.35	8.13	1.00	30.26	1.16	1.45	4.06	
10N		8.17	2.74	16.23	17.15	16.94	17.53	54.50	8.01	1.00	30.22	1.17	1.34	3.67	
-		8.16	2.7	16.75	17.35	17.12	17.59	9.44	1.40	0.17	5.25	0.20	0.24	0.64	
-		0.01	0.04	0.53	0.2	0.18	0.07	0.10	0.03	0.00	0.07	0.00	0.01	0.00	
PK	09.10. 2020	8.12	2.71	-	18.96	18.95	19.11	55.13	7.28	0.88	30.29	1.41	1.42	3.60	
	06.04. 2021	7.56	3.10	-	16.80	16.17	16.55	53.08	9.17	1.23	30.02	1.60	1.29	3.61	
	21.11. 2021	7.63	2.50	-	13.80	13.40	13.75	53.56	8.84	1.09	30.31	1.26	1.38	3.56	
<i>Black Sea, BSA stage</i>															
1	21.09. 2022	8.31	2.89	-	18.69	18.33	18.75	54.08	8.36	1.00	30.31	1.29	1.36	3.60	
2		8.30	2.98	-	18.82	18.43	18.94	54.04	8.37	0.99	30.44	1.24	1.41	3.51	
3		8.29	2.91	-	18.78	18.43	18.82	54.13	8.32	1.00	30.35	1.19	1.41	3.59	
4		8.32	2.95	-	18.76	18.44	18.89	54.21	8.23	0.96	30.25	1.33	1.46	3.56	
5		8.27	2.94	-	18.74	18.44	18.90	54.27	8.18	0.98	30.29	1.23	1.46	3.59	
6		8.28	2.87	-	18.72	18.43	18.84	54.30	8.16	1.00	30.26	1.28	1.36	3.66	
7		8.31	2.90	-	18.91	18.54	18.89	54.05	8.42	0.98	30.37	1.21	1.35	3.60	
8		8.31	2.93	-	18.78	18.46	18.80	54.23	8.20	0.99	30.40	1.20	1.42	3.56	
9		8.27	2.90	-	18.76	18.45	18.79	54.27	8.18	1.00	30.33	1.23	1.39	3.61	
10		8.28	2.85	-	18.57	18.32	18.71	54.39	8.04	0.99	30.22	1.30	1.42	3.64	
11		8.28	2.85	-	18.70	18.49	18.76	54.53	7.88	0.97	30.45	1.28	1.30	3.59	
-			8.29	2.91	-	18.75	18.43	18.83	54.23	8.21	0.99	30.33	1.25	1.39	3.59
-		0.02	0.04	-	0.08	0.06	0.07	0.14	0.15	0.01	0.07	0.04	0.05	0.04	
<i>Black Sea, BSC stage</i>															
A	29.09. 2022	8.11	3.05	-	19.00	18.67	18.87	54.21	7.95	0.93	31.40	1.26	1.20	3.06	
N		7.93	3.08	-	17.70	17.32	17.62	53.98	7.98	1.08	31.44	1.34	1.23	2.95	
BB		8.08	3.11	-	18.88	18.59	18.68	54.33	7.76	0.96	31.49	1.29	1.11	3.05	
G		8.15	3.05	-	18.59	18.20	18.46	54.01	8.02	1.01	31.45	1.36	1.18	2.98	
AO		8.01	3.07	-	18.90	18.55	18.77	54.14	7.93	0.98	31.51	1.25	1.19	2.99	
L		7.97	3.11	-	18.36	18.06	18.22	54.26	7.79	1.02	31.54	1.20	1.20	3.00	
T		8.03	3.07	-	18.67	18.34	18.70	54.20	7.86	0.99	31.49	1.26	1.23	2.98	
S		8.10	3.08	-	18.89	18.54	18.76	54.12	7.98	1.00	31.39	1.23	1.24	3.04	
-			8.04	3.08	-	18.59	18.25	18.47	54.16	7.90	0.99	31.47	1.28	1.19	3.00
-			0.07	0.02	-	0.41	0.43	0.40	0.12	0.09	0.04	0.04	0.05	0.04	0.04

Station	Date	pH	AT, mmol/kg	Salinity				Anions, %			Cations, %			
				<i>SP</i>	<i>SS</i>	<i>S_{Cl}</i>	<i>SA_p</i>	Cl ⁻	SO ₄ ²⁻	HCO ₃	Na ⁺	K ⁺	Ca ²⁺	Mg ²⁺
<i>Sea of Azov</i>														
<i>GV</i>	09.10. 2020	7.03	2,16	-	14.81	14.64	14.98	54.53	7.80	0.98	30.04	1.57	1.49	3.59
<i>Taman Bay</i>														
<i>D</i>	06.04. 2021	7.65	3.68	-	18.88	18.28	18.58	53.41	8.66	1.19	29.63	2.12	1.46	3.53
<i>P</i>	2021	7.44	6.97	-	22.12	21.48	22.00	53.56	7.71	2.15	30.17	1.67	1.22	3.53
<i>P</i>	06.07. 2021	8.31	2.87	-	18.64	18.17	18.18	53.77	8.72	0.88	30.47	1.34	1,37	3.46
<i>S</i>	2021	8.38	2.95	-	18.54	18.07	18.23	53.76	8.77	0.88	30.52	1.25	1,35	3.48
<i>D</i>	21.11. 2021	7.53	4.21	-	19.50	18.94	19.42	53.58	8.56	1.33	30.20	1.31	1.51	3.51
<i>T</i>	2021	7.1	2.49	-	16.07	15.58	15.88	53.46	9.05	0.96	30.37	1.30	1.31	3.55
<i>P</i>	2021	6.68	4.4	-	16.13	15.44	15.85	52.78	8.83	1.99	29.87	1.40	1.61	3.52
<i>LP</i>	06.07. 2021	7.66	3.18	-	39.61	38.66	39.82	53.84	9.30	0.47	29.75	1.23	1.57	3.84
	21.11. 2021	7.42	5.09	-	26.63	25.99	26.70	53.84	8.66	1.05	29.53	1.43	1.75	3.74

Note: Bold straight font shows the average values of hydrochemical characteristics, bold italic – *sd*.

In addition to the main results for each sample, the expedition average values of the obtained indicators and the standard deviation (*sd*) between them are listed here. Large differences in *sd* indicated heterogeneity and small differences indicated the homogeneity of waters in the study area. The mean values and *sd* were not calculated for the data from the Taman Bay, Port Kavkaz and the lagoon near Primorskiy village due to large time intervals between sampling, which would inevitably lead to large deviations in these indicators. Calculating the mean values at the BSC stage, characteristics from A and H stations were not taken into account due to their maximum and minimum salinity, respectively.

Major ion composition of the Black Sea waters. From Table 2 it can be seen that the salinity and relative content of the major ions in the samples have similar values, and the *sd* values are very small which indicates relative homogeneity of the alongshore Black Sea water mass in the direction from Sevastopol along the Kerch Strait to Lazarevskoe. The maximum (SS_{max}) and minimum (SS_{min}) salinity values of the Black Sea waters during the 2022 expedition were recorded at the BSC stage: $SS_{max} = 19.0$ near Anapa, $SS_{min} = 17.7$ near Novorossiysk. The reduced water salinity in the Novorossiysk Bay was probably due to the sea water desalination by the Tsemes River runoff entering the bay from the northwestern direction.

On average, AT was 2.90 mmol/kg ($AT_{max} = 3.08$ mmol/kg, $AT_{min} = 2.85$ mmol/kg). In the Black Sea, AT is represented mainly by carbonate alkalinity, while the proportion of borate, phosphate, silicon and other alkalinity ions is insignificant [1]. In the coastal zone of the Black Sea (BSC stage), AT was on average 9% higher than in the open sea (BSA stage).

The concentrations of major ions in the water samples collected from the vessel during the BSA stage and those obtained from the shore during the BSC stage were very similar (Table 2).

The study results of the ionic composition and salinity of surface waters in the northeastern Black Sea revealed that they had a very specific MIC, where

$SS = 18.66$ (which corresponded to $SP = 18.10$), $S_{Cl} = 18.29$ ($sd_{SS, SP, S_{Cl}} = 0.3$), $SA = 18.44$ ($sd_{SA} = 0.4$), and the relative content of the major ions (in %) was as follows:

$Cl^- = 54.05$ ($sd = 0.3$),

$SO_4^{2-} = 8.16$ ($sd = 0.3$),

$HCO_3^- = 1$ ($sd = 0.3$),

$Na^+ = 30.84$ ($sd = 0.4$),

$K^+ = 1.29$ ($sd = 0.1$),

$Ca^{2+} = 1.30$ ($sd = 0.1$),

$Mg^{2+} = 3.30$ ($sd = 0.2$).

Sulfate-chlorine ratio for the Black Sea surface waters (according to the BSA and BSC data) averaged 0.1492 ($sd = 0.004$).

Major ion composition of the Taman Bay waters. The data from Table 2 show significant seasonal fluctuations in the salinity of the Taman Bay waters and the lagoon adjacent to it. For example, samples obtained near Primorskiy village (station *P*) of the Taman Bay had a salinity of 22.12 in April, 18.64 in July and 16.13 in November. Less significant salinity fluctuations were observed on the opposite side of the Taman Bay, near the Dinskoy Bay (station *D*) (a small bay in the northwest of the Taman Peninsula, 8 km long, 2 km wide at the exit and no more than 4 m deep). This bay is a part of the Taman Bay and is separated from the Kerch Strait by the Chushka Spit ⁷. The salinity at station *D* was 18.88 in April and 19.50 in November.

AT values in the Primorskiy village area had large seasonal variations between an extremely high value of 6.97 mmol/kg in April (at pH = 7.44), a lower value of 2.87 mmol/kg in July (pH = 8.31) (corresponding to the Black Sea waters) and an intermediate value of 4.4 mmol/kg in November (pH = 6.68). Changes in the pH of surface waters of natural water bodies are significantly affected by phytoplankton activity accompanied by the processes of organic matter oxidation, photosynthesis and respiration, which leads to changes in the carbonic acid content. An increase in pH is usually influenced by river runoff enriched in bicarbonates and calcium [1]. With a decrease in the mean annual runoff of the Don and the salinity of the Sea of Azov waters, there has been a persistence of high intensity of biological productivity of phytoplankton and a change in its taxonomic groups [12]. The sulfate-chlorine ratio in the Taman Bay waters fluctuated in the range of 0.1320–0.1727 and in most cases decreased with increasing salinity.

The hydrochemical parameters of the Taman Bay waters are affected by water exchange with the lagoon waters (station *LP*) located near Primorskiy village and connected to the bay by a channel. Its characteristics are given in Table 2. It can be seen that the lagoon has high salinity (39.1 in July, 26.63 in November) and a composition different from other parts of the Taman Bay. There were more chlorides and magnesium ions in the lagoon and less bicarbonates and sodium ions than in other samples of the bay. In general, the waters of the lagoon represented the Taman Bay waters transformed, probably, due to evaporation and biological processes. The relative concentrations of chlorides were the lowest and sulfates –

the highest of any area in the bay. The sulfate-chlorine ratio was 0.1728 at $SS = 39.61$ in July and 0.1608 at $SS = 26.63$ in November.

Analyzing the results obtained, it can be assumed that the Kerch Strait waters entering the Taman Bay under certain conditions (for example, under the influence of the southwest wind) fill the bay and the adjacent lagoon. Due to insufficient horizontal circulation and the shallow waters of the Taman Bay, Kerch waters, entering the lagoon, stay here, partially evaporate and undergo biological processes changing their composition. Under the northeast wind (and/or other conditions) influence, these waters with increased salinity as a result of evaporation and a transformed composition flow back into the Kerch Strait along with less saline waters from the central part of the Sea of Azov. Thus, the Taman Bay plays an important role in the salt balance of the Kerch Strait waters.

The Kerch Strait. According to Table 2, the values of salinity and relative content of the major ions in the Kerch Strait water samples (excluding the Taman Bay waters) in September 2019 and 2022, July 2020 and December 2021 are very close, which demonstrates homogeneity of the waters, but at the same time these values have significant seasonal differences. The lowest salinity values were observed in May 2019, November (station *PK*) and December 2021 and were 15.25, 13.80 and 16.22, respectively. The lower salinity in these months compared to other seasons is associated with the inflow of both less saline (~ 14) waters of the Sea of Azov into the strait, which is facilitated by the northeast wind [22, 32] and salty waters of the Taman Bay. The major composition of the Kerch Strait waters at low salinity was different from the composition of the Black Sea waters (BSA and BSC stages) with a lower content of chlorides and a higher content of sulfates, characteristic of the central Sea of Azov waters. The highest salinity (18.01–19.04) and *AT* were observed in September 2019 and 2022. High salinity and the nature of MIC at this time of year indicate the distribution of Black Sea waters in the strait and the absence of inflow of Sea of Azov waters. The maximum thickness of the evaporation layer from the Sea of Azov surface in the Kerch Strait area is observed in late summer and autumn as a result of the entry of warmer Black Sea waters through the strait, increasing the temperature of the Sea of Azov waters [1]. The similar relative contents of the MIC components here and in the Black Sea waters (BSA stage) should be noted. In July 2020, the sum of ions in the strait waters had an intermediate value between the minimum and maximum and amounted to ~ 18.31 .

The pH values in the Kerch Strait for the entire observation period were 8–8.42, which indicates a slightly alkaline reaction of the aquatic environment. In the central Black Sea waters, the most common previously recorded pH values were 8.31–8.33 (maximum 8.45 in April–May, minimum 8.25 in late summer and winter) [1]. In the Kerch Strait in the summer of 2008, pH values reached 8.65 after the tanker disaster in 2007 [16].

Comparative analysis of MIC waters of the Kerch Strait and adjacent water areas. The data in Table 2 show significant differences in the relative content of major ions in the Kerch Strait and adjacent water areas. According to the data obtained and the materials from [31], the content of major ions in the Kerch Strait

and in SSW differs significantly. In all the studied samples, there was less chloride than in SSW (55.2%): in the Kerch Strait waters by 1–2%, in the Taman Bay – up to 2%, in the Black Sea waters – by ~ 1%. The similar differences in the Kerch Strait waters were observed earlier [3]. In most of the samples studied, the relative content of SO_4^{2-} was generally higher than in SSW, where it was 7.8% or lower. For all samples from the northeastern Black Sea (BSA and BSC stages), the SO_4^{2-} content was on the verge of determination error. For the Kerch Strait and the Taman Bay waters, these deviations were up to 1%. In all cases, there was significantly more HCO_3^- than in SSW (0.35%): in the waters of the Kerch Strait, the Black Sea (BSA and BSC stages) – 3 times, in the Taman Bay waters – up to 6 times. The relative Na^+ content in the Kerch Strait waters and in SSW (30.8%) was generally very similar and in some cases in the Kerch Strait and in all Black Sea samples of the BSA stage it was less by 0.5%. Only in May 2019, Na^+ was 3% higher in the Kerch Strait than in SSW. The Na^+ content in the Taman Bay waters was on average 1% less, in the waters at the BSC stage it was more by 1%. The relative K^+ content in the water samples from the BSA and BSC stages was ~ 1.3%, which is close to the content in SSW (1.2%). The K^+ concentration in the Kerch Strait was slightly different (less by ~ 0.2%) from the content in the SSW and in the Taman Bay it almost coincided with the SSW, but sometimes the excess was up to 1% (station *D*). The Ca^{2+} content in the studied samples was almost everywhere higher than in SSW: in the Kerch Strait and the Black Sea – by ~ 0.3%, in the Taman Bay waters – by ~ 0.6%. The Mg^{2+} content in the samples of the Taman Bay and the BSA stage was close to SSW (3.5%), in the Kerch Strait – 0.2% less, in the BSC stage waters – by 0.6%.

Fig. 2 shows the distribution of the relative content of MIC components of waters (at the corresponding salinity) in the studied samples. It can be seen that for the Black Sea waters, both coastal (blue diamonds) and outlying at a distance of ~ 10 km (red diamonds), the relative content of the major ions of MIC within *sd* had good convergence. This indicates that the surface water mass of the Black Sea is generally homogeneous over a distance of ~ 500 km.

The Kerch Strait waters differ from the Black Sea ones in greater heterogeneity and seasonal variability of MIC (Fig. 2). It is shown that when the sum of ions is greater or less than 18.66 (*sd* = 0.3), their relative content changes. A relationship between the content of Na^+ and Mg^{2+} is observed both in the Kerch Strait waters and at the BSA and BSC stages, which is associated with ion exchange processes at geochemical barriers when terrigenous suspended matter enters the sea with river runoff. Within each stage of the expedition, the Na^+ and Mg^{2+} contents were close. In the Kerch Strait waters, K^+ was sometimes slightly less than in the Black Sea waters; the deviation of its values was $\pm 0.5\%$. The Ca^{2+} content in the Kerch Strait and Black Sea waters was almost the same.

The studies showed that SS_{\max} in the Kerch Strait waters was 19.04 in September 2019. In the salinity range of 15–19, as shown by the trend line in Fig. 2, the content of chlorides and sodium ions in the composition of Kerch waters increases, and the content of sulfates, magnesium and calcium decreases. There are fluctuations in the relative content of potassium and bicarbonates, but no noticeable trend towards change is observed. The highest salinity and greatest variability in composition were observed in the Taman Bay, where metamorphism of the Kerch waters occurred

while they were in the adjacent lagoon. At the same time, the relative content of chlorides, bicarbonates and sodium ions in the lagoon water composition decreased, and the content of sulfates, magnesium and calcium increased. The potassium content did not change significantly. Under the influence of the northwestern wind, which facilitated the inflow of the Sea of Azov waters into the Kerch Strait [32, 33], the lagoon water masses were probably mixed successively with the Taman Bay and Kerch Strait waters. For this reason, the content of the major ions in the Kerch Strait waters has a wide variety – both seasonal and within the same expedition (Table 2, Fig. 2).

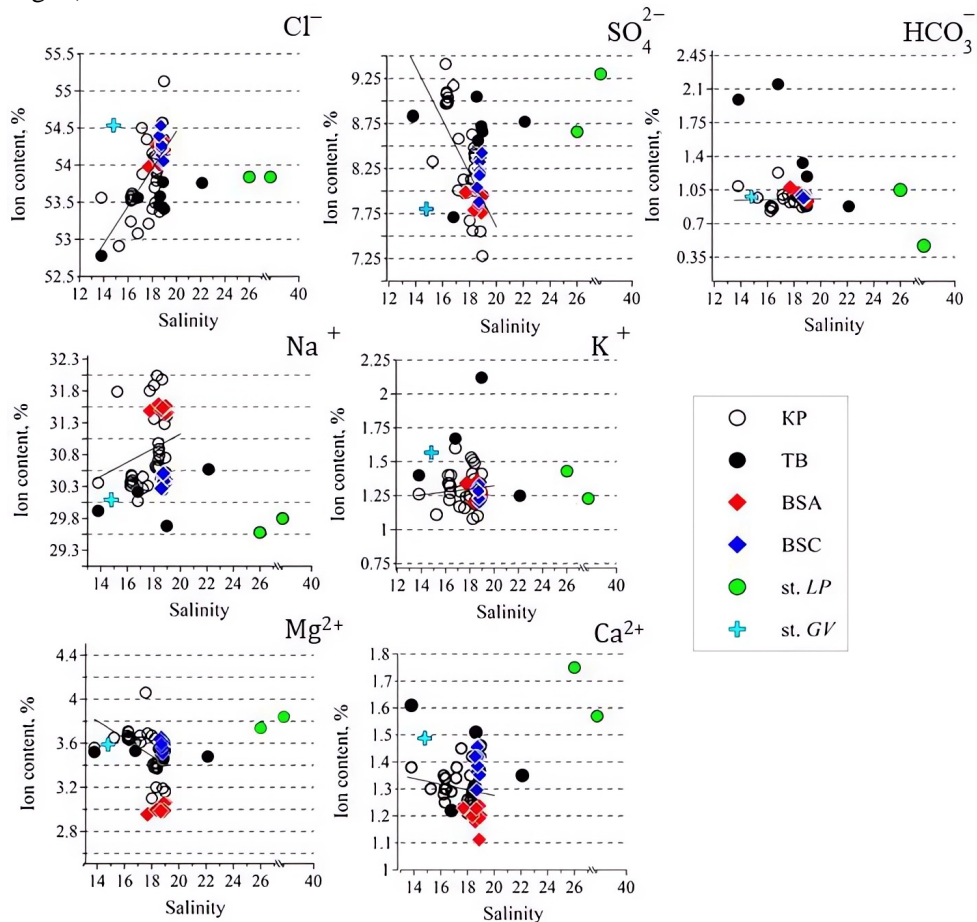


Fig. 2. Relative content of MIC components in the waters of the Kerch Strait (KS), the Taman Bay (TB), the northeastern Black Sea (stages BSA and BSC), lagoon in the Taman Bay (station LP) and in the Temryuk Gulf waters of the Sea of Azov (station GV). The trend line shows how the element content changes with increasing salinity in the Kerch Strait

Analysis of the relationship between MIC and salinity of all studied samples enables to distinguish the Black Sea waters in the Kerch Strait from the transformed the Sea of Azov waters and Taman Bay waters and to discover that the Kerch Strait waters can have different ratios of major ions with the same salinity.

The MIC influence on the salinity determination accuracy of the waters of the Kerch Strait and adjacent waters. The difference in the ionic composition of the waters of the Black Sea and the Sea of Azov and the Kerch Strait from the World Ocean waters leads to errors when measuring salinity and density using hydrophysical equipment and other methods [1, 3, 4 and 31]. The results of a study of the influence of variations in ionic composition on the accuracy of determining salinity in the surface waters of the Kerch Strait, the Black Sea and the Taman Bay are shown in Fig. 3.

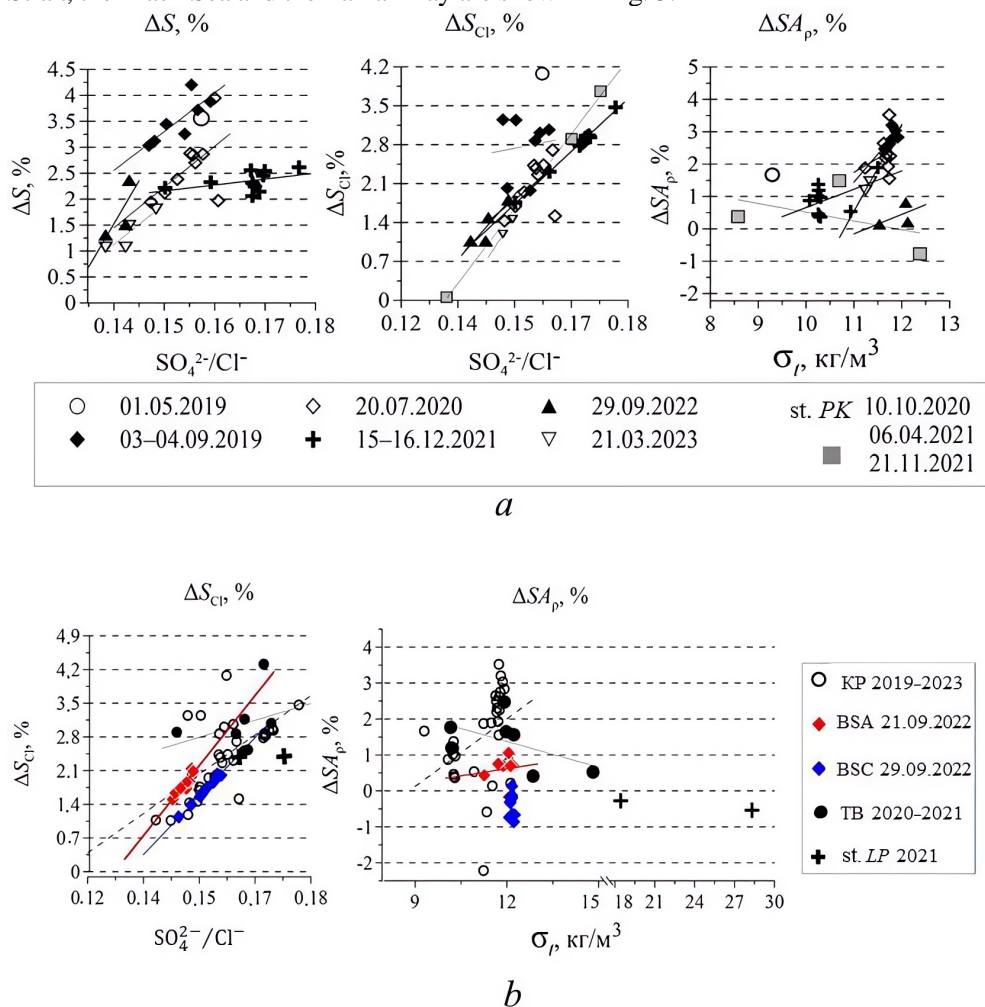


Fig. 3. ΔS , ΔS_{Cl} , ΔSA_p and their relationship with the ionic composition and density in the Kerch Strait (KS) waters (separately for 5 expeditions) (a); in the waters of the Kerch Strait (5 expeditions together), as well as the Black Sea (stages BSA and BSC), the Taman Bay (TB) and the lagoon (station LP) (b)

The largest deviations were observed between the SS and SP (ΔS) values, the smallest – between SS and SA_p (ΔSA_p). It can be noted that ΔS and ΔS_{Cl} depend on the ionic composition and grow with increasing SO_4^{2-}/Cl^- , and ΔSA_p depends on the water density and salinity and grows with their increase. These processes are observed both in the Kerch Strait and in the Taman Bay. It is noticeable that ΔSA_p in all samples generally increases to 12 kg/m^3 (at a temperature of $20\text{--}21 \text{ }^\circ\text{C}$ and salinity

~ 19), and then with increasing density, as can be seen in the example of water at station *LP*, ΔSA_p decreases under the influence of a significantly changed composition.

In the Kerch Strait, ΔS was 1–4%, on average 2.5% ($SS = 0.5$), i.e., the sum of ions was on average 2.5% greater than *SP*. CTD measurements in the Taman Bay and the Black Sea were not carried out, so ΔS was not calculated.

In the Kerch Strait, ΔS_{Cl} was 1–3%, on average 2.3% ($SS = 0.4$), i.e., the salinity calculated from chlorine was less than the sum of ions on average by 2.3%. In the Taman Bay, S_{Cl} was 0–3% less and in the Black Sea, it was on average 1.8% less ($SS = 0.3$) than *SS*.

The calculation of ΔSA_p showed that SA_p was generally less than the sum of ions, but in some samples with $SS > 18.66$ (i.e., greater than the average salinity of the Black Sea waters and therefore with a different ion composition) it was greater. Thus, in the Kerch Strait SA_p was generally less than *SS* by 2–3%, but at station *PK* in October 2020 (with a high *SS* value = 18.96) it was 0.8% higher. The SA_p value in the Taman Bay was lower than *SS* by 0.4–2.5%, but in the lagoon (with increased *SS*), on the contrary, the SA_p value was higher on average by 0.4%. In the Black Sea, in water samples of the BSA stage SA_p was 0.1–0.8% less than the sum of ions, and in water samples of the BSC stage it was ~ 1% higher, i.e., ΔSA_p for the Black Sea waters was on average ± 0.1 g/kg and thus the difference between ΔSA_p and *SS* was not significant. It follows from the foregoing that the calculation according to TEOS-10 for the Black Sea waters shows the closest (~ 1%) result to the sum of ions, if the salinity and ion ratio correspond to the composition of the Black Sea waters.

The hydrochemical MIC anomalies affect the accuracy of salinity calculations from electrical conductivity measured by a CTD probe, which leads to significant errors (up to 3%) [3]. Despite the fact that CTD probing was not carried out in the Black Sea waters of the BSA and BSC stages in 2022, some samples from the Kerch Strait with a sum of ions equal to ~ 18.8 have an ionic composition similar to the Black Sea waters and therefore ΔS component ~ 2.5% may also be typical for these waters. Due to the ΔS_{Cl} dependence on variations in salt composition, when determining salinity using the chlorine coefficient, it is necessary to take into account the ΔS_{Cl} correction equal to ~ 2% for the surface waters of the Black Sea and the Kerch Strait.

The SA_p value has the smallest deviation from the sum of ions in almost all the studied samples. Salinity calculations using the TEOS-10 equation are simpler than calculations using the sum of ions, but require laboratory conditions and special equipment (high-precision density meter), so this method cannot be called an alternative to CTD studies, but can be used to clarify the obtained *SP* data.

Conclusions

In the course of the research, new hydrochemical data were obtained on the waters of the Kerch Strait and the adjacent water areas of the northeastern Black Sea, the Taman Bay and the Sea of Azov, which significantly expands the understanding of water exchange through the Kerch Strait.

It was found that the studied Black Sea waters, including those moving through the strait, have a very definite content of major ions in MIC: $Cl^- = 54.2\%$, $SO_4^{2-} = 7.9\%$, $HCO_3^- = 1\%$, $Na^+ = 30.8\%$, $K^+ = 1.3\%$, $Ca^{2+} = 1.3\%$ and $Mg^{2+} = 3.3\text{--}3.6\%$. These waters

correspond to a sum of ions equal to 18.66 ($sd = 0.3$, which amounts to 1.5%). These Black Sea waters differ from the Taman Bay waters in a ratio of MIC ions, even with the same salinity.

The Taman Bay waters are characterized by higher salinity, and the ion-salt composition is formed by water exchange between the Black Sea, the central part of the Sea of Azov and the lagoon, where the water transformation occurs. It was revealed that the waters of the lagoon in the Taman Bay had a salinity of 39 in July and 26 in November and contained Cl^- and Na^+ on average 0.2 and 0.5% less than the Black Sea waters. In the waters of the lagoon, SO_4^{2-} was 1% more and Ca^{2+} and Mg^{2+} 0.4% more than in the Black Sea waters. The Taman Bay plays an important role in the salt balance of the Kerch Strait waters supplying transformed waters of the Sea of Azov and Black Sea with the increased salinity (up to 19) calculated by the sum of ions. The processes of water exchange with the salty lagoon partly explain great variability in the composition of the Taman Bay and the Kerch Strait waters.

Comparing the waters of the studied water areas and the SSW, it was found that the MIC of the Kerch Strait and the adjacent waters differed from the ocean one in the increased content of sulfates – on average up to 1%, the increased content of bicarbonates – 3–6 times, and the decreased content of chlorides – up to 2%. These differences were more pronounced when a larger proportion in the sample belonged to the freshwater continental runoff or the transformed waters of the Taman Bay, where, for example, the sulfate-chlorine ratio was higher than in the Black Sea and the Kerch Strait. The ionic variations contributed to underestimation of salinity values when calculated from the CTD probing data in all waters under study. For the samples from the Kerch Strait and, probably, the Black Sea, this underestimation averaged 2.5%, which corresponds to a sum of ions ~ 0.5 . When calculating salinity using the chlorine coefficient, deviations were found: in the Kerch Strait they were $\sim 2.3\%$, in the Taman Bay $\sim 2\%$ and in the Black Sea $\sim 2.5\%$.

The conducted studies showed that the Kerch Strait waters of various origins, even with the same salinity values, can differ in the content of the components of the major ion-salt composition.

In oceanological practice, it is necessary to take into account the errors in determining salinity associated with variations in the ion-salt composition in the waters of the Black Sea and the Sea of Azov and their water areas, especially pronounced in areas influenced by continental runoff and water exchange with other water bodies.

REFERENCES

1. Gershanovich, D.E., Ryabinin, A.I. and Simonov, A.I., eds., 1992. *Hydrometeorology and Hydrochemistry of Seas in the USSR. Vol. 4. The Black Sea. Issue 2. Hydrochemical Conditions and Oceanological Basis for the Formation of Biological Productivity*. Saint Petersburg: Gidrometeoizdat, 220 p. (in Russian).
2. Fedorov, Yu.A., Sapozhnikov, V.V., Agatova, A.I., Arzhanova, N.V., Belov, A.A., Kuznetsov, A.N., Lapina, N.M., Loginov, E.B., Predeina, L.M. [et al.], 2007. Multidisciplinary Ecosystem Studies in the Russian Part of the Sea of Azov (July 18–25, 2006). *Oceanology*, 47(2), pp. 294–297. doi:10.1134/S0001437007020166

3. Andrulionis, N.Yu., Zavalov, P.O. and Izhitskiy, A.S., 2022. Effect of Variations in the Ion-Salt Water Composition on the Accuracy of Salinity Measurements. *Physical Oceanography*, 29(5), pp. 463-479. doi:10.22449/1573-160X-2022-5-463-479
4. Goptareva, N.P., Simonova A.I., Zatuchnoy, B.M. and Gershanovich, D.E., 1991. *Hydrometeorology and Hydrochemistry of Seas in the USSR. Vol. 5: The Azov Sea*. Saint Petersburg: Gidrometeoizdat, 235 p. (in Russian).
5. Dubinin, A.V., Dubinina, E.O., Demidova, T.P. and Chasovnikov, V.K., 2017. Sulfur Isotopes in the Upper Part of the Black Sea Anoxic Zone. *Oceanology*, 57(6), pp. 797-805. doi:10.1134/S0001437017060030
6. Kremling, K., 1974. Relation between Chlorinity and Conductometric Salinity in Black Sea Water. In: E. T. Degens and D. A. Ross, 1974. *The Black Sea – Geology, Chemistry, and Biology*. Tulsa: American Association of Petroleum Geologists, pp. 151-154. doi:10.1306/M20377C44
7. Kononov, S.K. and Ryabinin, A.I., 1987. pH of the Black Sea Waters. *Meteorology and Hydrology*, (10), pp. 75-81 (in Russian).
8. Makkaveev, P.N. and Bubnov, P.V., 1993. Specific Features of the Vertical Distribution of Components of the Carbonate System in the Aerobic Zone of the Black Sea. *Okeanologiya*, 33(3), pp. 354-359 (in Russian).
9. Makkaveev, P.N., Nalbandov, Yu.R. and Vlasova, E.S., 2005. The Distribution of Dissolved Inorganic Carbon in the Zone of Contact of Aerobic and Anaerobic Waters of the Black Sea. *Oceanology*, 45(1), pp. S85-S92.
10. Hiscock, W.T. and Millero, F.J., 2006. Alkalinity of the Anoxic Waters in the Western Black Sea. *Deep Sea Research Part II: Topical Studies in Oceanography*, 53(17-19), pp. 1787-1801. doi:10.1016/j.dsr2.2006.05.020
11. Khoruzhii, D.S., Ovsyanyi, E.I. and Kononov, S.K., 2011. Comparison of the Results of Determination of the Carbonate System and the Total Alkalinity of Seawater According to the Data Obtained by Using Different Analytic Methods. *Physical Oceanography*, 21(3), pp. 182-194. doi:10.1007/s11110-011-9114-6
12. Kosenko, Yu.V., Barabashin, T.O. and Baskakova, T.E., 2017. Dynamics of Hydrochemical Characteristics of the Sea of Azov in Modern Period of Salinization. *Izvestiya Vuzov. Severo-Kavkazskii Region. Natural Science*, 3(1), pp. 76-82. doi:10.23683/0321-3005-2017-3-1-76-82 (in Russian).
13. Dashkevich, L.V., Berdnikov, S.V. and Kulygin, V.V., 2017. Many-Year Variations of the Average Salinity of the Sea of Azov. *Water Resources*, 44(5), pp. 749-757. doi:10.1134/S0097807817040042
14. Berdnikov, S.V., Kleshchenkov, A.V., Grigorenko, K.S., Oleinikov, E.P., Moskovets, A.Yu., Dashkevich, L.V., Kulygin, V.V., Sorokina, V.V. and Soier, V.G., 2019. Results of Marine Scientific Research of the Southern Scientific Centre of the Russian Academy of Sciences (SSC RAS) in the Sea of Azov in 2003–2018. Part 1: Hydrology and Hydrochemistry. *Aquatic Bioresources & Environment*, 2(3), pp. 7-19. doi:10.47921/2619-1024_2019_2_3_7 (in Russian).
15. Reshetnyak, O.S. and Komarov, R.S., 2023. Interannual and Seasonal Variability of Chemical Runoff along the Main Delta Branches of the Kuban River. *Lomonosov Geography Journal*, 78(1), pp. 95-105. doi:10.55959/MSU0579-9414.5.78.1.8 (in Russian).
16. Sapozhnikov, V.V., Arzhanova, N.V., Lapina, N.M., Agatova, A.I., Torgunova, N.I., Zozulya, N.M., Bondarenko, L.G., Vishnevsky, S.L., Radchenko, S.V. [et al.], 2013. Complex Ecological Studies in Kerch Strait and Taman' Bight after Oil Spill (2007-2010). *Trudy VNIRO*, 150, pp. 65-77 (in Russian).

17. Ginzburg, A.I., Kostyanoy, A.G., Serykh, I.V. and Lebedev, S.A., 2021. Climate Change in the Hydrometeorological Parameters of the Black and Azov Seas (1980–2020). *Oceanology*, 61(6), pp. 745-756. doi:10.1134/S0001437021060060
18. Demchenko, V.A., 2010. Features Impact Climate Change on Fish Community Basin of Azov Sea. *Bulletin of Zaporizhzhia National University. Biological Sciences*, 1, pp. 22-32 (in Russian).
19. Zavialov, P.O., Zavialov, I.B., Izhitskiy, A.S., Izhitskaya, E.S., Konovalov, B.V., Kremenskiy, V.V., Nemirovskaya, I.A. and Chasovnikov, V.K., 2022. Assessment of Pollution of the Kerch Strait and Adjacent Black Sea Area Based on Field Measurements of 2019-2020. *Oceanology*, 62(2), pp. 162-170. doi:10.1134/S0001437022020175
20. Radulescu, V., 2023. Environmental Conditions and the Fish Stocks Situation in the Black Sea, between Climate Change, War, and Pollution. *Water*, 15(6), 1012. doi:10.3390/w15061012
21. Ilyin, Yu.P., Fomin, V.V., Dyakov, N.N. and Gorbach, S.B., 2009. [*Hydrometeorological Conditions of the Ukrainian Seas. Vol. 1: The Sea of Azov*]. Sevastopol: ECOSI-Gidrofizika, 400 p. (in Russian).
22. Ivanov, V.A. and Belokopytov, V.N., 2013. *Oceanography of Black Sea*. Sevastopol: ECOSI-Gidrofizika, 210 p.
23. Zavialov, I.B., Osadchiev, A.A., Zavialov, P.O., Kremenskiy, V.V. and Goncharenko, I.V., 2021. Study of Water Exchange in the Kerch Strait Based on Historical Data and Contact Measurements in 2019. *Oceanology*, 61(3), pp. 329-337. doi:10.1134/S0001437021030176
24. Matishov, G.G., Dashkevich, L.V. and Kirillova, E.E., 2021. Cyclicity of Climate in the Sea of Azov Region: The Holocene and the Current Period (19th to 21st Centuries). *Doklady Earth Sciences*, 498(1), pp. 436-440. doi:10.1134/S1028334X21050093
25. Berdnikov, S.V., Dashkevich, L.V. and Kulygin, V.V., 2022. A New State in the Hydrological Regime of the Sea of Azov in the 21st Century. *Doklady Earth Sciences*, 503(1), pp. 123-128. doi:10.1134/S1028334X22030059
26. Konovalov, S.K., Vidnichuk, A.V. and Orekhova, N.A., 2018. Spatio-Temporal Characteristics of the Hydrochemical Structure of Water in the Deep-Sea Part of the Black Sea. In: A. P. Lisitzin, ed., 2018. *The Black Sea System*. Moscow: Scientific World, pp. 106-118. doi:10.29006/978-5-91522-473-4.2018 (in Russian).
27. Kondrat'ev, S.I., Romanov, A.S. and Vnukov, Yu.L., 2007. Peculiarities of Distribution of Hydrochemical Characteristics in the Region of the Continental Slope of the Northwestern Black Sea. *Morskoy Gidrofizicheskiy Zhurnal*, (5), pp. 69-79 (in Russian).
28. Millero, F.J., 2010. History of the Equation of State of Seawater. *Oceanography*, 23(3), pp. 18-33. doi:10.5670/oceanog.2010.21
29. Pawlowicz, R., 2013. Key Physical Variables in the Ocean: Temperature, Salinity, and Density. *Nature Education Knowledge*, 4(4), 13.
30. Andrulionis, N.Yu. and Zavialov, P.O., 2019. Laboratory Studies of the Main Component Composition of Hyperhaline Lakes. *Physical Oceanography*, 26(1), pp. 13-31. doi:10.22449/1573-160X-2019-1-13-31
31. Millero, F.J., Feistel, R., Wright, D.G. and McDougall, T.J., 2008. The Composition of Standard Seawater and the Definition of the Reference-Composition Salinity Scale. *Deep Sea Research Part I: Oceanographic Research Papers*, 55(1), pp. 50-72. doi:10.1016/j.dsr.2007.10.001
32. Zavialov, I., Osadchiev, A., Sedakov, R., Barnier, B., Molines, J.-M. and Belokopytov, V., 2020. Water Exchange between the Sea of Azov and the Black Sea through the Kerch Strait. *Ocean Science*, 16(1), pp. 15-30. doi:10.5194/os-16-15-2020

33. Zavialov, P., Izhitskiy, A.S. and Sedakov, R.O., 2018. Sea of Azov Waters in the Black Sea: Do They Enhance Wind-Driven Flows on the Shelf? In: M. G. Velarde, R. Yu. Tarakanov and A. V. Marchenko, eds., 2018. *The Ocean in Motion: Circulation, Waves, Polar Oceanography*. Cham: Springer, pp. 461-474. doi:10.1007/978-3-319-71934-4_28

About the authors:

Natalia Yu. Andrulionis, Researcher, Laboratory of Land-Ocean Interaction and Anthropogenic Processes, Shirshov Institute of Oceanology of RAS (30, 1st Line of Vasilievsky Island, St. Petersburg, 199004, Russian Federation); CSc (Geogr.), **ORCID ID: 0000-0001-9141-1945**, **Web of Science ResearcherID: AGP-4038-2022**, **Scopus Author ID: 57209575290**, natalya@ocean.ru

Ivan B. Zavialov, Junior Researcher, Laboratory of Land-Ocean Interaction and Anthropogenic Processes, Shirshov Institute of Oceanology of RAS (30, 1st Line of Vasilievsky Island, St. Petersburg, 199004, Russian Federation); **ORCID ID: 0009-0004-0083-4475**, **Web of Science ResearcherID: AGQ-4773-2022**, i.zav@ocean.ru

Sergey A. Rozhdestvenskiy, Leading Engineer, Laboratory of Land-Ocean Interaction and Anthropogenic Processes, Shirshov Institute of Oceanology of RAS (30, 1st Line of Vasilievsky Island, St. Petersburg, 199004, Russian Federation); **ORCID ID: 0000-0003-4654-9130**, sergeir92@list.ru

Submitted to 14.06.2023; approved after review 25.10.2023;
accepted for publication 15.11.2023.

Contribution of the co-authors:

Natalia Yu. Andrulionis - setting the goals and objectives of the research, selection of research methods ion-salt composition and salinity, field studies and sampling in the Black and Azov Seas and the Kerch Strait, carrying out laboratory analyzes, the obtained data analysis, graphic material and the paper text preparation

Ivan B. Zavialov - setting the goals and objectives of the research, graphic material preparation, field measurements and sampling in the Black Sea and the Kerch Strait

Sergey A. Rozhdestvenskiy - field measurements and sampling in the Black Sea and the Kerch Strait, discussion of the goals and objectives of the research, selection of literature on the research topic

The authors have read and approved the final manuscript.

The authors declare that they have no conflict of interest.

Original article

Energy Flows between the Mean Currents and the Mesoscale Eddies in the Eastern and Western Parts of the Black Sea

A. A. Pavlushin

Marine Hydrophysical Institute of RAS, Sevastopol, Russian Federation

✉ pavlushin@mhi-ras.ru

Abstract

Purpose. The study consists in analyzing the energy flows between the currents of different scales in the eastern and western parts of the Black Sea.

Methods and Results. The energy balance components were determined based on the results of numerical calculation of current fields in the Black Sea performed using a two-layer eddy-resolving model subjected to a forcing of a wind with cyclonic vorticity. A complete non-stationary large-scale sea circulation was represented conventionally as a sum of mean currents and mesoscale eddies. Conversions between the kinetic and available potential energy, as well as the energy flows between the mean currents and the mesoscale eddies were calculated separately for the eastern and western parts of the Black Sea. Besides, the advective energy flows across the meridional boundary between two parts of the sea were also calculated.

Conclusions. The main contribution to the potential energy advective transfer from the eastern part of the Black Sea to its western part is made by the mesoscale eddies. This advective energy transfer results in arising of differences in the energy flow directions in the currents of different scales in the eastern and western parts of the sea. In the Black Sea eastern part, energy is transferred from the mean currents to the mesoscale eddies, whereas in its western part, a reverse energy flow is observed. It is shown that the kinetic energy exchange between the movements of different scales is provided by the Coriolis force work, which for the initial currents is equal to zero, but turns out to be non-zero separately for the mean flows and the mesoscale eddies.

Keywords: Black Sea, large-scale circulation, mean currents, mesoscale eddies, energy balance, energy flow, β -effect, Rossby waves

Acknowledgements: The study was carried out within the framework of state assignment FNNN-2022-0003 “Development of operational oceanology methods based on interdisciplinary research of the processes of marine environment formation and evolution, and mathematical modelling using the data of remote and contact measurements”.

For citation: Pavlushin, A.A., 2024. Energy Flows between the Mean Currents and the Mesoscale Eddies in the Eastern and Western Parts of the Black Sea. *Physical Oceanography*, 31(1), pp. 99-119.

© 2024, A. A. Pavlushin

© 2024, Physical Oceanography

Introduction

Interaction among dynamic processes of various scales plays an important role in the formation and variability of horizontal water circulation in the oceans and seas. According to the classification by A.S. Monin¹, variability of interannual, seasonal and synoptic scales is relevant for the Black Sea circulation. Processes on

¹ Monin, A.S., Kamenkovich, V.M. and Kort, V.G., 1977. *Variability of the Oceans*. New York, London, Sydney, Toronto: John Wiley & Sons, 241 p.



an interannual and seasonal scale appear in the formation of currents limited by the basin size. In the Black Sea, there is the Rim Current which in some years spreads along the entire perimeter of the deep water and in other years breaks up into two or three sub-basin cyclonic gyres called “Knipovich glasses” [1]. Synoptic-scale processes include the Rim Current meanders, anticyclonic and cyclonic eddies formed in meander troughs, rings – detached meanders, quasi-stationary anticyclones (Sevastopol, Batumi) and Rossby waves with scales on the order of the baroclinic deformation radius [2, 3].

In [4–6], when describing the features of current fields, foreign authors use another classification more often. According to it, eddy formations, which, according to A. S. Monin’s definition, are synoptic [7], are classified as mesoscale objects. Such objects, from ten to several hundred kilometers in size, are called mesoscale eddies and their lifetime ranges from a week to several months [8]. Respectively, phenomena of a larger scale than mesoscale eddies are classified as large-scale, while phenomena of a smaller scale are classified as submesoscale. In the present paper, submesoscale dynamic objects are not considered, since the spatial resolution of the two-layer eddy-resolving model [9] used to calculate the fields of hydrophysical characteristics does not make it possible. In the future, some modernization of the model is planned in order to increase its spatial resolution so that to study the influence of submesoscale processes on larger scale ones, since this issue is of scientific interest [10–12].

For reasons of presentation, in this work we use the division of processes into large-scale and mesoscale ones, as it is customary in foreign literature. Mean currents (MCs) obtained by time averaging of instantaneous current fields are considered as large-scale ones, and deviations of instantaneous currents from this average state are eddy formations, more often called mesoscale eddies (MEs). In the Black Sea, mesoscale eddies are formed mainly due to the hydrodynamic instability of large-scale currents [13]. They participate in the energy transfer into the deep layers, influence the wind energy inflow and horizontal mixing of waters [14].

To study the Black Sea dynamics, the method of energy analysis is applied. It implies calculation and estimation of the energy parameters of currents: kinetic energy and potential energy, energy flows (transitions) among different types of energy and scales of movement, sources and sinks of energy. Knowledge of the energy of the considered processes is necessary for a better and correct understanding of their physics [15, 16].

Problem statement and description of the model

This paper aims to study the mutual transitions of kinetic and potential energy caused by large-scale and mesoscale dynamic processes in the Black Sea. At this stage of research, the aim was to calculate and analyze the average transitions of mechanical energy over a long time period among its various types and among movements of various scales separately for the eastern and western parts of the Black

Sea. Division of the sea into two halves was carried out along conventional boundary D , which coincides with the meridian passing through Cape Sarych (Fig. 1, a).

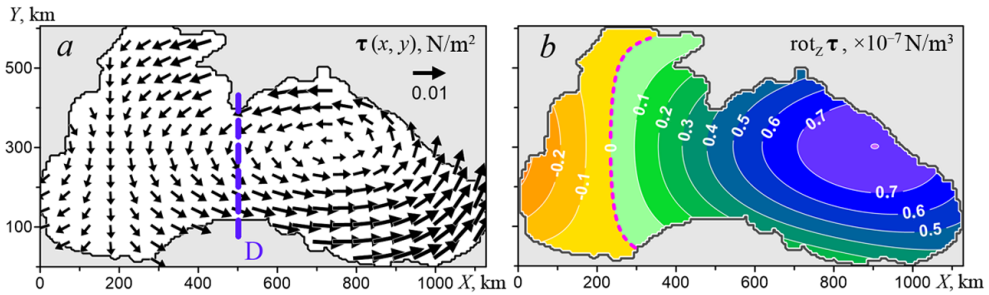


Fig. 1. Fields of tangential wind stress (a) and vorticity τ (b)

In previous work [17], also devoted to the analysis of the Black Sea energy, it was found that under the influence of the β -effect, an average advective transfer of potential energy was formed from the eastern half of the sea to the western one, resulting in spatial unevenness in the distribution of energy characteristics over the sea area. In the work, time-averaged integral flows and energy transitions in the western and eastern parts of the sea were analyzed, but they were not separated in accordance with the movement scale.

As initial data for calculating the energy characteristics, both in the previous work and in the present one, the results of numerical modelling of the Black Sea circulation using a two-layer eddy-resolving model [9] were used. This model takes into account the real bottom topography, friction at the interface between layers, bottom friction and horizontal turbulent viscosity.

Despite the apparent simplicity, the model used takes into account all the main factors that determine the formation and variability of the current field. With the correct choice of external and internal parameters, the model quite adequately simulates the known features of the large-scale Black Sea circulation – the Black Sea Rim Current with meanders and closely associated mesoscale eddy formations, Batumi and Sevastopol quasi-stationary anticyclones, “Knipovich glasses”, etc. Currents in the lower layer obtained using a two-layer model [18] correspond to observational data of deep currents in the Black Sea [19, 20].

If a stationary or periodically changing wind is used to excite motion in the model, then it is possible to obtain the model solution reaching a statistically equilibrium regime, in which the average values of all calculated characteristics and parameters of the model remain constant.

The model is based on a system of shallow water equations for a two-layer liquid and includes equations of motion and continuity for each layer:

$$(U_1)_t + (U_1 u_1)_x + (V_1 u_1)_y - fV_1 = gh_1 \zeta_x + \tau^x - R_{L1}^x + A_B h_1 (\Delta \Delta u_1),$$

$$(V_1)_t + (U_1 v_1)_x + (V_1 v_1)_y + fU_1 = gh_1 \zeta_y + \tau^y - R_{L1}^y + A_B h_1 (\Delta \Delta v_1),$$

$$(h_1)_t + (U_1)_x + (V_1)_y = 0,$$

$$(U_2)_t + (U_2 u_2)_x + (V_2 u_2)_y - fV_2 = gh_2 \zeta_x + g'h_2 (h_1)_x + R_{L2}^x - R_D^x + A_B h_2 (\Delta \Delta u_2),$$

$$(V_2)_t + (U_2 v_2)_x + (V_2 v_2)_y + fU_2 = gh_2 \zeta_y + g'h_2 (h_1)_y + R_{L2}^y - R_D^y + A_B h_2 (\Delta \Delta v_2),$$

$$(h_2)_t + (U_2)_x + (V_2)_y = 0,$$

where subscripts 1, 2 indicate the layer number; subscripts t , x , y mean differentiation with respect to the corresponding variable; (u_1, v_1) , (u_2, v_2) are horizontal components of current velocity in the upper and lower layers, directed along the X (east) and Y (north) axes; h_1, h_2 are layer thicknesses; ζ is sea level; τ^x, τ^y are components of the tangential wind stress acting on the sea surface; $(U_1 = u_1 h_1, V_1 = v_1 h_1)$, $(U_2 = u_2 h_2, V_2 = v_2 h_2)$ are components of flows in layers; (R_{L1}^x, R_{L1}^y) , (R_{L2}^x, R_{L2}^y) are friction force components at the lower boundary of the upper layer and the upper boundary of the lower layer, respectively (at the liquid boundary between the layers $R_{L1}^x = -R_{L2}^x, R_{L1}^y = -R_{L2}^y$); (R_D^x, R_D^y) are bottom friction components in the lower layer; $f = f_0 + \beta y$ is Coriolis parameter, $f_0 = 10^{-4}$ 1/s, $\beta = 2 \cdot 10^{-8}$ 1/(s·m); $g = 9.81 \text{ m/s}^2$ is free fall acceleration; $g' = g(\rho_2 - \rho_1)/\rho_2 = 0.032 \text{ m/s}^2$ is reduced gravitational acceleration, ρ_1, ρ_2 is water density in the upper and lower layers; A_B is coefficient of biharmonic horizontal turbulent viscosity; $\Delta = \frac{\partial^2}{\partial x^2} + \frac{\partial^2}{\partial y^2}$ is two-dimensional Laplace operator.

To close the system of equations, the model uses the continuity equation for total flows in the rigid-lid approximation $U_x + V_y = 0$, where $U = U_1 + U_2, V = V_1 + V_2$ is components of total flows. This makes it possible to introduce the integral stream function ψ , for which $U = -\psi_y, V = \psi_x$.

River runoff and water exchange through straits are not taken into account in the model; no-slip conditions are set at the lateral boundaries of the basin: $\mathbf{u}_1 = 0, \mathbf{u}_2 = 0$.

Since the biharmonic operator is used to parameterize horizontal turbulent viscosity in the model, it becomes necessary to determine the boundary conditions for the Laplacian of current velocity. By analogy with the $\mathbf{u}_1, \mathbf{u}_2$ conditions $\Delta \mathbf{u}_1 = 0, \Delta \mathbf{u}_2 = 0$ are set, yet with no physical sense.

Due to weak dissipativity, the model simulates well mesoscale eddies along with large-scale currents which, according to the results of the experiments, permits

to identify the shares of energy and work of forces associated with MCs and MEs. The analysis technique described in [21] makes it possible to calculate energy transitions during the interaction of mesoscale eddies and large-scale currents.

Initial data for calculating the energy characteristics are the fields of the thickness of the upper layer, sea level and current velocities in the upper and lower layers for 30 years with a discreteness of 1 day. The data were obtained in a numerical experiment with the following model parameters: horizontal cell size $\Delta x = \Delta y = 3000$ m, time integration step $\Delta t = 120$ s, upper layer thickness at rest $h_0 = 100$ m, horizontal turbulent viscosity coefficient $A_B = 2.0 \cdot 10^8$ m⁴/s, bottom friction coefficient $r_D = 0.002$, friction coefficient between layers $r_L = 2.0 \cdot 10^{-6}$ m/s.

The wind effect was set by stationary field of tangential wind stress $\tau(x, y)$ with an area-variable vorticity (Fig. 1, *a, b*), while the average vorticity over the sea area was cyclonic and amounted to $0.3 \cdot 10^{-7}$ N/m³. The choice of stationary field τ is explained by the fact that in this case the numerical model reaches a statistically equilibrium regime quickly.

Fig. 2 shows sea level fields $\zeta(x, y)$ obtained as a result of calculations characteristic of the statistically equilibrium regime, as well as Montgomery potential $M(x, y)$ – a function that characterizes the pressure at the interface of the layers². Due to the quasi-geostrophic nature of movements at the considered scale, the spatial distribution of ζ and M gives good indication of large-scale and mesoscale currents. In the upper layer, water moves along the ζ isolines, in the lower one – along the M isolines. The water moves in such a way that greater pressure is to the right of the current direction. The denser the isolines are, the greater the water flow velocity is.

The instantaneous field ζ (Fig. 2, *a*) shows the known features of the Black Sea circulation clearly. In the upper layer, the meandering Rim Current and mesoscale anticyclonic eddies to its right are observed. In the lower layer (Fig. 2, *b*), the movement of water has the cyclonic direction in the same way as in the upper layer, though at a lower speed (this can be seen from the span of the M scale). The circular current in the lower layer meanders strongly, and the meanders extend along the isobaths and move in a counterclockwise direction as the waves captured by the continental slope [9].

The next two fields (Fig. 2, *c, d*) were obtained by averaging the instantaneous fields ζ , M over a long period of time. They reflect large-scale circulation in the basin. According to the figure, in the upper layer the MC is a circular current located above the continental slope (middle Rim Current), and in the lower layer it is a current in which the current lines are close to the isobaths.

² Shakina, N.P., 2013. [*Lectures on Dynamic Meteorology*]. Moscow: Triada Ltd., 160 p. (in Russian).

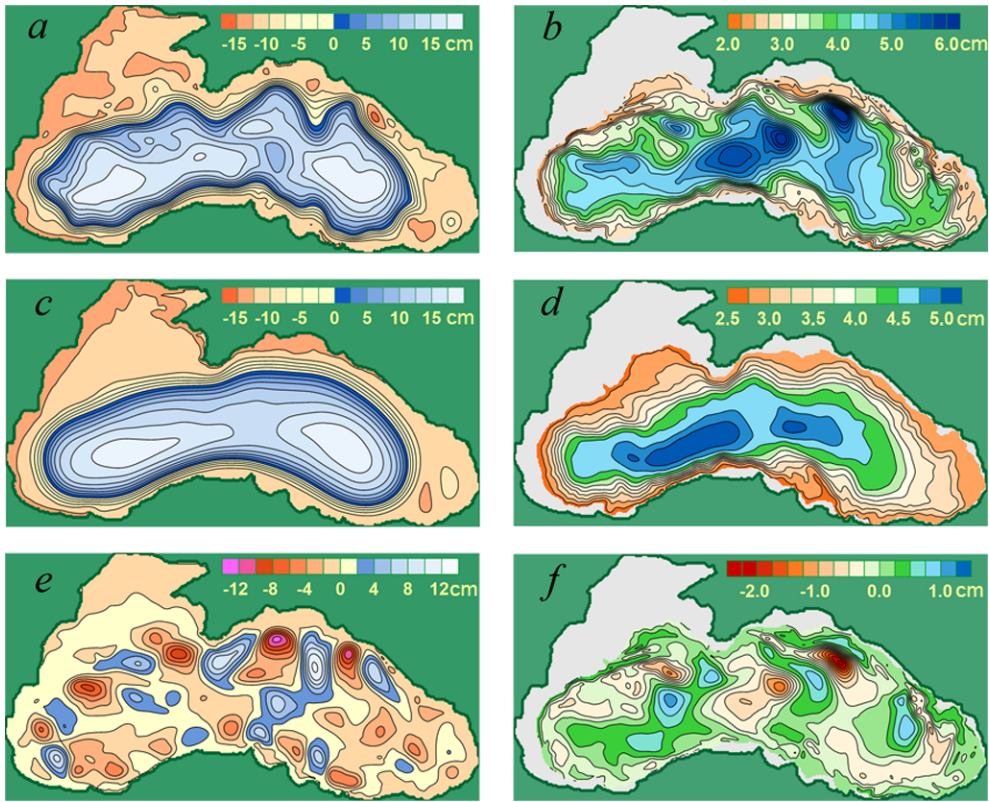


Fig. 2. Instantaneous fields ζ (a) and M (b), average fields $\bar{\zeta}$ (c) and \bar{M} (d), deviations of the instantaneous values from the average ones $\zeta - \bar{\zeta}$ (e) and $M - \bar{M}$ (f)

Fig. 2, *e, f* shows the deviations of instantaneous fields ζ , M from the average ones. Eddy structures in the lower and upper layers of the sea are clearly visible in it. These eddy formations are interconnected and move in the cyclonic direction with the same phase velocity [20].

Mechanical energy balance in a two-layer model

The two-layer eddy-resolving model used in the paper is energetically balanced and makes it possible to describe the processes of mechanical energy exchange between the upper and lower layers in a fairly simple form. Mechanical energy in the two-layer model consists of the kinetic energy of currents in individual layers and potential energy.

The kinetic energy of a water column of a unit cross section in upper and lower layers K_1 , K_2 is determined as follows:

$$K_1 = h_1 e_{K1}, \quad K_2 = h_2 e_{K2}, \quad e_{K1} = \rho_1 \frac{u_1^2 + v_1^2}{2}, \quad e_{K2} = \rho_2 \frac{u_2^2 + v_2^2}{2},$$

where e_{K1} , e_{K2} is kinetic energy per unit volume of water in the upper and lower layers; ρ_1 , ρ_2 is water density in the layers.

The potential energy of a water column position of a unit cross section from the sea surface to the bottom is equal to

$$PE = -\int_{\zeta}^H \rho(z)gzdz = -\int_{\zeta}^{h_1+\zeta} \rho_1gzdz - \int_{h_1+\zeta}^H \rho_2gzdz = \rho_2 \left(-g \frac{H^2}{2} + g \frac{\zeta^2}{2} + g' \frac{(h_1 + \zeta)^2}{2} - g' \frac{\zeta^2}{2} \right),$$

where $H(x, y)$ is sea depth.

Vertical coordinate axis Z is directed downward; the undisturbed sea surface is taken as the origin ($z = 0$). In this case, the potential energy is negative and equal to the work that should be carried out to raise all the water to zero level.

It is more convenient sometimes to use available potential energy (P), which is the difference between the current potential energy (PE) and the energy of the most stable state of the liquid (P_0), instead of potential energy. For a two-layer liquid, the most stable state is the state of rest, in which the sea surface and the interface between the layers are horizontal, therefore

$$P = PE - P_0 = \rho_2 \left(g \frac{\zeta^2}{2} + g' \frac{h_1^2}{2} + g'h_1\zeta - g' \frac{h_0^2}{2} \right),$$

where h_0 is upper layer thickness at rest.

$$\text{In the rigid-lid approximation } P = \rho_2 g' \frac{(h_1^2 - h_0^2)}{2}.$$

The two-layer model energy is described by a system of energy balance equations, consisting of two equations for kinetic energy (upper and lower layers) and an equation for potential energy. Energy balance equations K_1 and K_2 can be obtained by adding up the equations of motion for each layer multiplied by the corresponding components of the current velocity. The potential energy balance equation is obtained by differentiating the equation for P with respect to time and then using the Boussinesq and rigid-lid approximations:

$$\begin{cases} \frac{\partial K_1}{\partial t} + \frac{\partial U_1 e_{K1}}{\partial x} + \frac{\partial V_1 e_{K1}}{\partial y} = W_{C1} + W_{G1} + W_{\tau} + W_{RL1} + W_{AB1}, \\ \frac{\partial K_2}{\partial t} + \frac{\partial U_2 e_{K2}}{\partial x} + \frac{\partial V_2 e_{K2}}{\partial y} = W_{C2} + W_{G2} + W_{RL2} + W_{RD} + W_{AB2}, \\ \frac{\partial P}{\partial t} - \rho g' \left(\frac{\partial U_2 h_1}{\partial x} + \frac{\partial V_2 h_1}{\partial y} \right) - \rho g \left(\frac{\partial U \zeta}{\partial x} + \frac{\partial V \zeta}{\partial y} \right) = -W_{G1} - W_{G2}, \end{cases} \quad (1)$$

where $W_{C1} = U_1 \cdot f v_1 - V_1 \cdot f u_1 = 0$; $W_{C2} = U_2 \cdot f v_2 - V_2 \cdot f u_2 = 0$;

$W_{\tau} = \rho(u_1 \tau^x + v_1 \tau^y)$;

$W_{RL1} = \rho(u_1 R_{L1}^x + v_1 R_{L1}^y)$; $W_{RL2} = \rho(u_2 R_{L2}^x + v_2 R_{L2}^y)$; $W_{RD} = \rho(u_2 R_D^x + v_2 R_D^y)$;

$W_{G1} = \rho g(U_1 \zeta_x + V_1 \zeta_y)$; $W_{G2} = \rho g(U_2 \zeta_x + V_2 \zeta_y) + \rho g'(U_2 h_{1x} + V_2 h_{1y})$;

$W_{AB1} = \rho A_B(U_1(\Delta \Delta u_1) + V_1(\Delta \Delta v_1))$; $W_{AB2} = \rho A_B(U_2(\Delta \Delta u_2) + V_2(\Delta \Delta v_2))$;

ρ is mean water density in the Black Sea.

The left side of equations (1) includes local derivatives with respect to time and divergence of advective flows of corresponding energies.

The right side includes the terms that describe the work per time (power) unit of the forces from the equations of motion, determining corresponding energy flows: W_{C1} , W_{C2} is Coriolis force work in the upper and lower layers; W_t is tangential wind stress work, equal to kinetic energy influx into the sea (wind pumping); W_{RL1} , W_{RD} is work of friction forces (energy dissipation due to friction at the lower boundary of the upper and lower layers); W_{RL2} is work of friction forces (energy entering the lower layer from the upper due to friction between the layers); W_{G1} , W_{G2} is pressure gradient work (transition between kinetic and potential energy in the upper and lower layers); W_{AB1} , W_{AB2} is work of horizontal turbulent viscosity forces in layers (energy dissipation).

Flows W_{G1} , W_{G2} with different signs enter simultaneously into the balance equations of kinetic and potential energy, thereby providing energy connection between the upper and lower layers.

Work of the Coriolis force W_{C1} and W_{C2} in equations (1) is equal to zero, but it can be non-zero separately for MCs and MEs, as it will be shown below. Therefore, these terms are retained in the equations. In this case, the Coriolis force work determines the kinetic energy transitions between the MCs and the MEs.

Energy characteristics of MCs and MEs

Thus, the task requires to separate the energy characteristics of flows obtained using a numerical model by the scale of movement, namely: to calculate the time-average values of energy and its transitions separately for mean currents and mesoscale eddy formations. It is also necessary to determine how energy is exchanged between MCs and MEs. The separate calculations will be carried out for the eastern and western parts of the sea.

Consideration of average characteristics permits to exclude time derivatives of energy in the energy balance equations so that to reduce the number of factors influencing the variability of energy characteristics. This somewhat simplifies the analysis.

Let us rewrite equations (1) averaged over a long period of time in terms of energy transitions using construction $\{E_1, E_2\}$ to denote the time-average transition of one energy type to another [21]. If $\{E_1, E_2\} > 0$, this means that E_2 goes into E_1 , and vice versa: if $\{E_1, E_2\} < 0$, then E_1 goes into E_2 :

$$\left\{ \begin{array}{l} \frac{\partial \overline{U_1 e_{K1}}}{\partial x} + \frac{\partial \overline{V_1 e_{K1}}}{\partial y} = \overline{W_{C1}} + \{K_1, P\} + \{K_1, \tau\} + \{K_1, D_L\} + \{K_1, D_{T1}\}, \\ \frac{\partial \overline{U_2 e_{K2}}}{\partial x} + \frac{\partial \overline{V_2 e_{K2}}}{\partial y} = \overline{W_{C2}} + \{K_2, P\} + \{K_2, K_1\} + \{K_1, D_H\} + \{K_1, D_{T2}\}, \\ -\rho g' \left(\frac{\partial \overline{U_2 h_1}}{\partial x} + \frac{\partial \overline{V_2 h_1}}{\partial y} \right) - \rho g \left(\frac{\partial \overline{U \zeta}}{\partial x} + \frac{\partial \overline{V \zeta}}{\partial y} \right) = -\{K_1, P\} - \{K_2, P\}, \end{array} \right. \quad (2)$$

where $\overline{W_{C1}} = 0$; $\overline{W_{C2}} = 0$; $\{K_1, \tau\} = \overline{W_\tau}$; $\{K_1, P\} = \overline{W_{G1}}$; $\{K_2, P\} = \overline{W_{G2}}$; $\{K_1, D_L\} = \overline{W_{RL1}}$; $\{K_2, K_1\} = \overline{W_{RL2}}$; $\{K_1, D_H\} = \overline{W_{RD}}$; $\{K_1, D_{T1}\} = \overline{W_{AB1}}$; $\{K_1, D_{T2}\} = \overline{W_{AB2}}$; D_L is dissipation due to friction at the lower boundary of the upper layer; D_H is dissipation due to bottom friction; D_{T1} , D_{T2} is dissipation due to horizontal turbulent viscosity in the upper and lower layers; the overline means averaging over time.

Let us integrate equations (2) over space within the western and eastern regions, after which we obtain two systems of equations in which square brackets with the superscript W or E indicating the region of integration are used to write the energy characteristics total over the area:

$$\begin{aligned}
 [...]^W &= \iint_W (...) dx dy, \quad [...]^E = \iint_E (...) dx dy, \\
 \left\{ \begin{aligned}
 \iint_W \left(\frac{\partial \overline{U_1 e_{K1}}}{\partial x} + \frac{\partial \overline{V_1 e_{K1}}}{\partial y} \right) dx dy &= [W_{C1}]^W + [K_1, P]^W + [K_1, \tau]^W + [K_1, D_L]^W + [K_1, D_{T1}]^W, \\
 \iint_W \left(\frac{\partial \overline{U_2 e_{K2}}}{\partial x} + \frac{\partial \overline{V_2 e_{K2}}}{\partial y} \right) dx dy &= [W_{C2}]^W + [K_2, P]^W + [K_2, K_1]^W + [K_1, D_H]^W + [K_1, D_{T2}]^W, \\
 \iint_W \left(-\rho g' \left(\frac{\partial \overline{U_2 h_1}}{\partial x} + \frac{\partial \overline{V_2 h_1}}{\partial y} \right) - \rho g \left(\frac{\partial \overline{U \zeta}}{\partial x} + \frac{\partial \overline{V \zeta}}{\partial y} \right) \right) dx dy &= -[K_1, P]^W - [K_2, P]^W,
 \end{aligned} \right. \quad (3) \\
 \left\{ \begin{aligned}
 \iint_E \left(\frac{\partial \overline{U_1 e_{K1}}}{\partial x} + \frac{\partial \overline{V_1 e_{K1}}}{\partial y} \right) dx dy &= [W_{C1}]^E + [K_1, P]^E + [K_1, \tau]^E + [K_1, D_L]^E + [K_1, D_{T1}]^E, \\
 \iint_E \left(\frac{\partial \overline{U_2 e_{K2}}}{\partial x} + \frac{\partial \overline{V_2 e_{K2}}}{\partial y} \right) dx dy &= [W_{C2}]^E + [K_2, P]^E + [K_2, K_1]^E + [K_1, D_H]^E + [K_1, D_{T2}]^E, \\
 \iint_E \left(-\rho g' \left(\frac{\partial \overline{U_2 h_1}}{\partial x} + \frac{\partial \overline{V_2 h_1}}{\partial y} \right) - \rho g \left(\frac{\partial \overline{U \zeta}}{\partial x} + \frac{\partial \overline{V \zeta}}{\partial y} \right) \right) dx dy &= -[K_1, P]^E - [K_2, P]^E.
 \end{aligned} \right. \quad (4)
 \end{aligned}$$

Using the divergence theorem and the no-slip conditions on a solid boundary, the double area integrals are replaced from the divergence of advective energy flows on the left side of the equations with linear integrals from the x -component of these flows along boundary D :

$$\begin{aligned}
 \int_D \overline{F_{K1}}(y) dy &= \iint_W \left(\frac{\partial \overline{U_1 e_{K1}}}{\partial x} + \frac{\partial \overline{V_1 e_{K1}}}{\partial y} \right) dx dy = - \iint_E \left(\frac{\partial \overline{U_1 e_{K1}}}{\partial x} + \frac{\partial \overline{V_1 e_{K1}}}{\partial y} \right) dx dy, \\
 \int_D \overline{F_{K2}}(y) dy &= \iint_W \left(\frac{\partial \overline{U_2 e_{K2}}}{\partial x} + \frac{\partial \overline{V_2 e_{K2}}}{\partial y} \right) dx dy = - \iint_E \left(\frac{\partial \overline{U_2 e_{K2}}}{\partial x} + \frac{\partial \overline{V_2 e_{K2}}}{\partial y} \right) dx dy, \\
 \int_D \overline{F_P}(y) dy &= \iint_E \left(-\rho g' \left(\frac{\partial \overline{U_2 h_1}}{\partial x} + \frac{\partial \overline{V_2 h_1}}{\partial y} \right) - \rho g \left(\frac{\partial \overline{U \zeta}}{\partial x} + \frac{\partial \overline{V \zeta}}{\partial y} \right) \right) dx dy = \\
 &= - \iint_W \left(-\rho g' \left(\frac{\partial \overline{U_2 h_1}}{\partial x} + \frac{\partial \overline{V_2 h_1}}{\partial y} \right) - \rho g \left(\frac{\partial \overline{U \zeta}}{\partial x} + \frac{\partial \overline{V \zeta}}{\partial y} \right) \right) dx dy,
 \end{aligned} \quad (5)$$

where $\overline{F_{K1}} = \overline{U_1 e_{K1}}$, $\overline{F_{K2}} = \overline{U_1 e_{K1}}$, $\overline{F_p} = -\rho \left(g' \overline{U_2 h_1} + g \overline{(U_1 + U_2) \zeta} \right)$ are average advective flows of kinetic and potential energy between the western and eastern parts of the sea.

To divide the energy characteristics according to the movement scale, the above definition for MC and ME will be used. As already mentioned, MC is obtained by averaging instantaneous current fields over time, and ME is the deviation of instantaneous currents from MC. Superscript m is used to identify MC and its energy characteristics, and superscript p is used for ME.

Mathematically, the division of circulation according to the movement scale can be expressed through currents (water flows) in the layers as follows:

$$\begin{aligned} U_1 &= U_1^m + U_1^p = \overline{u_1 h_1} + (u_1 h_1)', & V_1 &= V_1^m + V_1^p = \overline{v_1 h_1} + (v_1 h_1)', \\ U_2 &= U_2^m + U_2^p = \overline{u_2 h_2} + (u_2 h_2)', & V_2 &= V_2^m + V_2^p = \overline{v_2 h_2} + (v_2 h_2)', \end{aligned} \quad (6)$$

where the prime symbol means a deviation (pulsation) from the average value; (U_1, V_1) , (U_2, V_2) are components of currents (flows) in layers; (U_1^m, V_1^m) , (U_2^m, V_2^m) are components of the mean current; (U_1^p, V_1^p) , (U_2^p, V_2^p) are components of pulsation flows, or MEs.

In the present paper, the current averaging period was chosen equal to the averaging period of equations (2).

If expressions (6) are substituted into system of equations (1), then after opening the brackets and dividing the terms of the equations according to the scale of motion, separate systems of energy balance equations for MC and ME will be obtained.

Let us show how separation by scale of motion works using the example of the term that describes the work of the Coriolis force in the first equation of system (1):

$$\begin{aligned} W_{C1} &= u_1 h_1 \cdot f v_1 - v_1 h_1 \cdot f u_1 = (U_1^m + U_1^p) \cdot f v_1 - (V_1^m + V_1^p) \cdot f u_1, \\ W_{C1} &= (U_1^m \cdot f v_1 - V_1^m \cdot f u_1) + (U_1^p \cdot f v_1 - V_1^p \cdot f u_1) = W_{C1}^m + W_{C1}^p, \end{aligned}$$

where $W_{C1}^m = U_1^m \cdot f v_1 - V_1^m \cdot f u_1$ and $W_{C1}^p = U_1^p \cdot f v_1 - V_1^p \cdot f u_1$ is work of the Coriolis force, carried out by MC and ME, respectfully.

Fig. 3 shows the vector of the instantaneous flow decomposed into the mean and pulsating flows, and the vector of the Coriolis force acting on the instantaneous flow.

According to the figure, the division of currents (flows) into mean (MCs) and pulsating (MEs) leads to the appearance of non-zero values of the Coriolis force work associated with them. In total, these values are equal to zero, i.e., they cancel each other out. However, when dividing the energy balance equations for real flows into equations for MC and ME, the corresponding Coriolis force work should be taken into account to harmonize the systems of equations. It is correct to consider this work imaginary (fictitious), since the division of flows into mean and pulsating ones is also imaginary, existing only within the framework of the representation method used.

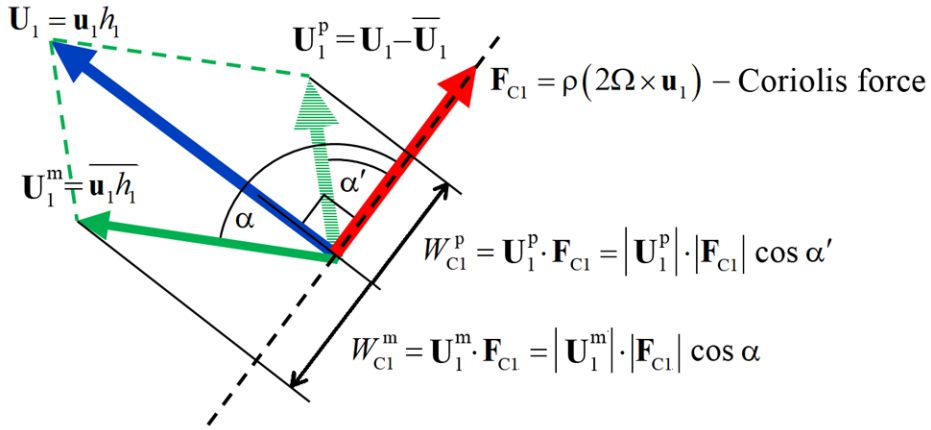


Fig. 3. Appearance of non-zero values of the Coriolis force work ($W_{Ci}^m = -W_{Ci}^p \neq 0$) at decomposing the flows into a sum of the average $\overline{u_1/h_1}$ and pulsation $(u_1/h_1)'$ values

In the energy balance equations of MC and ME, the Coriolis force work determines the transitions of kinetic energy between mean and pulsating flows. It can be said that mean and pulsating flows that do not actually exist exchange kinetic energy with each other due to the imaginary Coriolis force work, which itself is an imaginary (fictitious) force.

Considering that equations (3)–(5) are a consequence of equations (1), two systems of equations in which the terms related to MC and ME are separated into different equations for the western and eastern parts of the Black Sea are obtained:

$$\left\{ \begin{array}{l} \Phi_{K1}^m = [K_1^m, K_1^p]^W + [K_1^m, P^m]^W + [K_1^m, \tau]^W + [K_1^m, D_L^m]^W + [K_1^m, D_{T1}^m]^W, \\ \Phi_{K1}^p = [K_1^p, K_1^m]^W + [K_1^p, P^p]^W + [K_1^p, \tau]^W + [K_1^p, D_L^p]^W + [K_1^p, D_{T1}^p]^W, \\ \Phi_{K2}^m = [K_2^m, K_2^p]^W + [K_2^m, P^m]^W + [K_2^m, K_1^m]^W + [K_2^m, D_H^m]^W + [K_2^m, D_{T2}^m]^W, \\ \Phi_{K2}^p = [K_2^p, K_2^m]^W + [K_2^p, P^p]^W + [K_2^p, K_1^p]^W + [K_2^p, D_H^p]^W + [K_2^p, D_{T2}^p]^W, \\ \Phi_P^m = -[K_1^m, P^m]^W - [K_2^m, P^m]^W, \\ \Phi_P^p = -[K_1^p, P^p]^W - [K_2^p, P^p]^W, \end{array} \right. \quad (7)$$

$$\left\{ \begin{array}{l} -\Phi_{K1}^m = [K_1^m, K_1^p]^E + [K_1^m, P^m]^E + [K_1^m, \tau]^E + [K_1^m, D_L^m]^E + [K_1^m, D_{T1}^m]^E, \\ -\Phi_{K1}^p = [K_1^p, K_1^m]^E + [K_1^p, P^p]^E + [K_1^p, \tau]^E + [K_1^p, D_L^p]^E + [K_1^p, D_{T1}^p]^E, \\ -\Phi_{K2}^m = [K_2^m, K_2^p]^E + [K_2^m, P^m]^E + [K_2^m, K_1^m]^E + [K_2^m, D_H^m]^E + [K_2^m, D_{T2}^m]^E, \\ -\Phi_{K2}^p = [K_2^p, K_2^m]^E + [K_2^p, P^p]^E + [K_2^p, K_1^p]^E + [K_2^p, D_H^p]^E + [K_2^p, D_{T2}^p]^E, \\ -\Phi_P^m = -[K_1^m, P^m]^E - [K_2^m, P^m]^E, \\ -\Phi_P^p = -[K_1^p, P^p]^E - [K_2^p, P^p]^E, \end{array} \right. \quad (8)$$

$$\begin{aligned}
& \text{where } \Phi_{K_1}^m = \int_D F_{K_1}^m dy; \Phi_{K_2}^m = \int_D F_{K_2}^m dy; \Phi_P^m = \int_D F_P^m dy; \Phi_{K_1}^p = \int_D F_{K_1}^p dy; \\
& \Phi_{K_2}^p = \int_D F_{K_2}^p dy; \Phi_P^p = \int_D F_P^p dy; F_{K_1}^m + F_{K_1}^p = \overline{F_{K_1}}; F_{K_2}^m + F_{K_2}^p = \overline{F_{K_2}}; F_P^m + F_P^p = \overline{F_P}; \\
& F_{K_1}^m = U_1^m \cdot \overline{e_{K_1}}; F_{K_1}^p = \overline{F_{K_1}} - F_{K_1}^m; F_{K_2}^m = U_2^m \cdot \overline{e_{K_2}}; F_{K_2}^p = \overline{F_{K_2}} - F_{K_2}^m; \\
& F_P^m = -\rho(g'U_2^m \cdot \overline{h_1} + g(U_1^m + U_2^m)\overline{\zeta}); F_P^p = \overline{F_P} - F_P^m; \\
& [K_1^m, K_1^p]^W = [W_{C1}^m]^W = [U_1^m \cdot f \overline{v_1} - V_1^m \cdot f \overline{u_1}]^W; \\
& [K_1^p, K_1^m]^W = [W_{C1}^p]^W = -[K_1^m, K_1^p]^W; [K_1^m, P^m]^W = \rho g [U_1^m \cdot \overline{\zeta_x} + V_1^m \cdot \overline{\zeta_y}]^W; \\
& [K_1^p, P^p]^W = \rho g [\overline{U_1 \zeta_x} + \overline{V_1 \zeta_y}]^W - [K_1^m, P^m]^W; \\
& [K_1^m, \tau]^W = \rho [U_1^m \cdot \overline{\tau^x h_1^{-1}} + V_1^m \cdot \overline{\tau^y h_1^{-1}}]^W; [K_1^p, \tau]^W = \rho [\overline{u_1 \tau^x} + \overline{v_1 \tau^y}]^W - [K_1^m, \tau]^W; \\
& [K_1^m, D_L^m]^W = \rho [U_1^m \cdot \overline{R_{L1}^x h_1^{-1}} + V_1^m \cdot \overline{R_{L1}^y h_1^{-1}}]^W; \\
& [K_1^p, D_L^p]^W = \rho [\overline{u_1 R_{L1}^x} + \overline{v_1 R_{L1}^y}]^W - [K_1^m, D_L^m]^W; \\
& [K_1^m, D_{T1}^m]^W = \rho A_B [U_1^m (\Delta \Delta \overline{u_1}) + V_1^m (\Delta \Delta \overline{v_1})]^W; \\
& [K_1^p, D_{T1}^p]^W = \rho A_B [\overline{U_1 (\Delta \Delta u_1)} + \overline{V_1 (\Delta \Delta v_1)}]^W - [K_1^m, D_{T1}^m]^W; \\
& [K_2^m, K_2^p]^W = [W_{C2}^m]^W = [U_2^m \cdot f \overline{v_2} - V_2^m \cdot f \overline{u_2}]^W; \\
& [K_2^p, K_2^m]^W = [W_{C2}^p]^W = -[K_2^m, K_2^p]^W; \\
& [K_2^m, P^m]^W = \rho [g(U_2^m \cdot \overline{\zeta_x} + V_2^m \cdot \overline{\zeta_y}) + g'(U_2^m \cdot \overline{h_{1x}} + V_2^m \cdot \overline{h_{1y}})]^W; \\
& [K_2^p, P^p]^W = \rho [g(\overline{U_2 \zeta_x} + \overline{V_2 \zeta_y}) + g'(\overline{U_2 h_{1x}} + \overline{V_2 h_{1y}})]^W - [K_2^m, P^m]^W; \\
& [K_2^m, K_1^m]^W = \rho [U_2^m \cdot \overline{R_{L2}^x h_2^{-1}} + V_2^m \cdot \overline{R_{L2}^y h_2^{-1}}]^W; \\
& [K_2^p, K_1^p]^W = \rho [\overline{u_2 R_{L2}^x} + \overline{v_2 R_{L2}^y}]^W - [K_2^m, K_1^m]^W; \\
& [K_2^m, D_H^m]^W = \rho [U_2^m \cdot \overline{R_D^x h_2^{-1}} + V_2^m \cdot \overline{R_D^y h_2^{-1}}]^W; \\
& [K_2^p, D_H^p]^W = \rho [\overline{u_2 R_D^x} + \overline{v_2 R_D^y}]^W - [K_2^m, D_H^m]^W; \\
& [K_2^m, D_{T2}^m]^W = \rho A_B [U_2^m (\Delta \Delta \overline{u_2}) + V_2^m (\Delta \Delta \overline{v_2})]^W; \\
& [K_2^p, D_{T2}^p]^W = \rho A_B [\overline{U_2 (\Delta \Delta u_2)} + \overline{V_2 (\Delta \Delta v_2)}]^W - [K_2^m, D_{T2}^m]^W.
\end{aligned}$$

Formulas for calculating energy transitions in the eastern part of the sea are obtained by replacing W with E in the expressions above.

Expressions $[K_1^m, K_1^p]^W$, $[K_1^p, K_1^m]^W$, $[K_2^m, K_2^p]^W$, $[K_2^p, K_2^m]^W$, $[K_1^m, K_1^p]^E$, $[K_1^p, K_1^m]^E$, $[K_2^m, K_2^p]^E$ and $[K_2^p, K_2^m]^E$ are not equal to zero and determine the transitions of kinetic energy between MC and ME in the corresponding part of the sea.

Calculation results of energy characteristics

First of all, the time-average energy values of large-scale currents and mesoscale eddy formations in the western and eastern parts of the sea were determined, for which formulas for K_1 , K_2 , P , expressions (6) and representation $h_1 = h_1^m + h_1^p$ (where $h_1^m = \bar{h}_1$) were used:

$$K_1 = h_1 e_{K1} = \rho \frac{h_1 u_1^2 + h_1 v_1^2}{2} = \rho \frac{(U_1^m u_1 + V_1^m v_1) + (U_1^p u_1 + V_1^p v_1)}{2},$$

$$K_2 = h_2 e_{K2} = \rho \frac{h_2 u_2^2 + h_2 v_2^2}{2} = \rho \frac{(U_2^m u_2 + V_2^m v_2) + (U_2^p u_2 + V_2^p v_2)}{2},$$

$$P = \rho g' \frac{h_1^2 - h_0^2}{2} = \rho g' \frac{(h_1^m + h_1^p)^2 - h_0^2}{2} = \rho g' \frac{(h_1^m)^2 + 2h_1^m h_1^p + (h_1^p)^2 - h_0^2}{2}.$$

Averaging over time and dividing by scale of motion gives

$$\overline{K_1} = \rho \frac{(U_1^m \bar{u}_1 + V_1^m \bar{v}_1) + \overline{(U_1^p u_1 + V_1^p v_1)}}{2} = \rho \frac{(U_1^m \bar{u}_1 + V_1^m \bar{v}_1)}{2} + \rho \frac{\overline{(U_1^p u_1 + V_1^p v_1)}}{2},$$

$$\overline{K_1} = K_1^m + K_1^p, \quad K_1^m = \rho \frac{U_1^m \bar{u}_1 + V_1^m \bar{v}_1}{2}, \quad K_1^p = \rho \frac{\overline{(U_1^p u_1 + V_1^p v_1)}}{2} = \overline{K_1} - K_1^m,$$

$$\overline{K_2} = \rho \frac{(U_2^m \bar{u}_2 + V_2^m \bar{v}_2) + \overline{(U_2^p u_2 + V_2^p v_2)}}{2} = \rho \frac{(U_2^m \bar{u}_2 + V_2^m \bar{v}_2)}{2} + \rho \frac{\overline{(U_2^p u_2 + V_2^p v_2)}}{2},$$

$$\overline{K_2} = K_2^m + K_2^p, \quad K_2^m = \rho \frac{U_2^m \bar{u}_2 + V_2^m \bar{v}_2}{2}, \quad K_2^p = \rho \frac{\overline{(U_2^p u_2 + V_2^p v_2)}}{2} = \overline{K_2} - K_2^m,$$

$$\overline{P} = \rho g' \frac{(h_1^m)^2 - h_0^2 + \overline{(h_1^p)^2}}{2} = \rho g' \frac{(h_1^m)^2 - h_0^2}{2} + \rho g' \frac{\overline{(h_1^p)^2}}{2},$$

$$\overline{P} = P^m + P^p, \quad P^m = \rho g' \frac{(h_1^m)^2 - h_0^2}{2}, \quad P^p = \rho g' \frac{\overline{(h_1^p)^2}}{2} = \overline{P} - P^m.$$

After integrating the time-averaged MC and ME energies over the area for the western and eastern parts of the sea, the required values are obtained (see Table).

Time-averaged kinetic and available potential energy (TJ)

$[K_1]$	$[K_2^m]$	$[K_1^p]$	$[K_2]$	$[K_2^m]$	$[K_2^p]$	$[P]$	$[P^m]$	$[P^p]$
<i>Western part</i>								
313.7	238.3	75.4	48.4	1.9	46.4	881.1	756.0	125.0
<i>Eastern part</i>								
370.7	286.6	84.1	61.7	2.2	59.4	2915.0	2773.2	141.8

Time-averaged energies are stationary and do not affect energy transitions, but their knowledge is useful for a general understanding of the Black Sea energy and comparison of modelling results with observational data.

According to the data obtained, the MC and ME kinetic energy is distributed in the Black Sea quite evenly between its eastern and western parts. Slightly higher values of kinetic energy in the eastern part can be explained by the greater extent of large-scale currents in this part of the basin.

In the upper layer, the kinetic energy of MC is approximately three times greater than this of ME, and it is the other way around in the lower layer: ME contains 25 times more kinetic energy than MC.

Most of the average mechanical energy in the sea (~ 60%) falls on the available potential energy of MC concentrated in its eastern half. It is almost 10 times greater than the kinetic energy of MC in this part of the basin. In the western part, the total available potential energy of MC is three times higher than its kinetic energy. Moreover, it is three times less than the available potential energy of MC in the eastern part.

For ME, the difference in the P distribution between the western and eastern parts is proportional to the length of the average Rim Current in the corresponding area.

It is worth paying attention to the revealed pattern: in total, the kinetic energy of ME of the upper and lower layers turned out to be approximately equal to its available potential energy:

$$[K_1^p]^w + [K_2^p]^w \approx [P^p]^w, \quad [K_1^p]^e + [K_2^p]^e \approx [P^p]^e.$$

At the next stage, the average advective energy transfers between the western and eastern parts of the sea carried out by MC and ME were calculated. It is these flows resulting from the β -effect, as shown in [17], that are the cause of the spatial heterogeneity formation of the fields of energy characteristics in the Black Sea.

Fig. 4 shows the distribution of advective energy flows along the Y axis. In the upper layer, the maximum average transfer of kinetic energy is observed in the average Rim Current core (Fig. 4, *a*). The energy transfer direction coincides with the current direction. The main contribution to the kinetic energy advection is made by MC (Fig. 4, *b*), the maximum F_{K1}^m coincides with the mean flow core.

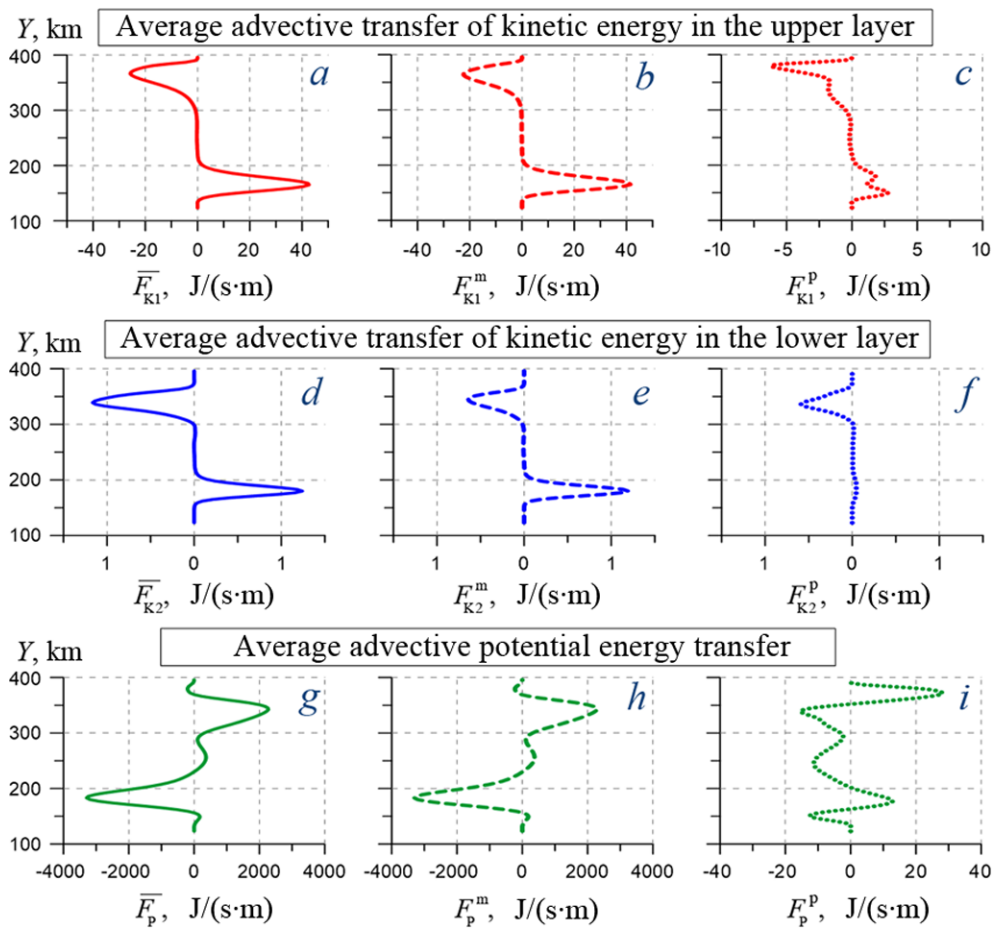


Fig. 4. Distribution of the energy advective flows along boundary D: mean flows are shown by a solid line, share of MCs – by a dashed line, share of MEs – by a dotted one

The southern MC branch transfers more energy than the northern one; as a result, the total flow of kinetic energy Φ_{K1}^m is 33 MJ/s, and it is directed from the western part of the sea to the eastern one (Fig. 5, *a*).



Fig. 5. Total advective energy flows (MJ/s) between the eastern and western parts of the sea: Φ_{K1}^m , Φ_{K1}^p (*a*); Φ_{K2}^m , Φ_{K2}^p (*b*); Φ_p^m , Φ_p^p (*c*)

Mesoscale eddy formations in the upper layer of the sea carry out the kinetic energy transfer in the same way as MCs, in the average Rim Current direction, but the maximum energy flows of MEs do not coincide with the average flow core, but are located next to it in the zones of the highest current velocity gradient (Fig. 4, *c*). Moreover, to the right of ME core the energy transfer is greater than to the left. Most likely, this happens because mesoscale anticyclonic eddies that are formed between the Rim Current and the coast contain more energy than cyclonic MEs that are formed mainly to the left of the Rim Current. The maximum advective flow of ME kinetic energy is observed to the right of the northern MC branch; it makes the main contribution to the total advective transport Φ_{k1}^p , which is 14 MJ/s in the western direction (Fig. 5, *a*). This is less than Φ_{k1}^m , therefore the total advective transfer of kinetic energy by currents in the upper layer is directed from the western half of the sea to the eastern one.

In the lower layer, the southern MC branch transports more kinetic energy in the eastern direction than the northern one in the western direction (Fig. 4, *e*). But the overall transfer of kinetic energy (Fig. 4, *d*) is still directed to the west due to the ME advective flow, which is maximum in the northern part of section D (Fig. 4, *f*). The total advective flow of kinetic MC energy Φ_{k2}^m directed to the east is 0.4 MJ/s, and the total flow of kinetic ME energy Φ_{k2}^p is directed to the west and is 0.5 MJ/s (Fig. 5, *b*).

The average advective transfer of potential ME energy occurs in the flow opposite direction in contrast to kinetic energy transfer (Fig. 4, *g, h*). The maximum values are noted in the MC core of the lower layer. They are much higher than the maxima of the kinetic MC energy flows in the upper and lower layers. However, the total flow in this case turns out to be of the same order of magnitude and is 25 MJ/s in the western direction due to the southern MC branch (Fig. 5, *c*).

The most interesting is the F_p^p advective flow distribution along section D (Fig. 4, *i*). Its maxima are in the MC core area in the lower layer, and it is directed along the flow. To the right of the MC core F_p^p , the flow changes direction to the opposite, reaches its maximum and becomes zero on the shore. It can be assumed that this F_p^p distribution is associated with mesoscale anticyclonic eddies formation and movement to the MC right (Fig. 1, *f*). In [9], it is shown that such eddies are elements of gradient-eddy waves (captured by the continental slope) which belong to the class of topographic Rossby waves. In general, the F_p^p flows between the MC core and the shore compensate each other due to their multidirectionality.

In the central part of section D (Fig. 4, *i*, between 200 and 300 km on the vertical scale) there is another maximum of F_p^p advective flow, which determines the main contribution of ME to the total potential energy transfer, resulting in a total flow $\Phi_p^p = 40$ MJ/s directed to the west (Fig. 5, *c*).

In general, it can be said that MEs transfer both kinetic and potential energy from the eastern part of the Black Sea to the western one, while MCs transfer only potential energy to the west. The greatest contribution to the western energy transfer is made by the Φ_p^p advective flow (Fig. 5, *c*), which is formed due to the potential energy transfer by mesoscale eddy formations through the central part of section D. According to [9, 22], such MEs are barotropic Rossby waves of a closed basin, formed in the deep sea due to the β -effect. As shown in ³, in a two-layer liquid basin under stationary wind action, it is barotropic Rossby waves that are generated. If a seasonally varying wind is used to excite motion in the model, then in addition to barotropic waves, baroclinic Rossby waves ³ will also be formed in the basin [23].

Let us consider the time-average transitions of mechanical energy that are a consequence of dynamic processes in the sea, taking into account the division of currents into MCs and MEs. These transitions calculated for the western and eastern parts of the Black Sea are shown diagrammatically in Fig. 6. The time averaging period was 20 model years which was enough for the time variability of the average energy characteristics to be close to zero.

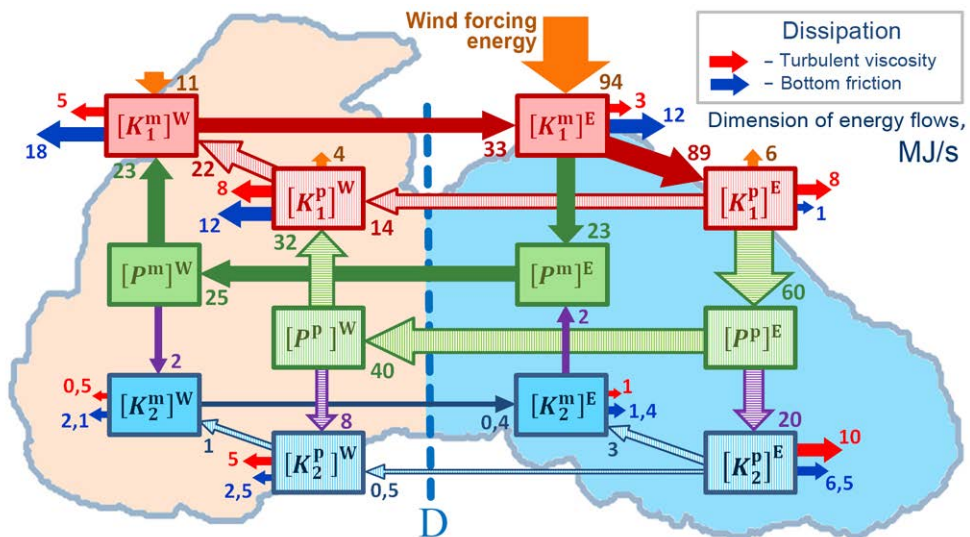


Fig. 6. Mean energy flows between the mean currents and the mesoscale eddies with regard to the sea division into two parts – the western and eastern ones

³ Safronov, G.F., 1985. [Excitation of Long Waves in the Ocean by Large-Scale Changes in the Tangential Wind Stress Field]. Moscow: Gidrometeoizdat, 108 p. (in Russian).

Let us note a number of features in energy transitions.

1. Wind energy pumping is observed mainly in the eastern part of the sea (94 MJ/s), which is explained by the wind field features used in the model and corresponds to observations [14]. In the western part, the wind energy influx is 11 MJ/s, which is 9 times less than in the eastern part.

2. All the energy coming from the wind goes to replenish the kinetic MC energy in the upper layer. The wind has an average braking effect on MEs, which leads to a loss of kinetic ME energy in both eastern (6 MJ/s) and western (4 MJ/s) parts of the sea.

3. MEs get kinetic energy from MCs in the upper layer of the eastern part of the sea, and a reverse transition of kinetic energy from MEs to MCs is observed in the western part.

4. The MC and ME kinetic energy transforms into the potential MC and ME energy in the upper layer of the eastern part of the sea, in the western part there is the opposite direction of energy transitions from potential to kinetic one.

5. Energy enters the lower layer of the sea due to the transition of the available potential ME energy into the kinetic ME energy in both eastern and western parts.

6. The kinetic MC energy of the lower layer in both parts of the sea is replenished by the kinetic ME energy, i.e., a transition of energy from small-scale movements to larger ones is observed. Such an energy transition is called the effect of negative viscosity in the theory of turbulence, but in this case it is the result of averaging of trapped waves moving over the continental slope, which transport a certain mass of water due to nonlinearity, i.e., have the properties of eddies.

7. Part of the kinetic MC energy of the lower layer transforms into the potential MC energy in the eastern half of the sea, and in the western one – vice versa: the potential MC energy partially transforms into the kinetic MC energy.

8. Despite the fact that the energy influx into the sea takes place predominantly in its eastern part, energy dissipation in the west is greater than in the east (53 and 42 MJ/s, respectively). Moreover, the most energy (67 MJ/s) is lost due to dissipation in the upper layer, with 43 MJ/s occurring in the western part of the sea.

Fig. 6 does not indicate the kinetic energy transitions from the upper layer to the lower one due to their smallness. The corresponding values are taken into account in the energy dissipation.

An important feature of the scheme presented, linking all its elements together, is the presence of the advective energy flows discussed above, directed from one part of the sea to the other (Fig. 5). On the one hand, it can be said that these advective flows compensate for differences in the size and direction of energy transitions in the western and eastern parts. On the other hand, these advective energy flows, being a consequence of the β -effect, are the main reason for the uneven distribution of energy transitions across the sea.

Conclusion

Consideration of the energy characteristics separately for the eastern and western parts of the Black Sea made it possible to identify a number of patterns in

the two-layer model energy and obtain new information about the course of dynamic processes in the sea. In particular, it turned out that the direction and size of mechanical energy transitions averaged over a long period of time among its types in different parts of the sea were significantly different from each other.

Differences in the direction and size of energy flows in the eastern and western parts were established. They were caused by advective energy flows, which in total are directed from the eastern half of the sea to the western one. As a result of calculating the contribution of average currents and mesoscale eddy formations to time-average advective energy flows, it was found that the main contribution to the western energy transfer was made by MEs localized in the central part outside the zone of large-scale currents distribution. On this basis, it was concluded that these MEs are Rossby waves formed as a result of the β -effect in a closed (bounded) basin. This conclusion confirms the β -effect importance for the formation of the Black Sea circulation once again.

The role of the Coriolis force work in the transitions of kinetic energy between MC and ME is shown. Thus, a reasonable question arises – how is this possible? It is known that the Coriolis force is an imaginary force and does not produce work. To resolve this contradiction, let us recall that the division of flows into MCs and MEs is artificial, or imaginary, and therefore the energy transitions between them are imaginary. These imaginary transitions are determined by the imaginary Coriolis force work which is equal to zero for total flows, but turned out to be non-zero separately for MCs and MEs.

At this stage of the research, energy characteristics averaged in a statistically equilibrium mode were analyzed over a long period of time, in which all average characteristics and model parameters remain constant. This approach simplifies energy analysis greatly, since it permits to eliminate time derivatives in the energy balance equations. At the same time, some important processes that are stochastic or periodic in their nature and are observed in different parts of the sea (e.g., baroclinic instability) are excluded from consideration. To study such processes when determining the average circulation, it is necessary to select the appropriate averaging period and take into account the spatiotemporal localization of the phenomenon itself. Further research is planned in this direction.

REFERENCES

1. Ivanov, V.A. and Belokopytov, V.N., 2013. *Oceanography of the Black Sea*. Sevastopol: ECOSY-Gidrofizika, 210 p.
2. Korotaev, G., Oguz, T., Nikiforov, A. and Koblinsky, C., 2003. Seasonal, Interannual, and Mesoscale Variability of the Black Sea Upper Layer Circulation Derived from Altimeter Data. *Journal of Geophysical Research: Oceans*, 108(C4), 3122. doi:10.1029/2002JC001508
3. Korotenko, K.A., 2015. Modeling Mesoscale Circulation of the Black Sea. *Oceanology*, 55(6), pp. 820-826. doi:10.1134/S0001437015060077
4. Zhang, Z., Zhang, Y., Wang, W. and Huang, R.X., 2013. Universal Structure of Mesoscale Eddies in the Ocean. *Geophysical Research Letters*, 40(14), pp. 3677-3681. doi:10.1002/grl.50736

5. Chelton, D.B., Schlax, M.G. and Samelson, R.M., 2011. Global Observations of Nonlinear Mesoscale Eddies. *Progress in Oceanography*, 91(2), pp. 167-216. doi:10.1016/j.pcean.2011.01.002
6. Chen, G., Hou, Y. and Chu, X., 2011. Mesoscale Eddies in the South China Sea: Mean Properties, Spatiotemporal Variability, and Impact on Thermohaline Structure. *Journal of Geophysical Research: Oceans*, 116(C6), C06018. doi:10.1029/2010JC006716
7. Kubryakov, A.A. and Stanichny, S.V., 2015. Mesoscale Eddies in the Black Sea from Satellite Altimetry Data. *Oceanology*, 55(1), pp. 56-67. doi:10.1134/S0001437015010105
8. Kantha, L.H. and Clayson, C.A., eds., 2000. *Numerical Models of Oceans and Oceanic Processes*. International Geophysics Series, vol. 66. San-Diego: Academic Press, 940 p. doi:10.1016/s0074-6142(00)x8001-1
9. Pavlushin, A.A., Shapiro, N.B. and Mikhailova, E.N., 2017. The Role of the Bottom Relief and the β -Effect in the Black Sea Dynamics. *Physical Oceanography*, (6), pp. 24-35. doi:10.22449/1573-160X-2017-6-24-35
10. Zatsepin, A.G., Baranov, V.I., Kondrashov, A.A., Korzh, A.O., Kremenetskiy, V.V., Ostrovskii, A.G. and Soloviev, D.M., 2011. Submesoscale Eddies at the Caucasus Black Sea Shelf and the Mechanisms of their Generation. *Oceanology*, 51(4), pp. 554-567. doi:10.1134/S0001437011040205
11. Capet, X., McWilliams, J.C., Molemaker, M.J. and Shchepetkin, A.F., 2008. Mesoscale to Submesoscale Transition in the California Current System. Part II: Frontal Processes. *Journal of Physical Oceanography*, 38(1), pp. 44-64. doi:10.1175/2007JPO3672.1
12. Kubryakov, A.A., Lishaev, P.N., Chepyzhenko, A.I., Aleskerova, A.A., Kubryakova, E.A., Medvedeva, A.V. and Stanichny, S.V., 2021. Impact of Submesoscale Eddies on the Transport of Suspended Matter in the Coastal Zone of Crimea Based on Drone, Satellite, and in Situ Measurement Data. *Oceanology*, 61(2), pp. 159-172. doi:10.1134/S0001437021020107
13. Kalashnik, M.V., Kurganskii, M.V. and Chkhetiani, O.G., 2022. Baroclinic Instability in Geophysical Fluid Dynamics. *Physics-USpekhi*, 65(10), pp. 1039-1070. doi:10.3367/UFNe.2021.08.039046
14. Zatsepin, A.G., Kremenetskiy, V.V., Stanichny, S.V. and Burdyugov, V.M., 2010. Black Sea Basin-Scale Circulation and Mesoscale Dynamics under Wind Forcing. In: A. V. Frolov and Yu. D. Resnyansky, eds., 2010. *Modern Problems of Ocean and Atmosphere Dynamics. The Pavel S. Lineykin Memorial Volume*. Moscow: Triada Ltd., pp. 347-368 (in Russian).
15. Kang, D. and Curchitser, E.N., 2015. Energetics of Eddy-Mean Flow Interactions in the Gulf Stream Region. *Journal of Physical Oceanography*, 45(4), pp. 1103-1120. doi:10.1175/JPO-D-14-0200.1
16. Demyshev, S.G. and Dymova, O.A., 2022. Analysis of the Lorenz Energy Cycle for Different Regimes of the Black Sea Circulation. *Transactions of the Karelian Research Centre RAS*, (6), pp. 26-40. doi:10.17076/lim1621 (in Russian).
17. Pavlushin, A.A., 2023. Features and Reasons for Spatial Heterogeneity of Mechanical Energy Flows in the Black Sea. *Physical Oceanography*, 30(3), pp. 302-314. doi:10.29039/1573-160X-2023-3-302-314
18. Pavlushin, A.A., Shapiro, N.B. and Mikhailova, E.N., 2019. Trapped Waves and the Rim Current Meandering. *Ecological Safety of Coastal and Shelf Zones of Sea*, (4), pp. 14-21. doi:10.22449/2413-5577-2019-4-14-21 (in Russian).
19. Markova, N.V. and Bagaev, A.V., 2016. The Black Sea Deep Current Velocities Estimated from the Data of Argo Profiling Floats. *Physical Oceanography*, (3), pp. 23-35. doi:10.22449/1573-160X-2016-3-23-35

20. Klyuvitkin, A.A., Ostrovskii, A.G., Lisitzin, A.P. and Konovalov, S.K., 2019. The Energy Spectrum of the Current Velocity in the Deep Part of the Black Sea. *Doklady Earth Sciences*, 488(2), pp. 1222-1226. doi:10.1134/S1028334X1910012X
21. Holland, W.R. and Lin, L.B., 1975. On the Generation of Mesoscale Eddies and Their Contribution to the Oceanic General Circulation. I. A Preliminary Numerical Experiment. *Journal of Physical Oceanography*, 5(4), pp. 642-657. doi:10.1175/1520-0485(1975)005<0642:OTGOME>2.0.CO;2
22. Stanev, E.V. and Rachev, N.H., 1999. Numerical Study on the Planetary Rossby Modes in the Black Sea. *Journal of Marine Systems*, 21(1-4), pp. 283-306. doi:10.1016/S0924-7963(99)00019-6
23. Pavlushin, A.A., 2022. Self-Oscillations of Large-Scale Circulation Intensity in the Black Sea. *Physical Oceanography*, 29(6), pp. 587-601. doi:10.22449/1573-160X-2022-6-587-601

Submitted 31.12.2022; approved after review 22.06.2023;
accepted for publication 15.11.2023.

About the author:

Andrey A. Pavlushin, Junior Research Associate, Marine Hydrophysical Institute of RAS (2 Kapitanskaya Str., Sevastopol, 299011, Russian Federation), **ORCID ID: 0000-0002-2098-5068**, **ResearcherID: R-4908-2018**, pavlushin@mhi-ras.ru

The author has read and approved the final manuscript.

The author declares that he has no conflict of interest.

Original article

Numerical Modeling of the Black Sea Response to the Intrusion of Abnormally Cold Air in January 23–25, 2010

V. V. Efimov , D. A. Yarovaya

Marine Hydrophysical Institute of RAS, Sevastopol, Russian Federation
 *vefim38@mail.ru*

Abstract

Purpose. The work is aimed at studying the response of the Black Sea upper layer to the intrusion of cold air in January 23–25, 2010.

Methods and Results. The NOW coupled mesoscale sea – atmosphere model with the 1 km resolution was used to study the sea fields numerically. The change in sea surface temperature in January 23–25, 2010 resulted from the cold intrusion was reproduced. The basic factors which had influenced the change in the upper layer temperature, namely horizontal advection, cooling of the sea surface due to the sensible and latent heat fluxes and the impact of vertical turbulent mixing were considered and quantitatively assessed. The main changes that took place in the cold intermediate layer were investigated.

Conclusions. The change in vertical distribution of the monthly average temperature, salinity and density is considered based on the Copernicus reanalysis data for 2009–2010. The presence of a cold intermediate layer at the average depth 60 m in all the months except for the transitional winter-spring period is shown. The results of NOW modeling reveal the fact that decrease in the surface temperature over the most sea area occurred as a result of heat and mass exchange with the atmosphere. The influence of horizontal advection and mixing through the lower boundary of the cold intermediate layer was manifested only in certain small areas, in other words, it produced a local effect. Convective cooling spanned the upper mixed layer up to the depths about 40–45 m and amounted to ~ 1°C. Besides, it is shown that during the cold air intrusion, the depth of cold intermediate layer increased. The notion that the local cold waters in the shallow northwestern part of the sea are secondary as a source of formation of the cold intermediate layer has been confirmed. The density of colder, but less saline coastal water prevents its sinking to the upper boundary of cold intermediate layer.

Keywords: cooling, cold intermediate layer, mesoscale modeling, coupled model, sea surface temperature

Acknowledgments: The work was carried out within the framework of project FNNN-2024-0014 “Fundamental studies of interaction processes in the ocean-atmosphere system determining variability of physical state of marine environment at various spatiotemporal scales”.

For citation: Efimov, V.V. and Yarovaya, D.A., 2024. Numerical Modeling of the Black Sea Response to the Intrusion of Abnormally Cold Air in January 23–25, 2010. *Physical Oceanography*, 31(1), pp. 120-134.

© 2024, V. V. Efimov, D. A. Yarovaya

© 2024, Physical Oceanography

Introduction

Seasonal cooling of the Black Sea in the autumn-winter period is sometimes accompanied by episodes of sharp decreases in air temperature as a result of intrusions of cold air masses through the northern and northeastern boundaries of the region. Cold intrusions are usually associated with the formation of such an interesting and important feature of the sea thermohaline structure as cold intermediate layer (CIL): it is believed that the minimum water temperature at depths of 50–90 m is the result of deep convection of cold-water masses in winter in

the centers of cyclonic gyres [1]. This process is facilitated by the development of cyclonic circulation in the atmosphere above the sea leading to a water rise in the central regions of the sea, a decrease in the thickness of the upper mixed layer there and its more intense cooling¹ [2].

The second mechanism for the CIL development is considered to be the slope advection of cold water from the shallow northwestern part of the sea to the southwestern and further to the southern and southeastern coastal parts of the sea by the Rim Current (RC). In this case, part of these coastal cold waters is captured by mesoscale anticyclonic eddies in the Rim Current region and then spreads to the entire Black Sea region [1, 3–7].

The study of CIL formation mechanisms in the Black Sea has intensified in the last two decades. This was facilitated by the implementation of the ARGO ocean monitoring program which made it possible to supplement significantly the existing database of long-term, though rather scattered, data on shipboard measurements of temperature, velocity and salinity [8]. In addition, modern numerical models of circulation in the atmosphere – sea system provide the solution of the problem of reconstructing the thermohydrodynamic fields and their variability in a wide range of spatio-temporal scales [9, 10]. Without dwelling on a detailed analysis of the current state of knowledge of thermodynamic processes in the Black Sea and, in particular, the CIL formation, we note [11, 12] in this regard. In [11], a sea circulation modeling on a climatic time scale was carried out using realistic meteorological forcing and the above-mentioned idea about the mechanisms of CIL formation in the Black Sea was confirmed. In [12], the results of an analysis of the accumulated array of measurement data from subsurface buoys are presented; this made it possible to study the details of the CIL structure formation, its interannual variability and confirm the trend towards a decrease in its depth observed in the last decade.

As a rule, periods of cold air masses intrusion across the northern and northeastern boundaries of the region are associated with such extreme weather phenomena as the Novorossiysk bora [13], icing of roads in the steppe part and a significant decrease in air temperature in the usually warm region of the Southern Coast of Crimea. In practice, cold air intrusions are accompanied by cases of heavy fog over bays in coastal cities, disruption of ferry service and formation of characteristic cloud “tracks” in the atmosphere above the sea [14, 15]. At the same time, the reaction of the sea itself to these cases of intrusion has not been studied sufficiently.

One of such cases considered in this paper refers to January 23–25, 2010. Previously, we considered it in [14, 15] in order to study the convection rolls (two-dimensional convection) in the atmosphere using the WRF numerical atmospheric circulation model. The work is purposed at studying the reaction of the Black Sea upper layer to this cold air intrusion using a coupled model that makes it possible to reconstruct the interaction processes in the atmosphere – sea system numerically.

¹ Blatov, A.S., Bulgakov, N.P., Ivanov, V.A., Kosarev, A.N. and Tuljulkin, V.S., eds., 1984. *Variability of the Black Sea Hydrophysical Fields*. Leningrad: Gidrometeoizdat, 240 p. (in Russian).

Numerical model

NOW coupled model consists of well-known WRF atmospheric model, NEMO marine model latest version 4 and OASIS application that exchanges data between WRF and NEMO [16]. This model is described in more detail in our previous works [17, 18].

The modeling used two nested grids with a resolution of 3 and 1 km. Data exchange took place both between main and nested domains. Every two hours, sea surface temperature and surface current velocity are transmitted from NEMO to WRF and short-wave and long-wave radiative heat fluxes, sensible and latent heat fluxes, wind friction stress as well as the difference between evaporated moisture and precipitation are transmitted from WRF to NEMO. 37 vertical levels were applied in the atmospheric model and 75 – in the sea model.

Yonsei University Scheme was used to parameterize the planetary boundary layer in WRF. To parameterize vertical turbulent mixing in NEMO, the Generic Length Scale scheme was applied. Output interval of the modeling results was 1 hour. In WRF and NEMO, the modeling time step was 15 and 300 s, respectively, for a computational grid with a resolution of 3 km and 5 and 100 s for a grid with a resolution of 1 km. As in our previous work [18], the initial conditions for the marine model as well as the bottom topography were taken from the global Copernicus² reanalysis with a resolution of $1/12^\circ$ and the initial and boundary conditions for the atmospheric model were taken from ERA5 reanalysis. Since the Copernicus reanalysis is derived from NEMO model with observational data assimilation and sea surface atmospheric forcing taken from ERA5 reanalysis, this reduces significantly the time required to adapt NEMO and WRF to each other during the coupled modeling.

The calculation began at 00:00 on January 22, one day before the start of the intrusion episode which lasted about 4 days, and the total duration of modeling was 5 days. Due to the short duration of modeling, the river runoff effect was not taken into account in the marine model. In the atmospheric model in the computational domain with a resolution of 3 km we used spectral “nudging” – a method in which during the modeling the atmospheric fields are adjusted every six hours, i.e. “nudged” to the large-scale reanalysis fields.

Results and discussion

Features of the cold air intrusion episode

As a rule, the cold air intrusion into the Black Sea through the northern, northeastern boundaries develops on the southeastern periphery of the anticyclone with its center above the Baltic States [13]. Moreover, the duration of such intrusion episodes is relatively short and amounts to 2–4 days. The case we are considering lasted about 3 days, during which the strong northerly wind changed to northeasterly

² Copernicus Marine Service. *Global Ocean Physics Reanalysis*. [online] Available at: https://resources.marine.copernicus.eu/product-detail/global_multiyear_phy_001_030/information [Accessed: 20 February 2024].

with maximum velocities in the central and southwestern parts of the sea. Without considering the details of wind field variability during the entire intrusion episode, we give an example of wind speed variability at two points in the sea as well as the main forcing that determined the reaction of the sea – sensible heat fluxes, shf, and latent heat fluxes, lhf, through the surface (radiative fluxes in winter can be neglected for this period).

Fig. 1 shows wind speed values at a height of 10 m at two points in the northwestern and eastern parts of the sea. Fig. 2 demonstrates total heat flux from the surface averaged over the cold intrusion (January 23–25), shf + lhf. It is clearly seen that for the entire sea the episode under consideration can indeed be considered a three-day cold air intrusion. During this period, the sea cooling was heterogeneous: the western and eastern halves of the sea are separated by a small area of reduced fluxes which is naturally explained by a wind speed decrease behind the leeward slope of rather high Crimean Mountains [13]. At the same time, heat loss from the surface in the northern part of the sea was 500–600 W/m², wind speed was about 10–14 m/s. In the southern half of the sea, heat loss through the surface is smaller than in the northern half since cold air warmed up when moving above a warmer sea.

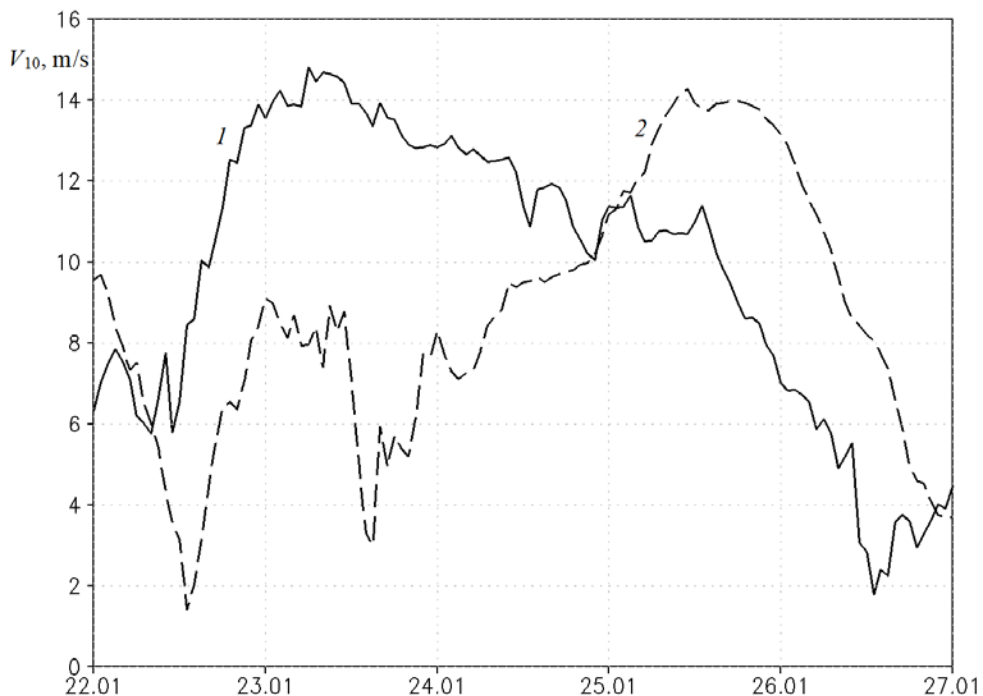


Fig. 1. Surface wind speed, m/s, at the points with coordinates 31°E, 44.5°N (1) and 37.5°E, 43°N (2) in January 22–26, 2010. The point positions are shown in Fig. 2

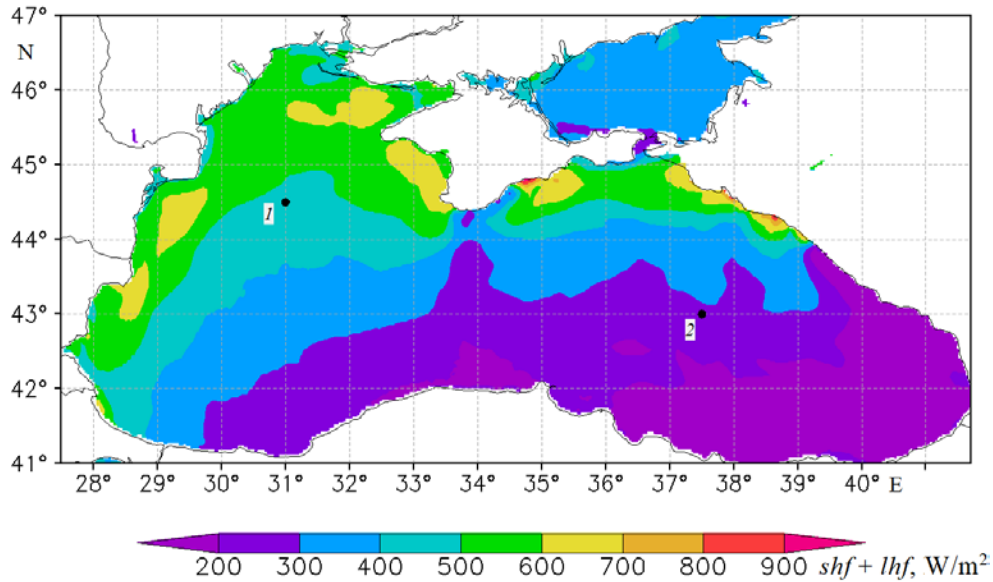


Fig. 2. Total heat flux directed from the sea surface, W/m^2 , averaged for January 23–25, 2010

Changes in sea surface temperature

Fig. 3, *a* shows the distribution of sea surface temperature (SST) and surface current velocity at the beginning of the cold invasion. A well-known climatic feature of the SST distribution – increased temperature values in the southeastern part and decreased in the northwestern one and Rim Current along the entire boundary area of the sea – is presented well. Fig. 3, *b* demonstrates the SST variations for the entire period of intrusion, from 00:00 on January 23 to 00:00 on January 26. As expected, the SST decrease is heterogeneous in area reflecting both synoptic heterogeneity of atmospheric forcing and mesoscale structure of eddy and jet currents in the sea upper layer. On average, the SST decreased during the intrusion by $1.5\text{ }^\circ\text{C}$ (in the deep sea) and even more in the coastal region of the northwestern shelf, where heat loss from the surface reached $500\text{--}600\text{ W/m}^2$. A comparison of current velocity fields immediately before and after the cold intrusion showed that on January 23–25 the Rim Current intensity increased, and in some areas near the Crimean coast, in the southwestern and southeastern corners of the sea, the velocity of alongshore surface current increased by $\sim 0.2\text{ m/s}$.

The SST decrease during winter cooling is determined by turbulence in the upper mixed layer, thickness of the upper mixed layer (UML) and advective heat transfer. All these processes are reproduced in detail in NEMO.

Fig. 3, *c – e* shows separately the contribution of the main factors to the SST variation: a decrease in the SST due to sensible and latent heat fluxes from the sea surface ΔT_{hf} (Fig. 3, *c*), the SST variation due to horizontal advection ΔT_{adv} (Fig. 3, *d*) and vertical turbulent mixing ΔT_{dif} (Fig. 3, *e*). The values given in Fig. 3, *c – e* are calculated using the following simple formulas:

$$\Delta T_{hf} = \frac{(shf + lhf)}{\rho C_p H} \Delta t, \quad (1)$$

$$\Delta T_{adv} = -\Delta t \int_{-H}^0 \left(u \frac{\partial T}{\partial x} + v \frac{\partial T}{\partial y} \right) dz, \quad (2)$$

$$\Delta T_{dif} = -\frac{\Delta t}{H} \left(K \frac{\partial T}{\partial z} \right) \Big|_{z=-H}, \quad (3)$$

where H is UML thickness; T is water temperature; u and v are zonal and meridional current velocities; K is coefficient of vertical turbulent heat diffusion (calculated in the model); ρ and C_p are density and specific heat capacity of water; Δt is time period (equal to 1 h). The details of numerical calculation by these formulas are given in [17]. H value in formulas (1)–(3) was assumed to be equal to the upper layer thickness with small (< 0.02 °C/m) vertical gradient T or to the sea depth if the water temperature at a given point does not almost vary with depth (near the coast and in the Sea of Azov).

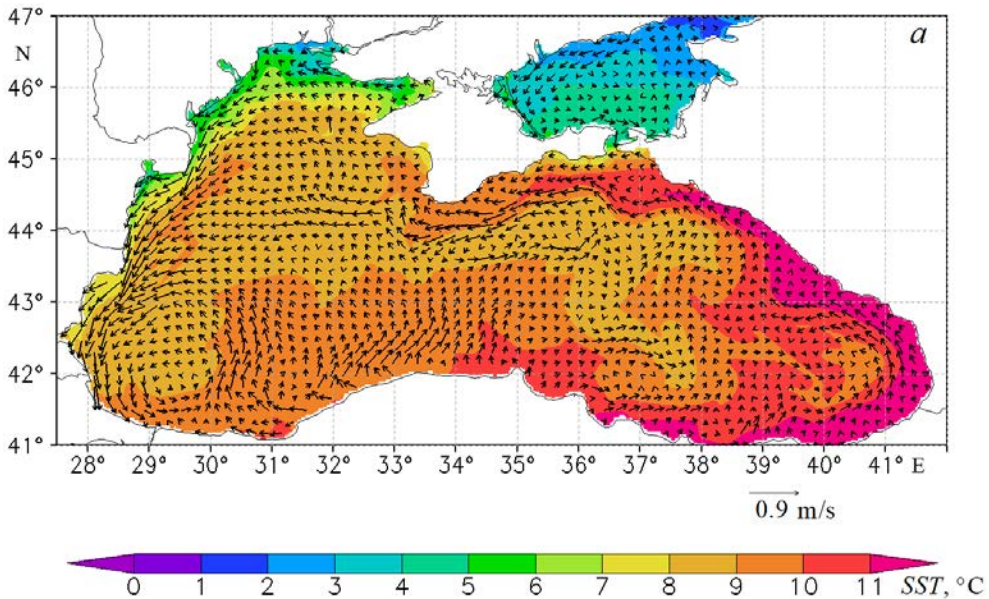
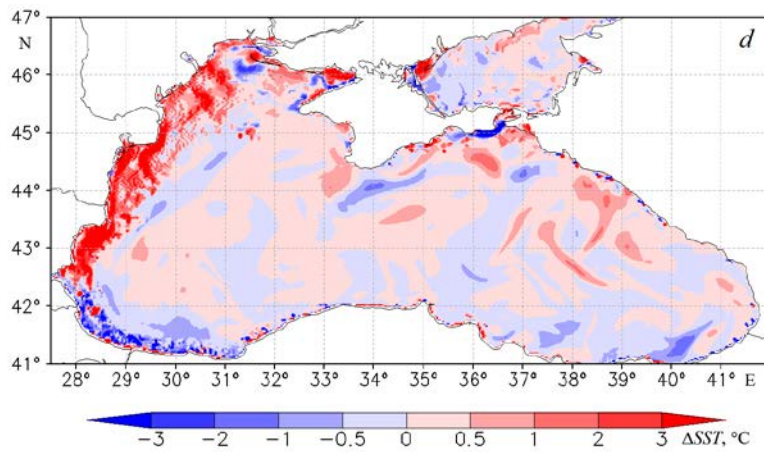
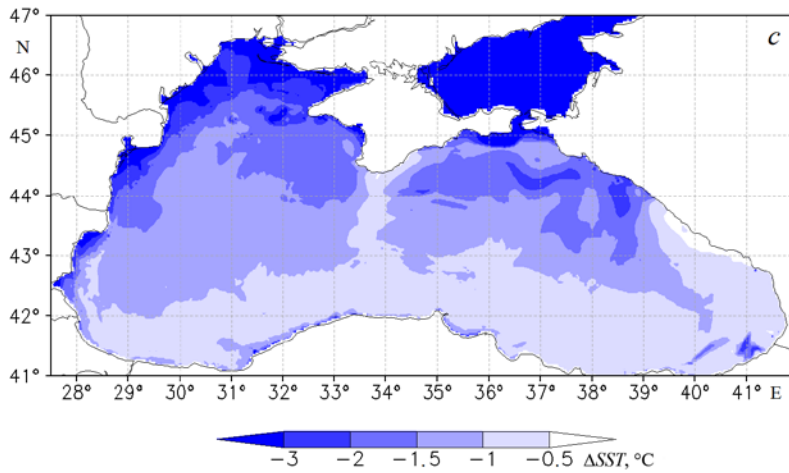
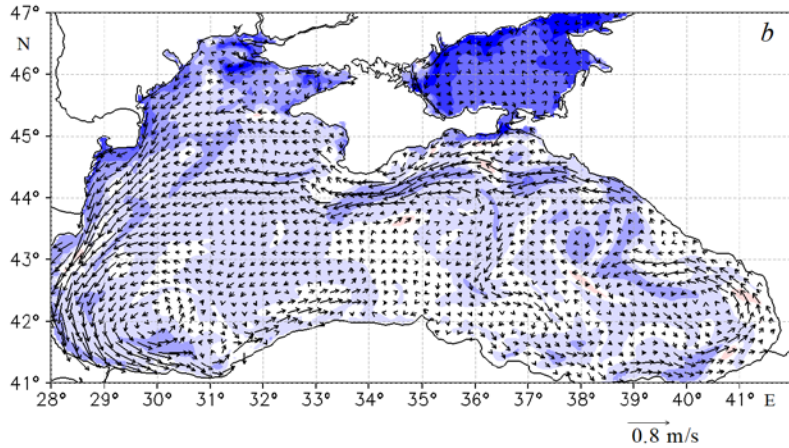
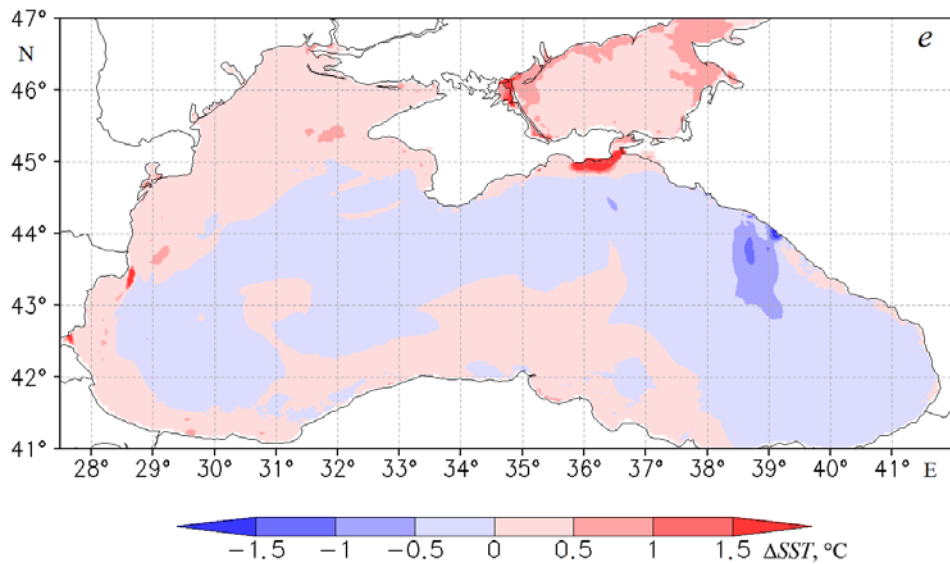


Fig. 3. Sea surface temperature (SST) at 00:00 on January 23 (*a*); change of SST for the period from 00:00, January 23, to 00:00, January 26, based on the results of modeling (*b*) and calculation using formulas (1) (*c*), (2) (*d*) and (3) (*e*). Arrows show the current velocity on the surface (m/s) at 00:00, January 23 (*a*), and the average one for the period from 00:00, January 23, to 00:00, January 26 (*b*). For clarity, the number of arrows is reduced along the longitude and latitude with the increments 15 and 12, respectively



Continuation of Fig. 3.



Continuation of Fig. 3.

Fig. 3, *c* shows the SST variation during the cold intrusion period due to heat fluxes. A significant SST decrease in the northern part of the sea is associated not only with high surface wind speed there, but also with shallow depths. Fig. 3, *c* distinguishes the region stretching from the Crimea to the south and the region near the Caucasian coast, eastwards of 39°E, where $|\Delta T_{\text{hf}}|$ value is smaller than in the deep sea. This is obviously due to the effect of the coastal Crimean and Caucasus mountains. Without providing illustrations, we note that in the atmospheric model, in the surface wind field averaged over January 23–25, qualitatively similar local features are observed – an area with reduced wind speed in the central part of the sea southwards of Crimea and low-velocity area near the high-mountainous Caucasian coast.

Fig. 3, *d* demonstrates temperature decrease averaged over depth H due to the horizontal transport of cold waters in the sea upper layer. As can be seen from Fig. 3, *b*, an area of the reduced SST arose southwards of Crimea despite the relatively small heat flux from the sea surface. Fig. 3, *d* shows that this occurred due to the transfer of cold waters from the northeastern part where heat exchange with the atmosphere was stronger, and as a result cooling was stronger as well. The Rim Current velocity increases as it goes around the Crimean Peninsula (Fig. 3, *a*) and, as a consequence, horizontal advection effect on the SST in this place increases. The advective Rim Current effect on the SST field is also manifested near the western coast where warmer water is transported from the central part of the sea and near the southwestern coast where colder water is transported from the northwestern part (Fig. 3, *b*). Note that the vertical transport effect on the SST field variation was insignificant and is not reflected in the figures.

As can be seen from Fig. 3, *e*, except for a small area near the Caucasian coast, the vertical mixing effect on the SST in the deep part of the sea was relatively small.

In the shallow part of the sea, e.g. near the Kerch Peninsula, owing to sharp sea surface cooling, convective instability could lead to the SST increase due to temperature equalization in the entire layer down to the bottom.

Thus, the Black Sea response to the cold intrusion consisted of the SST decrease mainly by 1–2 °C under effect of large sensible and latent heat fluxes (Fig. 3, *c*). The effect of horizontal advection (Fig. 3, *d*) and vertical turbulent mixing (Fig. 3, *e*) on the SST, as expected, led only to local inhomogeneities in the temperature field.

Changes in the sea upper layer temperature

As mentioned in the introduction, a characteristic feature of temperature distribution in the Black Sea upper layer is CIL – a relatively thin intermediate layer between the thermo- and halocline at depths of about 60 m. The current state of knowledge on the CIL is presented well in [12].

Fig. 4, *a, b* shows the vertical structure of temperature, salinity and density fields at vertical sections drawn along 31°E and 44°N before the start of the cold intrusion. Fig. 4, *a, b* confirms the idea that local cold waters in the shallow northwestern part of the sea are secondary as a source of CIL formation. Indeed, neither Fig. 4, *a, b*, nor other zonal and meridional vertical sections demonstrate signs of cold waters propagation from the coast towards the open part of the sea. The density of colder, though less saline, coastal water prevents it from sinking to the upper boundary of CIL, and its isolation from CIL is clearly visible.

The pattern of fields at vertical sections confirms the idea of CIL presence throughout the entire sea area except for certain local areas associated with coastal orography, river mouths and circulation features¹. Fig. 4, *b* demonstrates clearly the rise of CIL following the rise of UML and thermocline in the central part of the sea as a result of development of large-scale cyclonic circulation and the Rim Current [1]. Local deepening of CIL in the area of 33°–34°E is associated with a local effect – the proximity of the Southern Coast of Crimea which affects the Rim Current displacement and creates meridional heterogeneity of the density and temperature fields. Consideration of the features of CIL distribution throughout the sea as well as taking into account the CIL interannual temporal variability and its disappearance in individual years is beyond the scope of the work since the circulation was reproduced only for a relatively short time interval of the cold intrusion.

In Fig. 4, *c*, temperature and salinity variations during the cold intrusion are given at the same vertical section as in Fig. 4, *b*. In the near-surface layer, water cooling by up to 1.5–2 °C is clearly visible; this corresponds to the SST decrease in Fig. 3, *b*. In the CIL layer and below, the temperature varied insignificantly from –0.5 to 0.5 °C. To distinguish such a small reaction of the CIL temperature, we constructed vertical temperature profiles averaged over a large area (30°–38°E, 42.5°–44°N) and considered the period of cold intrusion in the annual cycle of CIL variation for 2009–2010.

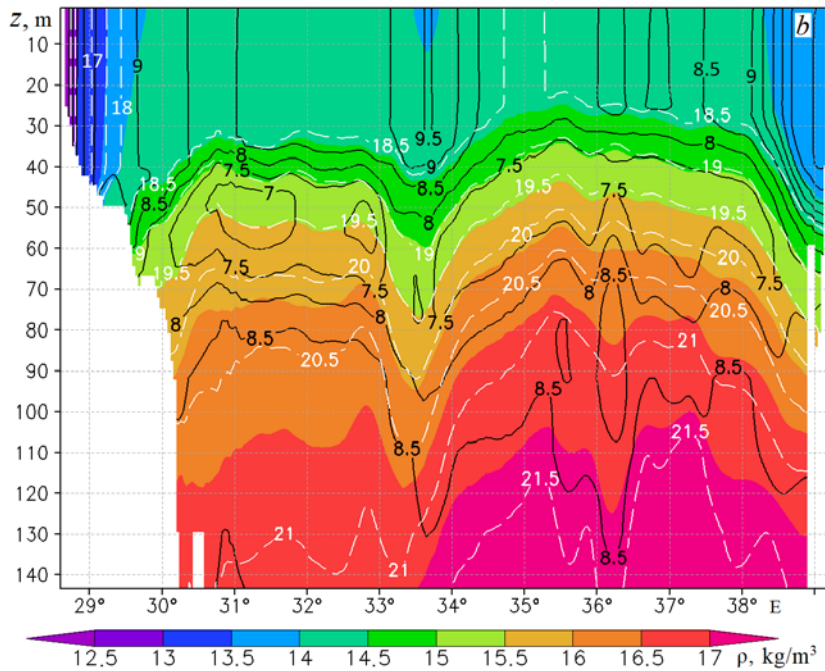
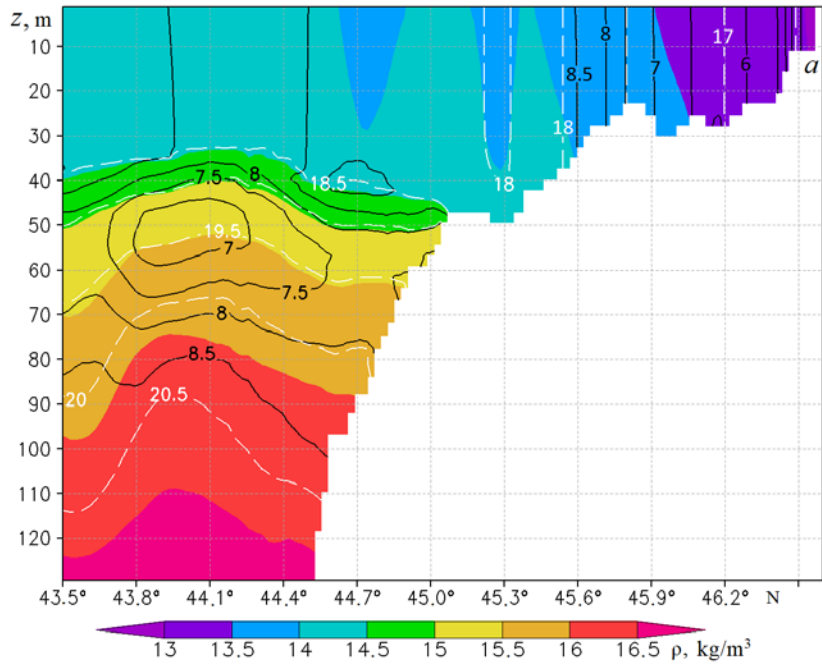
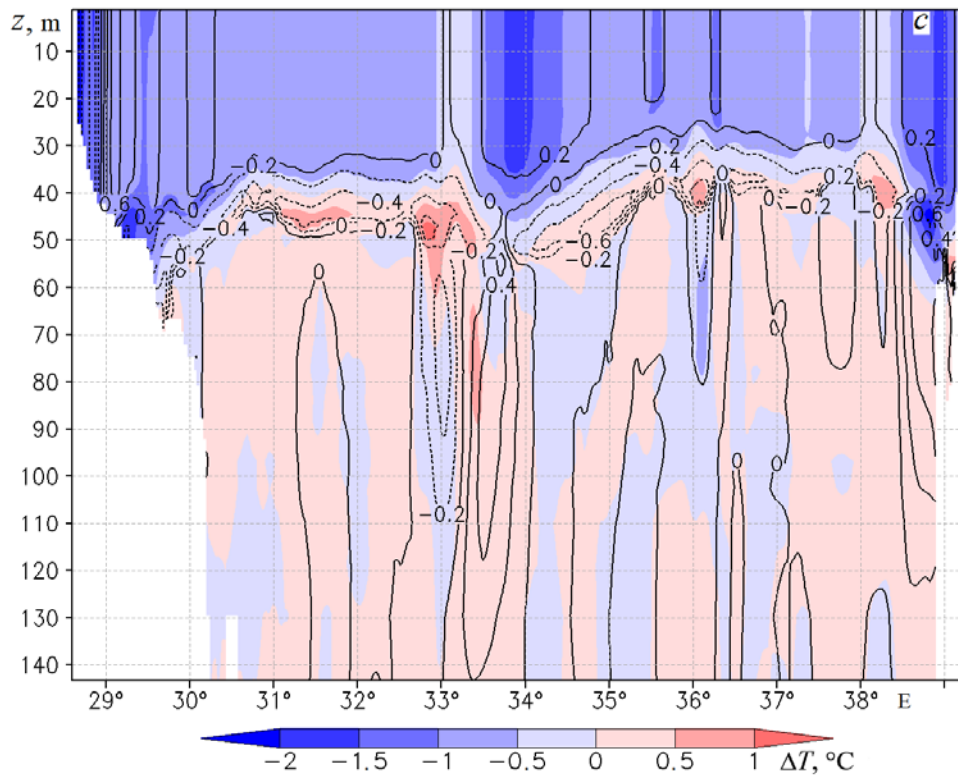


Fig. 4. Fields of density ρ , kg/m^3 , temperature T , $^{\circ}\text{C}$ (black isolines), and salinity S , ‰ (white isolines), at 00:00, January 23, at the meridional section along 31°E (*a*) and the zonal section along 44°N (*b*); change in temperature, $^{\circ}\text{C}$, and salinity, ‰ (isolines), for the period from 00:00, January 23, to 00:00, January 26, at the section along 44°N (*c*). For clarity, not the very value of ρ , but the difference ($\rho - 1000$), kg/m^3 , is shown in Fig. 4, *a*, *b*



Continuation of Fig. 4

Fig. 5 shows vertical profiles of temperature, density, and salinity averaged over the deep-sea part for several months of 2009–2010 and constructed using Copernicus data set. As can be seen, our cold intrusion episode occurred in mid-winter, when seasonal cooling brought the upper seasonal thermocline close to disappearing, although with the existence of CIL. Without dwelling on the features of seasonal variations in the vertical profiles of the main hydrophysical characteristics in the sea upper layer, we will only note well-pronounced temperature fluctuations in the annual cycle, a salinity decrease in summer in the upper layer associated with increased evaporation and a corresponding decrease in density. No deviations from the monotonic decrease in density and salinity were observed in the entire upper layer from August 2009 to February 2010. In all seasons except for the transitional winter-spring season we observe CIL with a minimum temperature value at an average depth of 60 m in the temperature profiles for our annual period of 2009–2010.

Taking into account that the cold air intrusion occurred when the sea upper layer had almost completely cooled, we will consider in more detail the development of this process according to our modeling results in which CIL was reproduced with a fairly high vertical resolution of ~ 2 m. Note that vertical resolution in Copernicus data set is about 5 m which smoothes out small-scale features of temperature profile variations in CIL.

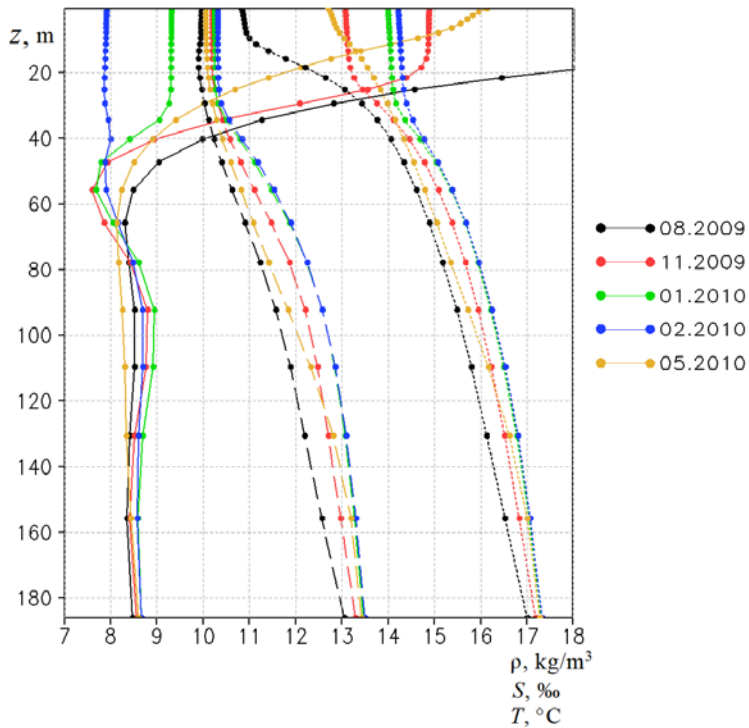


Fig. 5. Averaged over the deep-sea part (30° – 38° E, 42.5° – 44° N) monthly average vertical profiles of temperature T , $^{\circ}$ C (solid line), salinity S , ‰ (dashed line), and density ρ , kg/m^3 (dotted line), based on the Copernicus reanalysis data. For clarity, not the very values of S and ρ , but the differences ($S - 8$), ‰, and ($\rho - 1000$), kg/m^3 , are shown

Fig. 6 shows temperature and salinity profiles before, during and after the cold intrusion episode. The temperature field reaction is clearly visible: over 3 days the temperature of the entire upper layer decreased by $\sim 1^{\circ}$ C – this is consistent with the SST decrease shown in Fig. 3, *b*. It is interesting to note that the temperature decrease at the CIL upper boundary has a characteristic feature known for the UML evolution in the summer-autumn period – the entrainment of water from the seasonal thermocline into the UML associated with the penetration of turbulent pulsations from the UML into the thermocline.

It can be clearly seen from Fig. 6 that temperature decrease and salinity increase are accompanied by deepening of the CIL upper boundary. As a rule, summer mixed layer occurs as a result of dynamic instability associated with wind stress at the sea surface and wave orbital motions. In our case, they do not penetrate to depths of more than 30–40 m and shear instability effects associated with thermohaline currents can probably be also neglected. Unlike the summer mixed layer, the turbulence in our case is of a convective nature and the entrainment is limited to the region of the CIL upper boundary. Fig. 6 shows that in the CIL and below both temperature and salinity profiles can be considered unchanged during the intrusion period. This indicates directly the smallness of dissipative effects at these depths which explains the long lifetime of CIL after its development during winter convection.

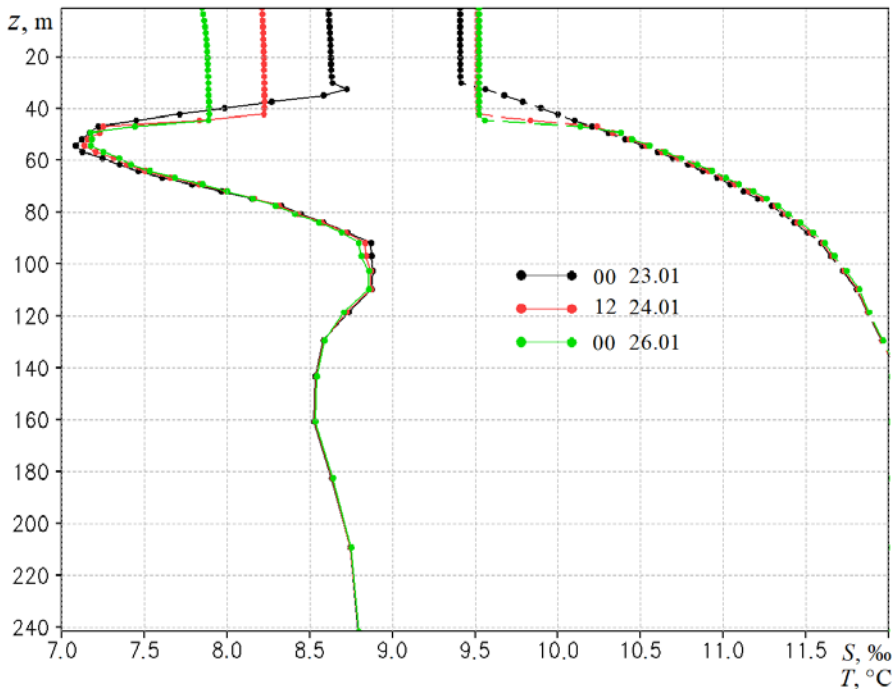


Fig. 6. Vertical profiles of temperature T , °C (solid line), and salinity S , ‰ (dashed line), at the point with coordinates 32°E, 44°N at 00:00 on January 23, 12:00 on January 24 and 00:00 on January 26, 2010. For clarity, not the very value of S , but the difference $(S - 8)$, ‰, is shown

Conclusion

Numerical modeling of the extreme case of cold air intrusion into the Black Sea using the coupled WRF-NEMO model with regard to the atmosphere-sea interaction made it possible to calculate the structure of thermohydrodynamic fields with a horizontal spatial resolution of 1 km. The intrusion itself lasted about three days during which wind speed reached 15 m/s and the total flux of sensible and latent heat was about 500 W/m^2 . The reaction of the sea directly to this cold atmospheric intrusion was distinguished. It was demonstrated that convective cooling influenced the upper mixed layer to the depths of about 40–45 m and amounted to $\sim 1 \text{ }^\circ\text{C}$.

It was demonstrated that the SST decrease over most sea occurred as a result of heat and mass exchange with the atmosphere. The effect of horizontal transport and vertical turbulent mixing on the SST appeared only in certain small areas, i.e. it had a local effect.

The case under study is of interest because it falls on the final lifetime stage of previously formed CIL: deepening of the CIL upper boundary (defined by the level of $8 \text{ }^\circ\text{C}$) due to autumn-winter cooling from the surface ended up with the example we considered. This is illustrated well by the temperature and salinity vertical profiles at the final stage of CIL lifetime as an intermediate layer between the thermo- and halocline. Small values of vertical diffusion and viscosity coefficients in CIL indicating the smallness of dissipative processes represent a characteristic feature.

CIL spatial distribution over the sea area is uneven. Nevertheless, in our case local areas of CIL absence are quite limited. At least, the given latitudinal section across the entire sea area and other sections (not presented here) do not manifest its development only in rare coastal areas. The corresponding climate analysis of CIL spatio-temporal structures as well as the statistics of cold intrusion cases in the Black Sea region (similar to the previously obtained statistics of Novorossiysk bora cases) are beyond the scope of this work and are proposed for the future.

REFERENCES

1. Korotaev, G.K., Knysh, V.V. and Kubryakov, A.I., 2014. Study of Formation Process of Cold Intermediate Layer Based on Reanalysis of Black Sea Hydrophysical Fields for 1971-1993. *Izvestiya, Atmospheric and Oceanic Physics*, 50(1), pp. 35-48. doi:10.1134/S0001433813060108
2. Simonov, A.I., Ryabinina, A.I. and Gershanovich, D.E., eds., 1992. *Hydrometeorology and Hydrochemistry of Seas in the USSR. Vol. IV. Black Sea. Issue 2. [Hydrochemical Conditions and Oceanographic Basis of Formation of Biological Productivity]*. Saint-Petersburg: Gidrometoizdat, 219 p. (in Russian).
3. Ivanov, V.A. and Belokopytov, V.N., 2013. *Oceanography of the Black Sea*. Sevastopol: ECOSI-Gidrofizika, 210 p.
4. Kuklev, S.B., Zatsepin, A.G. and Podymov, O.I., 2019. Formation of the Cold Intermediate Layer in the Shelf-Slope Northeastern Part Zone of the Black Sea. *Journal of Oceanological Research*, 47(3), pp. 58-71. doi:10.29006/1564-2291.JOR-2019.47(3).5 (in Russian).
5. Ovchinnikov, I.M. and Popov, Yu.I., 1987. Cold Intermediate Layer Formation in the Black Sea. *Oceanology*, 27(5), pp. 739-746 (in Russian).
6. Piotukh, V.B., Zatsepin, A.G., Kazmin, A.S. and Yakubenko, V.G., 2011. Impact of the Winter Cooling on the Variability of the Thermohaline Characteristics of the Active Layer in the Black Sea. *Oceanology*, 51(2), pp. 221-230. doi:10.1134/S0001437011020123
7. Titov, V.B., 2006. Zones of the Cold Intermediate Layer Formation and the Volume of Waters in the Black Sea Depending on Winter Severity. *Meteorologiya i Gidrologiya*, (6), pp. 62-68 (in Russian).
8. Akpinar, A., Fach, B.A. and Oguz, T., 2017. Observing the Subsurface Thermal Signature of the Black Sea Cold Intermediate Layer with Argo Profiling Floats. *Deep-Sea Research Part I: Oceanographic Research Papers*, 124, pp. 140-152. doi:10.1016/j.dsr.2017.04.002
9. Bruciaferri, D., Shapiro, G.I. and Wobus, F., 2018. A Multi-Envelope Vertical Coordinate System for Numerical Ocean Modelling. *Ocean Dynamics*, 68(10), pp. 1239-1258. doi:10.1007/s10236-018-1189-x
10. Bruciaferri, D., Shapiro, G., Stanichny, S., Zatsepin, A., Ezer, T., Wobus, F., Francis, X. and Hilton, D., 2020. The Development of a 3D Computational Mesh to Improve the Representation of Dynamic Processes: The Black Sea Test Case. *Ocean Modelling*, 146, 101534. doi:10.1016/j.ocemod.2019.101534
11. Miladinova, S., Stips, A., Garcia-Gorritz, E. and Macias, M.D., 2018. Formation and Changes of the Black Sea Cold Intermediate Layer. *Progress in Oceanography*, 167, pp. 11-23. doi:10.1016/j.pocean.2018.07.002
12. Stanev, E.V., Peneva, E. and Chtirkova, B., 2019. Climate Change and Regional Ocean Water Mass Disappearance: Case of the Black Sea. *Journal of Geophysical Research: Oceans*, 124(7), pp. 4803-4819. doi:10.1029/2019JC015076
13. Efimov, V.V., Komarovskaya, O.I. and Bayankina, T.M., 2019. Temporal Characteristics and Synoptic Conditions of Extreme Bora Formation in Novorossiysk. *Physical Oceanography*, 26(5), pp. 361-373. doi:10.22449/1573-160X-2019-5-361-373
14. Efimov, V.V. and Yarovaya, D.A., 2014. Numerical Simulation of Air Convection in the Atmosphere during the Invasion of Cold Air over the Black Sea. *Izvestiya, Atmospheric and Oceanic Physics*, 50(6), pp. 610-620. doi:10.1134/S0001433814060073

15. Iarovaia, D.A. and Efimov, V.V., 2018. Cloud Cells by Data of Satellite Measurements and Convective Energy Balance on Invasion of Cold Air into the Atmosphere over the Black Sea. *Izvestiya, Atmospheric and Oceanic Physics*, 54(9), pp. 1214-1222. doi:10.1134/S000143381809044X
16. Samson, G., Masson, S., Lengaigne, M., Keerthi, M.G., Vialard, J., Pous, S., Madec, G., Jourdain, N.C., Jullien, S. [et al.], 2014. The NOW Regional Coupled Model: Application to the Tropical Indian Ocean Climate and Tropical Cyclone Activity. *Journal of Advances in Modeling Earth Systems*, 6(3), pp. 700-722. doi:10.1002/2014MS000324
17. Iarovaia, D.A. and Efimov, V.V., 2021. Development of Cold Sea Surface Temperature Anomalies in the Black Sea. *Izvestiya, Atmospheric and Oceanic Physics*, 57(4), pp. 413-424. doi:10.1134/S0001433821040228
18. Efimov, V.V., Iarovaya, D.A. and Barabanov, V.S., 2023. Numerical Modelling of Upwelling near the South Coast of Crimea on 24–25 September 2013. *Ecological Safety of Coastal and Shelf Zones of Sea*, (1), pp. 6-19. doi:10.29039/2413-5577-2023-1-6-19

Submitted 19.04.2023; approved after review 22.05.2023;
accepted for publication 15.11.2023.

About the authors:

Vladimir V. Efimov, Head of Atmosphere and Ocean Interaction Department, Marine Hydrophysical Institute of RAS (2 Kapitanskaya Str., Sevastopol, 299011, Russian Federation), DSc (Phys.-Math.), Professor, **ResearcherID: P-2063-2017**, **Scopus Author ID: 6602381894**, vefim38@mail.ru

Daria A. Yarovaya, Senior Research Associate, Marine Hydrophysical Institute of RAS (2 Kapitanskaya Str., Sevastopol, 299011, Russian Federation), CSc (Phys.-Math.), **ResearcherID: Q-4144-2016**, **ORCID ID: 0000-0003-0949-2040**, **Scopus Author ID: 57205741734**, darik777@mhi-ras.ru

Contribution of the co-authors:

Vladimir V. Efimov – problem statement, discussion of modeling results, formulation of conclusions

Daria A. Yarovaya – carrying out calculations, discussion of modeling results, participating in drawing conclusions

The authors have read and approved the final manuscript.

The authors declare that they have no conflict of interest.

Mathematical Model of a Flooding Process in the Don Delta during Extreme Surges

A. L. Chikin ¹ ✉, L. G. Chikina ²

¹ *Federal Research Center Southern Scientific Center of Russian Academy of Sciences,
Rostov-on-Don, Russian Federation*

² *South Federal University, Rostov-on-Don, Russian Federation*
✉ *chikin1956@gmail.com*

Abstract

Purpose. The work consists in developing a mathematical model to study the flooding processes in the Don delta during the extreme surges.

Methods and Results. The level fluctuations in the Taganrog Bay are calculated based on solving a system of equations for long waves in a homogeneous incompressible fluid in the Coriolis force field. The problem is solved by the finite-difference methods on high-performance computing systems. The algorithm for determining the area of the Don delta flooding in the process of a surge is given. It is based on comparing the heights of the delta area to the water level and on taking a decision whether to flood or drain a computational cell. The calculation results are compared to the water level values observed at the gauging station, and are also displayed as a map diagram of the flooded area.

Conclusions. The proposed model should be applied in case of the extreme surges when a significant delta area is flooded. The model makes it possible to calculate accurately the hydrodynamic parameters of a flow including the magnitude of water level difference. The proposed algorithm determining whether flooding or draining is required for a computational domain, permits to reveal the areas in the Don delta where flooding depends on the wind conditions.

Keywords: shallow water equations, surge oscillations, computational experiment, flooding

Acknowledgements: The paper was prepared within the framework of state assignment of the Southern Scientific Center of RAS, state registration number of the project is 122011900153-9. The calculations were performed at the cluster in CCU “High-Performance Computing” of Southern Federal University.

For citation: Chikin, A.L. and Chikina, L.G., 2024. Mathematical Model of a Flooding Process in the Don Delta during Extreme Surges. *Physical Oceanography*, 31(1), pp. 135-147.

© 2024, A. L. Chikin, L. G. Chikina

© 2024, Physical Oceanography

Introduction

The Don water level surge oscillations are essentially manifested in its mouth area, which extends from a conventional line connecting the Dolzhanskaya and Belosarai spits in the Taganrog Bay in the west, to the village of Razdorskaya in the east ¹ [1]. Catastrophic floods have recently become more frequent in the Taganrog Bay and the Don River delta, which is caused by the extreme activity of the Black Sea cyclones [2–4]. An analysis of extreme natural phenomena (the inflow of salty transformed Black Sea waters into the Don delta, ice invasion

¹ Simov, V.G., 1989. [*Hydrology of the Mouths of the Rivers of the Sea of Azov*]. Moscow: Gidrometeoizdat, 328 p. (in Russian).



from the Sea of Azov into the Kerch Strait, etc.) observed in the Sea of Azov waters in recent years is presented in [5]. It discusses public safety problems that appear during surge processes in the Don delta.

In late March 2013, a large area in the Don delta was flooded with water extremely quickly as a result of a strong storm surge; more than 2 thousand households and over 5 thousand people were affected by flooding in 21 settlements. Material losses for the population and economy of the region are estimated at more than 500 million rubles. Significant damage was also caused to the scientific expedition base of the Southern Scientific Center of the Russian Academy of Sciences, located on the Swinoeye mouth shore. According to preliminary estimates, the flood area in the lower Don was 40 km wide and 50 km long (up the Don to Aksai).

Level rises dangerous for the Don delta can be caused by wind fields over the sea with significant pressure gradients and wind speeds (10–15 m/s or more). Southwestern winds over the entire Sea of Azov are especially dangerous, causing the greatest level rise in the Taganrog Bay and the Don delta [3].

The methods based on the construction and study of mathematical models of natural systems represent one of the ways for objective analysis of these problems.

Many works have been devoted to calculating the Don water level oscillations. In paper ², it is proposed to calculate the free surface levels for the Don main channel using the formula, where the desired upsurge in a given section depends on the upsurge near the town of Azov. This method gives satisfactory results only in the years when the Don water flow is close to normal.

Based on observation data from a standard hydrometeorological network, surges in the Don estuary area were studied and a catalog of maximum annual and dangerous surges was compiled at observation points on the coastal estuary and the Don estuary from the beginning of observation period to 2014. The possibility of forecasting surges was identified according to the synoptic situation over the Sea of Azov with the advance time of three days using hydrodynamic models. It made it possible to create a prognostic scheme for calculating the transformation of surges [6, 7].

A robust system for forecasting coastal river floods is presented in [8]. The technique combines statistical and hydrodynamic models to determine the probability of floods caused by multiple factors. The method includes extreme value analysis, assessment of dependencies and interactions among flood factors, multivariate joint dependency-based probability estimation, hydrodynamic modeling of flood scenarios derived from multivariate statistical analysis and flood mapping as the final result [8].

Many works using neural networks and machine learning methods to model floods have appeared [9]. In [10], the identification of flood-prone areas in an urban environment is shown with the help of neural networks. Such models can be used to

² Mikhaylov, V.N., Rogov, M.M. and Chistyakov, A.A., 1986. [*River Deltas: Hydrological and Morphological Processes*]. Leningrad: Gidrometeoizdat, 280 p. (in Russian).

map flood-prone urban areas which hydraulic models are not suitable for due to the lack of data. In addition, the combination of artificial neural networks and HEC-RAS hydrodynamic model makes it possible to determine the hydrodynamic parameters of currents, as well as to map floods in channels [11, 12]. To train and test the model, both weather station data and topographic humidity index are used.

Papers [13, 14] study the magnitude of storm surge oscillations in the Sea of Azov level based on the analysis of observational data and modeling results. These storm surge oscillations lead to extreme floods in the coastal areas of the Sea of Azov and the Taganrog Bay, when atmospheric cyclones become effective generators of significant sea level rises.

Paper [15] studies “surge oscillations in the Sea of Azov level, which occur during long-term atmospheric impacts of the same type and are the cause of floods/drying in coastal areas. Based on the analysis of the results of the three-dimensional hydrodynamic Princeton Ocean Model, spatial maps and reference data sets of the extent of flooding/drying of the Sea of Azov coast were created” [15, p. 185]. Flood areas are considered with a flat bottom of constant slope. It is assumed that there are no channels, eriks or ravines in the flood area.

A geometric approach to modeling flood areas using e-vector maps of territories is given in [16]. One of the intermediate stages of generating auxiliary cartographic data based on the use of pseudoposts is considered, and a 2D fragment of a map with a flood area is shown.

In [17], a numerical study of the process of flooding of the Lower Don floodplain as a result of high floods is presented. This model is based on 2D Saint-Venant differential equations using digital 3D terrain models. In addition, a similar model was used to clarify the hydrodynamic dependencies of the watercourse and estimate the impact of the Don floodplain transformation [18].

Long-term observations have shown that the Don delta flooding occurs not only because of seasonal floods, but as a result of extreme surges from the Taganrog Bay influenced by westerly winds. The present paper is aimed at numerical study of exactly this phenomenon. The use of a mathematical model based on the equations of motion of an incompressible fluid makes it possible to obtain the Don delta pictures in the process of its flooding. In this case, a digital terrain model of the delta is used, taking into account branches, erics and creeks.

Materials & methods

Downstream after Rostov-on-Don, the Don channel is divided into creeks and branches. The Don delta is characterized by intersected riverbed branches and numerous eriks, where delta islands rise low above the water level. Taking into account these features, the proposed model is used in the case of extreme surges, i.e., when the entire floodplain is flooded and it is necessary to apply 2D equations of water movement. In the case when the water level rises only in the Don branches, it is necessary to consider a model containing the equations of water movement in an open channel.

Mathematical modeling of hydrophysical processes in the Don delta region was carried out according to the classical scheme as follows:

- expression of the most important relations and laws inherent to a natural object (water body) under study in mathematical terms;
- development of model implementation algorithms on a modern computer;
- creation and debugging of software necessary for carrying out a large number of calculations and implementing selected mathematical models and algorithms on high-performance computing systems;
- establishing the adequacy of the constructed model to the original object;
- carrying out computational experiments allowing to obtain all the required qualitative and quantitative properties and characteristics of the object ³.

Calculations of the Taganrog Bay level oscillations are based on solving a system of equations for long waves in a homogeneous incompressible fluid in the Coriolis force field [19]:

$$\begin{aligned} \frac{\partial u}{\partial t} + u \frac{\partial u}{\partial x} + v \frac{\partial u}{\partial y} - \Omega v &= -g \frac{\partial \zeta}{\partial x} + \frac{\tau_{sx}}{H} - \frac{\tau_{bx}}{H}, \\ \frac{\partial v}{\partial t} + u \frac{\partial v}{\partial x} + v \frac{\partial v}{\partial y} + \Omega u &= -g \frac{\partial \zeta}{\partial y} + \frac{\tau_{sy}}{H} - \frac{\tau_{by}}{H}, \\ \frac{\partial \zeta}{\partial t} + \frac{\partial(Hu)}{\partial x} + \frac{\partial(Hv)}{\partial y} &= 0, \end{aligned}$$

where $H = h + \zeta$; $h = h(x, y)$ is water body depth; $u = u(x, y, t)$, $v = v(x, y, t)$ are velocities; τ_{sx}, τ_{sy} are projections of the wind friction force on the water surface on the OX and OY axes; τ_{bx}, τ_{by} are projections of the fluid friction force on the bottom on the OX and OY axes. These values depend on wind speed $\bar{W}_B = \{W_x; W_y\}$ and current $\bar{W}_T = \{u; v\}$ and are defined as follows [20]:

$$\bar{\tau}_s = \gamma |\bar{W}_B| \bar{W}_B, \quad \bar{\tau}_b = \beta |\bar{W}_T| \bar{W}_T,$$

where $|\bar{W}_B| = \sqrt{W_x^2 + W_y^2}$, $|\bar{W}_T| = \sqrt{u^2 + v^2}$, $\beta(x, y)$ is friction coefficient of fluid on the bottom; γ is coefficient of wind friction on the free water surface.

Slip conditions are specified on the solid boundary $\partial\Omega_b$:

$$\mathbf{V}_n \Big|_{\partial\Omega_b} = 0, \quad \frac{\partial \mathbf{V}_\tau}{\partial \bar{n}} \Big|_{\partial\Omega_b} = 0,$$

³ Chikin, A.L., 2009. [Development and Implementation of a Two-Layer Mathematical Model of Hydrophysical Processes in Reservoirs with Vast Areas of Shallow Water on High-Performance Computing Systems]. Thesis Dr. Phys.-Math.Sci. Moscow, 233 p. (in Russian).

and in places where water flows in or out, $\partial\Omega_r$, the corresponding velocity values are set:

$$u|_{\partial\Omega_r} = u_1, v|_{\partial\Omega_r} = v_1,$$

where V_n is normal component of the velocity vector; V_t is tangential component of the velocity vector.

As initial data, any known velocity distribution can be set:

$$u = u^0, v = v^0, \zeta = \zeta^0 -$$

or considered these velocities to be zero.

The algorithm of the coastline change as a result of drainage or flooding of the calculation area is quite simple and is based on determining whether the calculation cells belong to land or water.

On the surface of the studied water body, together with the expected flooding area, a 2D rectangular grid, being uniform in each direction, with h_1 and h_2 steps, is constructed. Depth values are entered into the nodes of a flat rectangular difference grid covering the water area, and height values are entered into the grid nodes covering the expected flooding area.

Taking into account the depth values at the flat grid nodes, cells located in water or on land are determined. Logical array $KG0$, which characterizes the type of cells (“water”, “land”), sets the initial configuration of the entire computational domain and does not change until the end of the calculation.

During the calculation process, some cells with shallow depths may dry out due to the downsurge and become classified as “land”. This happens when the value $H + \zeta$ ceases to be positive. Cells that have passed into the “land” category due to the downsurge, can return to the “water” category. The “water” category may also include “land” cells in the probable flood area. This occurs if there is an increase in the water level and the average depth over neighboring cells is not less than set critical value h_{cr} . The depth value in the current cell is set taking into account the law of conservation of mass. Logical array KG can change during the calculation process and characterizes the type of cells (“water”, “land”) that can be drained or flooded.

Fig. 1 shows a block diagram of the algorithm for determining the water body shoreline in the case of surges. The algorithm is based on determining the water body depth depending on the value of the water surface level difference. When iterating over all calculation cells based on the values of logical variable $KG0$, those that are obviously not included in the calculation area are immediately discarded ($KG0 = false$). Then, KG variable makes it possible to determine which process is taking place in the cell: drainage, flooding, or none.

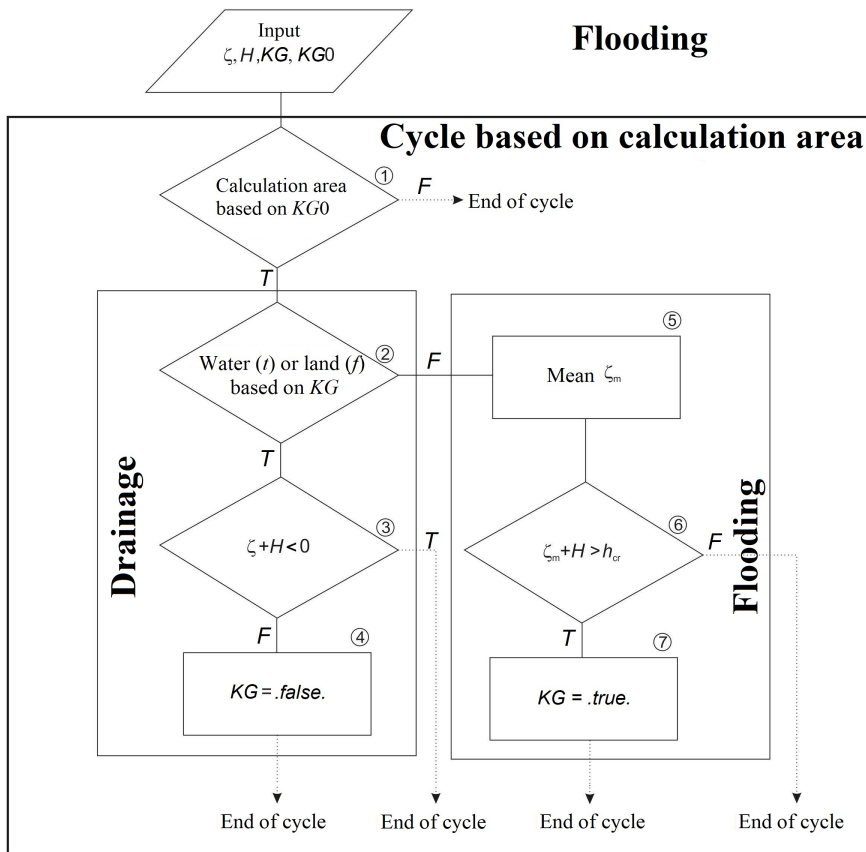


Fig. 1. Block diagram of the algorithm for calculating the area of flooding and drainage ⁴

If the cell was in a water body ($KG = true$), then in case $H + \zeta \leq 0$ this cell goes into the “land” category, and the KG variable takes the value *false*. Otherwise, drainage does not take place in this cell.

If a cell located in the calculation area ($KG0 = true$) is currently land ($KG = false$), then it can be flooded. This will happen if $\zeta_m + H \geq h_{cr}$, where ζ_m is the average value of the water level difference over neighboring cells. In this case, the cell goes into the “water” category, and the KG variable takes the value *true* ⁴.

In all cases of changes in the nature of difference cells, it is necessary to re-index the entire computational area. When indexing, it should be taken into account that the tape width in the matrix obtained after approximating a system of linear algebraic equations depends on the enumeration order of the indices. To narrow the tape, it is

⁴ Chikin, A.L. and Chikina, L.G., 2021. Numerical Study of Flooding of the Don Delta during Surges. In: SSC RAS, 2021. *Regularities of Formation and Impact of Marine and Atmospheric Hazardous Phenomena and Disasters on the Coastal Zone of the Russian Federation under the Conditions of Global Climatic and Industrial Challenges («Dangerous Phenomena - III»)*: Proceedings of the III International Scientific Conference in Memory of RAS Corresponding Member D.G. Matishov (Rostov-on-Don, 15-19 June 2021). Rostov-on-Don: SSC RAS Publishers, pp. 142-145 (in Russian).

necessary to start enumerating nodes with the index corresponding to the smallest dimension of the calculation area and end with the index corresponding to the largest dimension.

The problem is solved using finite difference methods. The algorithm for calculating the parameters of water flow on the $(n + 1)^{\text{th}}$ time layer is based on the principle that each equation is “defining” for its unknown. All other variables are considered to be known and are taken from the n^{th} layer.

The 1st step, the level difference at the $(n + 1)^{\text{th}}$ time layer, is calculated according to the following scheme:

$$\frac{\zeta_{i,j}^{n+1} - \zeta_{i,j}^n}{\Delta t} = - \left[\frac{u_{i+1,j} \frac{f_{i,j} + f_{i+1,j}}{2} - u_{i,j} \frac{f_{i-1,j} + f_{i,j}}{2}}{\Delta x} + \frac{v_{i,j} \frac{f_{i,j} + f_{i,j+1}}{2} - v_{i,j-1} \frac{f_{i,j-1} + f_{i,j}}{2}}{\Delta y} \right]^n,$$

where $f_{ij} = H_{ij} + \zeta_{ij}$.

The 2nd step is as follows: the values of the velocity components u and v are found from the difference momentum equations ⁵

$$\begin{aligned} & \frac{u_{s_{i,j}}^{n+1} - u_{s_{i,j}}^n}{\tau} + \frac{u_{s_{i,j}}^n + |u_{s_{i,j}}^n|}{2} \frac{u_{s_{i,j}}^{n+1} - u_{s_{i-1,j}}^{n+1}}{h_1} + \frac{u_{s_{i,j}}^n - |u_{s_{i,j}}^n|}{2} \frac{u_{s_{i+1,j}}^{n+1} - u_{s_{i,j}}^{n+1}}{h_1} + \\ & + \frac{v_{s_{i,j}}^n + |v_{s_{i,j}}^n|}{2} \frac{u_{s_{i,j}}^{n+1} - u_{s_{i,j-1}}^{n+1}}{h_2} + \frac{v_{s_{i,j}}^n - |v_{s_{i,j}}^n|}{2} \frac{u_{s_{i,j+1}}^{n+1} - u_{s_{i,j}}^{n+1}}{h_2} - \Omega \tilde{v}_{s_{i,j}} = \\ & = -g \frac{\zeta_{i,j}^n - \zeta_{i-1,j}^n}{h_1} + \left(\frac{\tau_{sx}}{H_{ij}} - \frac{\tau_{bx}}{H_{ij}} \right)_{i,j}^n, \end{aligned}$$

$$\tilde{v}_{s_{i,j}} = \frac{1}{4} \left(v_{s_{i,j}}^n + v_{s_{i-1,j}}^n + v_{s_{i-1,j-1}}^n + v_{s_{i,j-1}}^n \right).$$

$$\begin{aligned} & \frac{v_{s_{i,j}}^{n+1} - v_{s_{i,j}}^n}{\tau} + \frac{v_{s_{i,j}}^n + |v_{s_{i,j}}^n|}{2} \frac{v_{s_{i,j}}^{n+1} - v_{s_{i-1,j}}^{n+1}}{h_1} + \frac{v_{s_{i,j}}^n - |v_{s_{i,j}}^n|}{2} \frac{v_{s_{i+1,j}}^{n+1} - v_{s_{i,j}}^{n+1}}{h_1} + \\ & + \frac{v_{s_{i,j}}^n + |v_{s_{i,j}}^n|}{2} \frac{v_{s_{i,j}}^{n+1} - v_{s_{i,j-1}}^{n+1}}{h_2} + \frac{v_{s_{i,j}}^n - |v_{s_{i,j}}^n|}{2} \frac{v_{s_{i,j+1}}^{n+1} - v_{s_{i,j}}^{n+1}}{h_2} - \Omega \tilde{u}_{s_{i,j}} = \\ & = -g \frac{\zeta_{i,j+1}^n - \zeta_{i,j}^n}{h_2} + \left(\frac{\tau_{sx}}{H_{ij}} - \frac{\tau_{bx}}{H_{ij}} \right)_{i,j}^n, \end{aligned}$$

$$\tilde{u}_{s_{i,j}} = \frac{1}{4} \left(u_{s_{i,j}}^n + u_{s_{i+1,j}}^n + u_{s_{i,j+1}}^n + u_{s_{i+1,j+1}}^n \right).$$

⁵ Chikin, A.L., 2009. The Two-Layer Mathematical Model of the Wind Currents in the Basin with Different Level of Deep. *Mathematical Modeling*, 21(12), pp. 152-160 (in Russian).

Then, these steps are repeated on a new time layer until the counting end condition is met. Such a condition can represent a certain time period (in hours, days, etc.) during which the calculation should be carried out.

An analytical study of the presented algorithm stability has not been carried out. However, numerical studies have shown that a stable count is observed at time step $\tau \leq 120$ s.

The software is coded in FORTRAN, the numerical implementation of the model was carried out on high-performance computing systems in the MPI environment using the Aztec package of parallel routines.

Calculation results and discussion

In the study area, which includes the Sea of Azov, the Taganrog Bay and the Don delta, a grid of depths and heights was constructed in the Baltic height system. The grid step was $\Delta x = 660$ m, $\Delta y = 685$ m with the number of nodes 550×342 , which gave about 190,000 cells. After indexing, the number of cells in the computational domain with unknown hydrodynamic parameters became approximately 84,000.

The model verification was carried out both by a numerical comparison of the calculated and measured values of the water level at observation points and by a visual comparison of the calculated and actually flooded Don delta area. Water level values were taken at the gauging station in the khutor of Donskoy, located in the Sary Don branch. Wind situations during surges in September 2014 and April 2018 were considered.

When visualizing the flooding area, a finer grid with 100 m resolution was constructed in the Don delta, onto which the results of water level calculations were transferred. This made it possible to display the flooded area landscape more clearly. Using this grid in calculations would require approximately 50 times more computer resources and computation time, so calculations were carried out on a coarser grid.

At the beginning of the period from 19 April 2018 to 23 April 2018, the wind blew from the west at a speed of 9–11 m/s. Then it changed its direction to the north and weakened to 4–6 m/s, but then strengthened again to 11–13 m/s and became southwestern. This led to a repeated increase of the surge. Fig. 2 shows the calculated and measured water level oscillations at the Donskoy gauging station from 19 April 2018 to 23 April 2018. A comparison of measured and calculated values of water level in Donskoy showed that the calculation error is 23%.

In the last third of September 2014, the wind situation developed in such a way that the eastern wind blew at a speed of 3–4 m/s on 23 September 2014, which led to some water runoff in the Taganrog Bay. Then, the wind direction changed sharply to the southwest and winds began to blow at a speed of 2–24 m/s, which led to an extreme surge into the Don delta. During the extreme surge on 24–25 September

2014, not only water level oscillations were recorded, but also the flooded area in the Don delta which made it possible to visually compare the real and calculated flooding patterns. During this surge, unusually high salinity was also observed in the Azov port area (5.6 ‰) [21].

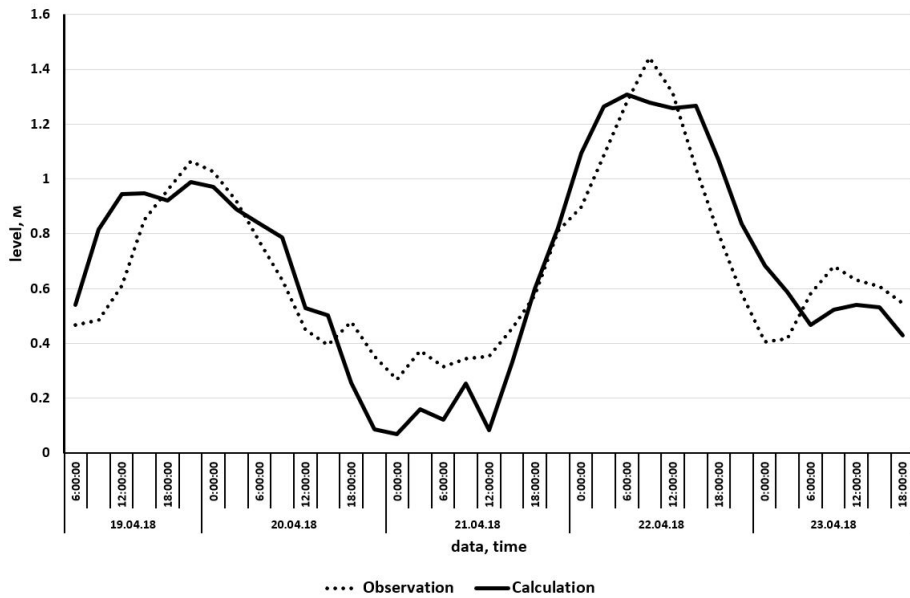


Fig. 2. Changes of water level in Donskoy from 19 April 2018 to 23 April 2018

Fig. 3 shows the Don delta region in its initial state, when level oscillations are insignificant. The water surface, including the Don branches and fish-breeding ponds, is highlighted in blue; the area with possible flooding is highlighted in light green. Fig. 4 shows the same area at the time of the maximum water level rise at 18:00 on 24 September 2014. The error in calculating the water level in the khutor of Donskoy was 17%.

A.Yu. Moskovets, a Southern Scientific Center specialist, tracked the flooding area in the Don delta region. The real picture of flooding is shown in Fig. 5. Flooded areas are indicated by shading. Unflooded areas of the delta are highlighted in red. The flood area obtained as a result of the surge simulation agrees quite well with the real picture in the specified area, although the differences between the modeled picture and the real one have not been quantified. The existing differences in flooded areas are explained by the fact that the calculations were carried out on a fairly coarse grid, and the calculation results were transferred to a fine grid only for visualization.

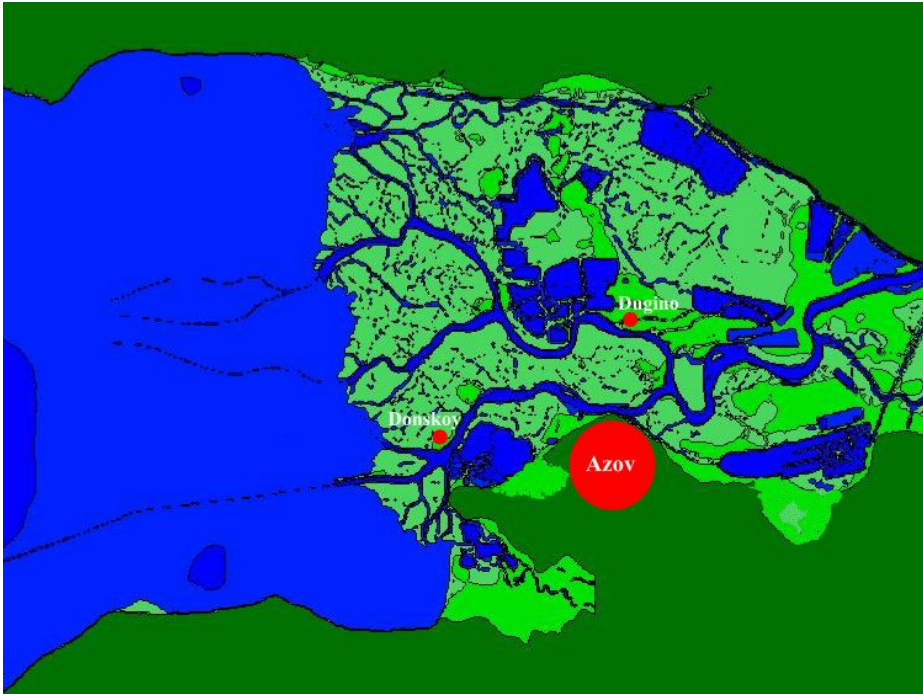


Fig. 3. Region of the Don delta at the beginning of upsurge on 24 September 2014

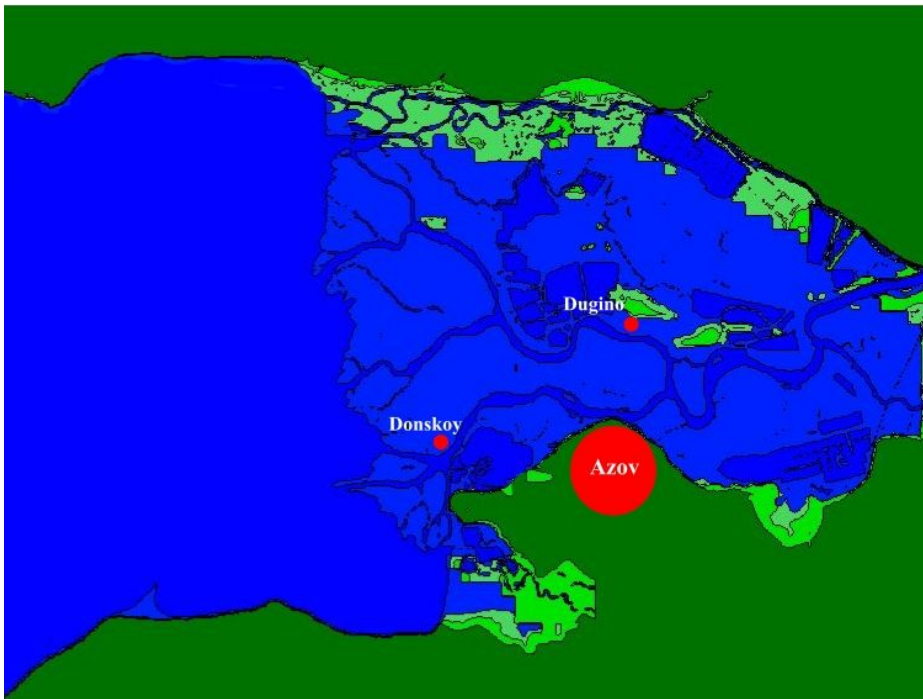


Fig. 4. Region of the Don delta at the time of the water level maximum rise on 24 September 2014



Fig. 5. Scheme of the flooded area of the Don River delta on 24 September 2014 (highlighted by hatching) performed by A.Yu. Moskovets

Conclusions

The proposed model should be used in the case of extreme upsurges, when the water level rise in the Don branches is so great that it floods the entire delta region. In this case, it is appropriate to use 2D hydrodynamic equations. In the case of small water level oscillations in the Taganrog Bay, the water flow in the Don channel is determined by the equations for channel flows.

Calculations have shown that this model makes it possible to calculate quite accurately the hydrodynamic parameters of the wind current, including the water level drop value. The proposed algorithm for determining flooding or drainage of the computational area permits to determine the locations of the Don delta flooding depending on the wind situation. Comparison of the measured water level values at the gauging station with the calculated ones indicates the correspondence of the proposed hydrodynamic model and the algorithm for determining flood areas during extreme water upsurges in the Taganrog Bay to the real flooding picture.

REFERENCES

1. Mishin, D.V. and Polonskiy, V.F., 2013. Research of Non-Stationary Water Streams in Nontidal Mouth of Don River. *Proceedings of SOI*, 214, pp. 166-179 (in Russian).

2. Matishov, G.G., Gargopa, Yu.M., Berdnikov, S.V. and Dzhenyuk, S.L., 2006. [*Regularities of Ecosystem Processes in the Sea of Azov*]. Moscow: Nauka, 304 p. (in Russian).
3. Matishov, G.G., Berdnikov, S.V., Sheverdyayev, I.V. and Chikin, A.L., 2014. The Extreme Flood in the Don River Delta, March 23-24, 2013, and Determining Factors. *Doklady Earth Sciences*, 455(1), pp. 360-363. doi:10.1134/S1028334X14030295
4. Matishov, G.G., Chikin, A.L., Berdnikov, S.V., Sheverdyayev, I.V., Kleshchenkov, A.V. and Kirillova, E.E., 2014. Extreme Flooding of the Don Delta in Spring 2013: Chronology, Formation Conditions, and Consequences. *Vestnik SSC RAS*, 10(1), pp. 17-24 (in Russian).
5. Matishov, G.G., 2015. The Kerch Strait and the Don Delta: The Security of Communications and Population. *Vestnik SSC RAS*, 11(1), pp. 6-15 (in Russian).
6. Vishnevskaya, I.A. and Ostroumova, L.P., 2019. Dangerous (Surge) Phenomena in the Estuarine Area of the Don River. In: SSC RAS, 2019. *Regularities of Formation and Impact of Marine and Atmospheric Hazardous Phenomena and Disasters on the Coastal Zone of the Russian Federation under the Conditions of Global Climatic and Industrial Challenges ("Dangerous Phenomena")*: Proceedings of the International Scientific Conference (Rostov-on-Don, 13-23 June 2019). Rostov-on-Don: SSC RAS Publishers, pp. 28-32 (in Russian).
7. Ostroumova, L.P., 2017. Investigation of Surges in Marine Estuaries (A Case Study for the Don River Mouth). *Russian Meteorology and Hydrology*, 42(12), pp. 792-802. doi:10.3103/S106837391712007X
8. Olbert, A.I., Moradian, S., Nash, S., Comer, J., Kazmierczak, B., Falconer, R.A. and Hartnett, M., 2023. Combined Statistical and Hydrodynamic Modelling of Compound Flooding in Coastal Areas - Methodology and Application. *Journal of Hydrology*, 620(A), 129383. doi:10.1016/j.jhydrol.2023.129383
9. Tayfur, G., Singh, V.P., Moramarco, T. and Barbetta, S., 2018. Flood Hydrograph Prediction Using Machine Learning Methods. *Water*, 10(8), 968. doi:10.3390/w10080968
10. Lei, X., Chen, W., Panahi, M., Falah, F., Rahmati, O., Uemaa, E., Kalantari, Z., Ferreira, C.S.S., Rezaie, F. [et al.], 2021. Urban Flood Modeling Using Deep-Learning Approaches in Seoul, South Korea. *Journal of Hydrology*, 601, 126684. doi:10.1016/j.jhydrol.2021.126684
11. Tamiru, H. and Dinka, M.O., 2021. Application of ANN and HEC-RAS Model for Flood Inundation Mapping in Lower Baro Akobo River Basin, Ethiopia. *Journal of Hydrology: Regional Studies*, 36, 100855. doi:10.1016/j.ejrh.2021.100855
12. Tawfik, A.M., 2023. River Flood Routing Using Artificial Neural Networks. *Ain Shams Engineering Journal*, 14(3), 101904. doi:10.1016/j.asej.2022.101904
13. Polozok, A.A., Fomin, V.V. and Lemeshko, E.E., 2020. Spatial Characteristics of Storm Surges in the Sea of Azov at Different Phases of Cyclone Movement. In: SSC RAS, 2020. *Regularities of Formation and Impact of Marine and Atmospheric Hazardous Phenomena and Disasters on the Coastal Zone of the Russian Federation under the Conditions of Global Climatic and Industrial Challenges ("Dangerous Phenomena – II")*: Proceedings of the II International Scientific Conference in Memory of Corresponding Member RAS D.G. Matishov (Rostov-on-Don, 6-10 July 2020). Rostov-on-Don: SSC RAS Publishers, pp. 63-67 (in Russian).
14. Cherkesov, L.V., Shul'ga, T.Ya., Dyakov, N.N. and Stanichnaya, R.R., 2017. Numerical Study of Storm Surge Processes and Currents of the Sea of Azov During a Period of Extreme Winds. *Physical Oceanography*, (5), pp. 3-18. doi:10.22449/1573-160X-2017-5-3-18
15. Shul'ga, T.Ya. and Matuzayeva, O.V., 2020. Predictive Simulation of the Duration of Wind-Induced Flooding/Drying of the Sea of Azov Coast. In: N. E. Galakhina, A. V. Tolstikov and T. I. Regerand, eds., 2020. *Water Resources: Research and Management (School and Workshop)*. Proceedings of the 6th International Young Scientists Conference, September 1-5, 2020, Petrozavodsk. Petrozavodsk: KRC RAS, pp. 185-189 (in Russian).
16. Sirazetdinova, D.D., Klein, A.N. and Abdullin, A.H., 2017. Simulation of Flooding of Territories Using ARCGIS PRO. In: R. N. Bakhtizin, ed., 2017. *Information Technology. Problems and Solutions: Proceedings of the International Scientific-Practical Conference*. Ufa: USPTU, 1(4), pp. 195-199 (in Russian).

17. Belikov, V.V., Alekseyuk, A.I., Borisova, N.M., Glotko, A.V. and Rumyantsev, A.B., 2022. Estimation of the Level of Floodplain Inundation in the Lower Don under the Effect of Economic Activity. Retrospective Hydrodynamic Modeling. *Water Resources*, 49(6), pp. 941-949. doi:10.1134/S0097807822060021
18. Glotko, A.V., Belikov, V.V., Borisova, N.M. and Rumjanzev, A.B., 2020. Study of the Impact of Human Activity on the Hydrological Regime in the Floodplain of the Don River near Rostov-on-Don. In: O. Makarieva and A. Zemlianskova, eds., 2020. *IV Vinogradov Conference Hydrology: From Learning to Worldview*. Proceedings of International Scientific Conference in Memory of Outstanding Russian Scientist Yury Vinogradov. Saint Petersburg: St. Petersburg State University, pp. 584-588 (in Russian).
19. Fillipov, Yu.G., 2014. Calculations of a Degree in the Eastern Part of the Taganrog Bay. *Proceedings of SOI*, 215, pp. 136-143 (in Russian).
20. Filippov, Yu.G., 1970. [On a Method for Calculations of Marine Currents]. In: SOI, 1970. *Proceedings of N.N. Zubov State Oceanographic Institute*. Moscow: Moskovskoe Otdelenie Gidrometeoizdata. Iss. 103, p. 87-94 (in Russian).
21. Chikin, A.L., Kleshchenkov, A.V. and Chikina, L.G., 2019. Simulating Salinity Variations in the Gulf of Taganrog at Storm Surges. *Water Resources*, 46(6), pp. 919-925. doi:10.1134/S0097807819060046

About the authors:

Aleksey L. Chikin, Chief Researcher, Southern Scientific Centre of RAS (41 Chekhov Ave., Rostov-on-Don, 344006, Russian Federation), DSc (Phys.-Math.), **ORCID ID: 0000-0002-4065-010X**, **Scopus Author ID: 8240627300**, chikin1956@gmail.com

Lyubov' G. Chikina, Professor, Southern Federal University (105 Bolshaya Sadovaya Str., Rostov-on-Don, 344006, Russian Federation), DSc (Phys.-Math.), **ORCID ID: 0000-0002-2935-5839**, **Scopus Author ID: 6506085787**, lchikina@sfnu.ru

Contribution of the co-authors:

Aleksey L. Chikin – research initiation, development of mathematical model, preparation of the initial version of the text, text revision, plotting

Lyubov' G. Chikina – selection and justification of numerical methods for solving equations, correction of mathematical model and calculations, computer implementation of algorithms

The authors have read and approved the final manuscript.

The authors declare that they have no conflict of interest.